MODELLING SIZE-SEGREGATION IN DENSE GRANULAR FLOWS

A THESIS SUBMITTED TO THE UNIVERSITY OF MANCHESTER
FOR THE DEGREE OF DOCTOR OF PHILOSOPHY
IN THE FACULTY OF ENGINEERING AND PHYSICAL SCIENCES

2016

Parmesh Jitesh Sakarlal Gajjar
School of Mathematics

Contents

Word count 69218

The University of Manchester

Parmesh Jitesh Sakarlal Gajjar
Doctor of Philosophy
Modelling size-segregation in dense granular flows
June 10, 2016

Dense flows of grains are commonplace throughout natural and industrial environments, from snow-avalanches down the sides of mountains to flows of cereal down chutes as it is transported from one part of a factory to another. A ubiquitous feature in all of these flows is their ability to separate the different grain types when shaken, stirred, sheared or vibrated. Many flows are sheared through gravity and these flows are particularly efficient at segregating particles based on their size, with small particles percolating to the bottom of the flow and large particles collecting at the top.

Within this mechanism, an asymmetry between the large and small particles has been observed, with small particles percolating downwards through many large particles at a faster rate than large particles rise upwards through many small particles. This alternative format thesis presents a revised continuum model for segregation of a bidisperse mixture that can account for this asymmetry. A general class of asymmetric segregation flux functions is introduced that gives rise to asymmetric velocities between the large and small grains. Exact solutions for segregation down an inclined chute, with homogenous and normally graded inflow conditions, show that the asymmetry can significantly enhance the distance for complete segregation.

Experiments performed using a classical shear-box with refractive index matched scanning are able to quantify the asymmetry between large and small particles on both bulk and particle scales. The dynamics of a single small particle indicate that it not only falls down faster than a single large particle rises, but that it also exhibits a step-like motion compared to the smooth ascent of the large grain. This points towards an underlying asymmetry between the different sized constituents. The relationship between the segregation-time and the volume fraction of small grains is analysed, and solutions presented for the steady-state balance between segregation and diffusive remixing. These help to show the good agreement between the asymmetric model and experimental data.

Segregation at the front of natural avalanches produces a recirculation zone, known as a 'breaking size-segregation wave', in which large particles are initially segregated upwards, sheared towards the front of the flow, and overrun before being resegregated again. Solutions for the structure of this recirculation zone are derived using the asymmetric flux model, revealing a novel 'lens-tail' structure. Critically, it is seen that a few large particles starting close to the bottom of the flow are swept a long way upstream and take a very long time to recirculate.

The breaking size-segregation waves highlight the important interplay between segregation and the bulk velocity field. The properties of flowing monodisperse grains are explored through experiments on a cone that produce a beautiful radial fingering pattern. Equations developed in a conical coordinate system reproduce the measured linear relationship between fingering radius and initial flux, whilst also predicting the slowing and thinning dynamics of the flow. Overall, these results illustrate the complex nature of the granular rheology and provide perspectives for future modelling of segregation in dense granular flows.

DECLARATION

No portion of the work referred to in the thesis has been submitted in support of an application for another degree or qualification of this or any other university or other institute of learning.

COPYRIGHT STATEMENT

Acknowledgements

I would like to thank my supervisor Professor Nico Gray for providing me with many of the problems featured in this thesis, and helping me to draw the work together in suitable publications. I would also like to thank my research group and collaborators, in particular Kasper van der Vaart, Anthony Thornton, Sylvain Viroulet, James Baker, Pete Kokelaar and Chris Johnson who have not only provided valuable additional scientific input to the publications, but have also been a source of many enlightening and illuminating discussions and moral support. I am also grateful for the technical support provided by Paul Tipler, David Chorlton, Dave Haigh, Malcolm Walker and Jonathan Hird, who have helped to design and build the experiments that I have used during the course of my PhD. Apart from the beautifully constructed cone that features in chapter 5, there were many other experiments that do not feature explicitly in this thesis, but were instrumental in helping shape my knowledge of the subject.

I would like to thank my examiners Dr. Lydie Staron and Dr. Raphael Assier for a thoroughly enjoyable viva. It was a pleasure and a joy discussing my work with them. I very much enjoyed the experience, and I hope that they also gained something from the scientific discussion.

Claire Hughes, the manager of Manchester Doctoral College, has been an immense source of support throughout the entire duration of my PhD studies. Not only has she been a willing listener to many of my problems, but she provided a platform for me to implement many activities related to student experience on a University scale. Organising the Postgraduate Summer Research Showcase, and other activities have been a constructive channel for my energy, and have allowed me to remain refreshed and focused on my research. I do not think I would have gotten this far if it were not for Claire.

My friends and colleagues within the University and outside have also supported me and backed me when I was struggling for motivation or feeling despondent. Out of the many names I could give, I would like to give a special mention to Grace Rice, Edgar Häner, Pallav Kant, Neeral Dodhia and Aswin Chari.

Finally, I am indebted to my dear Parents, my dear brother Vinay and my dear sister Devyani. My PhD has been at times, very stressful, but nevertheless, they have remained by my side and supported me when outside it felt like complete darkness.

FUNDING

This PhD was funded by the Engineering and Physical Sciences Research Council (EPSRC) Doctoral Training Grant EP/K502947/1.

Additional financial support for the research was provided by EPSRC grants EP/I019189/1, EP/K00428X/1 and EP/M022447/1, Natural Environment Research Council (NERC) grant NE/E003206/1, and Swiss SNF grant no. 200021-149441. Support for collaboration and conference visits was also provided by the aforementioned NERC grant and Swiss SNF grant, the EPSRS MAPLE platform grant EP/I01912X/1, and both the School of Mathematics and the Margaret Elizabeth Lee Fellowship at the University of Manchester.

CONTRIBUTIONS

This thesis constitutes a body of research conducted at the University of Manchester for consideration of the degree of Doctor of Philosophy. The major body of the thesis consists of 4 chapters: the first three chapters contain published papers, whilst the fourth is a traditional chapter. Since the majority of the original research conducted by the candidate has already been published, it is felt that the presentation in alternative format is the most appropriate.

Chapter 2 is a copy of the paper titled "*Asymmetric flux models for particle-size segregation in granular avalanches*" authored by Parmesh Gajjar (PG) and Nico Gray (JMNTG). This was published in 2014 in volume 757 of the Journal of Fluid Mechanics. The work was conducted by PG, who also wrote the paper. JMNTG initially suggested the problem, and provided editorial comments on the manuscript.

Chapter 3 is a copy of the letter titled "*Underlying Asymmetry within Particle Size Segregation*" that was published in 2015 in volume 114 of Physical Review Letters. The authors of the letter were Kasper van der Vaart (KvdV), Parmesh Gajjar (PG), Gael Epely-Chauvin (GEC), Nicolas Andreini (NA), Nico Gray (JMNTG) and Christophe Ancey (CA). The paper was jointly written by KvdV and PG. The experiments were conducted by KvdV, whilst the theory was developed by PG. Editorial comments to the manuscript were provided by JMNTG and CA. The initial experimental setup was jointly developed by GEC, NA, JMNTG and CA.

Chapter 4 is a copy of the paper titled "*Asymmetric breaking size-segregation waves in dense granular free-surface flows*" that was published in 2016 in volume 794 of the Journal of Fluid Mechanics. The authors of the article are Parmesh Gajjar (PG), Kasper van der Vaart (KvdV), Anthony R. Thornton (ART), Chris G. Johnson (CGJ), Christophe Ancey (CA) and Nico Gray (JMNTG). The paper was written by PG, who also performed all of the work on asymmetric breaking wave structures and

particle paths. The moving-bed flume experiments were performed by KvdV, with input from CA and CJG, whilst the numerical DEM simulations were performed by KvdV and ART. KvdV and ART both contributed text to the introduction section of the paper. Editorial comments were provided by KvdV, ART, CGJ, and JMNTG, whilst JMNTG kindly provided the initial problem to solve.

Chapter 5 contains some preliminary work that has not been published, and so is presented as a traditional thesis chapter. The theory and scaling was done by Parmesh Gajjar (PG). The experimental setup was designed by PG, whilst the experiments were conducted with the help of Sylvain Viroulet and Francisco Melo Da Rocha. Chris Johnson, Peter Kokelaar and Nico Gray provided direction and ideas, and the idea for the conical setup was provided by Nico Gray.

1. INTRODUCTION

1.1 Context

When many individual grains act in a collective manner, they are said to be a granular material with a rich and wonderful diversity of behaviour. Granular media occur on a vast range of scales, from 100 μm powders to ice-belts in Saturns rings that span hundreds of kilometres in size (fig. 1.1). Although the individual particles are rigid solids, acting together they can behave like solids, liquids or gases, with their own unique characteristics (Jaeger *et al.*, 1996). Granular media have shaped, and continue to shape, the physical landscape in which we live, from desert sand dunes to asteroids and interplanetary aggregates. As well as providing fascination for generation after generation, granular materials are also inter-twinned with the progress and development of mankind. Engineers as long ago as the ancient Egyptians recognised the special properties of sand as a granular material, and utilised these properties to move large, heavy obelisks into upright positions (Standelmann, 1988). As shown in figure 1.2, a temporary pit was constructed that was initially filled with sand. This sand acted like a solid, and supported the weight of the obelisk as it was moved horizontally over the pit. An orifice at the bottom of the pit was then opened up, allowing the sand to flow out of the pit under gravity. The sand continued to support the weight of the obelisk as it flowed, but as the pit emptied, the obelisk was slowly lowered into its upright position. The temporary side walls could then be removed, leaving the obelisk standing.

One of the special properties of granular materials is their natural ability to separate different particle types when agitated through shaking, stirring, shearing or vibrating. This property is very easy to observe, as simply shaking a box of muesli quickly sorts the larger nuts to the top (fig. 1.3, Rosato *et al.*, 1987). This

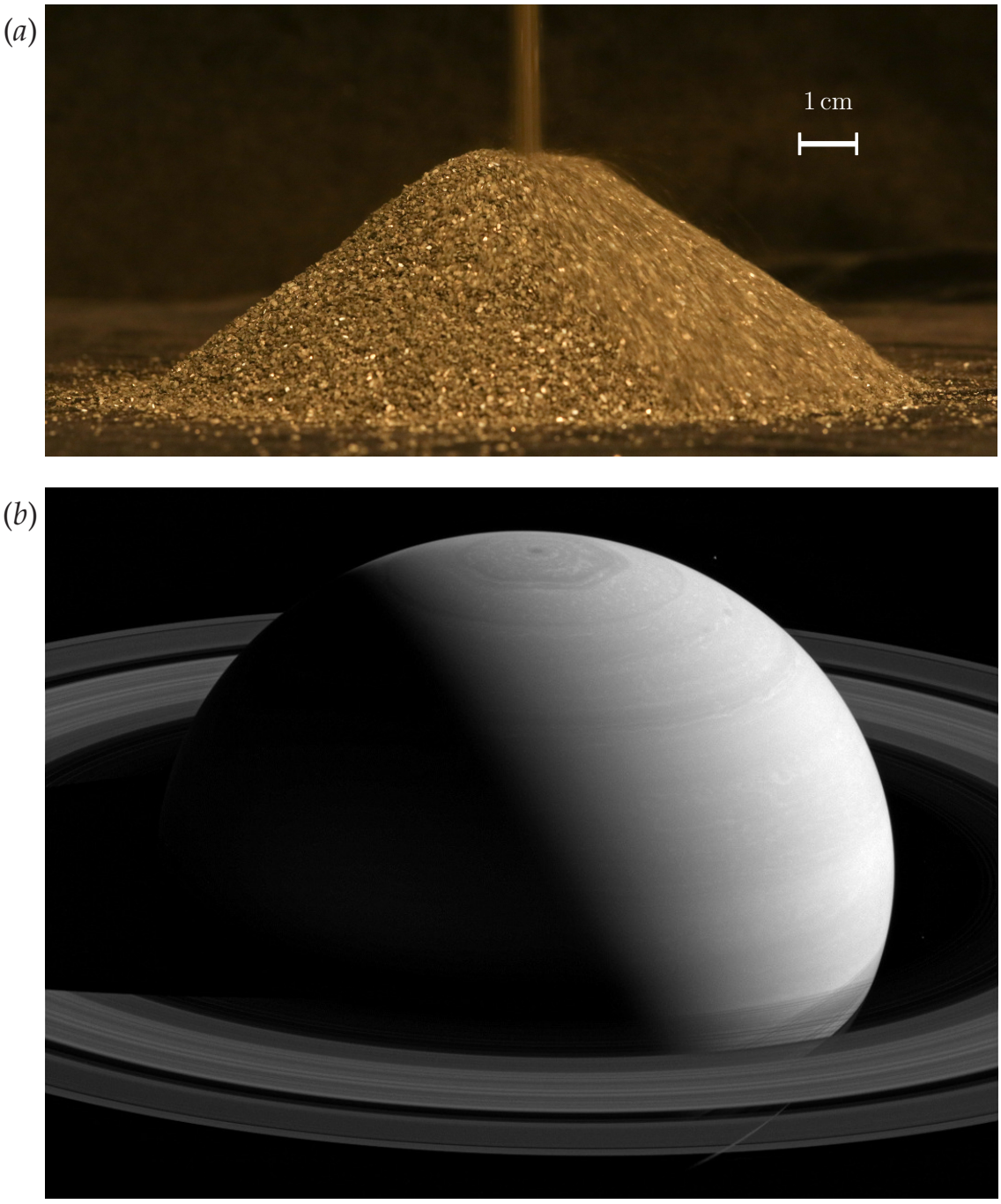

Figure 1.1: Granular media occur on a vast range of scales, from piles of 400–700 μm black coloured aquarium sand (*a*) to ice-belts in Saturns rings that span hundreds of kilometres in size (*b*). The small jet in (*a*) continually adds mass to the surface of the sand-pile, causing it to become unstable. This triggers a thin dense granular flow on the surface of the sand pile, which can be seen on the right hand side with the blurred region highlighting the motion of the grains. The white bar indicates the scale of 1 cm. The photo in (*b*) is courtesy of NASA.

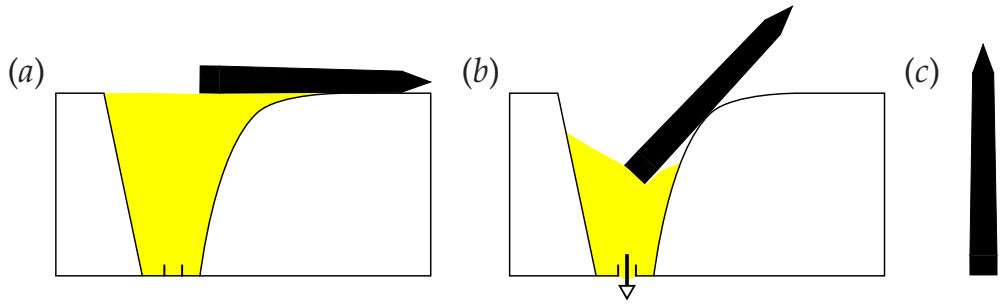

Figure 1.2: Ancient Egyptian engineers used granular materials to move large, heavy obelisks into position. (*a*) A large, temporary pit was constructed, which was filled with sand. The obelisk was moved to the top of the pit on a gently inclined plane using rope systems. The sand in the pit acted as a solid and supported the weight of the obelisk. (*b*) An orifice at the bottom of the pit was then opened, allowing the sand to drain out under gravity. The sand continued to support the weight of the obelisk, but as the amount of sand in the pit reduced, the obelisk was gently lowered into position. (*c*) Finally, once the sand drained away, the temporary pit was removed, leaving the obelisk standing in its upright position.

natural segregation has also been utilised throughout man's history to sort useful grains from stones, and even to sort potatoes from soil (Aranson & Tsimring, 2008). Mining industries also designed special devices to maximise the un-mixing of the components, so that different minerals could be easily separated (McClenaghan, 2011). However, the ubiquitous nature of the segregation process means that it also occurs in many situations where it is undesirable (Train, 1960; Johanson, 1978). Granular materials are the second most manipulated material in industry (after water), and are encountered in chemical and pharmaceutical engineering, agriculture, food-processing and construction industries to name but a few (Duran, 1999). The UK production of granular construction aggregates alone was almost 195 million tonnes in 2013, at a value of £3.3 billion (Bide *et al.*, 2014). Many of these industries require a completely homogeneous mixing; Even small separation of the constituent grains can critically degrade the product quality, leading to huge economic losses. As a consequence, understanding segregation has been the subject of study in a number of industrial fields for many years (e.g. Dyer, 1929; Maitra & Coulson, 1948; Lacey, 1954; Bourne, 1964; Olsen & Rippie, 1964; Rippie *et al.*, 1964; Rogers & Clements, 1972; Williams, 1968, 1976).

Segregation is a complex phenomena that is dependent on many factors. Differences in particle size, shape, density, surface roughness, or frictional properties

Figure 1.3: The natural ability of granular materials to segregate, i.e. separate their constituents is readily observable with a box of muesli. Simply shaking the box quickly sorts the larger nuts, fruit and raisins to the top.

can all cause separation, whilst the energy input can come through shaking, vibrating or shearing. Dense granular flows (GDR Midi, 2004) are often sheared under gravity, and are very efficient at segregating different sized particles in their thin liquid-like flows. These flows occur in many industrial environments, for example in thin layers at the free-surface layers of rotating mixer drums (Nityanand *et al.*, 1986; Shinbrot & Muzzio, 2000), during the filling of silos (Schulze, 2008; Cellai *et al.*, 2012), or when grains are transported through chutes and hoppers (Khakhar *et al.*, 1999). However, dense flows of grains are also commonplace in natural environments where they take the form of snow avalanches (Bartelt & McArdell, 2009; McElwaine & Nishimura, 2000), debris flows (Iverson, 1997) and subaqueous grain flows (Dingler & Anima, 1987). Natural granular flows can often be on the scale of several kilometres, compared to flows on the scale of several meters in industrial environments. Despite the larger scale, these flows still experience segregation, with many deposits displaying a grading (layering) of the particle sizes (e.g. Schminck, 1967; Hunter, 1985; Hunter & Kocurek, 1986; Cas & Wright, 1987). As the granular flows sort the larger grains towards the top, in a similar manner to the box of muesli, many of these deposits report 'reverse-grading' with an upward coarsening of the

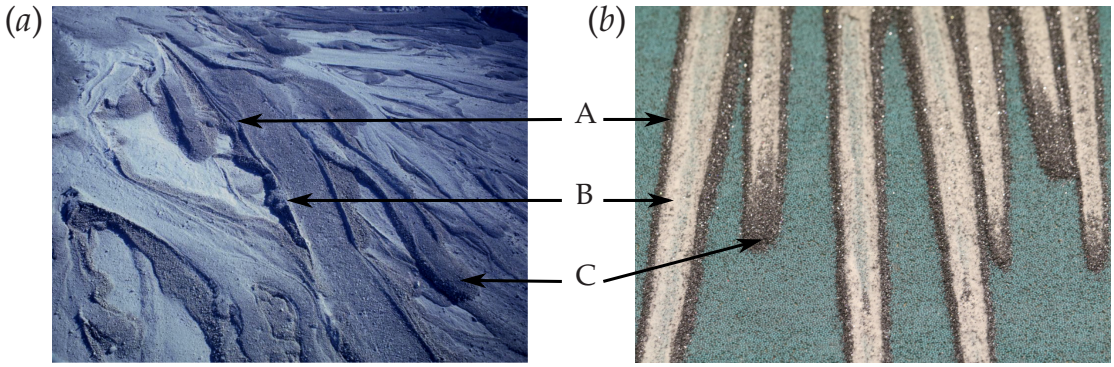

Figure 1.4: Segregation in natural geophysical granular flows allows large particles to be sheared towards the front, where they accumulate and form a resistive margin (C). This front is unstable, and can break into a series of channels that have large-particle levees (A) lined with fine particles (B). (*a*) All of these features can be seen in Pumiceous pyroclastic flow deposits from Mount St. Helens, 1980. Photograph courtesy of Dan Miller and USGS. (*b*) Laboratory experiments using a mixture of white $75 - 150\,\mu\mathrm{m}$ ballotini and $350\,\mu\mathrm{m}$ carborundum flowing over a fixed base of green $750 - 1000\,\mu\mathrm{m}$ glass beads readily produces the same features, except on a much smaller length scale to the geophysical flows. The channel in the centre of the flow deposits in part (*a*) is 10 m wide, whilst each of the channels produced in the laboratory experiments in (*b*) is approximately 1.5 cm wide.

particle-size distribution (e.g. Fisher & Mattinson, 1968; Middleton, 1970). However, the coarser grains are often sheared to the front of the flow, and so deposits also display a lateral grading in which the particle-size distribution coarsens downstream (e.g. Costa & Williams, 1984; Middleton & Hampton, 1976; Sohn & Chough, 1993). The accumulation of coarse grains at the front creates a resistive margin, which is unstable and can break into a series of finger-like channels (Pouliquen *et al.*, 1997; Pouliquen & Vallance, 1999; Woodhouse *et al.*, 2012). Such channels are evident in the Pumiceous pyroclastic flow deposits from Mount St. Helens 1980 pictured in figure 1.4(*a*), but can also be reproduced easily in the laboratory experiments shown in figure 1.4(*b*). Despite the different length scales, all of the channels exhibit coarse-grained levees (Pierson, 1986; Johnson *et al.*, 2012), which can also be lined with less frictional fine material (Kokelaar *et al.*, 2014). These features allow the flow to run-out further at higher velocities, increasing the potential destructive capabilities of the avalanche.

Understanding and modelling the segregation within densely flowing granular materials is thus of great importance for both industrial and geophysical contexts, and is the subject of this thesis. The remainder of this introduction overviews some

basic concepts of dense granular flows, provides a short summary of previous work on modelling size-segregation and outlines the problem for the thesis.

1.2 Dense granular flows

Many flows of grains, such as flows through hoppers or surface avalanches inside rotating drums are considered to be dense granular flows since they have a high solids volume fraction $0.5 < \nu < 0.65$ (e.g. Silbert *et al.*, 2001; Kumaran, 2006, 2008). The individual grains interact through collisions and friction, with transient force chains that act over short distances. These dense flows exhibit many properties of traditional liquids and can be described using continuum quantities such as the local density $\rho(\boldsymbol{x}, \boldsymbol{t})$, the local velocity $\boldsymbol{u}(\boldsymbol{x}, \boldsymbol{t})$, the local pressure $p(\boldsymbol{x}, \boldsymbol{t})$ and the local deviatoric stress $\boldsymbol{\tau}(\boldsymbol{x}, \boldsymbol{t})$. These continuum quantities can be constructed from discrete particles through the 'coarse-graining' technique (Goldhirsch, 2010; Weinhart *et al.*, 2013), which uses a continuum function to smooth over the effects of individual grains. This smoothing operation helps to overcome the problem that the length-scale of the grains in a granular system can be of the same order, or even larger than the suitable averaging lengthscale, whilst also often being similar orders of magnitude in size to the size of the system (Batchelor, 1967).

The kinematic quantities are related through mass and momentum conservation

$$\frac{\partial \rho}{\partial t} + \nabla \cdot (\rho \boldsymbol{u}) = 0, \tag{1.1}$$

$$\frac{\partial}{\partial t}(\rho \boldsymbol{u}) + \nabla \cdot (\rho \boldsymbol{u} \otimes \boldsymbol{u}) = -\nabla p + \nabla \cdot \boldsymbol{\tau} + \rho \boldsymbol{g}, \tag{1.2}$$

where ∇ is the vector differential operator, $\otimes$ is the dyadic product and $\boldsymbol{g}$ is the gravitational acceleration vector. It is the constitutive law that links the deviatoric stress $\boldsymbol{\tau}$ to other dynamic variables which characterises the 'liquid-like' flow; the specific form for dense granular flows comes from the $\mu(I)$-rheology (GDR Midi, 2004; Jop *et al.*, 2005, 2006) with a pressure and strain-rate dependence

$$\boldsymbol{\tau} = \mu(I) p \frac{\mathbf{D}}{\|\mathbf{D}\|}. \tag{1.3}$$

The strain rate tensor $\mathbf{D}$ is defined as

$$\mathbf{D} = \frac{1}{2}\left(\nabla \boldsymbol{u} + \nabla \boldsymbol{u}^{\mathrm{T}}\right), \tag{1.4}$$

with superscript T representing the transpose and $\|\mathbf{D}\| = \sqrt{\frac{1}{2}\mathrm{tr}\,\mathbf{D}^2}$. The final relation is the basal friction law (Jop *et al.*, 2005; Pouliquen *et al.*, 2006)

$$\mu(I) = \mu_1 + \frac{\mu_2 - \mu_1}{I_0/I + 1}, \tag{1.5}$$

with I the non-dimensional inertial number and I_0 a constant

$$I = \frac{2\|\mathbf{D}\|d}{\sqrt{p/\rho^*}}, \qquad I_0 = \frac{5\beta d}{2\mathscr{L}\sqrt{\nu}}. \tag{1.6a,b}$$

Here, d is the diameter of the grains, ν is the solids volume fraction, β is an empirical constant, and $\mathscr{L}$ is an empirical length scale. Angles $\mu_1 = \tan\zeta_1$ and $\mu_2 = \tan\zeta_2$ are related to the minimum and maximum slope inclinations for which steady uniform flow is possible (Forterre & Pouliquen, 2008). The lower angle ζ_1 is the angle at which the granular material starts to flow, whilst the upper angle ζ_2 is the angle above which the material will continually accelerate. In between these angles, the flow down an inclined plane has a constant steady velocity and a uniform height. For each inclination angle $\zeta \in (\zeta_1, \zeta_2)$, ζ_1 and ζ_2 also define a critical height $h_{stop}(\zeta)$ at which material will stop flowing (Pouliquen, 1999). In addition to ζ_1 and ζ_2, a third angle ζ_3 helps to define a second critical height $h_{start}(\zeta)$ which any stationary material must reach before it can be mobilised again (Pouliquen & Forterre, 2002). The five quantities β, $\mathscr{L}$, ζ_1, ζ_2 and ζ_3 determine all of the basal frictional properties, and may be empirically determined for any grains flowing over a particular base.

The $\mu(I)$-rheology has been successfully used to model several different dense granular flow regimes, for example: surface velocity profiles for steady uniform chute flows (Jop *et al.*, 2006), granular Kapitza (Forterre, 2006), granular column collapses (Lagrée *et al.*, 2011), and the discharge of silos (Staron *et al.*, 2012, 2013, 2014). Adaptations have also been made to account for dependence on the solids volume fraction (Pouliquen *et al.*, 2006), dilute flows (Jenkins, 2006) and granular elasticity (Kamrin, 2010). A recent depth-integrated version of the $\mu(I)$ rheology (Gray & Edwards, 2014; Baker *et al.*, 2016) was also shown to predict the dynamics of roll-wave instabilities and erosion-deposition waves (Razis *et al.*, 2014; Edwards & Gray, 2014). Despite this significant progress, the equations still remain mathematically ill-posed at both low and high inertial numbers (Barker *et al.*, 2015). Mathematical ill-posed problems are defined as those which are (Hadamard) unstable to short wavelength perturbations (Hadamard, 1922; Joseph & Saut, 1990).

These short wavelengths exhibit infinite growth rates, and so no mathematical solutions can be found. Numerically integrating the ill-posed equations may produce reasonably looking results, but they will change as the numerical grid is refined. Whilst, the equations are well-posed at intermediate values of the inertial number, $10^{-3} \lesssim I \lesssim 10^{-1}$ corresponding to the the dense flowing regime, problems occur at high values of $I > 10^{-1}$ where the flow becomes dilute and for quasi-static flows at low $I < 10^{-3}$. Even so-called simple flows through a silo or within a rotating drum contain regions of high and low inertial number alongside densely flowing material, and so it is important to find a modified formulation that yields well-posed behaviour at all inertial numbers. Models based around kinetic theory of gases are well developed for dilute flows (e.g. Jenkins & Savage, 1983; Campbell, 1990), and Jenkins (2006) has worked on using these models to regularise the $\mu(I)$ rheology at the transition towards dilute flows at high inertial numbers. Non-local effects, such as the dependence on the local volume fraction, are also important for quasi-static flows at low inertial numbers, and attempts have been made to use these ideas to regularise the rheology in this limit (Pouliquen & Forterre, 2009). The complex nature of these dense granular flows continues to reveal new behaviour, and chapter 5 presents some novel experiments that demonstrate how the rheology can give rise to a beautiful radial instability.

Although there has been an extensive amount of work developing the $\mu(I)$ rheology for monodisperse flows, there have only been limited attempts to develop a similar formulation for flows containing multiple grain types. Rognon *et al.* (2007) suggested an inertial number $I_{\bar{d}}$ for bidisperse flows containing two grain sizes based upon the average local grain size $\bar{d}$

$$I_{\bar{d}} = \frac{2\|\mathbf{D}\|\bar{d}}{\sqrt{p/\rho^*}}. \tag{1.7}$$

The average local grain diameter $\bar{d}$ is the mean of the small particle diameter d^s and the large particle diameter d^l, weighted by the solids volume fractions of small and large particles, $\nu^s(z)$ and $\nu^l(z)$,

$$\bar{d} = \frac{\nu^s(z)d^s + \nu^l(z)d^l}{\nu(z)}. \tag{1.8}$$

A rheology using $I_{\bar{d}}$ was shown to have reasonable correspondence with discrete element method simulations of 2D disks and 3D spheres (Rognon *et al.*, 2007; Tripathi

& Khakhar, 2011). The total local solids fraction

$$\nu(z) = \nu^s(z) + \nu^l(z) \tag{1.9}$$

refers to the total proportion of solid material in a given volume, and is equal to the sum of the local solids volume fractions of small and large particles. The total solids volume fraction ν also features in the constant I_0 (1.6b). In all current models, ν is taken to be a constant value. However, there are subtle variations in ν that depend on the local particle concentrations of a bidisperse mixture: a mixture of two grain sizes has a higher solids volume fraction than either phase in isolation, since the small grains are able to fill in the gaps between the large particles in the grain matrix. As far as the author is aware, however, no work has been done to incorporate these variations in ν within a description of bidiperse rheology. Whilst the above work has had limited success in explaining how the rheology changes with the relative local concentrations of the constituent species, they cannot directly explain the segregation that causes the changing distribution of grains. A separate equation is needed to model the segregation, which will be explored in the following section.

1.3 Size-segregation

One of the unique properties of granular materials is their ability to sort constituent particles based on their size, density, shape or even frictional differences. Out of these, size is the most efficient with even small differences in the size-ratio causing grains to to separate (Ottino & Khakhar, 2000).

1.3.1 Mechanisms for size-segregation

A number of different mechanisms have been identified to explain size-segregation (Williams, 1976; Schröter *et al.*, 2006), but it is generally accepted that the process of *kinetic sieving* (Middleton, 1970) plays a key role in segregation within dense granular flows. As the particles are sheared, the flow dilates slightly with gaps created in the grain matrix. Particle-particle contacts still dominate, with collisions between particles causing the grain matrix to continuously evolve. Gaps in the matrix regularly open up, and since smaller particles are statistically more likely to fall through

the available space than large particles, the flow acts as a *kinetic sieve* (Savage & Lun, 1988) that sorts the smaller particles downwards. One theory for the net motion of large particles is known as *squeeze expulsion* (Savage & Lun, 1988), with the almost constant solids volume fraction throughout depth (Rognon *et al.*, 2007) forcing a return flow of the larger grains towards the surface. An alternative explanation is that kinetic stress associated with velocity fluctuations (known as granular temperature) drive particles towards regions of low shear rate (Fan & Hill, 2011; Hill & Tan, 2014). Work is currently under-way to try to ascertain the fundamental driving mechanisms at work during segregation (e.g. Guillard *et al.*, 2014; Staron & Phillips, 2015).

The complete segregation of a mixture is hindered by the random walk nature of the grains, causing *diffusive-remixing* across the interface between two constituents. While this process is important at higher slope angles and faster flow velocities (Gray & Chugunov, 2006), where particles have more kinetic energy, segregation is the dominant force for slower, less kinetic flows and leads to sharp interfaces separating the constituents.

Whatever the exact mechanisms behind segregation are, it is clear that it can be a very efficient process which sorts different sized constituents into an upward coarsening grain distribution. All the models for segregation share a similar structure, which will be examined in the following section.

1.3.2 Continuum models for size-segregation

The segregation of a bi-disperse mixture of large (l) and small (s) particles flowing in the dense regime can also be described using a continuum approach. The concentrations of small and large particles, ϕ^s and ϕ^l, may be calculated as

$$\phi^s = \frac{\nu^s}{\nu}, \qquad \phi^l = \frac{\nu^l}{\nu}, \tag{1.10}$$

namely the ratio of the local solids volume fractions of small/large particles to the total local solids volume fraction. This provides suitably continuous concentration fields provided that the local solids volume fractions ν^s, ν^l are constructed using the 'coarse-graining technique' to smooth over the effects of individual particles

(Tunuguntla *et al.*, 2015). From (1.9), it can be trivially seen that

$$\phi^s + \phi^l = 1. \tag{1.11}$$

This definition effectively incorporates the void spaces within the concentration field, and each point in space in the continuum approach may only be occupied by either large or small particles (Morland, 1992). For simplicity, $\phi^s = \phi$, with $\phi^l = 1 - \phi$. The evolution of the small particle concentration ϕ can be modelled as

$$\frac{\partial \phi}{\partial t} + \nabla \cdot \left(\phi \boldsymbol{u}\right) - \frac{\partial}{\partial z}\tilde{F}\left(\phi, \dot{\gamma}, d^l/d^s\right) = \frac{\partial}{\partial z}\left(D\,\frac{\partial \phi}{\partial z}\right), \tag{1.12}$$

where the first term on the left hand side describes the time dependence of the concentration and the second term represents advection with the bulk flow. The third term models the segregation, with the segregation flux $\tilde{F}$ depending on the local particle concentration ϕ, the shear rate $\dot{\gamma}$ and other dynamic variables such as the particle size ratio d^l/d^s. It is positive to ensure that there is a net motion of small particles downwards. The sole term on the right hand side represents the diffusive remixing with diffusivity D. The following summary of different segregation models is based on the review article by Gray, Gajjar & Kokelaar (2015).

Although segregation had previously been experimentally studied for many years, the first continuum model was presented by Bridgwater *et al.* (1985). Their model resembled equation (1.12), with only the advection due to the bulk flow absent. The model was based on extensive experimental data (Bridgwater, 1976; Scott & Bridgwater, 1975; Bridgwater, 1994) which showed that both the segregation flux $\tilde{F}$ and the diffusivity D may depend on a number of kinetic variables such as the local concentration ϕ, the height of the flow z, the shear rate $\dot{\gamma}$, as well as dynamic parameters such as the particle size ratio d^s/d^l and the particle roughness. The segregation flux $\tilde{F}$ was taken as a simple product of the small particle concentration ϕ, the dilute percolation velocity p, and an arbitrary function $F(\phi)$ representing the concentration dependence. Whilst Bridgwater *et al.* (1985) were unsure of the exact form of $F(\phi)$, Dolgunin & Ukolov (1995) postulated that the concentration dependence of F was a product of the large and small particle concentrations, i.e. $F(\phi) = \phi(1 - \phi)$. Whilst both models largely shared the form of (1.12), neither presented a formal derivation. For slow, steady uniform flows at low angles of repose,

Savage & Lun (1988) used statistical mechanics and information entropy to formulate exact expressions for processes of kinetic sieving and squeeze expulsion, which balanced the downslope advection with the bulk velocity $\boldsymbol{u} = (u(z), 0, 0)$. The segregation flux $\tilde{F}$ shared a similar $\phi(1-\phi)$ concentration dependence, but with an explicit dependence on other variables such as the shear rate $\dot{\gamma}$ and the particle size ratio d^l/d^s. One drawback was that although gravity is the reason for the downward percolation of fines, it did not appear explicitly in their segregation flux. Using the method of characteristics, Savage & Lun (1988) were able to derive two dimensional non-diffuse ($D = 0$) steady state concentration profiles that matched chute flows experiments analysed using splitter plates (Savage & Lun, 1988; Vallance & Savage, 2000).

A derivation of (1.12) using mixture theory (Morland, 1992) was presented by Gray & Thornton (2005) and Gray & Chugunov (2006), which has provided a broad theoretical framework for understanding segregation. From individual momentum balances for each constituent, Gray and co-workers show that segregation results from a redistribution of the bulk pressure between the constituents. A new pressure scaling for the partial pressures p^ν ($\nu = l, s$) supported by each constituent was introduced, with

$$p^l = f^l p, \qquad p^s = f^s p, \tag{1.13}$$

where factors f^l and f^s determine the proportion of lithostatic pressure carried by the large and small particles. The large particles support a greater proportion of the overburden pressure than a volume weighted distribution ($f^l - \phi^l > 0$), and so there is a net upwards force driving the coarse grains towards the surface against gravity. The smaller particles support a smaller proportion of the overburden pressure than a volume weighted distribution ($f^s - \phi^s < 0$), and so the gravitational force is dominant, causing a net force acting downwards. Gray and co-workers employed the simplest perturbation away from a volume weighted average,

$$f^l = \phi^l + B\phi^l\phi^s, \qquad f^s = \phi^s - B\phi^l\phi^s, \tag{1.14}$$

with B a positive constant representing the magnitude of the perturbation. Since the large and small particle concentrations satisfy $\phi^s + \phi^l = 1$, the segregation flux

$\tilde{F}(\phi)$ became

$$\tilde{F}(\phi) = q\,\phi(1-\phi), \tag{1.15}$$

where $q = (B/c)g\cos\zeta$ is the mean segregation velocity, c is the co-efficient of inter-particle drag, and ζ is the slope inclination angle. The diffusive-remixing term on the right hand side of (1.12), with constant diffusivity D, arises naturally from the interaction drag between constituents in the constituent momentum balances (Gray & Chugunov, 2006).

Physically, q determines the maximum percolation of the grains, and is dependent on the particle-size ratio (Hajra & Khakhar, 2004; Thornton *et al.*, 2012), the strength of gravity and the degree of dilation/agitation in the flow. Thornton *et al.* (2006) accounted for the presence of an interstitial fluid through a reduced gravity $\hat{g} = \hat{\rho}g$, where $\hat{\rho} = (\rho^{p^*} - \rho^{f*})/\rho^{p*}$ is the relative density difference between the intrinsic density of the particles ρ^{p*} and the density of the interstitial fluid ρ^{f*}. The effect of the reduced gravity $\hat{g}$ is to slow down the segregation time-scales, which is consistent with the chute flow experiments of Vallance & Savage (2000). In the dense flow regime, particle-particle contacts determine the dynamics and so the buoyancy effect of the interstitial fluid is more important that the fluid viscosity. When the particles have the same density as the fluid, and are neutrally buoyant ($\hat{\rho} = 0$), no segregation takes place.

In dense fluid-like avalanche flows, the local shear rate $\dot{\gamma}$ affects the dilation and agitation, thus is related to the mean segregation velocity through the ratio B/c. Behind assuming B and c to be constant is the implicit assumption that the shear rate $\dot{\gamma}$ is constant throughout the depth of the flow. Whilst this is a good leading order approximation for gravity driven free surface flows (GDR Midi, 2004; May *et al.*, 2010*b*; Gray & Ancey, 2011), it breaks down in confined granular systems where the shear rate can become non-uniform. In order to model this, May *et al.* (2010*b*) assumed that the ratio B/c was an increasing function of the shear rate $\dot{\gamma}$, with no segregation in regions of no shear and rapid segregation with strong shear. It was found that the shear rate was highest close to the lower boundary of an annular shear cell and decreased significantly above a few particles deep (May *et al.*, 2010*a*). This motivated the height dependent segregation flux

$$\tilde{F}(\phi) = q(z)\phi(1-\phi), \tag{1.16}$$

with the mean segregation speed $q(z)$ decreasing with the height z. A different approach by Marks & Einav (2011) and Fan *et al.* (2014) directly included the shear rate dependence by assuming $q \propto \dot{\gamma}$. In order to match experimental results for segregation in bounded heaps (Fan *et al.*, 2012, 2013), Fan *et al.* (2014) also employed a spatially non-uniform velocity profile $u = u(x, z)$ and an extra downstream diffusion term, so that the total diffusive terms were

$$\frac{\partial}{\partial x}\left(D\,\frac{\partial \phi}{\partial x}\right) + \frac{\partial}{\partial z}\left(D\,\frac{\partial \phi}{\partial z}\right). \tag{1.17}$$

Using this, Fan *et al.* were able to quantify different regimes in which the advection, segregation and diffusion terms dominate. In general, the diffusive remixing could take the form $\nabla \cdot \big(D\,\nabla\phi \big)$, where the diffusivity D is isotropic as the random motion of the grains has no preferential direction (Bridgwater, 1994). However, normally only the normal z derivatives are considered when assuming a steady uniform flow in the stream wise x direction (Pouliquen, 1999; Rognon *et al.*, 2007; Gray *et al.*, 2006).

An alternative explanation for segregation by Fan & Hill (2011) and Hill & Tan (2014) holds fluctuations in kinetic stress gradients (also known as granular temperature fluctuations) to be the cause of segregation, rather than it being a gravity driven process. Fan & Hill (2011) examined segregation inside a vertical chute, where there is no lithostatic pressure as the flow is entirely in the vertical direction. Instead, the segregation occurs as a result of a redistribution of kinetic stress gradients, with the segregation flux

$$\tilde{F}(\phi, \partial\sigma_{zz}/\partial z) = \frac{1}{\rho}\frac{B}{c}\phi(1-\phi)\frac{\partial \sigma_{zz}}{\partial z}, \tag{1.18}$$

where σ_{zz} is the kinetic stress. This has a close resemblance to (1.15), where $g\cos\zeta$ is the gradient of the lithostatic pressure $p = g\cos\zeta(h-z)$. Hill & Tan (2014) showed in their simulations that gravity-driven pressure fluctuations between the constituents are not active in a rotating drum, with gravity acting only implicitly through kinetic stress gradients. Recently Staron & Phillips (2015) attempted to distinguish between the pressure redistribution (1.14) and kinetic stress gradients, but were not able to conclusively decide which process was dominant.

It is interesting to note that both size and density differences can be incorporated into the general framework of (1.12) by appropriately defining the segregation flux

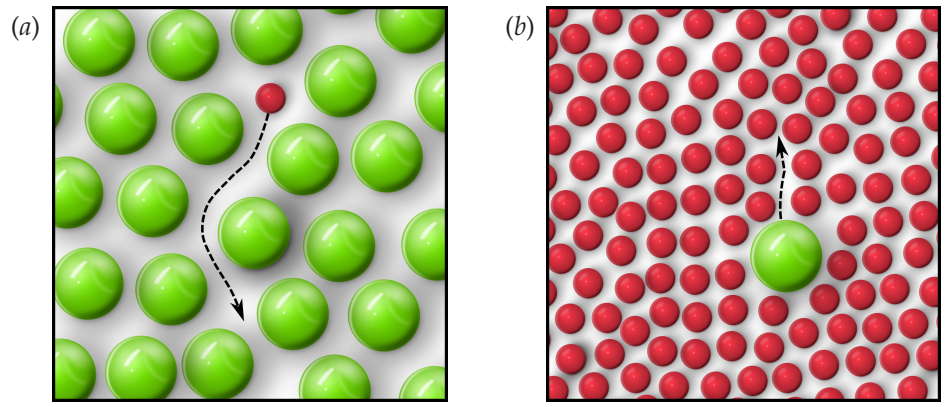

Figure 1.5: Golick & Daniels (2009) recently observed that a single small particle is able to percolate through a matrix of fine particles at a faster rate (*a*) than a single large particle is squeezed upwards through a matrix of fines (*b*). However, no quantitative model was provided. This thesis develops a continuum model to account for these observations.

$\tilde{F}$. The mixture theory derivation of Gray & Ancey (2015) retains the quadratic $\phi(1-\phi)$ form of (1.15), but also includes a concentration dependence in the mean segregation speed, which takes account of the density differences $q = q^s(\rho^s, \rho^l)$. Here, ρ^s and ρ^l are the densities of the small and large particles respectively. Depending on the size and density ratios, there are eight qualitatively different flux functions that may form, with the theory able to predict size and density combinations that display zero segregation (Vallance & Savage, 2000). The bulk flow is no longer incompressible in this theory, and so a similar equation governs the large particle behaviour, except $q = q^l(\rho^s, \rho^l)$. A different formulation for size and density segregation by Tunuguntla *et al.* (2014) incorporates the shear-rate dependence alongside the size and density differences,

$$\tilde{F} = \frac{g\cos\zeta}{c}\dot{\gamma}(\hat{s}^a - \hat{\rho})\frac{\phi(1-\phi)}{\phi + (1-\phi)\hat{s}^a}. \tag{1.19}$$

Here $\hat{s} = d^l/d^s$ is the ratio of the large and small particle diameters, $\hat{\rho} = \rho^l/\rho^s$ is the ratio of the densities of the two particles, and $a = 1$, 2 or 3 for scalings with length, surface-area or volume of the particles. This latter approach of Tunuguntla *et al.* (2014) was motivated by Marks *et al.* (2012), who derived an expression for segregation of a polydisperse material with a continuous size and density distribution.

1.4 Problem: modelling an asymmetry between different sized constituents

Golick & Daniels (2009) recently observed that a single small particle is able to percolate downwards through a matrix of large particles at a faster rate (fig. 1.5*a*) than a single large particle is squeezed upwards through a matrix of fines (fig. 1.5*b*); However, they did not provide a quantitative model. Similar observations to these were also found at École Polytechnique Fédérale de Lausanne during early work on the shearbox set-up (van der Vaart *et al.*, 2015). Given that segregation is such a ubiquitous process with wide ranging technological, economic and environmental consequences, and that none of the models in § 1.3.2 had previously assessed these observations, it was felt that a refined segregation model should be developed that could capture the behaviour in figure 1.5.

This thesis contains a body of work which has developed the continuum model for segregation (1.12) to account for the asymmetry between large and small particles. The unique contribution is to generalise the dependence of the segregation flux $\tilde{F}$ on the small particle concentration ϕ through the use of asymmetric flux functions. These flux functions result in an asymmetry in the particle velocities, with the maximum speed of small particles faster than the maximum speed of large particles. The effects of the asymmetry are examined by deriving exact solutions for a number of different flow conditions. The model also shows very good agreement with experimental data obtained from a shearbox experiment. This revised continuum model draws parallels with the original postulations by Bridgwater *et al.* (1985), but the work in this thesis provides an extensive analysis on the effects of this asymmetric concentration dependence. A summary of each chapter is provided in the following section.

1.5 Structure and chapter synopsis

This alternative format thesis is structured as 4 main chapters, which includes work that has already been published. Chapters 2–4 include published articles which

retain their own formatting, page numbering and equation numbering. Chapter 5 is a traditional thesis chapter.

Chapter 2 contains the article by Gajjar & Gray (2014) titled "*Asymmetric flux models for particle-size segregation in granular avalanches*", which was published in the Journal of Fluid Mechanics. The paper derives an asymmetric flux model for segregation in dense granular flows from a mixture theory formulation. Using the method of characteristics, exact solutions are presented for homogeneous and normally graded inflow conditions. These solutions allow the effects of the asymmetric particle behaviour to be analysed. Chapter 3 contains the letter by van der Vaart *et al.* (2015) titled "*Underlying Asymmetry within Particle Size Segregation*", which has been published in Physical Review Letters. The letter presents experimental results from segregation in a classical shear box coupled with refractive index matched scanning. The asymmetric behaviour is quantified on both bulk and particle scales, and demonstrates good quantitative agreement with the asymmetric flux model. Additional material is presented at the end of chapter 3 that explains the theoretical results used to fit the model with the experimental data. Chapter 4 contains the article by Gajjar *et al.* (2016) titled "*Asymmetric breaking size-segregation waves in dense granular free-surface flows*". This was published in the Journal of Fluid Mechanics. The article reports observations from experiments and discrete element method simulations in a moving-bed flume, which reveal that a few large particles travel very slowly through regions of many small particles at the rear of the flow. The previously derived asymmetric model is used to solve for the structure of the recirculation, known as a 'breaking size-segregation wave'. The exact solutions derived using the method of characteristics have similar behaviour to both the experiments and simulations. Chapter 5 takes a different direction to the previous 3 chapters, and examines a monodisperse flow with no segregation. Experimental results are presented of flow in a conical geometry, with the front seen to develop an instability that produces a regular pattern of fingers similar to those in figure 1.4. This chapter highlights the complexity of flowing granular mixtures, and helps to provide a context for future directions in segregration modelling. Finally, chapter 6 draws together the research in this thesis with conclusionary remarks.

1.5.1 Equation numbering

A note should be made of the equation numbering employed in this thesis. As the thesis is presented in alternative format with 3 of the chapters containing self-contained papers that have been published, there is duplication of the equation numbers between the main thesis body and the individual chapters. As a consequence, when an equation from one of the papers is referenced in the main thesis body, it will be proceeded by a superscript asterisk along with a reference to the chapter in which it is found. For example:

...in equation (2.10) of chapter 2, it is shown that...*

refers to equation (2.10) of Gajjar & Gray (2014) which is contained in chapter 2. If the equation number is not proceeded by a superscript asterisk, then it refers to an equation from the main thesis body.

2. Asymmetric flux models for particle-size segregation in granular avalanches

---

This chapter is a reprint of the article titled "*Asymmetric Flux Models for Particle Size Segregation*" by P. Gajjar and J. M. N. T. Gray, which was published in volume 757 of the Journal of Fluid Mechanics (2014), on pages 297–329. The digital object identifier (DOI) for this article is http://dx.doi.org/10.1017/jfm.2014.503.

J. Fluid Mech. (2014), *vol.* 757, *pp.* 297–329.
doi:10.1017/jfm.2014.503

Asymmetric flux models for particle-size segregation in granular avalanches

P. Gajjar[1,†] and J. M. N. T. Gray[1]

[1]School of Mathematics and Manchester Centre for Nonlinear Dynamics, University of Manchester, Manchester M13 9PL, UK

(Received 4 April 2014; revised 25 July 2014; accepted 23 August 2014)

Particle-size segregation commonly occurs in both wet and dry granular free-surface flows through the combined processes of kinetic sieving and squeeze expulsion. As the granular material is sheared downslope, the particle matrix dilates slightly and small grains tend to percolate down through the gaps, because they are more likely than the large grains to fit into the available space. Larger particles are then levered upwards in order to maintain an almost uniform solids volume fraction through the depth. Recent experimental observations suggest that a single small particle can percolate downwards through a matrix of large particles faster than a large particle can be levered upwards through a matrix of fines. In this paper, this effect is modelled by using a flux function that is asymmetric about its maximum point, differing from the symmetric quadratic form used in recent models of particle-size segregation. For illustration, a cubic flux function is examined in this paper, which can be either a convex or a non-convex function of the small-particle concentration. The method of characteristics is used to derive exact steady-state solutions for non-diffuse segregation in two dimensions, with an inflow concentration that is (i) homogeneous and (ii) normally graded, with small particles above the large. As well as generating shocks and expansion fans, the new asymmetric flux function generates semi-shocks, which have characteristics intersecting with the shock just from one side. In the absence of diffusive remixing, these can significantly enhance the distance over which complete segregation occurs.

Key words: granular materials, mixing, pattern formation

1. Introduction

Granular avalanches are dense shallow flows of grains down an incline, which may be continuous or intermittent (Pudasaini & Hutter 2007). As well as occurring in chute flows (Savage & Hutter 1989; Gray, Wieland & Hutter 1999; Khakhar, McCarthy & Ottino 1999; Pouliquen 1999), avalanches are an integral component of more complex granular flows that involve static or slowly moving regions, such as in hoppers, heaps and rotating drums (Nityanand, Manley & Henein 1986; Gray 2001; GDR MiDi 2004; Fan *et al.* 2012, 2014). There is a wide body of literature modelling avalanches, which makes the following assumptions: (i) the granular material is an incompressible continuum (Savage & Hutter 1989; Hutter, Wang &

†Email address for correspondence: parmesh.gajjar@alumni.manchester.ac.uk

Pudasaini 2005); (ii) the transient and constantly evolving force chains only act over short distances and are well approximated by a lithostatic pressure balance (Pitman *et al.* 2003; Rognon *et al.* 2007); and (iii) the solids volume fraction Φ is constant in the range 0.49–0.64 (Silbert *et al.* 2001; Kumaran 2006, 2008), a slight dilation from a static arrangement of random close-packed spheres (Berryman 1983). These three assumptions are also good approximations for bidisperse and polydisperse flows (Rognon *et al.* 2007; Tripathi & Khakhar 2011; Marks, Rognon & Einav 2012). Avalanches are notoriously good at sorting particles by size. Not only can this lead to a rich variety of patterns in flowing mixtures arrested by shock waves or basal deposition (e.g. Williams 1976; Gray & Hutter 1997; Hill *et al.* 1999; Ottino & Khakhar 2000), but also it can be problematic in a wide range of sectors, from agriculture and food manufacturing, to mining, bulk chemical processing and pharmaceutical production (e.g. Dyer 1929; Johanson 1978; Shinbrot & Muzzio 2000; Marks *et al.* 2013). Segregation also occurs in many granular flows in our natural environment, including snow avalanches (Savage & Hutter 1989; Bartelt & McArdell 2009), debris flows (Iverson 1997; Stock & Dietrich 2006), pyroclastic surges (Calder, Sparks & Gardeweg 2000) and subaqueous grain flows (Dingler & Anima 1987), which create a diverse array of sedimentary deposits (Branney & Kokelaar 1992) as well as subtle feedback effects that can enhance flow run-out (Iverson & Vallance 2001; Johnson *et al.* 2012; Kokelaar *et al.* 2014).

The dominant segregation mechanisms in granular avalanches are widely thought to be those of *kinetic sieving* (Middleton 1970) and *squeeze expulsion* (Savage & Lun 1988). As the grains avalanche downslope, adjacent layers of grains are sheared over one another, and the volume fraction is slightly dilated. This creates a random fluctuating sieve in which smaller grains preferentially fall down through gaps that open up beneath them, because they are statistically more likely than the larger grains to fit into the available space (Savage & Lun 1988). The solids volume fraction in monodisperse avalanches is almost constant with depth (Silbert *et al.* 2001) and this is also true in bidisperse systems (Rognon *et al.* 2007). As a result, there has to be a return flow of large particles towards the free surface due to force imbalances, which Savage & Lun (1988) termed ‘squeeze expulsion’. The combination of kinetic sieving and squeeze expulsion is a highly efficient mechanism for sorting, with even slight differences in the size ratio causing the grains to separate into inversely graded layers, with large particles lying on top of the fines. This upward coarsening of the particle-size distribution is also referred to as ‘reverse grading’ (e.g. Schminck 1967; Fisher & Mattinson 1968; Sohn & Chough 1993).

Gray & Thornton (2005) derived a bidisperse continuum model for segregation using mixture theory (e.g Morland 1992), with the segregation dependent on a redistribution of partial pressures. The fundamental idea behind this model is that larger particles support a greater proportion of the lithostatic overburden pressure as the small particles percolate downwards. This is consistent with the kinetic sieving idea, but Golick & Daniels (2009) suggested that the physical reason for increased forces may simply be that the large grains have significantly more contacts than the fines, and are, therefore, more likely to be part of force chain networks. In standard mixture theory, coarse grains would support a volume-fraction-weighted proportion of the pressure, in order to balance the gravitational force pulling them downwards. However, because they support a larger fraction of the overburden pressure, the pressure gradient pushing them upwards is slightly bigger than the gravitational force pulling them downwards, which produces a net upward force that drives them towards the surface. Conversely, the gravitational force acting on the small particles is larger

than the pressure gradient that they experience, and hence they percolate downwards. The perturbations of the pressure away from the volume-fraction-weighted lithostatic pressure distribution in standard mixture theory are therefore crucial for segregation.

When either of the large or small particles are in a pure phase, they must carry all of the load, and the pressure perturbation must be zero for no net motion. Gray & Thornton (2005) postulated a quadratic concentration dependence for the pressure perturbations, with zero perturbation at 0 and 100 % concentration of particles. This yields a flux function that is symmetric about 50 % concentration. When this model is combined with diffusive remixing of the particles (Gray & Chugunov 2006), it is able to quantitatively match experimental measurements of segregation in chute flow experiments (Savage & Lun 1988; Dolgunin & Ukolov 1995; Vallance & Savage 2000; Wiederseiner *et al.* 2011) as well as discrete element simulations of segregation in periodic boxes (Thornton *et al.* 2012). It has also been successfully extended to include interstitial fluid (Thornton, Gray & Hogg 2006), particle deposition (Gray & Ancey 2009), non-lithostatic pressure (Fan & Hill 2011), depth averaging (Gray & Kokelaar 2010*b*,*a*; Woodhouse *et al.* 2012) and polydisperse distributions with discrete grain-size classes (Gray & Ancey 2011) as well as a continuous spectrum of particle sizes (Marks *et al.* 2012).

Although the quadratic model has proved to be very effective at modelling segregation, Golick & Daniels (2009) observed, in their annular ring shear cell experiments, that a small particle falls through a matrix of large particles faster (figure 1*a*) than a large particle rises through a matrix of small particles (figure 1*b*). Equivalently, a single small particle is more likely to find a percolation path through a matrix of large grains, than a single large grain is able to push the fines out of the way as it is squeezed upwards. It is important to stress from the outset that this asymmetry in the segregation velocities is still consistent with the mass balance of both species, because the differential segregation rates occur at different concentrations. Several authors have found asymmetric segregation rates by modelling the segregation velocity with a dependence on the shear strain rate (May *et al.* 2010*a*; May, Shearer & Daniels 2010*b*; Marks & Einav 2011). As these models only include a symmetric quadratic concentration dependence, the local asymmetry in the segregation rates is independent of the local particle concentration, and only dependent on the flow height. In some flows, however, the shear strain rate can be approximated by a constant (GDR MiDi 2004; May *et al.* 2010*b*; Gray & Ancey 2011), and so asymmetric segregation rates must instead be a result of the local particle concentration. This paper examines the impact of the local particle concentration by modelling the non-reciprocity of the segregation rates using a concentration-dependent flux function that is asymmetric about its maximum point.

The asymmetry can be achieved by using higher-order flux functions, such as cubic or quartic ones, which harks back to some of the early work on segregation by Bridgwater, Foo & Stephens (1985), who directly postulated a cubic form of the flux function with a repeated root when the small-particle concentration equalled 100 %. Savage & Lun's (1988) information entropy approach also yielded an even more complex nonlinear concentration dependence. The asymmetric flux functions studied here can either be (i) convex or (ii) non-convex, with a single inflection point that occurs at high small-particle concentrations. The non-convex case implies that the maximum large-particle velocity occurs when there are several large particles in close proximity to each other (figure 1*c*) as opposed to the convex case where the maximum rise rate occurs for a single particle on its own (figure 1*b*). This is the segregation equivalent of the well-known sedimentation problem (Kynch 1952; Rhee,

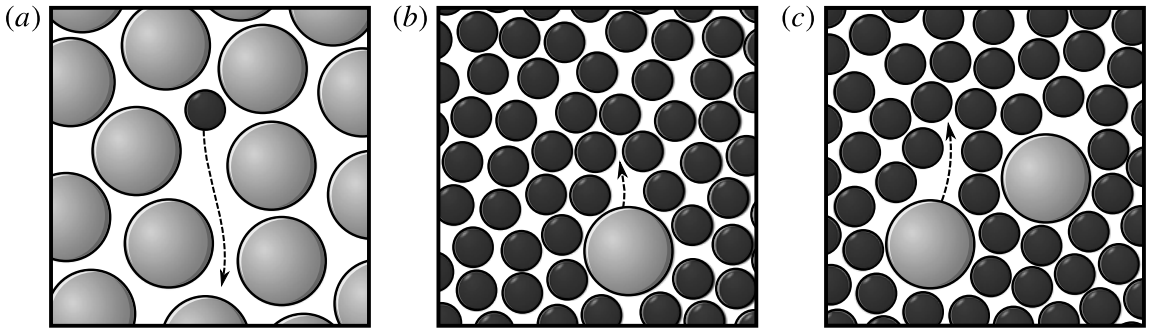

FIGURE 1. Experimental observations (Golick & Daniels 2009) suggest that a single small particle (*a*) percolates downwards through a matrix of large particles at a faster rate than a single large particle (*b*) rises through a matrix of small particles. This asymmetry at the extremes of local concentration can be modelled by an asymmetric segregation flux, which can be either convex or non-convex, with an inflection point at high small-particle concentrations (see § 3). In the latter case, a single large particle (*b*) will rise towards the surface slower than an intermediate concentration when there are several large particles (*c*) rising at the same time.

Aris & Amundson 1986) in which two particles settle under gravity in a viscous fluid faster than a single particle alone (Batchelor 1972). Similar mathematical problems also occur in traffic flow (Lighthill & Whitham 1955), where the velocity of cars tends to zero very rapidly as the road approaches maximum density. In order to model the asymmetric behaviour in these environments, a number of flux functions have been proposed, including logarithmic, cubic and quartic forms (Greenberg 1959; Shannon, Stroupe & Tory 1963). In this paper, the mixture theory derivation of the segregation equation is extended to the case of asymmetric flux functions and the implications for the homogeneous and normally graded inflow problems of Gray & Thornton (2005) and Thornton *et al.* (2006) are investigated.

2. The governing segregation equation

2.1. *Mixture theory*

Consider a bidisperse mixture of large (l) and small (s) particles of the same density flowing down a slope inclined at an angle ζ to the horizontal. As shown in figure 2, a coordinate system $Oxyz$ is defined with the x coordinate pointing down the slope, the y coordinate pointing horizontally across the plane and the z coordinate being the upward-pointing normal. Following Gray & Thornton (2005), the interstitial fluid is neglected. This implicitly assumes that the solids volume fraction is constant and uniform throughout the mixture (Rognon *et al.* 2007) and that the density of the interstitial fluid is incorporated into the density of the grains (Thornton *et al.* 2006). In this framework, each constituent ($\nu = l, s$) occupies a local volume fraction ϕ^ν per unit granular volume (Morland 1992) and the sum of the local volume fractions is equal to unity,

$$\phi^l + \phi^s = 1. \tag{2.1}$$

Each constituent has a partial density ρ^ν, a partial velocity $\boldsymbol{u}^\nu$ and a partial pressure p^ν. These are defined per unit volume of the mixture, and are related to the intrinsic properties of the constituents, defined per unit volume of the constituent, by

$$\rho^\nu = \phi^\nu \rho^{\nu*}, \quad \boldsymbol{u}^\nu = \boldsymbol{u}^{\nu*}, \quad p^\nu = \phi^\nu p^{\nu*}, \tag{2.2a–c}$$

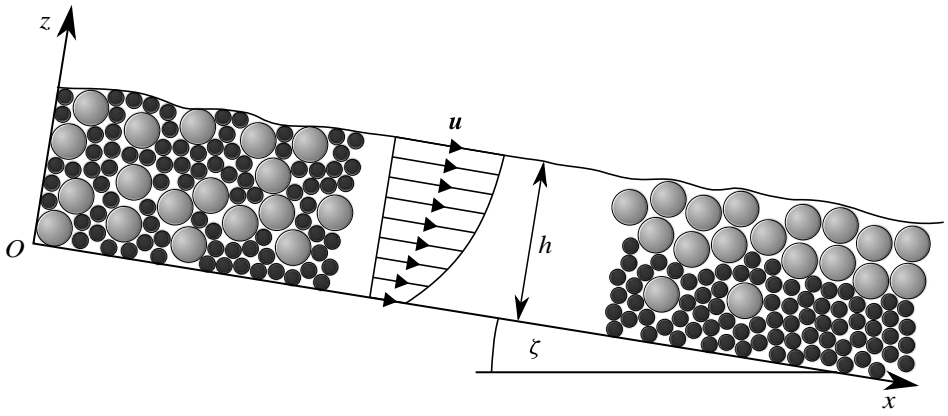

FIGURE 2. A coordinate system $Oxyz$ is defined with the x-axis pointing down the plane, the y-axis horizontally across the plane (pointing into the page) and the z-axis being the upward-pointing normal. The slope is inclined at an angle ζ to the horizontal, h is the flow depth and $\boldsymbol{u}$ is the bulk velocity, which generally includes both shear and basal slip. From a homogeneously mixed inflow at the origin, the particles segregate into inversely graded layers, with large particles overlying fines. With asymmetric segregation models, the distance for complete segregation is dependent on the inflow concentration and can be significantly longer than the quadratic flux case.

where a starred quantity denotes an intrinsic property. The bulk density, bulk velocity and bulk pressure of the flow are defined as

$$\rho = \rho^l + \rho^s, \quad \rho\boldsymbol{u} = \rho^l\boldsymbol{u}^l + \rho^s\boldsymbol{u}^s, \quad p = p^l + p^s, \tag{2.3a–c}$$

where the partial velocity $\boldsymbol{u}^\nu$ and the bulk velocity $\boldsymbol{u}$ have components (u^ν, v^ν, w^ν) and (u, v, w) in the (x, y, z) directions, respectively.

Each constituent satisfies its own mass conservation law,

$$\frac{\partial \rho^\nu}{\partial t} + \boldsymbol{\nabla}\cdot(\rho^\nu\boldsymbol{u}^\nu) = 0 \quad (\nu = l, s), \tag{2.4}$$

where $\boldsymbol{\nabla}$ is the standard vector differential operator 'del' and $\cdot$ is the dot product. The bulk mass balance is obtained by summing (2.4) over both constituents. Since the intrinsic densities of the two phases are assumed to be equal, it follows from (2.1)–(2.4) that the bulk velocity field is incompressible, i.e. $\boldsymbol{\nabla}\cdot\boldsymbol{u} = 0$. Each constituent also satisfies its own momentum conservation law,

$$\frac{\partial}{\partial t}(\rho^\nu\boldsymbol{u}^\nu) + \boldsymbol{\nabla}\cdot(\rho^\nu\boldsymbol{u}^\nu\otimes\boldsymbol{u}^\nu) = -\boldsymbol{\nabla}p^\nu + \rho^\nu\boldsymbol{g} + \boldsymbol{\beta}^\nu \quad (\nu = l, s), \tag{2.5}$$

where $\otimes$ denotes the dyadic product, $\boldsymbol{g}$ is the gravitational force and $\boldsymbol{\beta}^\nu$ is the interaction force exerted on constituent ν by the other constituent. By Newton's third law, these interaction forces are equal and opposite, $\boldsymbol{\beta}^l = -\boldsymbol{\beta}^s$.

2.2. *Normal momentum balance*

It is assumed that the flow is shallow, i.e. the depth of the flow is much less than its length, so that the normal acceleration terms in the constituent momentum balances (2.5) may be neglected. The individual constituent momentum balances may be summed to give the bulk normal momentum balance,

$$0 = -\frac{\partial p}{\partial z} - \rho g\cos\zeta\,. \tag{2.6}$$

By assuming the pressure to be zero at the free surface $z=h$, (2.6) can be integrated to show that the bulk pressure field is lithostatic,

$$p=\rho g(h-z)\cos\zeta\,. \tag{2.7}$$

Following Gray & Thornton (2005), each constituent is assumed to support a proportion of the bulk lithostatic pressure,

$$p^s=f^s p, \quad p^l=f^l p, \tag{2.8a,b}$$

where (2.3c) implies that the scaling factors f^ν must sum to unity,

$$f^l+f^s=1. \tag{2.9}$$

Each constituent cannot support negative pressure, so f^ν lies in the range $0\leqslant f^\nu\leqslant 1$.

Following Gray & Thornton (2005) and Gray & Chugunov (2006), the interaction drag $\boldsymbol{\beta}^\nu$ in the constituent momentum balance (2.5) is assumed to take the form

$$\boldsymbol{\beta}^\nu=p\,\boldsymbol{\nabla}f^\nu-\rho^\nu c(\boldsymbol{u}^\nu-\boldsymbol{u})-\rho d\,\boldsymbol{\nabla}\phi^\nu \quad (\nu=l,\,s). \tag{2.10}$$

The first term on the right-hand side combines with the partial pressure gradient term in (2.5) to ensure that the particles are driven by intrinsic pressure gradients rather than partial ones. The second term is a linear drag between constituent ν and the bulk particle matrix, and has coefficient c. Finally, the third term represents the diffusive remixing, whose strength is given by the diffusion coefficient d. It models the random walks that particles experience as they are sheared in the flow (Dolgunin & Ukolov 1995; Gray & Chugunov 2006). With the interaction drag (2.10) and the lithostatic pressure distribution (2.7), the momentum balance (2.5) implies that the normal particle flux of constituent ν is

$$\phi^\nu w^\nu=\phi^\nu w+(f^\nu-\phi^\nu)\frac{g}{c}\cos\zeta-\frac{d}{c}\frac{\partial\phi^\nu}{\partial z} \quad (\nu=l,\,s), \tag{2.11}$$

where the first term on the right-hand side gives the normal advection due to the bulk velocity, the second term gives the segregation flux and the last term gives the flux due to diffusive remixing. The factor $f^\nu-\phi^\nu$ controls whether a particle will rise or fall due to segregation, and is essentially the proportion by which the pressure deviates away from the volume-fraction-weighted average. In the absence of diffusion, large particles carry excess pressure and will therefore rise, while small grains carry less of the overburden and fall relative to the bulk. In general, the factors $f^\nu-\phi^\nu$ are functions of the large- and small-particle concentrations, ϕ^l and ϕ^s (see e.g. Gray & Ancey 2011), but in the bidisperse case $\phi^l=1-\phi^s$ from (2.1) and thus $f^\nu-\phi^\nu$ can be written solely in terms of the small-particle concentration ϕ^s as

$$\left.\begin{aligned} f^l-\phi^l&=+bF(\phi^s),\\ f^s-\phi^s&=-bF(\phi^s),\end{aligned}\right\} \tag{2.12}$$

where the function F describes the dependence of the segregation on the small-particle concentration ϕ^s, and b is a parameter that is dependent on the shear rate, the local pressure, the grain-size ratio and possibly other variables. The opposite signs in (2.12) ensure that the segregation fluxes are equal and opposite for either constituent, which preserves the global mass balance, i.e. summing (2.11) over both constituents,

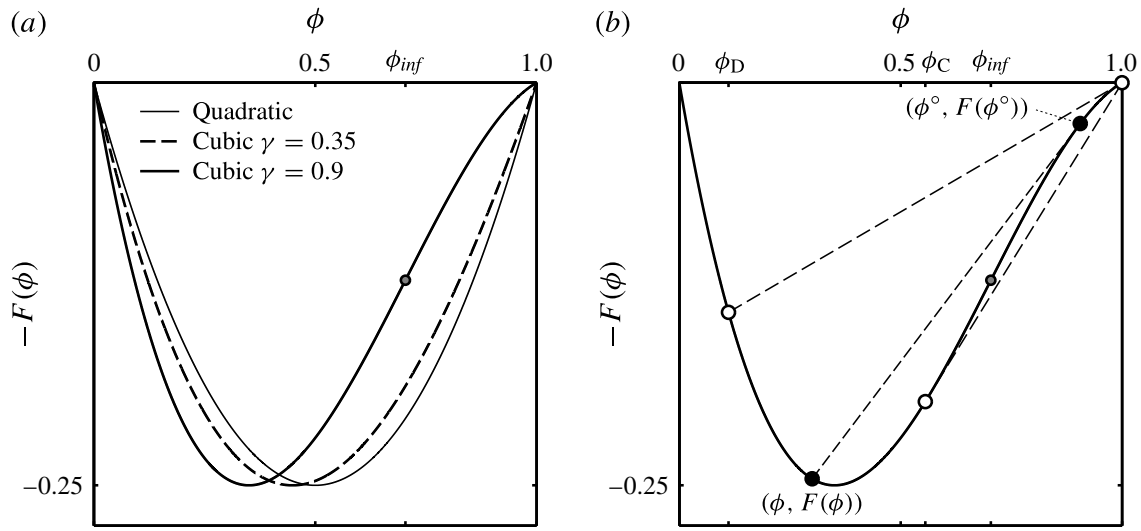

FIGURE 3. (*a*) The simple cubic function (3.4) demonstrates the behaviour of the entire class of asymmetric functions, with parameter γ in the range $0 < \gamma \leqslant 1$. For small amounts of asymmetry ($\gamma = 0.35$, thick dashed line), the flux function remains convex, but larger amounts of asymmetry ($\gamma = 0.90$, thick solid line) causes the flux function to be non-convex, with a single inflection point at ϕ_{inf} (grey circle). The symmetric quadratic flux function (2.14) is shown for comparison (thin solid line) and corresponds to $\gamma \to 0$. (*b*) Non-convex flux functions yield a special feature in the exact solution known as a *semi-shock*. A semi-shock is formed between two points ϕ and ϕ° (black circles), where the chord between the two points is tangential to the flux curve F at ϕ°. There are two pairs of points $\{1, \phi_C\}$ and $\{\phi_D, 1\}$ (open circles) that are of particular importance in the construction of the exact solution. The chord between ϕ_C and $\phi = 1$ is tangential to the flux curve at ϕ_C, whilst the chord linking ϕ_D and $\phi = 1$ is tangential to the flux curve at $\phi = 1$. Negative values of the flux function, $-F(\phi)$, are plotted since the gradients then correspond to the gradients in the exact solution, as explained in § 4.

using (2.1) and (2.12), implies that $\sum_{\nu=l,s} \phi^\nu w^\nu = w$, which is consistent with (2.3b). For large particles to rise, F must be positive, and, in order that there is no net motion whenever the particles are in a pure phase, it must satisfy the constraints

$$\left.\begin{aligned} F = 0, \quad \phi^s = 0, \\ F = 0, \quad \phi^s = 1. \end{aligned}\right\} \tag{2.13}$$

Gray & Thornton (2005) postulated a quadratic flux function,

$$F(\phi^s) = \phi^s(1 - \phi^s), \tag{2.14}$$

which is symmetric about the maximum, $F(\phi_{max}) = 1/4$ at $\phi_{max} = 1/2$, as shown in figure 3. This is the simplest function that satisfies the constraints (2.13) and it appears to capture the leading-order behaviour observed in experiments quite well (Wiederseiner *et al.* 2011). In this paper, more general asymmetric flux functions are investigated to understand some of the more subtle physical effects that are observed.

2.3. *The segregation equation*

The constituent velocities in the down- and cross-slope directions are assumed to be equal to the bulk velocity,

$$u^\nu = u, \quad v^\nu = v. \tag{2.15a,b}$$

Substituting the particle velocities (2.11) and (2.15), together with the segregation flux (2.12), into the constituent mass balance (2.4) implies that the segregation–remixing equation for small particles is

$$\frac{\partial \phi^s}{\partial t} + \boldsymbol{\nabla} \cdot (\phi^s \boldsymbol{u}) + \frac{\partial}{\partial z}(-qF(\phi^s)) = \frac{\partial}{\partial z}\left(D \frac{\partial \phi^s}{\partial z} \right), \tag{2.16}$$

where $q = (b/c)g\cos\zeta$ is the maximum segregation velocity, and $D = d/c$ is the diffusivity. The first term is the time rate of change of the concentration, the second term is the local advection by the bulk flow, the third term drives the particle-size segregation, whilst the fourth term accounts for diffusive remixing.

The avalanche thickness H is typically much less than the downslope length scale L. Incompressibility of the bulk flow implies that, if U is a typical downslope velocity, typical normal velocities will be of magnitude εU, where $\varepsilon = H/L \ll 1$ is the aspect ratio of the avalanche. This suggests introducing non-dimensional variables, denoted by the tildes, using the scalings

$$(x, y, z) = L(\tilde{x}, \tilde{y}, \varepsilon\tilde{z}), \quad (u, v, w) = U(\tilde{u}, \tilde{v}, \varepsilon\tilde{w}), \quad t = (L/U)\tilde{t}. \tag{2.17a–c}$$

Dropping the tildes, the non-dimensional segregation equation (2.16) therefore becomes

$$\frac{\partial \phi}{\partial t} + \boldsymbol{\nabla} \cdot (\phi \boldsymbol{u}) + \frac{\partial}{\partial z}(-S_r F(\phi)) = \frac{\partial}{\partial z}\left(D_r \frac{\partial \phi}{\partial z} \right), \tag{2.18}$$

where for simplicity ϕ, without the superscript 's', is the small-particle concentration. The large-particle concentration is $1-\phi$ from (2.1). The non-dimensional segregation and diffusive-remixing numbers are

$$S_r = \frac{qL}{HU}, \quad D_r = \frac{DL}{H^2 U}, \tag{2.19a,b}$$

respectively, and their ratio, S_r/D_r, is known as a Péclet number Pe for segregation. It quantifies the strength of the segregation compared to diffusive remixing within the flow. While diffusion is very important on steep slopes or when the particle-size differences are small, it is useful to consider the non-diffuse limit in which $D_r = 0$, because it allows considerable insight to be gained. Such conditions develop on low-inclination slopes with large size differences between the particles (Gray & Hutter 1997; Dasgupta & Manna 2011), where Péclet numbers exceeding 10 have been measured in experiments (Gray & Chugunov 2006; Wiederseiner *et al.* 2011). In the remainder of this paper, the segregation equation (2.18) is therefore considered in the non-diffuse limit, which reduces it to

$$\frac{\partial \phi}{\partial t} + \boldsymbol{\nabla} \cdot (\phi \boldsymbol{u}) + \frac{\partial}{\partial z}(-S_r F(\phi)) = 0. \tag{2.20}$$

In the absence of erosion and deposition, (2.20) is solved subject to a no-flux condition at the surface and base of the avalanche, $z = s(x, t)$ and $z = b(x, t)$, respectively (see e.g. Gray & Ancey 2011). When $D_r = 0$, these boundary conditions reduce to

$$F(\phi) = 0 \quad \text{at } z = s(x, t) \text{ and } z = b(x, t). \tag{2.21}$$

Since, by definition (2.13), the flux $F(\phi)$ is zero when either of the particles are in a pure phase, the no-flux condition (2.21) is satisfied when either $\phi = 0$ or $\phi = 1$.

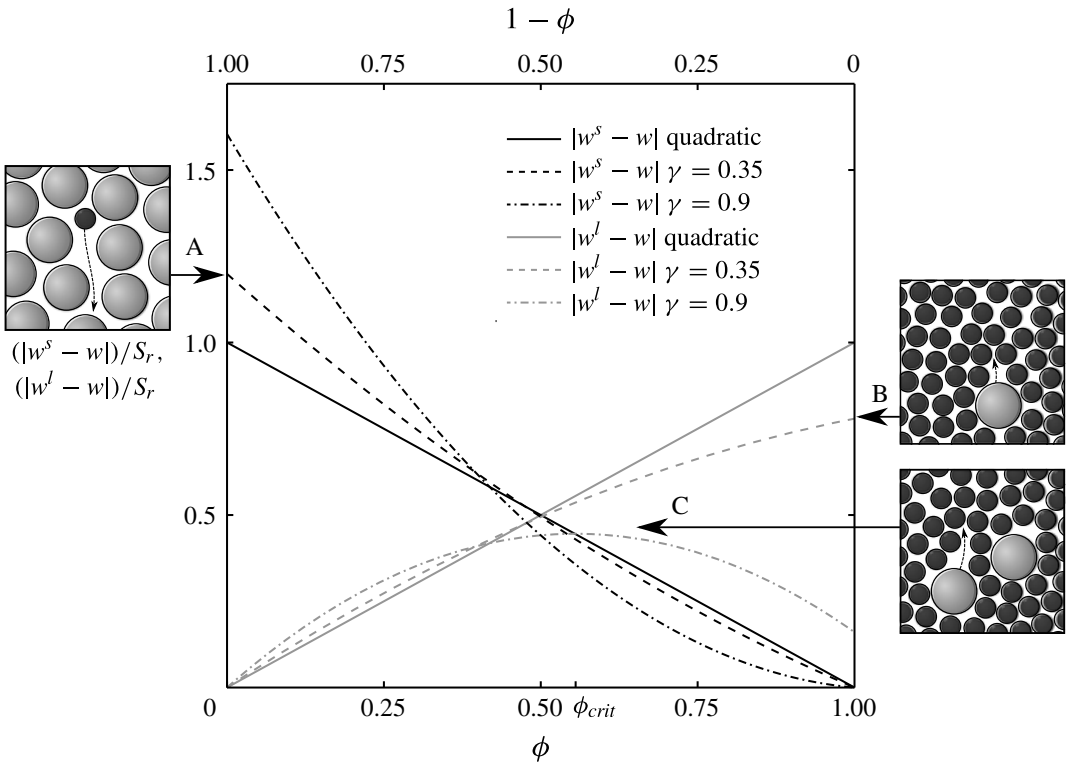

FIGURE 4. The modulus of the large (grey) and small (black) normal segregation velocities, relative to the bulk velocity w, plotted as a function of the small-particle concentration ϕ (lower axis) and large-particle concentration $1-\phi$ (upper axis). The velocities for large and small particles with the quadratic flux function (2.14) are straight (solid) lines, which attain the same maximum speed at $\phi=1$ and $\phi=0$, respectively. An asymmetric flux function is required to model the observation that small particles (A) can percolate through a matrix of large particles at a faster rate than a large particle (B) rises up through a matrix of small particles, e.g. for the convex cubic flux function (3.4) with $\gamma=0.35$ (dashed lines). For asymmetric non-convex flux functions (e.g. $\gamma=0.9$, dash-dotted lines), the maximum large-particle rise velocity occurs at ϕ_{crit}, which implies that a group of large particles (C) may rise faster than an isolated large grain.

3. Asymmetric flux functions

In the absence of diffusion, the large- and small-particle segregation velocities in the normal direction can be derived by substituting (2.12) into (2.11) and using the scalings (2.17) to give

$$w^l(\phi)=w+S_r\frac{F(\phi)}{1-\phi},\qquad w^s(\phi)=w-S_r\frac{F(\phi)}{\phi}. \tag{3.1a,b}$$

For the quadratic flux function (2.14), proposed by Gray & Thornton (2005), this implies that, relative to the bulk flow, the normal segregation velocities are linear functions of the small-particle concentration, i.e.

$$w^l(\phi)=w+S_r\phi,\qquad w^s(\phi)=w-S_r(1-\phi). \tag{3.2a,b}$$

Figure 4 shows the rise/fall rate of large/small particles (grey/black solid lines) for the quadratic flux (3.2) as a function of the small-particle concentration ϕ. The maximum rise velocity of the large particles is S_r at $\phi=1$ (i.e. in the limit of 100 % small

particles and 0 % large particles), whilst the small particles percolate downwards at a maximum speed $-S_r$ when $\phi = 0$ (i.e. in the limit of 0 % small particles and 100 % large particles). The segregation speed $|w^\nu - w|$ of each species ($\nu = l, s$) has the same linear behaviour when plotted against the concentration of that species ϕ^ν (where $\phi^s = \phi$ and $\phi^l = 1 - \phi$ from (2.1)). Critically, there is no asymmetry in the maximum rise/fall rates, as the maximum speed of small particles falling is the same as the maximum speed at which large particles rise.

In order to capture the effect that a single small particle falls through a matrix of large particles at a faster rate than a single large particle rises through a matrix of fines, asymmetric flux functions $F(\phi)$ are considered. These are skewed towards $\phi = 0$, with a maximum occurring at $0 < \phi_{max} < 1/2$, as shown in figure 3. The flux functions are normalised so that they all have the same maximum as the quadratic flux function (2.14). For asymmetric convex flux functions, with no inflection points, the maximum small-particle percolation velocity (figure 4-A) still occurs when $\phi = 0$, as in the quadratic case, but it is faster than the maximum rate at which large particles are squeezed up to the surface at $\phi = 1$ (figure 4-B). In addition, for singly non-convex flux functions with an inflection point at ϕ_{inf} in the interval $(\phi_{max}, 1)$, the maximum large-particle rise velocity occurs at $\phi_{crit} \neq 1$, as shown in figure 4(C), which satisfies

$$(1 - \phi_{crit})F'(\phi_{crit}) + F(\phi_{crit}) = 0, \tag{3.3}$$

where F' is the first derivative, $\mathrm{d}F/\mathrm{d}\phi$. Functions with inflection points are, therefore, also able to capture the observation that a group of large particles will sometimes rise faster than an isolated large particle on its own.

The behaviour of an entire class of asymmetric flux functions is illustrated in this paper by a simple one-parameter cubic function,

$$F(\phi) = A_\gamma \phi(1 - \phi)(1 - \gamma\phi), \tag{3.4}$$

where $\gamma \in (0, 1]$ is a parameter that controls the amount of asymmetry and hence the non-reciprocity of the segregation rates, as shown in figures 3(*a*) and 4. The constant A_γ is chosen so that the maximum, $F(\phi_{max}) = 1/4$, is the same as for the quadratic case, whilst $\gamma \leqslant 1$ ensures that F is positive for $\phi \in [0, 1]$. In the limit $\gamma \to 0$, the quadratic flux function is recovered. For $\gamma \leqslant 0.5$, the flux function $-S_r F$ in (2.18) remains convex (i.e. $-S_r F''(\phi) > 0$ for all $\phi \in [0, 1]$), but, when $\gamma > 0.5$, the flux function becomes non-convex, with a single inflection point ϕ_{inf} at

$$\phi_{inf} = \frac{1 + \gamma}{3\gamma}, \tag{3.5}$$

where $\gamma \in (0.5, 1]$ means that $2/3 \leqslant \phi_{inf} \leqslant 1$. The rise/fall rates for the convex flux functions ($\gamma = 0.35$, dashed lines) and non-convex flux functions ($\gamma = 0.9$, dash-dotted lines) are shown in figure 4. It can be seen that the rise/fall rates $|w^\nu - w|$ of large/small particles ($\nu = l, s$) are close to linear at low concentrations of large/small particles ϕ^ν, but there is nonlinear behaviour at large ϕ^ν. Some evidence of this nonlinearity is provided by the discrete element method (DEM) simulations of Fan *et al.* (2014). All the results in this paper are derived for a general flux function F with a maximum skewed towards low concentrations of fines. The specific cubic form (3.4) is used to illustrate the results in a practical example. Further experiments and DEM simulations will need to be performed to determine the precise form of the flux function.

For the non-convex case, it is useful to define the *image point* ϕ° of a concentration ϕ as the point where the gradient of the tangent to the flux function $F'(\phi^\circ)$ is equal to the gradient of the chord joining ϕ to ϕ° on F, i.e. the point ϕ° satisfies

$$F'(\phi^\circ) = \frac{F(\phi) - F(\phi^\circ)}{\phi - \phi^\circ}. \tag{3.6}$$

Comparing (3.3) with (3.6) implies that ϕ_{crit} is the image point of unity, i.e. $\phi_{crit} = 1^\circ$, which is also defined as ϕ_C in figure 3(*b*). For the cubic flux (3.4), the image point of ϕ is

$$\phi^\circ = \frac{1}{2}\left(\frac{1+\gamma}{\gamma} - \phi\right). \tag{3.7}$$

The chord joining one such pair $\{\phi, \phi^\circ\}$ is shown by the black circles in figure 3(*b*). In particular, the image point of $\phi = 1$ is $\phi_C = \phi_{crit}$, which for the cubic function gives

$$1^\circ = \phi_C = \phi_{crit} = \frac{1}{2\gamma}, \tag{3.8}$$

whereas $\phi = 1$ is the image point of

$$\phi_D = \frac{1-\gamma}{\gamma}, \quad \text{so } \phi_D^\circ = 1. \tag{3.9}$$

The chords joining $\{1, \phi_C\}$ and $\{\phi_D, 1\}$ are shown by dashed lines in figure 3(*b*).

4. The method of characteristics

It is assumed that the depth is constant and that the transverse and normal components of the bulk velocity are zero everywhere, $v = 0$, $w = 0$. Incompressibility then implies that the downslope velocity $u = u(z)$ is only dependent on z, i.e. the flow is steady and uniform in x (Pouliquen 1999; Silbert *et al.* 2001; Rognon *et al.* 2007; Forterre & Pouliquen 2008). This downslope velocity profile could, for instance, be the well-known Bagnold-like profile (Bagnold 1954; GDR MiDi 2004; Jop, Forterre & Pouliquen 2005; Gray & Edwards 2014), or a velocity profile with both shear and basal slip such as that sketched in figure 2. Scaling the height with the flow thickness implies that $z \in [0, 1]$. For steady-state non-diffuse solutions, the segregation equation (2.20) reduces to

$$\frac{\partial}{\partial x}(\phi u(z)) + \frac{\partial}{\partial z}(-S_r F(\phi)) = 0. \tag{4.1}$$

By making the change of variables

$$\xi = x, \quad \psi = \int_0^z u(\hat{z})\,\mathrm{d}\hat{z}, \tag{4.2a,b}$$

the steady-state segregation equation (4.1) is mapped into a velocity-independent form

$$\frac{\partial \phi}{\partial \xi} + \frac{\partial}{\partial \psi}(-S_r F(\phi)) = 0, \tag{4.3}$$

provided $u(z) \neq 0$. This coordinate transformation was first introduced by Gray & Thornton (2005) and is equivalent to solving the problem in streamfunction coordinates (e.g. Gray & Ancey 2009). By virtue of the velocity scaling (2.17), the free surface that lies at $z = 1$ can be mapped to $\psi = 1$, without loss of generality.

Transformation (4.2) is valid for any velocity profile $u = u(z)$, and so the inverse transformation allows the solution in the streamfunction domain (ξ, ψ) to be mapped back to physical space (x, z) for any velocity profile $u = u(z)$. The conservative equation (4.3) can be written in quasi-linear form as

$$\frac{\partial \phi}{\partial \xi} - S_r F'(\phi) \frac{\partial \phi}{\partial \psi} = 0, \tag{4.4}$$

where a prime denotes a derivative. This is a scalar conservation law, which can be solved by the method of characteristics (e.g. Courant & Hilbert 1962; Whitham 1974; Rhee *et al.* 1986). The concentration ϕ is constant along characteristic curves, which may be written in the parametric form $(\xi(s), \psi(s))$, where s is the distance along the curve. As the concentration ϕ is constant, the total derivative is zero, so

$$\frac{\mathrm{d}\phi}{\mathrm{d}s} = \frac{\mathrm{d}\xi}{\mathrm{d}s}\frac{\partial \phi}{\partial \xi} + \frac{\mathrm{d}\psi}{\mathrm{d}s}\frac{\partial \phi}{\partial \psi} = 0. \tag{4.5}$$

By comparing (4.4) with (4.5) it follows that

$$\frac{\mathrm{d}\xi}{\mathrm{d}s} = 1, \quad \frac{\mathrm{d}\psi}{\mathrm{d}s} = -S_r F'(\phi), \tag{4.6a,b}$$

which, eliminating s, implies that the characteristic curves are given by solving

$$\frac{\mathrm{d}\psi}{\mathrm{d}\xi} = -S_r F'(\phi) = c(\phi). \tag{4.7}$$

Since ϕ is constant on each curve, the gradient of the characteristic, $c(\phi)$, is also constant. Thus, in (ξ, ψ) space, the characteristics are straight lines, whose gradient is equal to the gradient of the flux function, i.e. $c(\phi) = -S_r F'(\phi)$, as shown in figure 5(*a*,*b*). If there is a discontinuity in the concentration field at $(\xi_\lambda, \psi_\lambda)$, with ϕ_+ on the forward side and ϕ_- on the rearward side (defined in the direction of increasing ψ), then, provided $\phi_+ > \phi_-$, the gradients satisfy $c(\phi_+) > c(\phi_-)$ and the characteristics diverge from one another. The void between the diverging characteristics is filled by a rarefaction fan, centred at $(\xi_\lambda, \psi_\lambda)$, within which the concentration is determined by characteristics with concentrations lying in the range $\phi \in [\phi_-, \phi_+]$, as shown in figure 5(*c*,*d*).

Conversely, if the initial discontinuity is such that $\phi_+ < \phi_-$, then, for a convex flux function, the gradients satisfy $c(\phi_+) < c(\phi_-)$, and the characteristics intersect to form a shock. The shock path is governed by the jump condition, which can be derived from an integral form of (4.3) using a limiting argument (see e.g. Chadwick 1976; Gray & Thornton 2005). The jump condition for (4.3) in the mapped coordinate system is

$$-[\![\phi]\!]\frac{\mathrm{d}\psi}{\mathrm{d}\xi} + [\![-S_r F(\phi)]\!] = 0, \tag{4.8}$$

where the 'jump' brackets $[\![\cdot]\!]$ indicates the difference in the enclosed quantity between the forward $(+)$ and rearward $(-)$ sides of the shock. This implies that the gradient of the shock is

$$\frac{\mathrm{d}\psi}{\mathrm{d}\xi} = -S_r \frac{[\![F(\phi)]\!]}{[\![\phi]\!]} = c(\phi_+, \phi_-), \tag{4.9}$$

where the function $c(\phi_+, \phi_-)$, with two arguments ϕ_+ and ϕ_-, is the gradient of the chord joining ϕ_+ with ϕ_- on the segregation flux curve $-S_r F(\phi)$, as shown in figure 5(*e*). Since the characteristics on the forward $(+)$ side have a lower gradient than those on the rearward $(-)$ side, all the characteristics intersect with the shock, as shown in figure 5(*f*) for the cubic convex flux function with $\gamma = 0.35$ and $S_r = 1.0$.

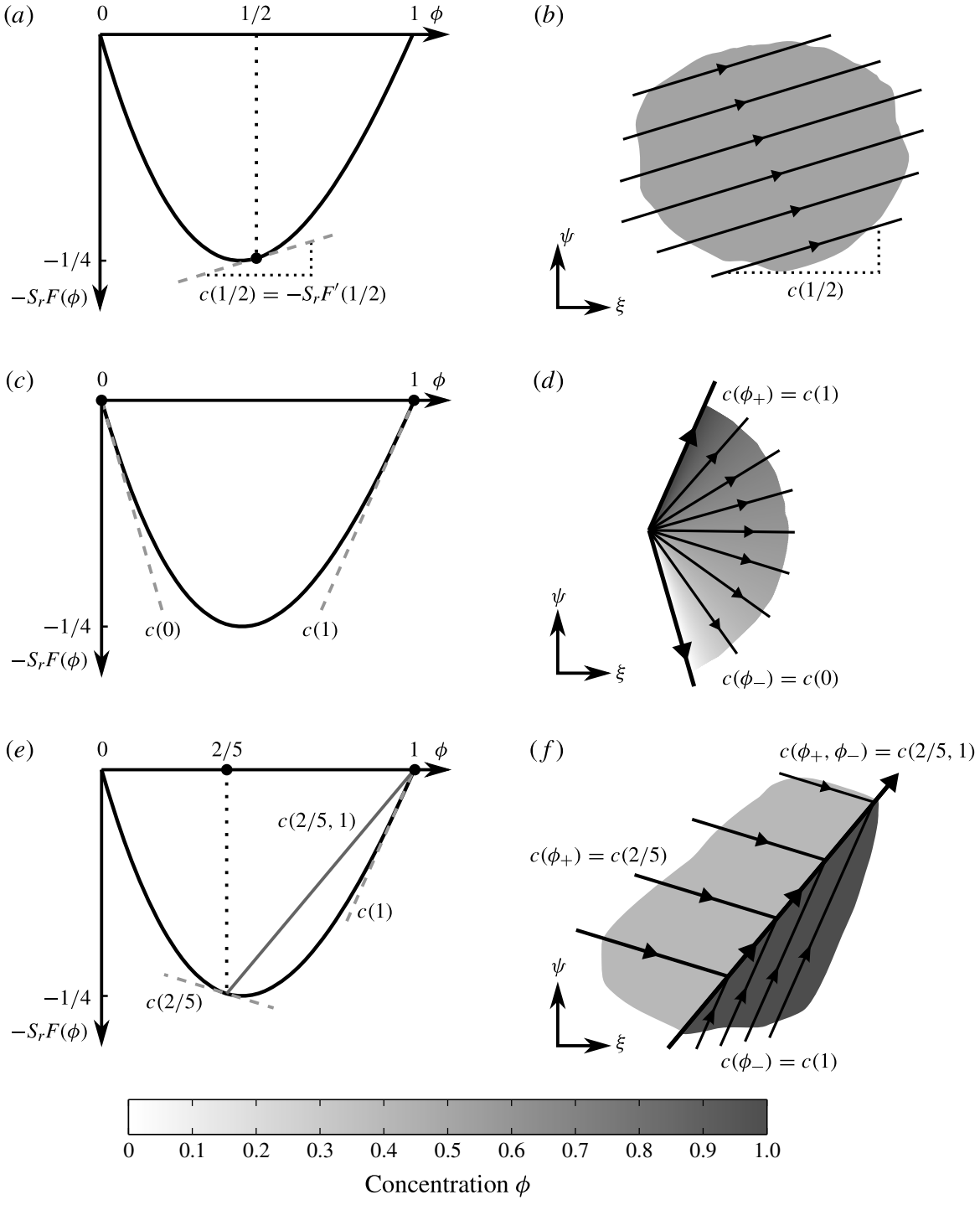

FIGURE 5. The segregation flux $-S_rF(\phi)$ determines the structure of the solution by setting the gradient of the characteristics $c(\phi) = -S_rF'(\phi)$ (4.7), as shown for the convex function (3.4) with $\gamma = 0.35$ and $S_r = 1.0$. At concentration $\phi = 1/2$, the gradient $c(1/2)$ is tangent to the flux curve (*a*) and has the same gradient as the characteristics (*b*). For a discontinuity (*c*) with $\phi_+ = 1$ above and $\phi_- = 0$ below, the gradients satisfy $c(1) > c(0)$ and so the characteristics (*d*) diverge. The region is filled with a rarefaction fan. While for a discontinuity (*e*) with $\phi_+ = 2/5$ and $\phi_- = 1$, the gradients satisfy $c(2/5) < c(1)$ and the characteristics (*f*) converge to form a shock. The gradient of the shock is set by the gradient $c(2/5, 1)$ of the chord joining ϕ_+ to ϕ_- on the flux curve (*e*).

For convex flux functions, the gradient is monotonically increasing with increasing ϕ, so $c(\phi_+) < c(\phi_-)$ when $\phi_+ < \phi_-$, and the characteristics always converge. However, in the non-convex case, there is an inflection point at ϕ_{inf}, which implies that the gradients of the characteristics increase up to ϕ_{inf}, but decrease again afterwards. If two states $\phi_+ < \phi_-$ that lie on either side of the inflection point are joined by a chord with gradient $c(\phi_+, c_-)$, then the ϕ_+ characteristics will intersect with the shock, but the ϕ_- characteristics will diverge away from it, which is unphysical. The non-convex flux functions therefore introduce a new feature into the solution, a semi-shock, which has the ϕ_+ characteristics intersecting it from one side, and characteristics tangential to it on the other side. In this problem, an expansion fan lies adjacent to the semi-shock with characteristics of concentrations between ϕ_+° and ϕ_-. By the definition of the image point (3.6), the ϕ_+° characteristic lies tangential to the shock, and so characteristics only intersect with the semi-shock from one side. In general, a shock is only admissible if the area bounded by the flux curve, $-S_r F(\phi)$, lies completely to the left of the chord joining ϕ_- to ϕ_+ when traversed from ϕ_- to ϕ_+ (Rhee *et al.* 1986; Laney 1998). There is a well-defined flow direction due to the bulk velocity $u(z)$, so both x and ξ are time-like variables. The above admissible shock condition is thus equivalent to the entropy condition of Oleinik (1959), and is compatible with the entropy condition of Lax (1957) for the convex case. Non-convex scalar conservation laws have been widely analysed in other contexts, for example in two-phase porous media flow (Buckley & Leverett 1942), and so the semi-shock construction may also be found in the literature as a 'generalised Lax shock', a 'one-sided contact discontinuity' or an 'intermediate discontinuity' (e.g. Liu 1974; Jeffrey 1976).

For example, consider the cubic flux function (3.4) with $\gamma = 0.9$ in figure 6. The area bounded by the flux curve in figure 6(*a*) lies to the left as one moves along the chord from $\phi_- = 0.65$ to $\phi_+ = 0.0$, and so the lower $\phi_- = 0.65$ characteristics collide with the upper $\phi = 0.0$ characteristics to form the shock shown in figure 6(*b*). However, a shock between $\phi_- = 0$ and $\phi_+ = 1$ is not admissible, because the area bounded by the flux curve lies to the right as one moves along the chord joining $\phi_- = 0$ to $\phi_+ = 1$, in figure 6(*c*). A single rarefaction fan is also not possible owing to the presence of the inflection point $0 < \phi_{inf} = 0.704 < 1$. Instead, a semi-shock and an adjacent expansion fan are formed. The semi-shock joins $\phi_+ = 1$ and its image point $\phi_- = 1^\circ$, whilst the expansion fan contains the characteristics generated by $\phi \in [0, 1^\circ]$. As one now moves along the chord from $\phi_- = 1^\circ$ to $\phi_+ = 1$, the dark grey area in figure 6(*c*) lies to the left and so the shock is admissible. The structure of the semi-shock and the adjacent fan is shown in figure 6(*d*). Semi-shock–fan structures also occur for $\phi_- = 1.0$ and $\phi_+ = \phi_0$, when ϕ_0 lies in the range $\phi_D < \phi_0 < \phi_{inf}$. Finally, the area bounded by the flux function lies to the right of the chord joining $\phi_- = 1$ to $\phi_+ = 0.75$, as shown in figure 6(*e*), so a shock is not admissible, and a semi-shock does not form because the inflection point $\phi_{inf} = 0.704$ does not lie in the interval (ϕ_+, ϕ_-). Instead, a rarefaction fan forms, as shown in figure 6(*f*).

5. Homogeneous inflow

Following Gray & Thornton (2005), the steady-state solution is now constructed for segregation in a steady uniform flow (Pouliquen 1999; Rognon *et al.* 2007; Forterre & Pouliquen 2008) in which the inflow at $\xi = 0$ is of homogeneous concentration ϕ_0 through the depth,

$$\phi(0, \psi) = \phi_0, \quad 0 \leqslant \psi \leqslant 1. \tag{5.1}$$

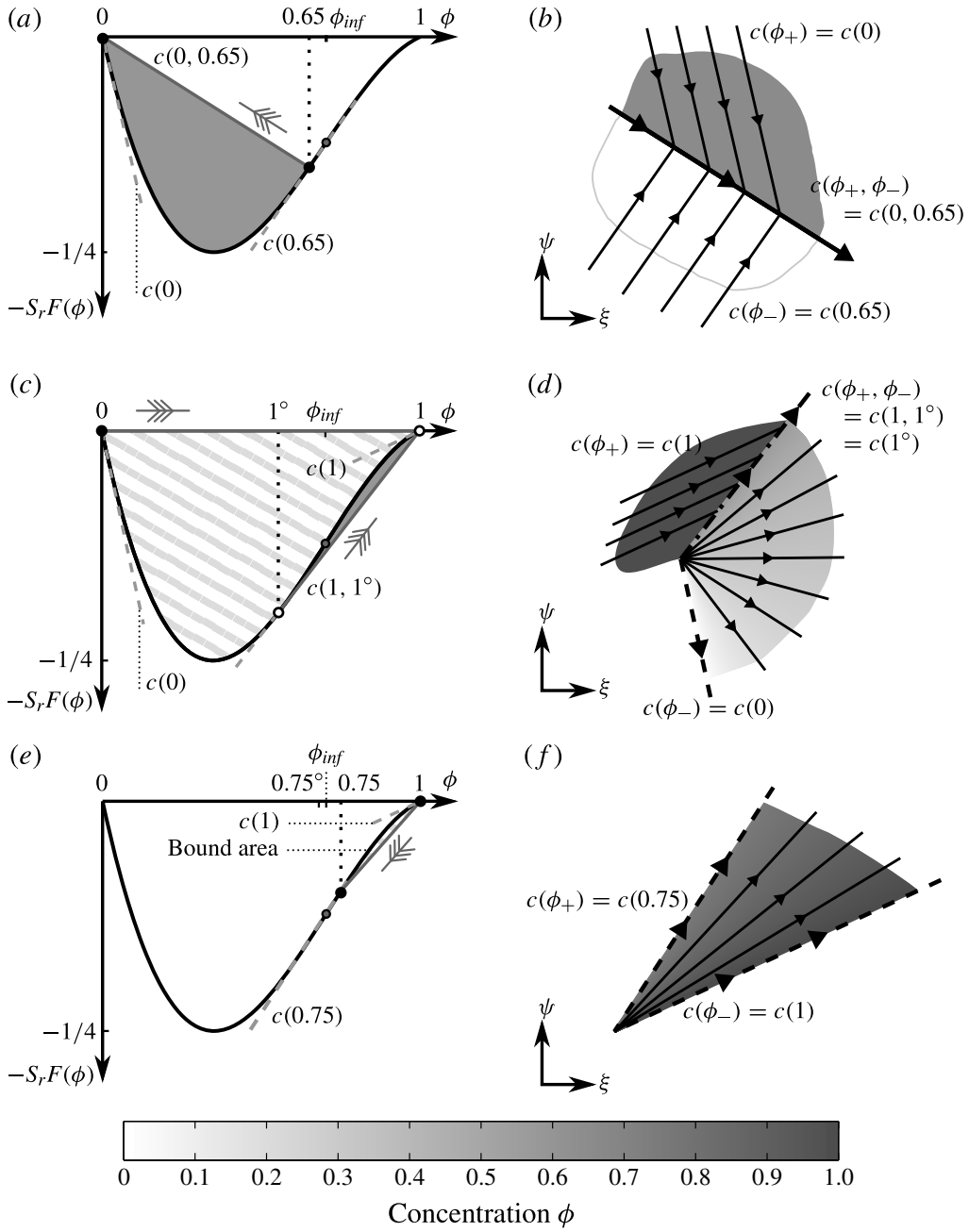

FIGURE 6. Non-convex flux functions, such as the cubic function (3.4) with $\gamma = 0.9$ and $S_r = 1$, are more complicated because of the inflection point ϕ_{inf}, which causes the maximum large-particle velocity to occur at $\phi = \phi_{crit} = \phi_C$. In order for a shock to be admissible, the area bounded by the flux curve must lie to the left of the chord joining ϕ_- to ϕ_+. (*a*) When $\phi_- = 0.65$ and $\phi_+ = 0$, the bounded area (grey) lies completely to the left as one moves along the chord from ϕ_- to ϕ_+ in the direction indicated, so (*b*) the shock is admissible and the characteristics converge from either side. (*c*) The cross-hatched area lies to the right of the chord joining $\phi_- = 0$ and $\phi_+ = 1$, and so the shock is not admissible. However, the area (grey) lies to the left of the chord joining $\phi = 1°$ to $\phi = 1$. A semi-shock (*d*) is therefore formed, whose gradient is equal to the gradient of the $\phi = 1°$ characteristic, together with an adjacent fan for $\phi \in [0, 1°]$. The semi-shock coincides with the $\phi = 1.0°$ characteristic that is at the edge of the rarefaction fan. (*e*) The cross-hatched and labelled area lies to the right of the chord joining $\phi_- = 1$ to $\phi_+ = 0.75$, and so a shock is not admissible. In addition, a semi-shock does not form because the inflection point ϕ_{inf} does not lie in the range [0.75, 1]. (*f*) Instead, the characteristics diverge to form a rarefaction fan.

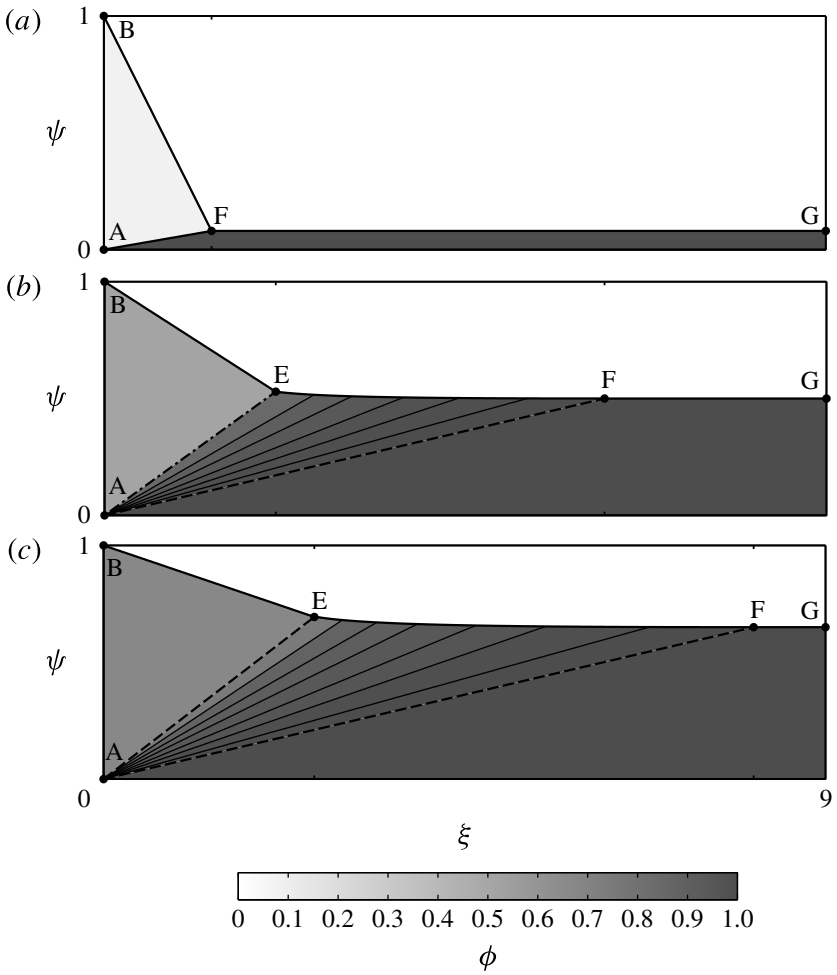

FIGURE 7. Exact solutions for the small-particle concentration ϕ in mapped coordinates (ξ, ψ) using the cubic flux function (3.4) with $\gamma = 0.9$ and $S_r = 0.5$. At the inflow $(\xi = 0)$, the grains are initially homogeneously mixed with concentration (a) $\phi_0 = 0.08$, (b) $\phi_0 = 0.50$ and (c) $\phi_0 = 0.65$. Thick solid lines represent shocks, thick dash-dotted lines represent semi-shocks whilst thick dashed lines represent the edge of rarefaction fans. Characteristics are shown with thin solid black lines.

There are three distinct solution structures that are dependent on ϕ_0 and the particular form of the flux function $F(\phi)$. For convex flux functions, and non-convex flux functions with the condition $\phi_0 \leqslant \phi_D$, where ϕ_D is defined in (3.9), the solution consists of three shocks separating the homogeneous inflow from a layer of large particles above and a layer of small particles below. Concentration ϕ_D is significant because it is the maximum concentration at which the image point ϕ° lies outside the range [0, 1). These solutions therefore have essentially the same structure as those for the quadratic flux (Gray & Thornton 2005), as shown in figure 7(a). Non-convex flux functions also give rise to two new solutions. When the initial concentration is in the range $\phi_D < \phi_0 < \phi_{inf}$, a semi-shock with an adjacent fan separates the homogeneous region from the lower layer of small particles, as shown in figure 7(b). If the initial concentration is increased further, $\phi_0 > \phi_{inf}$, the homogeneous region and region of small particles are separated by just a rarefaction fan, as in figure 7(c).

These new structures arise because, for $\phi > \phi_{crit}$, the velocity of large particles decreases with increasing small-particle concentration. A few large particles therefore rise at a very slow rate, and so they are swept a long distance downstream with the

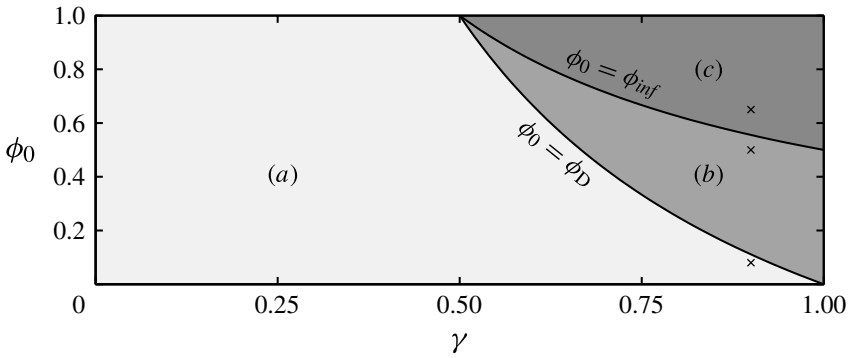

FIGURE 8. The (γ, ϕ_0) parameter space for the homogeneous inflow problem (figure 7) using the cubic family of flux functions (3.4). (*a*) A three-shock solution similar to that in Gray & Thornton (2005) occurs for convex flux functions ($\gamma \leqslant 0.5$) and non-convex functions ($\gamma > 0.5$) with a low inflow concentration of small particles, $\phi_0 < \phi_D$. (*b*) For non-convex flux functions $\gamma > 0.5$ with an inflow concentration of small particles $\phi_D \leqslant \phi_0 < \phi_{inf}$, a semi-shock with an adjacent fan separates the homogeneous region from the region of small particles. (*c*) For even higher initial concentrations of small particles, $\phi_0 \geqslant \phi_{inf}$, this separation becomes a smooth rarefaction fan. The curves $\phi_0 = \phi_D$ and $\phi_0 = \phi_{inf}$ are given by (3.9) and (3.5) respectively. Parameter values for the structures in figure 7 are marked with crosses.

bulk flow before they finally join the large-particle layer above. All three solutions are found using the family of cubic flux functions (3.4) parametrised by γ, with $F(\phi)$ convex for $\gamma \leqslant 0.5$ and non-convex for $0.5 < \gamma \leqslant 1$. The (γ, ϕ_0) parameter space is shown in figure 8, with regions (*a–c*) corresponding to the three different structures in figure 7(*a–c*), respectively. The three structures in (ξ, ψ) space are explained in more detail below, and can be transformed back to physical (x, z) space using the results of § 6.4, as shown in, for example, Gray & Thornton (2005), Thornton *et al.* (2006), Thornton & Gray (2008) and Gray & Ancey (2011). Note that this inverse transformation locally stretches and compresses the normal coordinate, but leaves the downstream coordinate unaffected.

5.1. *Three-shock solution*

The characteristics sweep the initial concentration downstream to create a region adjacent to the inflow that is still at $\phi = \phi_0$. Within this region, there is a flux of small particles percolating downwards, and an equal and opposite flux of large grains being squeezed upwards. However, at the base, $\psi = 0$, the boundary condition (2.21) implies that there is no flux of large particles and, consequently, the small particles have to separate out into a pure phase across the concentration shock AF shown in figure 7(*a*). This can be computed by solving the jump condition (4.9) with $\phi_+ = \phi_0$ and $\phi_- = 1$, subject to the condition that the shock starts at point A, which has coordinates $(0, 0)$, to give the straight line

$$\psi_{AF} = S_r \frac{F(\phi_0)}{1 - \phi_0} \xi . \tag{5.2}$$

Similarly, the upper shock BF separates the homogeneous region ($\phi_- = \phi_0$) from the layer of large particles ($\phi_+ = 0$) that collect at the surface. By integrating (4.9), subject

to the initial condition that the shock starts from point B with coordinates (0, 1), shock BF has coordinates $(\xi, \psi_{\mathrm{BF}})$ given by

$$\psi_{\mathrm{BF}} = 1 - S_r \frac{F(\phi_0)}{\phi_0}\,\xi. \tag{5.3}$$

The two shocks AF and BF meet at point F, whose coordinates $(\xi_{\mathrm{F}}, \psi_{\mathrm{F}})$ are found by equating (5.2) and (5.3) to give

$$\xi_{\mathrm{F}} = \frac{\phi_0(1-\phi_0)}{S_r F(\phi_0)}, \qquad \psi_{\mathrm{F}} = \phi_0. \tag{5.4a,b}$$

At point F the flow has reached its final segregated state with a third shock FG separating the two inversely graded layers, with large particles above ($\phi_+ = 0$) and small particles below ($\phi_- = 1$). Integrating (4.9) implies that the shock FG has coordinates

$$\psi_{\mathrm{FG}} = \phi_0, \qquad \xi \geqslant \xi_{\mathrm{F}}, \tag{5.5a,b}$$

which is independent of F (and hence γ), as the flux function and the asymmetry have no influence on the final non-diffuse segregated state. Convex flux functions always give rise to this three-shock structure, and hence the solution resembles that derived by Gray & Thornton (2005) for the quadratic flux function.

5.2. *Semi-shock solution with adjacent fan*

For non-convex flux functions with an inflow concentration $\phi_{\mathrm{D}} \leqslant \phi_0 \leqslant \phi_{inf}$, the homogeneous region and the lower layer of small particles are separated by a semi-shock AE with an adjacent expansion fan AEFA centred at point A = (0, 0), as shown in figure 7(*b*). Semi-shock AE starts at point A and separates the characteristics of the homogeneous region $\phi_+ = \phi_0$ from the $\phi_- = \phi_0^\circ$ characteristic, which lies immediately adjacent and tangential to the shock. From (3.6) and (4.9), it follows that the semi-shock AE has coordinates $(\xi, \psi_{\mathrm{AE}})$ given by

$$\psi_{\mathrm{AE}} = -S_r F'(\phi_0^\circ)\xi, \tag{5.6}$$

with $0 \leqslant \xi \leqslant \xi_{\mathrm{E}}$. The rarefaction fan occurs between the $\phi = 1$ and ϕ_0° characteristics, and is given by

$$\psi = -S_r F'(\phi)\xi, \qquad \text{for } \phi \in [\phi_0^\circ, 1]. \tag{5.7}$$

The upper shock BE separates the homogeneous region from the layer of large particles above and satisfies the same equation as shock BF in the three-shock structure (5.3). The semi-shock AE meets the upper shock BE at point E, which from (5.3) and (5.6) has coordinates

$$\xi_{\mathrm{E}} = \frac{\phi_0}{S_r(F(\phi_0) - \phi_0 F'(\phi_0^\circ))}, \qquad \psi_{\mathrm{E}} = -S_r F'(\phi_0^\circ)\xi_{\mathrm{E}}. \tag{5.8a,b}$$

Another shock EF separates the rarefaction fan ($\phi_- = \phi$) from the layer of large particles above ($\phi_+ = 0$). Using the chain rule, the shock gradient (4.9) can be written as

$$\frac{\mathrm{d}\psi}{\mathrm{d}\phi} = -S_r \frac{F(\phi)}{\phi}\frac{\mathrm{d}\xi}{\mathrm{d}\phi}, \tag{5.9}$$

while the equation for the characteristics of the fan (5.7) can be differentiated with respect to ϕ to give

$$\frac{\mathrm{d}\psi}{\mathrm{d}\phi} = -S_r F''(\phi)\xi - S_r F'(\phi)\frac{\mathrm{d}\xi}{\mathrm{d}\phi}. \tag{5.10}$$

Equating (5.9) and (5.10) yields an ordinary differential equation (ODE) for the shock path EF,

$$\frac{1}{\xi}\frac{\mathrm{d}\xi}{\mathrm{d}\phi} = \frac{\phi F''(\phi)}{F(\phi) - \phi F'(\phi)}, \tag{5.11}$$

which can be integrated, subject to the initial condition that the shock starts from point $(\xi_{\mathrm{E}}, \psi_{\mathrm{E}})$. Using (5.7) and the definition of the image point (3.6) to reformulate the initial condition (5.8), it follows that the shock EF is parametrised by

$$\xi_{\mathrm{EF}} = \frac{\phi_0}{S_r(F(\phi) - \phi F'(\phi))}, \quad \psi_{\mathrm{EF}} = -S_r F'(\phi)\xi_{\mathrm{EF}}, \quad \text{for } \phi \in [\phi_0^\circ, 1]. \tag{5.12a,b}$$

Shock EF ends at F, whose coordinates are given by (5.12) with $\phi = 1$, i.e.

$$\xi_{\mathrm{F}} = \frac{\phi_0}{-S_r F'(1)}, \quad \psi_{\mathrm{F}} = \phi_0. \tag{5.13a,b}$$

A final shock FG separates the large- and small-particle layers in the final inversely graded state, as in (5.5).

5.3. *Rarefaction fan solution*

Here the solution is essentially the same as that in § 5.2 except that there is no semi-shock, i.e. the homogeneous inflow and the layer of small particles are separated by a rarefaction fan AEFA centred at point $\mathrm{A} = (0, 0)$. The characteristics in the expansion fan (5.7) now lie in the range $\phi \in [\phi_0, 1]$. The left-hand edge of the rarefaction fan AE is given by the $\phi = \phi_0$ characteristic, and therefore ϕ_0 replaces ϕ_0° in (5.8) for E. Similarly, shock EF given by (5.12) is now parametrised by $\phi \in [\phi_0, 1]$.

5.4. *Final segregation distance*

For the class of asymmetric flux functions $F(\phi)$ under consideration, if $F(\phi)$ is convex, or $F(\phi)$ is non-convex and $\phi_0 \leqslant \phi_{\mathrm{D}}$, then the maximum segregation distance ξ_{F} is given by (5.4), while if $F(\phi)$ is non-convex and $\phi_0 > \phi_{\mathrm{D}}$, the maximum segregation distance is given by (5.13). For the cubic family of flux functions (3.4), this implies that

$$\xi_{\mathrm{F}} = \begin{cases} \dfrac{1}{S_r A_\gamma (1 - \gamma\phi_0)}, & \gamma \leqslant 0.5 \quad \text{or} \quad \gamma > 0.5 \quad \text{with } \phi_0 \leqslant \phi_{\mathrm{D}}, \\ \dfrac{\phi_0}{S_r A_\gamma (1 - \gamma)}, & \gamma > 0.5 \quad \text{with } \phi_0 > \phi_{\mathrm{D}}, \end{cases} \tag{5.14}$$

which is an increasing function of ϕ_0, as shown in figure 9. Note that, for the quadratic model (2.14), when $\gamma = 0$, the segregation distance $\xi_{\mathrm{F}} = 1/S_r$, which is independent of the inflow concentration, as shown by the grey line in figure 9. The dashed line shows the segregation distance for the cubic flux function with $\gamma = 0.35$. There is a weak dependence on ϕ_0: for $\phi_0 < 1/2$, the distance for complete segregation ξ_{F} is shorter than in the quadratic model, reflecting the fact that there

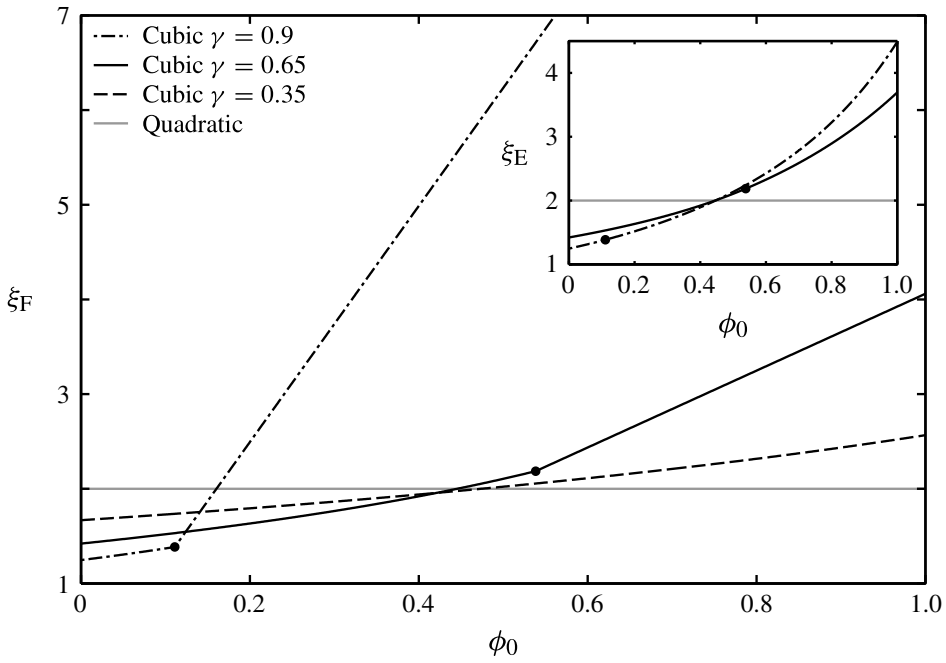

FIGURE 9. The maximum segregation distance ξ_F plotted as a function of the inflow concentration ϕ_0 for the quadratic model (grey line), the convex cubic model with $\gamma = 0.35$ (dashed line) and two cases of the non-convex cubic model (solid and dot-dashed lines) for $\gamma = 0.65$ and 0.9, respectively. The black circles denote the change in the functional form of ξ_F in (5.14) due to the presence of a rarefaction fan in the solution structure. The curves have been plotted for $S_r = 0.5$. Inset: The intermediate point ξ_E given by (5.8) also increases with the inflow concentration ϕ_0, showing that the increasing behaviour of the final segregation distance should be identifiable in experiments.

are only a few small particles that percolate down faster; whilst for $\phi_0 > 1/2$, the segregation distance is longer than in the quadratic model, reflecting the fact that a few large particles segregate to the top at a slower rate, when they are surrounded by high concentrations of fines, as shown in figure 4. This effect becomes stronger with increasing γ. The non-convex models with $\gamma = 0.65$ and $\gamma = 0.9$ (solid and dot-dashed lines, respectively) exhibit the same behaviour, as well as a change in the dependence of ξ_F at ϕ_D, which are shown by the black circles in figure 9. This is the point where the lower shock becomes a semi-shock with an adjacent expansion fan. At ϕ_D, the segregation distance ξ_F switches from the first to the second formula in (5.14), which has a much stronger dependence on the inflow concentration ϕ_0 owing to the decreasing rise rate of the large particles at high concentrations of fines. Moreover, in the limit as $\gamma \to 1$, the rarefaction fan becomes infinitely wide, because there is a double zero in the flux function (3.4) and the large-particle rise rate tends to zero at the outer edge of the expansion fan, $w_l(1) \to 0$.

As the concentration difference between E and F is small, small amounts of diffusive remixing may cause the two points to be indistinguishable in experiments. However, the inset of figure 9 shows that the intermediate distance ξ_E given by (5.8) also shows increasing behaviour with ϕ_0, and so an experimental measure of the final segregation distance is predicted to show increasing behaviour.

6. Normally graded inflow

Consider next the normally graded (see e.g. Tucker 2003) inflow problem of Thornton *et al.* (2006), where the small particles initially lie on top of the large

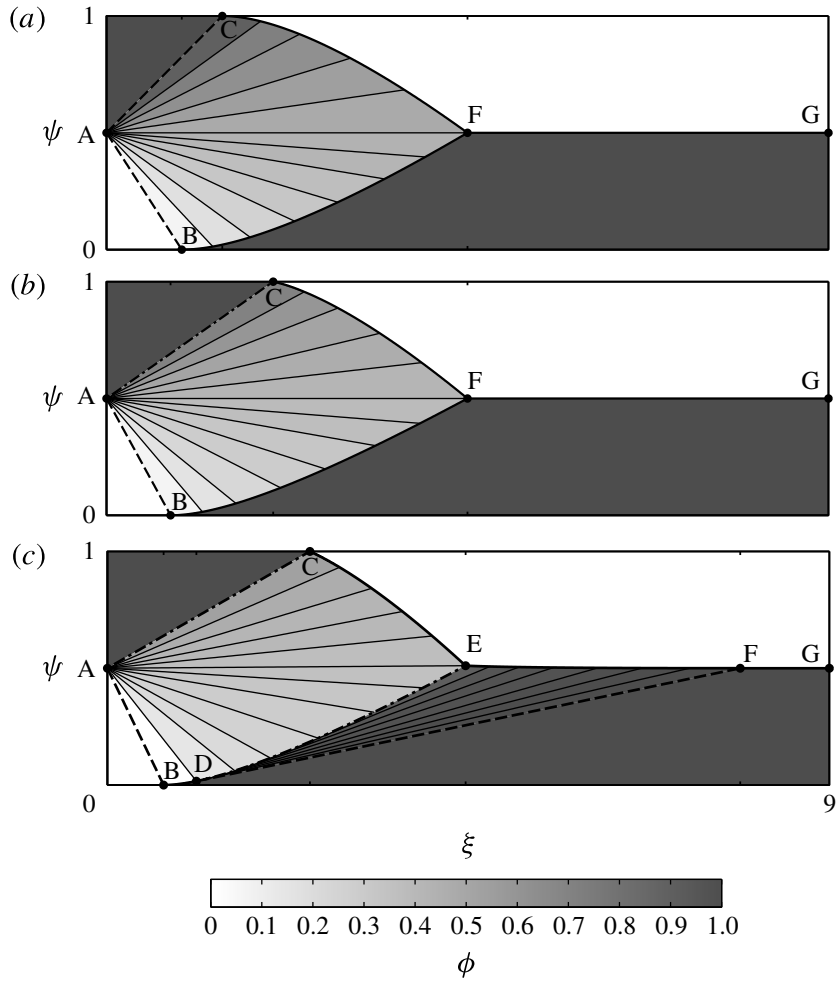

FIGURE 10. Exact solutions for an initially normally graded mixture at the inflow $\xi = 0$, where $\psi_A = 1/2$ and $S_r = 0.5$. The cubic flux function (3.4) has been used with (*a*) $\gamma = 0.35$, (*b*) $\gamma = 0.65$ and (*c*) $\gamma = 0.90$. Thick solid lines represent shocks, thick dot-dashed lines are semi-shocks, whilst thick dashed lines represent the edge of rarefaction fans. Characteristics are shown with thin solid black lines.

particles. The inflow at $\xi = 0$ thus satisfies

$$\phi(0, \psi) = \begin{cases} 1, & \psi_A \leqslant \psi \leqslant 1, \\ 0, & 0 \leqslant \psi < \psi_A, \end{cases} \tag{6.1}$$

where ψ_A is the height of the initial discontinuity. The small particles, which are initially at the top, percolate downwards and accumulate at the bottom, whilst the large particles at the bottom are squeezed upwards and accumulate at the top. This causes a transition from the initial normally graded concentration profile to a final inversely graded concentration profile some distance downstream.

There are three distinct solution structures for the concentration field that are dependent on the initial discontinuity height ψ_A and the nature of the flux function $F(\phi)$. These are shown for the cubic flux function (3.4) in figure 10. Convex flux functions ($\gamma = 0.35$) give the simple structure shown in figure 10(*a*). A rarefaction fan develops, which separates the small particles above from the large particles below. The leading-edge characteristics of the fan, $\phi = 0$ and $\phi = 1$, intersect the base and the free surface at B and C, respectively, and two shocks are generated that eventually intersect

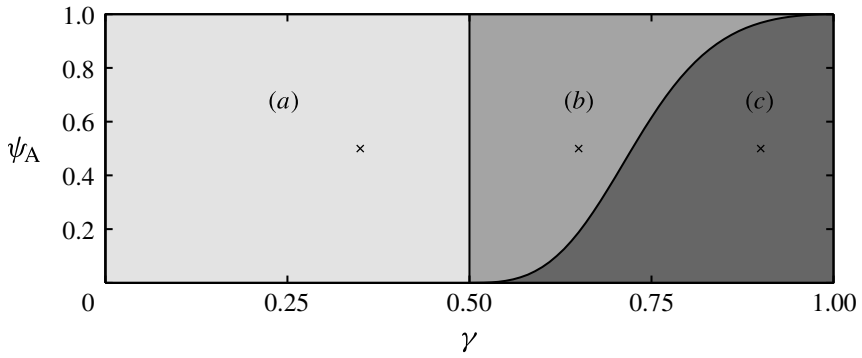

FIGURE 11. The (γ, ψ_A) parameter space for the three distinct structures (*a–c*) shown in figure 10. There is one solution for (*a*) convex flux functions ($\gamma \leqslant 0.5$), whilst for non-convex flux functions ($\gamma > 0.5$) either (*b*) or (*c*) may occur. The curve separating these two states is given by (6.26). Increasing the cubic asymmetry parameter γ, or decreasing the initial discontinuity height ψ_A, causes the transition from structure (*b*) to (*c*). The parameter values used in both figures 10 and 13 are marked with crosses.

to create the final reverse-graded state. This is similar to the solution structure for the quadratic flux derived by Thornton *et al.* (2006). One key difference is that, for the quadratic flux, points B and C lie the same distance downstream for $\psi_A = 1/2$, but for the asymmetric flux functions they do not. Non-convex flux functions ($\gamma = 0.65, 0.9$) give rise to two new structures shown in figure 10(*b*,*c*). The initial pure phase layers are separated by a semi-shock between the rarefaction fan and the initial upper layer of small particles. The expansion fan is always separated from the final upper pure phase of large particles by a shock; however, it may be separated from the lower layer of small particles by either a single shock (figure 10*b*) or a semi-shock with another adjacent fan (figure 10*c*), leading to two different structures. When the cubic flux function is used, the three structures have the (γ, ψ_A) parameter dependence shown in figure 11, where regions (*a–c*) correspond to the three different structures in figure 10(*a–c*), respectively. As the cubic asymmetry parameter γ is increased or the initial discontinuity height ψ_A is decreased, the structure changes from figure 10(*b*) to (*c*). The three solution structures will be examined in more detail below. It is also shown how to transform the solutions in velocity-integrated coordinates (ξ, ψ), given by equation (4.2), back to physical (x, z) space.

6.1. *Structure for convex flux functions*

The simple structure in figure 10(*a*) occurs for convex flux functions, such as the cubic flux function (3.4) with $\gamma \leqslant 0.5$. The initial inversely graded layers are separated by a rarefaction fan centred at point A, whose characteristics are given by

$$\psi = \psi_A - S_r F'(\phi)\xi, \quad \text{for } \phi \in [0, 1]. \tag{6.2}$$

The $\phi = 1$ characteristic determines point C, where the first large particle reaches the surface, whilst the $\phi = 0$ characteristic determines point B, where the first small particle reaches the base. Points B and C have coordinates $(\xi_B, 0)$ and $(\xi_C, 1)$ respectively, where

$$\xi_B = \frac{\psi_A}{S_r F'(0)} = \frac{\psi_A}{S_r A_\gamma}, \tag{6.3}$$

$$\xi_C = -\frac{1-\psi_A}{S_r F'(1)} = \frac{1-\psi_A}{S_r A_\gamma (1-\gamma)}, \tag{6.4}$$

with the general result followed by the result specific to the cubic flux function (3.4). A shock CF with coordinates $(\psi_{\rm CF}, \xi_{\rm CF})$ starts from point C and separates the rarefaction fan $(\phi_- = \phi)$ from the layer of large particles that accumulates at the top $(\phi_+ = 0)$. In the same manner as the derivation of (5.11), the equation for the rarefaction characteristics (6.2) may be differentiated and combined with the shock gradient (4.9) to give an implicit equation governing shock CF,

$$\frac{1}{\xi}\frac{{\rm d}\xi}{{\rm d}\phi} = \frac{\phi F''(\phi)}{F(\phi) - \phi F'(\phi)}. \tag{6.5}$$

This can be integrated with the initial condition that the shock starts from point C to give coordinates $(\xi_{\rm CF}, \psi_{\rm CF})$ as

$$\xi_{\rm CF} = \frac{1-\psi_{\rm A}}{S_r(F(\phi) - \phi F'(\phi))}, \quad \psi_{\rm CF} = \psi_{\rm A} - S_r F'(\phi)\xi_{\rm CF}, \quad \text{for } \phi \in [\phi_{\rm F}, 1], \tag{6.6a,b}$$

where the characteristic $\phi = \phi_{\rm F}$ in the expansion fan intersects with point F. Similarly, a shock BF separates the rarefaction fan $(\phi_+ = \phi)$ from the lower layer of small particles $(\phi_- = 1)$ with the implicit equation

$$\frac{1}{\xi}\frac{{\rm d}\xi}{{\rm d}\phi} = \frac{-(1-\phi)F''(\phi)}{F(\phi) + (1-\phi)F'(\phi)}. \tag{6.7}$$

The coordinates $(\xi_{\rm BF}, \psi_{\rm BF})$ of BF are found by integrating (6.7) subject to the initial condition that shock BF starts from point B, yielding

$$\xi_{\rm BF} = \frac{\psi_{\rm A}}{S_r(F(\phi) + (1-\phi)F'(\phi))}, \quad \psi_{\rm BF} = \psi_{\rm A} - S_r F'(\phi)\xi_{\rm BF}, \quad \text{for } \phi \in [0, \phi_{\rm F}]. \tag{6.8a,b}$$

The two shocks and the $\phi = \phi_{\rm F}$ characteristic meet at point F. An equation for the concentration $\phi_{\rm F}$ is obtained by equating (6.6) to (6.8), to give

$$\frac{1-\psi_{\rm A}}{\psi_{\rm A}} = \frac{F(\phi_{\rm F}) - \phi_{\rm F}F'(\phi_{\rm F})}{F(\phi_{\rm F}) + (1-\phi_{\rm F})F'(\phi_{\rm F})} = \frac{\phi_{\rm F}^2(1+\gamma-2\gamma\phi_{\rm F})}{(1-\phi_{\rm F})^2(1-2\gamma\phi_{\rm F})}, \tag{6.9}$$

where the last result is specific to the cubic flux function (3.4). The two shocks therefore meet at $(\xi_{\rm F}, \psi_{\rm F})$, which has coordinates

$$\xi_{\rm F} = \frac{1-\psi_{\rm A}}{S_r(F(\phi_{\rm F}) - \phi_{\rm F}F'(\phi_{\rm F}))}, \quad \psi_{\rm F} = 1 - \psi_{\rm A}. \tag{6.10a,b}$$

A third shock FG starts from point F separating the two inversely graded layers, with coordinates $(\xi, \psi_{\rm FG})$,

$$\psi_{\rm FG} = 1 - \psi_{\rm A}, \quad \xi \geqslant \xi_{\rm F}. \tag{6.11a,b}$$

Similar to (5.5), the final segregated state is independent of F (and hence γ).

6.2. *Structure for non-convex flux functions*

The two different solution structures shown in figure 10(*b*,*c*) occur for non-convex flux functions, such as the cubic flux function (3.4) with $\gamma > 0.5$. Within the expansion

fan, small particles percolate downwards and large particles are squeezed upwards, as before. However, because of the non-convexity, the maximum large-particle rise rate occurs at concentration $\phi = \phi_{crit} = \phi_C$ rather than at $\phi = 1$. An expansion over the interval $\phi \in [0, 1]$ (as in the convex case) is not possible, because, for ϕ greater than ϕ_{inf}, the characteristics overlap with those generated by lower values of ϕ. Instead, a semi-shock AC is formed between the initial upper layer of small particles $\phi_+ = 1$ and the $\phi_- = 1^\circ = \phi_C$ characteristic at the edge of the fan. Integrating the shock gradient (4.9) and using the definition of the image point (3.6) implies that the coordinates (ξ, ψ_{AC}) of semi-shock AC are given by

$$\psi_{AC} = \psi_A - S_r F'(\phi_C)\xi. \tag{6.12}$$

The characteristics of the fan are given by (6.2) with $\phi \in [0, \phi_C]$. The $\phi = 0$ characteristic again determines point B for the first small particle to reach the base, which has coordinates $(\xi_B, 0)$ given by (6.3). However, semi-shock AC now governs the position of point C for the first large particle to reach the surface, with coordinates $(\xi_C, 1)$, where

$$\xi_C = -\frac{1 - \psi_A}{S_r F'(\phi_C)} = 4\gamma \frac{1 - \psi_A}{S_r A_\gamma}. \tag{6.13}$$

The two different non-convex solutions are dependent on whether the concentration $\phi = \phi_F$, defined in (6.9), satisfies $\phi_F \leqslant \phi_D$ or $\phi_F > \phi_D$. In the former case (shown in figure 10*b*), the rarefaction fan ($\phi_- = \phi$) is separated from the upper layer of large particles ($\phi_+ = 0$) by a shock CF. The shock starts from C, and its coordinates (ξ_{CF}, ψ_{CF}) are given by (6.6) with $\phi \in [\phi_F, \phi_C]$. A second shock BF also starts from B and separates the rarefaction fan ($\phi_+ = \phi$) from the lower layer of small particles ($\phi_- = 1$). Similarly, this has coordinates (ξ_{BF}, ψ_{BF}) given by (6.8) with $\phi \in [0, \phi_F]$. A final shock FG separates the inversely graded state, with coordinates (ξ_{FG}, ψ_{FG}) given by (6.11).

The solution in the latter case ($\phi_F > \phi_D$) is more complex and gives rise to the structure shown in figure 10(*c*). The rarefaction fan ($\phi_- = \phi$) is separated from the upper layer of large particles ($\phi_+ = 0$) by a shock CE that starts from point C. The shock gradient (4.9) and the rarefaction characteristics (6.2) can be used to show that CE has coordinates (ξ_{CE}, ψ_{CE}) that satisfy (6.6). This is the same equation as satisfied by the coordinates of shock CF in the non-convex case, but here ϕ lies in the range $\phi \in [\phi_E, \phi_C]$. A shock BD together with a semi-shock DE and adjacent fan DEFD separate the initial rarefaction fan ($\phi_+ = \phi$) from the layer of small particles that accumulates at the bottom of the flow ($\phi_- = 1$). Shock BD starts from B, and integrating the shock gradient (4.9) shows that BD has coordinates (ξ_{BD}, ψ_{BD}) that satisfy (6.8). This is the same equation as the coordinates of shock BF in the non-convex case, but with $\phi \in [0, \phi_D]$. Point D has coordinates (ξ_D, ψ_D) given by (6.8) with $\phi = \phi_D$, where

$$\left.\begin{aligned} \xi_D &= \frac{\psi_A}{S_r(F(\phi_D) + (1 - \phi_D)F'(\phi_D))} = \frac{\psi_A \gamma^2}{S_r A_\gamma (2\gamma - 1)^3}, \\ \psi_D &= \psi_A - S_r F'(\phi_D)\xi_D = \psi_A \frac{(1 - \gamma)^2(3\gamma - 1)}{(2\gamma - 1)^3}. \end{aligned}\right\} \tag{6.14}$$

A local semi-shock with an adjacent non-centred expansion fan occurs in the region DEFD, which separates the rarefaction fan from the layer of small particles below.

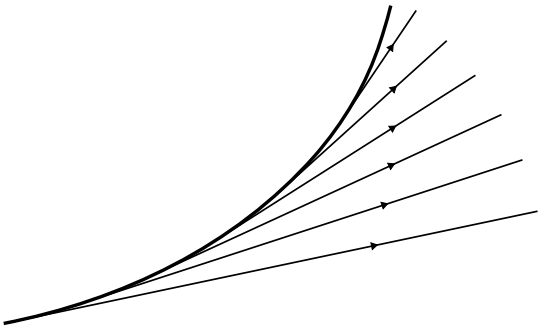

FIGURE 12. A sketch of the non-centred expansion fan arising within the region DEFD, where each characteristic of the rarefaction is tangential to the semi-shock.

Each incoming characteristic from the rarefaction fan (6.2) intersects semi-shock DE and generates a new characteristic that lies locally tangent to it. The semi-shock DE therefore separates each rarefaction characteristic $\phi_+ = \phi$ from its image point concentration $\phi_- = \phi^\circ$. Using the chain rule and the definition of the image point (3.6), the shock gradient (4.9) can be solved implicitly by differentiating the expansion fan characteristics (6.2) with respect to ϕ, to obtain a separable ODE for the semi-shock DE, i.e.

$$\frac{1}{\xi}\frac{\mathrm{d}\xi}{\mathrm{d}\phi} = \frac{F''(\phi)}{F'(\phi^\circ) - F'(\phi)}. \tag{6.15}$$

For a general flux function,

$$\frac{\mathrm{d}}{\mathrm{d}\phi}(F'(\phi^\circ) - F'(\phi)) = F''(\phi^\circ)\frac{\mathrm{d}\phi^\circ}{\mathrm{d}\phi} - F''(\phi), \tag{6.16}$$

but, since $F''(\phi^\circ)\,\mathrm{d}\phi^\circ/\mathrm{d}\phi \neq 0$, (6.15) cannot normally be integrated to give a simple logarithmic form as with (5.11), (6.5) and (6.7). Instead, (6.15) must be numerically integrated with the initial condition that the semi-shock starts at point D. However, the cubic flux function (3.4) satisfies

$$\frac{\mathrm{d}}{\mathrm{d}\phi}(F'(\phi^\circ) - F'(\phi)) = \frac{\mathrm{d}}{\mathrm{d}\phi}\left(-\frac{1}{4\gamma}(3\gamma\phi - (1+\gamma))^2\right) = -\frac{3}{4}F''(\phi), \tag{6.17}$$

and so (6.15) may be integrated exactly. As semi-shock DE starts from point D, it has the implicit coordinates $(\xi_{\mathrm{DE}}, \psi_{\mathrm{DE}})$,

$$\xi_{\mathrm{DE}} = \frac{\psi_{\mathrm{A}}\gamma^2}{S_r A_\gamma}\left(\frac{256}{(2\gamma-1)(3\gamma\phi - (1+\gamma))^8}\right)^{1/3}, \quad \psi_{\mathrm{DE}} = \psi_{\mathrm{A}} - S_r F'(\phi)\xi_{\mathrm{DE}}, \tag{6.18a,b}$$

for $\phi \in [\phi_{\mathrm{D}}, \phi_{\mathrm{E}}]$. The non-centred fan is formed from each of the ϕ° characteristics that are local tangents to the semi-shock DE and are given by the straight lines

$$\psi = \psi_{\mathrm{DE}}(\phi) - S_r F'(\phi^\circ)(\xi - \xi_{\mathrm{DE}}(\phi)), \quad \text{for } \phi \in [\phi_{\mathrm{D}}, \phi_{\mathrm{E}}]. \tag{6.19}$$

This forms the beautiful structure sketched in figure 12.

Semi-shock DE meets the upper shock CE at point E. Equating $\xi_{\mathrm{DE}} = \xi_{\mathrm{CE}}$ using (6.19) and (6.6) gives both the coordinates $(\xi_{\mathrm{E}}, \psi_{\mathrm{E}})$ and concentration ϕ_{E}. A further shock EF separates the upper layer of large particles ($\phi_+ = 0$) from the local

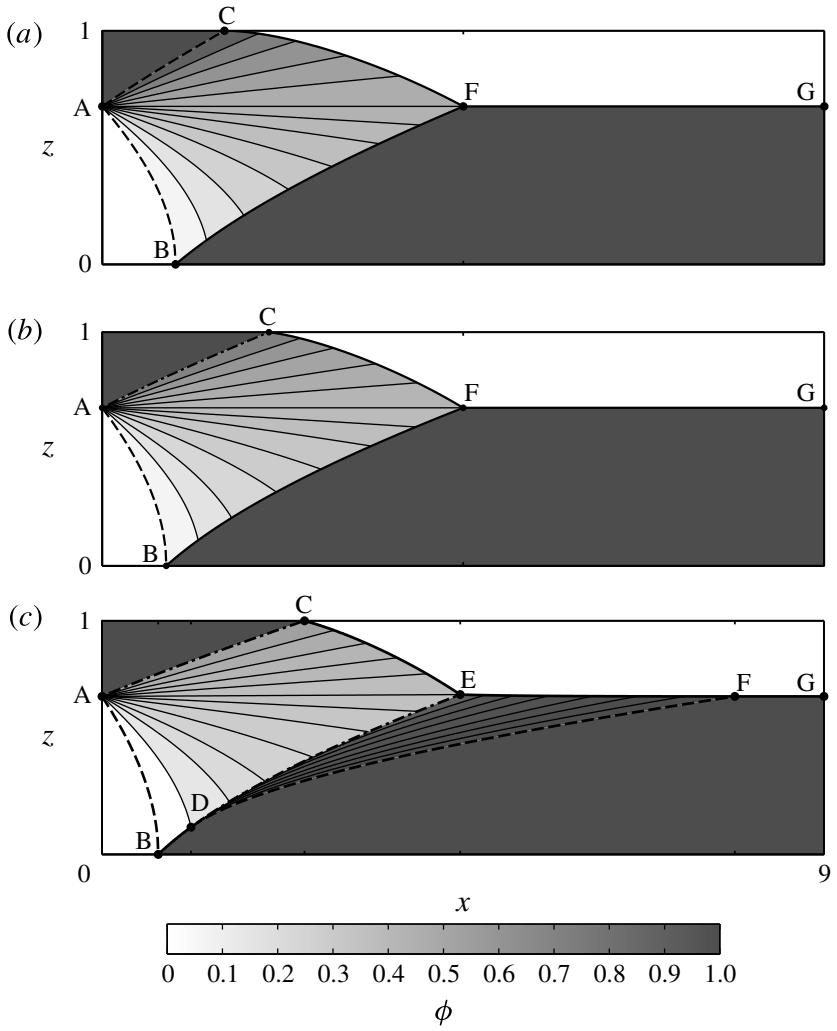

FIGURE 13. Exact solutions for an initially normally graded mixture in physical (x, z) coordinates with a Bagnold velocity profile (6.34). As in figure 10, $\psi_A = 0.50$ (which maps to $z_A = 0.676$), $S_r = 0.5$, and the cubic flux function (3.4) has been used with (a) $\gamma = 0.35$, (b) $\gamma = 0.65$ and (c) $\gamma = 0.90$. Thick solid lines represent shocks, thick dash-dot lines are semi-shocks whilst thick dashed lines represent the edge of rarefaction fans. Characteristics are shown with thin solid black lines. The velocity is monotonically increasing with height, so the large-particle layer at the top is thinner to conserve mass.

rarefaction fan ($\phi_- = \phi^\circ$). Using the chain rule, the shock gradient (4.9) can be rearranged to give

$$\frac{\mathrm{d}\psi}{\mathrm{d}\phi^\circ} = -S_r \frac{F(\phi^\circ)}{\phi^\circ} \frac{\mathrm{d}\xi}{\mathrm{d}\phi^\circ}, \tag{6.20}$$

whilst the rarefaction fan characteristics (6.19) may be differentiated implicitly with respect to ϕ° to give

$$\frac{\mathrm{d}\psi}{\mathrm{d}\phi^\circ} - \frac{\mathrm{d}\psi_{\mathrm{DE}}}{\mathrm{d}\phi^\circ} = -S_r \frac{\mathrm{d}^2 F(\phi^\circ)}{\mathrm{d}(\phi^\circ)^2}(\xi - \xi_{\mathrm{DE}}) - S_r \frac{\mathrm{d}F(\phi^\circ)}{\mathrm{d}\phi^\circ}\left(\frac{\mathrm{d}\xi}{\mathrm{d}\phi^\circ} - \frac{\mathrm{d}\xi_{\mathrm{DE}}}{\mathrm{d}\phi^\circ}\right). \tag{6.21}$$

By combining (6.20) and (6.21), the coordinates of EF can be shown to satisfy the inhomogeneous differential equation

$$-\frac{\mathrm{d}}{\mathrm{d}\phi^\circ}[(F(\phi^\circ) - \phi^\circ F'(\phi^\circ))\xi] = \phi^\circ \frac{\mathrm{d}}{\mathrm{d}\phi^\circ}\left(\frac{\psi_{\mathrm{DE}}(\phi)}{S_r} + F'(\phi^\circ)\xi_{\mathrm{DE}}(\phi)\right). \tag{6.22}$$

The image point concentration ϕ° has been treated as the independent variable, with the relationship between ϕ and ϕ° governed by (3.6). Equation (6.22) is a first-order differential equation of the form

$$-\frac{\mathrm{d}}{\mathrm{d}\phi^\circ}(f(\phi^\circ)\xi) = \phi^\circ \frac{\mathrm{d}}{\mathrm{d}\phi^\circ} g(\phi^\circ, \phi), \tag{6.23}$$

and since (6.18) expresses DE exactly for the cubic flux function, (6.22) can be integrated by parts with the boundary condition that $\phi = \phi_\mathrm{E}$, $\phi^\circ = \phi^\circ_\mathrm{E}$ at $\xi = \xi_\mathrm{E}$. This gives the implicit coordinates $(\xi_{\mathrm{EF}}(\phi), \psi_{\mathrm{EF}}(\phi))$ of EF as

$$\left.\begin{aligned} \xi_{\mathrm{EF}}(\phi) &= \frac{g_1(\phi_\mathrm{E})\xi_\mathrm{E} + g_2(\phi) - g_2(\phi_\mathrm{E})}{g_1(\phi)}, \\ \psi_{\mathrm{EF}}(\phi) &= \psi_{\mathrm{DE}}(\phi) - S_r F'(\phi^\circ)(\xi_{\mathrm{EF}}(\phi) - \xi_{\mathrm{DE}}(\phi)), \end{aligned}\right\} \tag{6.24}$$

where $\phi_\mathrm{D} \leqslant \phi \leqslant \phi_\mathrm{E}$ and the functions $g_1(u)$ and $g_2(u)$ are defined as

$$g_1(u) = \frac{A_\gamma}{4\gamma} u(1+\gamma-\gamma u)^2, \quad g_2(u) = \frac{\psi_\mathrm{A}\gamma}{S_r}\left(\frac{4}{2\gamma-1}\right)^{1/3} u(3\gamma u - (1+\gamma))^{-2/3}. \tag{6.25a,b}$$

The $\phi = 1$ characteristic that is tangential at point D meets the upper layer at point F, whose coordinates $(\xi_\mathrm{F}, \psi_\mathrm{F})$ are given by (6.24) with $\phi = \phi_\mathrm{D}$. A final shock FG separates the final inversely graded flow, with coordinates $(\xi_{\mathrm{FG}}, \psi_{\mathrm{FG}})$ given by (6.11).

The change between the two non-convex structures (figure 10*b*,*c*) occurs when point D coincides with point E and point F. For the cubic flux function, equating ψ_F (6.10) with ψ_D (6.14) determines the curve in figure 11 as

$$\psi_\mathrm{A} = \frac{8\gamma^3 - 12\gamma^2 + 6\gamma - 1}{11\gamma^3 - 19\gamma^2 + 11\gamma - 2}. \tag{6.26}$$

6.3. *Comparison with the symmetric model*

The asymmetric flux functions lead to several differences in the solution for normally graded inflow that are not found in the structure for the quadratic flux derived by Thornton *et al.* (2006). Firstly, although the convex flux structure shown in figure 10(*a*) appears similar to that of the convex quadratic flux (2.14), the positions of points B and C are modified due to the particles percolating downwards and rising upwards at different rates. Thornton *et al.* (2006) found the ratio of ξ_C to ξ_B to be dependent on the initial discontinuity height ψ_A, i.e.

$$\frac{\xi_\mathrm{C}}{\xi_\mathrm{B}} = \frac{(1-\psi_\mathrm{A})}{\psi_\mathrm{A}}, \tag{6.27}$$

but, using (6.3) and (6.4), for convex flux functions,

$$\frac{\xi_\mathrm{C}}{\xi_\mathrm{B}} = -\frac{F'(0)}{F'(1)}\frac{(1-\psi_\mathrm{A})}{\psi_\mathrm{A}} = \frac{1}{(1-\gamma)}\frac{(1-\psi_\mathrm{A})}{\psi_\mathrm{A}}, \tag{6.28}$$

which, for the cubic flux function (3.4), has an additional dependence on γ. In the limit as $\gamma \to 0$ the quadratic result is recovered. This asymmetry is also seen with

the non-convex flux functions in figure 10(*b*,*c*), but now several large particles rise together at concentration $\phi_{crit} = \phi_C$ and reach the top at C. From (6.13), this gives

$$\frac{\xi_C}{\xi_B} = -\frac{F'(0)}{F'(\phi_C)}\frac{(1-\psi_A)}{\psi_A} = 4\gamma\frac{(1-\psi_A)}{\psi_A}. \tag{6.29}$$

The ratio ξ_C/ξ_B given by (6.28) and (6.29) could provide a sensitive experimental test for measuring the asymmetry between the maximum large- and small-particle velocities. For example, consider run 22 in the chute flow experiment of Wiederseiner *et al.* (2011), with $z_A = 0.7$. The velocity data were found to fit an exponential velocity profile

$$u = \frac{\beta\exp(\beta z)}{\exp(\beta)-1}, \tag{6.30}$$

with $\beta = 3.3$, which maps z_A to $\psi_A = 0.374$ through transformation (4.2). Using the $\phi = 0$ contour in figure 7(a) of their paper, it is possible to estimate $\xi_B = 0.17$ and $\xi_C = 0.53$, which give

$$\frac{\xi_C/\xi_B}{(1-\psi_A)/\psi_A} = 1.86. \tag{6.31}$$

Note that this ratio is greater than the ratio 1 of the quadratic flux (6.27), but less than 2. Assuming the cubic flux (3.4), comparing (6.31) with (6.28) implies that

$$\gamma = 0.46. \tag{6.32}$$

A second difference between the quadratic flux model and the asymmetric flux functions is the presence of semi-shocks and adjacent expansion fans, such as DEFD in figure 10(*c*) for non-convex flux functions. A similar semi-shock and adjacent fan AEFA also develops in the homogeneous case in figure 7(*b*,*c*). In both cases, these are a direct result of the decreasing rise velocity of large particles above concentration $\phi = \phi_C$.

6.4. *Solution in physical coordinates*

The solution in physical coordinates (x, z) may easily be derived from the mapped coordinates (ξ, ψ) by prescribing a downslope velocity field $u = u(z)$ and inverting the coordinate transformation (4.2). A Bagnold velocity profile typically develops for steady uniform flows (e.g Bagnold 1954; Silbert *et al.* 2001; GDR MiDi 2004; Rognon *et al.* 2007), which in dimensional variables is

$$u = \frac{2}{3}\frac{I_\zeta}{d}\sqrt{g\Phi\cos\zeta}\,(h^{3/2} - (h-z)^{3/2}), \tag{6.33}$$

where I_ζ is the constant inertial number at a given inclination angle ζ (GDR MiDi 2004; Jop *et al.* 2005; Gray & Edwards 2014), Φ is the solids volume fraction and d is a measure of the average diameter of the grains. Applying the non-dimensionalisation (2.17), with the velocity magnitude U chosen so that $\psi(1) = 1$, gives the non-dimensional downstream velocity

$$u(z) = \tfrac{5}{3}(1 - (1-z)^{3/2}). \tag{6.34}$$

The transformation to mapped coordinates (4.2) gives

$$\psi = \tfrac{5}{3}z - \tfrac{2}{3}(1 - (1-z)^{5/2}). \tag{6.35}$$

This transformation cannot be inverted to produce an explicit function for $z(\psi)$; however, contour plots of the results are easy to produce by numerically inverting the normal coordinate, and are shown in figure 13. The inverse transformation effectively stretches the vertical coordinate, and transforms straight lines in mapped (ξ, ψ) coordinates to curves in physical (x, z) coordinates. Shock FG is the only line to remain straight after the transformation, but it is translated to a new height $z(1-\psi_{\mathrm{A}})$. The velocity is monotonically increasing towards the surface, and thus there is also an increasing mass flux with height. In order to conserve mass, layers in regions of high velocity near the surface will be thinner than layers in regions of lower velocity near the base. Hence, for the example shown in figure 10, the layer of large particles at the top is the same thickness as the layer of small particles at the bottom in (ξ, ψ) space. After the transformation to physical coordinates, the large-particle layer at the surface is thinner, whilst the small-particle layer is expanded. The transformation leaves the downstream coordinate unchanged, and so horizontal coordinates of points A–G and the final segregation distances are left unaffected.

7. Discussion and conclusions

This paper generalises the particle-size segregation model of Gray & Thornton (2005) to asymmetric flux functions, in order to model the observation that a single small particle will percolate down through a matrix of large particles faster than a single large grain will rise up through a matrix of fines. A general class of asymmetric flux functions is considered, whose maximum amplitude is skewed towards lower concentrations of fines, and which may be either convex or non-convex, as shown for the cubic case in figure 3. For convex flux functions, the maximum percolation velocity of the fines, which occurs in the limit as the concentration of fines tends to 0 %, is enhanced above that obtained with the simple quadratic flux used by Gray & Thornton (2005). Conversely, the maximum rise rate of large particles occurs in the limit of 100 % fines, and is decreased from that of the quadratic case, as shown in figure 4. For non-convex flux functions, the maximum rise rate of large particles occurs at an intermediate concentration, which directly leads to the formation of more complex solutions that include semi-shocks and non-centred expansion fans, as well as shocks and centred fans.

In the limit of no diffusive remixing, the method of characteristics is used to derive exact steady-state concentration solutions for the homogeneous and normally graded inflow problems of Gray & Thornton (2005) and Thornton *et al.* (2006). The results are illustrated for the case of the cubic flux function in figures 7, 10 and 13. In each case, there are three qualitatively different forms of the solution, which are dependent on the inflow concentration distribution and whether the flux function is convex or non-convex. The parameter dependence of the solutions is illustrated in figures 8 and 11. For convex flux functions, the solutions look very similar to those constructed by Gray & Thornton (2005) and Thornton *et al.* (2006), except that the position of key points in the solution are now dependent on the inflow composition and the strength of asymmetry. In particular, the asymmetry causes the final segregation distance for homogeneous flow to be dependent on the inflow concentration (5.14), and in the normally graded problem the ratio of the positions for the first large particle to reach the surface and the first small particle to reach the base, (6.28) and (6.29), is dependent on the skewness. Comparing the theory to the experiments of Wiederseiner *et al.* (2011) suggests that $\gamma = 0.46$, which is close to the boundary between convex and non-convex flux functions. For non-convex

flux functions, semi-shocks with adjacent centred rarefaction fans (such as AEFA in figure 7) and non-centred rarefaction fans (such as DEFD in figure 10) appear, which will also not be completely smeared out by diffusive remixing.

The asymmetric theory of segregation analysed in this paper can easily be extended to account for multi- or polydisperse mixtures (Gray & Ancey 2011; Marks *et al.* 2012), and flows that include erosion and deposition (Gray & Ancey 2009; Fan *et al.* 2014). Although a cubic form has been used in this paper to illustrate the effects of an asymmetric flux function, the actual flux function may also take a more complicated form, potentially depending on a number of flow parameters (Bridgwater 1994). For example, the amount of asymmetry is likely to be physically dependent on the size ratio of the particles, with similar sized particles displaying less asymmetry, but more asymmetry experienced as the spontaneous percolation limit is approached (Bridgwater & Ingram 1971; Savage & Lun 1988). However, this is still to be experimentally verified, and the actual functional form for the segregation flux and its parameter dependences are open questions.

Acknowledgements

The authors would like to thank K. van der Vaart for many enlightening discussions. This research was supported by NERC and EPSRC grants NE/K003011/1 and EP/K00428X/1. P.G. also acknowledges support from the Margaret Elizabeth Lee Fellowship, and J.M.N.T.G. acknowledges support from the programme on 'Fluid-Mediated Particle Transport in Geophysical Flows' at the Kavli Institute for Theoretical Physics, Santa Barbara, CA, USA.

REFERENCES

BAGNOLD, R. A. 1954 Experiments on gravity-free dispersion of large solid spheres in a Newtonian fluid under shear. *Proc. R. Soc. Lond.* A **225**, 49–63.

BARTELT, P. & MCARDELL, B. W. 2009 Granulometric investigations of snow avalanches. *J. Glaciol.* **55** (193), 829–833.

BATCHELOR, G. K. 1972 Sedimentation in a dilute dispersion of spheres. *J. Fluid Mech.* **52**, 245–268.

BERRYMAN, J. G. 1983 Random close packing of hard spheres and disks. *Phys. Rev.* A **27**, 1053–1061.

BRANNEY, M. J. & KOKELAAR, B. P. 1992 A reappraisal of ignimbrite emplacement: progressive aggradation and changes from particulate to non-particulate flow during emplacement of high-grade ignimbrite. *Bull. Volcanol.* **54**, 504–520.

BRIDGWATER, J. 1994 Mixing and segregation mechanisms in particle flow. In *Granular Matter* (ed. A. Mehta), pp. 161–193. Springer.

BRIDGWATER, J., FOO, W. & STEPHENS, D. 1985 Particle mixing and segregation in failure zones – theory and experiment. *Powder Technol.* **41**, 147–158.

BRIDGWATER, J. & INGRAM, N. D. 1971 Rate of spontaneous inter-particle percolation. *Trans. Inst. Chem. Engrs* **49** (3), 163–169.

BUCKLEY, S. E. & LEVERETT, M. C. 1942 Mechanism of fluid displacement in sands. *Trans. AIME* **146**, 107–116.

CALDER, E. S., SPARKS, R. S. J. & GARDEWEG, M. C. 2000 Erosion, transport and segregation of pumice and lithic clasts in pyroclastic flows inferred from ignimbrite at Lascar volcano, Chile. *J. Volcanol. Geotherm. Res.* **104**, 201–235.

CHADWICK, P. 1976 *Continuum Mechanics. Concise Theory and Problems*. George Allen & Unwin.

COURANT, R. & HILBERT, D. 1962 *Methods of Mathematical Physics*, vol. II. Interscience.

DASGUPTA, P. & MANNA, P. 2011 Geometrical mechanism of inverse grading in grain-flow deposits: an experimental revelation. *Earth-Sci. Rev.* **104** (1–3), 186–198.

DINGLER, J. R. & ANIMA, R. J. 1987 Subaqueous grain flows at the head of Carmel submarine canyon, California. *J. Sedim. Petrol.* **59** (2), 280–286.

DOLGUNIN, V. N. & UKOLOV, A. A. 1995 Segregation modelling of particle rapid gravity flow. *Powder Technol.* **83**, 95–103.

DYER, F. C. 1929 The scope for reverse classification by crowded settling in ore-dressing practice. *Eng. Min. J.* **127** (26), 1030–1033.

FAN, Y., BOUKERKOUR, Y., BLANC, T., UMBANHOWAR, P. B., OTTINO, J. M. & LUEPTOW, R. M. 2012 Stratification, segregation, and mixing of granular materials in quasi-two-dimensional bounded heaps. *Phys. Rev.* E **86**, 051305.

FAN, Y. I. & HILL, K. M. 2011 Theory for shear-induced segregation of dense granular mixtures. *New J. Phys.* **13** (9), 095009.

FAN, Y., SCHLICK, C. P., UMBANHOWAR, P. B., OTTINO, J. M. & LUEPTOW, R. M. 2014 Modelling size segregation of granular materials: the roles of segregation, advection and diffusion. *J. Fluid Mech.* **741**, 252–279.

FISHER, R. V. & MATTINSON, J. M. 1968 Wheeler gorge turbidite–conglomerate series California – inverse grading. *J. Sedim. Petrol.* **38** (4), 1013–1023.

FORTERRE, Y. & POULIQUEN, O. 2008 Flows of dense granular media. *Annu. Rev. Fluid Mech.* **40** (1), 1–24.

GDR MiDi 2004 On dense granular flows. *Eur. Phys. J.* E **14**, 341–365.

GOLICK, L. A. & DANIELS, K. E. 2009 Mixing and segregation rates in sheared granular materials. *Phys. Rev.* E **80** (4), 042301.

GRAY, J. M. N. T. 2001 Granular flow in partially filled slowly rotating drums. *J. Fluid Mech.* **441**, 1–29.

GRAY, J. M. N. T. & ANCEY, C. 2009 Segregation, recirculation and deposition of coarse particles near two-dimensional avalanche fronts. *J. Fluid Mech.* **629**, 387–423.

GRAY, J. M. N. T. & ANCEY, C. 2011 Multi-component particle-size segregation in shallow granular avalanches. *J. Fluid Mech.* **678**, 535–588.

GRAY, J. M. N. T. & CHUGUNOV, V. A. 2006 Particle-size segregation and diffusive remixing in shallow granular avalanches. *J. Fluid Mech.* **569**, 365–398.

GRAY, J. M. N. T. & EDWARDS, A. N. 2014 A depth-averaged $\mu(I)$-rheology for shallow granular free-surface flows. *J. Fluid Mech.* **755**, 503–534.

GRAY, J. M. N. T. & HUTTER, K. 1997 Pattern formation in granular avalanches. *Contin. Mech. Thermodyn.* **9**, 341–345.

GRAY, J. M. N. T. & KOKELAAR, B. P. 2010*a* Large particle segregation, transport and accumulation in granular free-surface flows. *J. Fluid Mech.* **652**, 105–137.

GRAY, J. M. N. T. & KOKELAAR, B. P. 2010*b* Large particle segregation, transport and accumulation in granular free-surface flows – Erratum. *J. Fluid Mech.* **657**, 539.

GRAY, J. M. N. T. & THORNTON, A. R. 2005 A theory for particle size segregation in shallow granular free-surface flows. *Proc. R. Soc. Lond.* A **461**, 1447–1473.

GRAY, J. M. N. T., WIELAND, M. & HUTTER, K. 1999 Free surface flow of cohesionless granular avalanches over complex basal topography. *Proc. R. Soc. Lond.* A **455**, 1841–1874.

GREENBERG, H. 1959 An analysis of traffic flow. *Oper. Res.* **7** (1), 79–85.

HILL, K. M., KHARKAR, D. V., GILCHRIST, J. F., MCCARTHY, J. J. & OTTINO, J. M. 1999 Segregation driven organization in chaotic granular flows. *Proc. Natl Acad. Sci. USA* **96**, 11701–11706.

HUTTER, K., WANG, Y. Q. & PUDASAINI, S. P. 2005 The Savage–Hutter avalanche model: how far can it be pushed?. *Phil. Trans. R. Soc. Lond.* A **363** (1832), 1507–1528.

IVERSON, R. M. 1997 The physics of debris-flows. *Rev. Geophys.* **35**, 245–296.

IVERSON, R. M. & VALLANCE, J. W. 2001 New views of granular mass flows. *Geology* **29** (2), 115–118.

JEFFREY, A. 1976 *Quasilinear Hyperbolic Systems and Waves*. Pitman.

JOHANSON, J. R. 1978 Particle segregation ... and what to do about it. *Chem. Engng*, 8 May, pp. 183–188.

JOHNSON, C. G., KOKELAAR, B. P., IVERSON, R. M., LOGAN, M., LAHUSEN, R. G. & GRAY, J. M. N. T. 2012 Grain-size segregation and levee formation in geophysical mass flows. *J. Geophys. Res.* **117**, F01032.

JOP, P., FORTERRE, Y. & POULIQUEN, O. 2005 Crucial role of sidewalls in granular surface flows: consequences for the rheology. *J. Fluid Mech.* **541**, 167–192.

KHAKHAR, D. V., MCCARTHY, J. J. & OTTINO, J. M. 1999 Mixing and segregation of granular materials in chute flows. *Chaos* **9** (3), 594–610.

KOKELAAR, B. P., GRAHAM, R. L., GRAY, J. M. N. T. & VALLANCE, J. W. 2014 Fine-grained linings of leveed channels facilitate runout of granular flows. *Earth Planet. Sci. Lett.* **385**, 172–180.

KUMARAN, V. 2006 The constitutive relation for the granular flow of rough particles, and its application to the flow down an inclined plane. *J. Fluid Mech.* **561**, 1–42.

KUMARAN, V. 2008 Dense granular flow down an inclined plane: from kinetic theory to granular dynamics. *J. Fluid Mech.* **599**, 121–168.

KYNCH, G. J. 1952 A theory of sedimentation. *Trans. Faraday Soc.* **48**, 166–176.

LANEY, C. B. 1998 *Computational Gasdynamics*. Cambridge University Press.

LAX, P. D. 1957 Hyperbolic systems of conservation laws II. *Commun. Pure Appl. Maths* **10** (4), 537–566.

LIGHTHILL, M. J. & WHITHAM, G. B. 1955 On kinematic waves: II. A theory of traffic flow on long crowded roads. *Proc. R. Soc. Lond.* A **229** (1178), 317–345.

LIU, T. P. 1974 The Riemann problem for general 2×2 conservation laws. *Trans. Am. Math. Soc.* **199**, 89–112.

MARKS, B. & EINAV, I. 2011 A cellular automaton for segregation during granular avalanches. *Granul. Matt.* **13** (3), 211–214.

MARKS, B., ROGNON, P. & EINAV, I. 2012 Grainsize dynamics of polydisperse granular segregation down inclined planes. *J. Fluid Mech.* **690**, 499–511.

MARKS, B., VALAULTA, A., PUZRIN, A. & EINAV, I. 2013 Design of protection structures: the role of the grainsize distribution. In *Powders and Grains 2013: Proceedings of the 7th International Conference on Micromechanics of Granular Media, Sydney, Australia, 8–12 July* (ed. A. Yu, K. Dong, R. Yang & S. Luding), AIP Conference Proceedings, vol. 1542, pp. 658–661. American Institute of Physics.

MAY, L. B. H., GOLICK, L. A., PHILLIPS, K. C., SHEARER, M. & DANIELS, K. E. 2010*a* Shear-driven size segregation of granular materials: modeling and experiment. *Phys. Rev.* E **81**, 051301.

MAY, L. B. H., SHEARER, M. & DANIELS, K. E. 2010*b* Scalar conservation laws with non-constant coefficients with application to particle size segregation in granular flow. *J. Nonlinear Sci.* **20** (6), 689–707.

MIDDLETON, G. V. 1970 Experimental studies related to problems of flysch sedimentation. In *Flysch Sedimentology in North America* (ed. J. Lajoie), Geological Association of Canada, Special paper 7, pp. 253–272. Business and Economic Service.

MORLAND, L. W. 1992 Flow of viscous fluids through a porous deformable matrix. *Surv. Geophys.* **13** (3), 209–268.

NITYANAND, N., MANLEY, B. & HENEIN, H. 1986 An analysis of radial segregation for different sized spherical solids in rotary cylinders. *Metall. Trans.* B **17** (2), 247–257.

OLEINIK, O. A. 1959 Uniqueness and stability of the generalized solution of the Cauchy problem for a quasi-linear equation. *Usp. Mat. Nauk (NS)* **14**, 165–170.

OTTINO, J. M. & KHAKHAR, D. V. 2000 Mixing and segregation of granular materials. *Annu. Rev. Fluid Mech.* **32** (1), 55–91.

PITMAN, E. B., NICHITA, C. C., PATRA, A., BAUER, A., SHERIDAN, M. & BURSIK, M. 2003 Computing granular avalanches and landslides. *Phys. Fluids* **15** (12), 3638–3646.

POULIQUEN, O. 1999 Scaling laws in granular flows down rough inclined planes. *Phys. Fluids* **11** (3), 542–548.

PUDASAINI, S. P. & HUTTER, K. 2007 *Avalanche Dynamics: Dynamics of Rapid Flows of Dense Granular Avalanches*. Springer.

RHEE, H. K., ARIS, R. & AMUNDSON, N. R. 1986 *First-order Partial Differential Equations, Theory and Applications of Single Equations*, vol. 1. Prentice-Hall.

ROGNON, P. G., ROUX, J. N., NAAIM, M. & CHEVOIR, F. 2007 Dense flows of bidisperse assemblies of disks down an inclined plane. *Phys. Fluids* **19** (5), 058101.

SAVAGE, S. B. & HUTTER, K. 1989 The motion of a finite mass of granular material down a rough incline. *J. Fluid Mech.* **199**, 177–215.

SAVAGE, S. B. & LUN, C. K. K. 1988 Particle size segregation in inclined chute flow of dry cohesionless granular solids. *J. Fluid Mech.* **189**, 311–335.

SCHMINCK, H. U. 1967 Graded lahars in type sections of Ellensburg Formation, south-central Washington. *J. Sedim. Petrol.* **37** (2), 438–448.

SHANNON, P. T., STROUPE, E. & TORY, E. M. 1963 Batch and continuous thickening – basic theory – solids flux for rigid spheres. *Ind. Engng Chem. Fundam.* **2** (3), 203–211.

SHINBROT, T. & MUZZIO, F. J. 2000 Non-equilibrium patterns in granular mixing and segregation. *Phys. Today* **53** (3), 25–30.

SILBERT, L. E., ERTAS, D., GREST, G. S., HALSEY, T. C., LEVINE, D. & PLIMPTON, S. J. 2001 Granular flow down an inclined plane: Bagnold scaling and rheology. *Phys. Rev.* E **64** (5), 051302.

SOHN, Y. K. & CHOUGH, S. K. 1993 The Udo tuff cone, Cheju Island, South Korea: transformation of pyroclastic fall into debris fall and grain flow on a steep volcanic cone slope. *Sedimentology* **40** (4), 769–786.

STOCK, J. D. & DIETRICH, W. E. 2006 Erosion of steepland valleys by debris flows. *Geol. Soc. Am. Bull.* **118**, 1125–1148.

THORNTON, A. R. & GRAY, J. M. N. T. 2008 Breaking size-segregation waves and particle recirculation in granular avalanches. *J. Fluid Mech.* **596**, 261–284.

THORNTON, A. R., GRAY, J. M. N. T. & HOGG, A. J. 2006 A three-phase mixture theory for particle size segregation in shallow granular free-surface flows. *J. Fluid Mech.* **550**, 1–25.

THORNTON, A. R., WEINHART, T., LUDING, S. & BOKHOVE, O. 2012 Modeling of particle size segregation: calibration using the discrete particle method. *Intl J. Mod. Phys.* C **23** (8), 1240014.

TRIPATHI, A. & KHAKHAR, D. V. 2011 Rheology of binary granular mixtures in the dense flow regime. *Phys. Fluids* **23**, 113302.

TUCKER, M. E. 2003 *Sedimentary Rocks in the Field*. Wiley.

VALLANCE, J. W. & SAVAGE, S. B. 2000 Particle segregation in granular flows down chutes. In *IUTAM Symposium on Segregation in Granular Materials* (ed. A. D. Rosato & D. L. Blackmore), Kluwer.

WHITHAM, G. B. 1974 *Linear and Nonlinear Waves*. Wiley.

WIEDERSEINER, S., ANDREINI, N., EPELY-CHAUVIN, G., MOSER, G., MONNEREAU, M., GRAY, J. M. N. T. & ANCEY, C. 2011 Experimental investigation into segregating granular flows down chutes. *Phys. Fluids* **23**, 013301.

WILLIAMS, J. C. 1976 The segregation of particulate materials – review. *Powder Technol.* **15** (2), 245–251.

WOODHOUSE, M. J., THORNTON, A. R., JOHNSON, C. G., KOKELAAR, B. P. & GRAY, J. M. N. T. 2012 Segregation-induced fingering instabilities in granular free-surface flows. *J. Fluid Mech.* **709**, 543–580.

3. Underlying Asymmetry within Particle Size Segregation

This chapter is a reprint of the article titled "*Underlying Asymmetry within Particle Size Segregation*" by K. van der Vaart, P. Gajjar, G. Epely-Chauvin, N. Andreini, J. M. N. T. Gray, and C. Ancey, published on page 238001, volume 114 of Physical Review Letters in 2015. The first page shows the front cover on which the article featured. The digital object identifier (DOI) for this article is: http://dx.doi.org/10.1103/PhysRevLett.114.238001.

Additional theoretical material that was used to match the asymmetric segregation model of chapter 2 with the experimental data is presented in 3.2. Note that the asymmetry parameter in this chapter is κ, which is directly equivalent to asymmetry parameter γ in chapters 2 and 4.

PHYSICAL REVIEW LETTERS

Articles published week ending 12 JUNE 2015

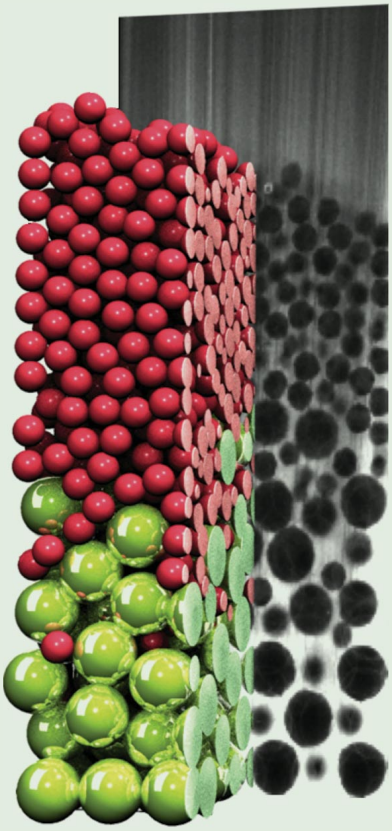

Published by
American Physical Society

APS physics

Volume 114, Number 23

Underlying Asymmetry within Particle Size Segregation

K. van der Vaart,[1,†] P. Gajjar,[2] G. Epely-Chauvin,[1] N. Andreini,[1] J. M. N. T. Gray,[2] and C. Ancey[1,*]
[1]Environmental Hydraulics Laboratory, École Polytechnique Fédérale de Lausanne, Écublens, 1015 Lausanne, Switzerland
[2]School of Mathematics and Manchester Centre for Nonlinear Dynamics, University of Manchester, Manchester M13 9PL, United Kingdom

(Received 1 August 2014; revised manuscript received 26 January 2015; published 10 June 2015)

We experimentally study particle scale dynamics during segregation of a bidisperse mixture under oscillatory shear. Large and small particles show an underlying asymmetry that is dependent on the local particle concentration, with small particles segregating faster in regions of many large particles and large particles segregating slower in regions of many small particles. We quantify the asymmetry on bulk and particle scales, and capture it theoretically. This gives new physical insight into segregation and reveals a similarity with sedimentation, traffic flow, and particle diffusion.

DOI: 10.1103/PhysRevLett.114.238001 PACS numbers: 45.70.Mg, 05.45.-a, 47.57.Gc

The natural tendency of granular media to self-organize when agitated or sheared produces a rich diversity of complex and beautiful patterns [1–3]. Although it is counterintuitive that the components of a heterogeneous mixture will readily separate, this property has serious technical implications as the cause of product nonuniformity in many industrial processes [4–6] and also plays a pivotal role in the enhanced run-out of large scale geophysical granular flows, such as debris flows, pyroclastic flows, and snow avalanches [7–10]. A firm knowledge of the segregation process is thus of universal importance.

Although there has been considerable recent progress in developing continuum based segregation models for sheared granular flows [11–16], the individual particle dynamics are still poorly understood. Discrete particle method (DPM) simulations [17–20] produce a wealth of microscale information, but are models in themselves. It is vital to directly measure particle segregation dynamics in real experiments, but such an analysis is difficult with conventional techniques such as binning and sidewall observation [21–24]. Nonintrusive imaging techniques, such as x-ray tomography [25] and refractive index-matched scanning (RIMS) [26,27] allow examination of the interior of a granular medium, with RIMS recently developing into a powerful tool for examining monodisperse and bidisperse flows [28–30]. In particular, the work of Harrington *et al.* [30] on the emergence of granular segregation demonstrates how particle scale analysis can give new physical insights.

In this Letter, we analyze particle scale dynamics during segregation of a bidisperse mixture under oscillatory shear. We find that the behavior of small and large particles exhibits an asymmetry related to the local particle concentration, with small grains moving faster through regions of many large particles and large particles rising slower through regions of many small particles. This asymmetry is quantified on both particle and bulk length scales, and it is shown how to incorporate the behavior within the theoretical framework.

Methods.—A shearbox 51 mm deep and 37 mm wide is filled to a height $h = 87 \pm 3$ mm with a bidisperse mixture of borosilicate glass spheres ($\rho_p = 2.23$ g/cm^3) with diameters $d_l = 8$ and $d_s = 4$ mm. The larger particles are placed at the bottom, the surface flattened, and the smaller particles placed on top. The sidewalls oscillate while remaining parallel, applying a periodic shear $\gamma(t) = \gamma_0 \sin(\omega t)$ [31] as shown in Fig. 1. The corresponding shear rate $\dot{\gamma}(t) = \gamma_0 \omega \cos(\omega t)$, frequency $\omega = 2\pi/T$ rad s^{-1}, period $T = 13$ s, and strain amplitude $\gamma_0 = \tan\theta_{\max}$. The sidewalls displace to a maximum angle $\theta_{\max} = \pm 30°$, giving a maximum shear rate of $\dot{\gamma}_0 = \gamma_0 \omega$ and a maximum grain displacement amplitude $A = h\gamma_0$. The angle is decreased to $\theta_{\max} = \pm 10°$ for the particle trajectory data in order to slow down the segregation and increase the temporal resolution. Nondimensional time $\hat{t} = t/T$ corresponds to the number of elapsed cycles. We follow a sample using RIMS, with the index-matched liquid a mixture of benzylalcohol and ethanol (viscosity $\mu = 3$ mPa s) containing a fluorescent dye (rhodamine). The low viscosity of the interstitial liquid means that fluid

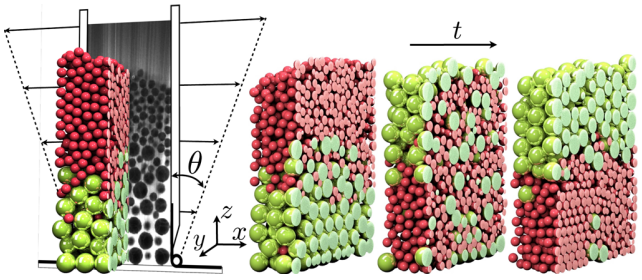

FIG. 1 (color online). Left: The experimental setup. A raw data image is shown and a cross section of a reconstructed sample with 3 and 6 mm beads. Right: cross sections at different times during an experiment.

drag forces are small compared to both gravitational forces and the applied shear (Stokes number > 1 [32]). The mixture is lit with a 532 nm laser sheet perpendicular to the oscillating walls, giving a stack of vertical cross sections. A scan is performed after each full oscillation with the shearbox in the upright position. The images were processed using convolution [33] to give three dimensional particle positions, which are coarse grained in order to determine a continuous volume fraction [34]. Some sidewall effects exist, with small particles preferentially located near the stationary vertical walls, but this does not affect the overall segregation. The horizontal particle motion is diffusive; hence, the concentration is spatially averaged to give a uniform concentration in the x-y plane. We observe no convection rolls [35], although for $|\phi_{\max}| > 45°$ geometrical squeezing was seen to cause convection.

Results.—The typical behavior is shown in Fig. 1: The initial state with large particles on the bottom evolves to a final state with large particles on top, because small particles sink and large particles rise. Interestingly, some large particles remain below when all the others have reached the top. These particles are not stuck but rise at a slower rate than the ones that have reached the top before them. Although this has been inferred before, it has not yet been explained [24].

We define a segregation time $\hat{t}_s$ as the time needed for the vertical centers of mass of the two species to reach a steady state, as shown in Fig. 2(a). We record $\hat{t}_s$ for mixtures with varying global volume fraction of small particles $\Phi(\%) = V_s/(V_l + V_s)$, while keeping the total mixture volume constant. Figure 2(b) shows that $\hat{t}_s$ scales linearly with Φ; i.e., with more small particles in the mixture the segregation is slower [20]. Similar trends were observed over the entire range of angles that can be accessed in our setup. This behavior is usually given a two-part explanation: At low Φ, small particles move slower when there are more small particles [36]. At high Φ, it takes a longer time for large particles to travel to the top when the layer of small particles above them is thicker [20,24]. In both explanations the behavior of the other species is ignored. So how do these explanations combine at an intermediate Φ? A clue is given by Ref. [24], which reported that for a $\Phi = 50\%$ mixture the transition from the state with small particles on top to a mixed state was faster than the subsequent transition from the mixed state to the final segregated state. This points to two separate processes that are likely to be related to the distinct behavior of small and large particles.

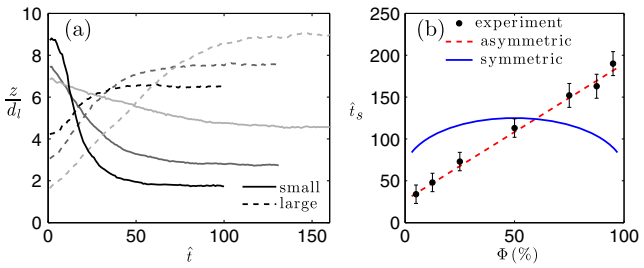

FIG. 2 (color online). (a) Time evolution of the vertical center of mass position $((1/n)\sum_{i=1}^{n} z_i)$ for large and small particles in $\Phi = 25\%$ (black), 50% (dark gray), and 75% (light gray) mixtures. $\theta_{\max} = \pm 30°$. (b) Segregation time $\hat{t}_s$ as a function of Φ; solid line is a fit for the symmetric model with $S_r = 0.016$, while the dashed line is a fit for the asymmetric model with $S_r = 0.030$ and $\kappa = 0.89$.

Particle dynamics.—We are thus motivated to study a single small particle segregating in a mixture of large particles and a single large particle segregating in a mixture of small particles, which we refer to as $\Phi = 0^+\%$ and $\Phi = 100^-\%$ mixtures, respectively. The trajectories of the two particles, shown in Fig. 3(a), are quite different: (i) the large particle segregates roughly 3 times slower than the small particle; and (ii) the large particle rises smoothly at an almost constant speed, whereas the small particle shows a stepwise motion with steps of the order of d_l. This suggests that the small particle falls through gaps in the large particle matrix under gravity, typically traversing just a single layer.

In order to more precisely understand the nature of these trajectories, we study the displacement after $\hat{\tau}$ cycles: $\Delta r(\hat{\tau}) = r(\hat{t} + \hat{\tau}) - r(\hat{t})$. The root mean square displacement (RMSD) $\sigma(\hat{\tau}) = \sqrt{\langle \Delta r^2(\hat{\tau}) \rangle}$ is plotted in Fig. 3(b). The dynamics are diffusive (logarithmic slope $1/4$) for both particles at short time scales and superdiffusive (logarithmic slope $1/2$) at longer time scales. The crossover length

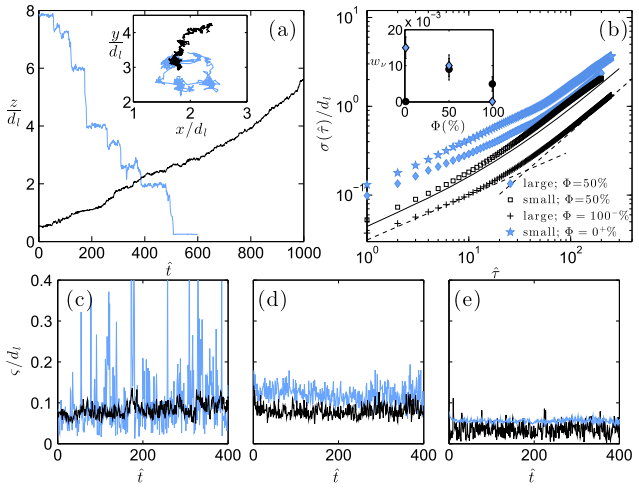

FIG. 3 (color online). Individual particle dynamics for small particles (blue, gray) and large particles (black) with $\theta_{\max} = \pm 10°$. (a) Vertical trajectories of a small particle segregating in a $\Phi = 0^+\%$ mix; and a large particle segregating in a $\Phi = 100^-\%$ mix. Inset: Particle movement in the horizontal plane. (b) RMSD $\sigma(\hat{\tau})$ for different mixtures (see legend), with the solid line a fit of $\sigma_s = \sqrt{D_0\hat{\tau} + w_s^2\hat{\tau}^2}$ at $\Phi = 50\%$ (shifted for clarity). The dotted lines show the slopes $1/2$ and 1. Inset: $w_\nu(\Phi)$ for large ($\nu = l$) and small particles ($\nu = s$). (c)–(e) ς for single cycles in $\Phi = 0^+\%$, 50%, and $100^-\%$ mixtures, respectively.

scale between the diffusive and segregation (superdiffusive) regimes for the small particle is approximately d_l, which corresponds to the typical segregation step size of the small particle. The crossover length scale for the large particle is lower, roughly $0.2d_l$ ($0.4d_s$), and is likely to be related to the scale of the rearrangements of the surrounding small particles. To confirm this, we measure the RMSD per cycle $\varsigma = \sqrt{\langle \Delta r^2 \rangle}$, as shown in Figs. 3(c) and 3(e). The typical value of ς for the single large particle lies just below ς for the surrounding small particles [Fig. 3(e)]. Although the displacements ς for the single small particle experiences large variations, as a result of falling through layers, the mean value is of the same order as that of the surrounding large particles [Fig. 3(c)].

The plot of $\sigma(\hat{\tau})$ for a $\Phi = 50\%$ mixture in Fig. 3(b) shows that the curves lie between those for $\Phi = 0^{+}\%$ and $\Phi = 100^{-}\%$, but with a comparable amount of segregation. Fitting each of the curves with $\sigma_\nu(\hat{\tau}) = \sqrt{D_0\hat{\tau} + w_\nu^2\hat{\tau}^2}$ with diffusion coefficient D_0 allows us to examine the segregation velocities w_ν for large ($\nu = l$) and small ($\nu = s$) particles at different Φ. The inset of Fig. 3(b) shows that $w_s(\Phi)$ decreases with increasing Φ, whereas $w_l(\Phi)$ increases to a maximum at $\Phi = 50\%$ and then decreases, although not to zero, at $\Phi = 100^{-}\%$. To understand the peak in $w_l(\Phi)$, we plot ς for $\Phi = 50\%$ in Fig. 3(d). The values of ς for both small and large particles increase with respect to the $\Phi = 100^{-}\%$ mix; however, the large particle movement is still less compared to the small particles.

At this point we can hypothesize an explanation for the trend in Fig. 2(b): the individual dynamics of small and large grains have a different significance on the overall segregation dynamics at different Φ. At high Φ, the significant dynamics are of the "slow" large particle, which are governed by the scale of rearrangements of the surrounding small particles. At low Φ, it is the "fast" small particle that is significant, as it can make big segregation steps between large particle layers. At an intermediate Φ both processes combine; small particles slow down, because layering disappears, while large particles speed up, because the scale of rearrangements increases.

Displacement statistics.—To study this behavior at the particle scale for each species ($\nu = l, s$), we measure the conditional probabilities $P(\Delta z_\nu|\phi)$ of the vertical displacement Δz_ν given that the local small particle volume fraction is ϕ. Note that shear gradients [37] do not play a role, because of the linear shear profile that is applied. Here, $\phi = 0$ corresponds to regions of only large particles and $\phi = 1$ to only small particles. The results in Figs. 4(a) and 4(b) demonstrate that large particles are less likely to segregate at high ϕ compared to small particles segregating at low ϕ. In the following, we will refer to this as "asymmetry." Similar to the data for $w_l(\Phi)$ in the inset of Fig. 3(b), we observe that the large particles have their greatest displacement at an intermediate ϕ.

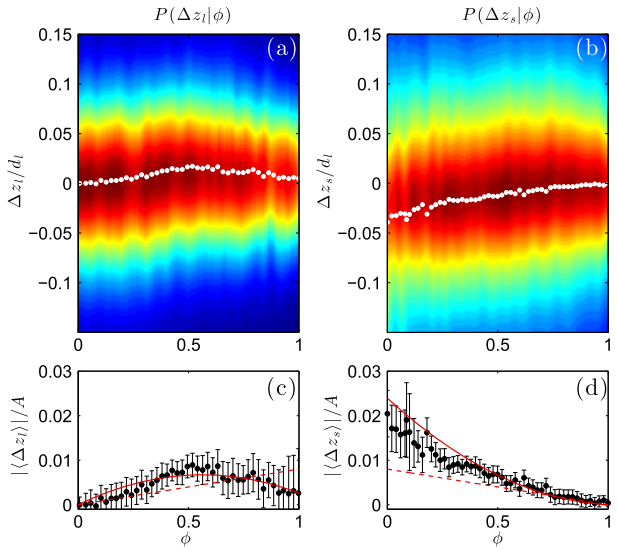

FIG. 4 (color online). (a)–(b) Conditional probabilities $P(\Delta z_l|\phi)$ and $P(\Delta z_s|\phi)$. The probability increases from blue to red. White curves are the mean values $\langle \Delta z_l \rangle$ and $\langle \Delta z_s \rangle$. (c)–(d) $|\langle \Delta z_l \rangle|/A$ and $|\langle \Delta z_s \rangle|/A$ as a function of ϕ, with error bars indicating the standard error of the mean. Dashed and solid lines are plots of Eq. (5) for quadratic and cubic flux functions $F(\phi)$ with $S_r = 0.008$ and $S_r = 0.015$, respectively. The values of S_r were scaled to account for the lower shear rate $\gamma_0\omega$ at $\theta_{\max} = \pm 10°$.

The effect of asymmetry at a mesoscale can be seen in the temporal development of $\phi(z, \hat{t})$ for a $\Phi = 50\%$ mixture in Fig. 5(a). Two important features exist: (i) small particles reach the bottom of the flow faster compared to large particles reaching the top; (ii) large particles appear to rise predominantly together (indicated by the band of low ϕ). The first feature is easily explained by asymmetry: small particles beginning the experiment near the interface

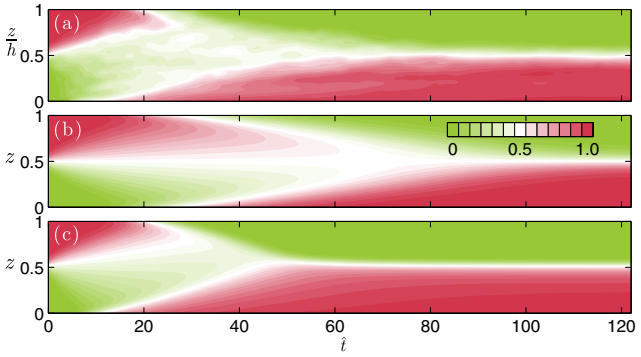

FIG. 5 (color online). (a) Temporal development of $\phi(z, \hat{t})$ versus normalized flow height z/h for a $\Phi = 50\%$ mixture with $\theta_{\max} = \pm 30°$. (b)–(c) Theoretical predictions from Eq. (4). (b) Prediction using the symmetric flux function (2), with $S_r = 0.016$ and $S_r/D_r = 20.9$ [38]. (c) Prediction using the asymmetric flux function (3), with $S_r = 0.030$, $S_r/D_r = 29.6$ and $\kappa = 0.89$.

between the two species quickly travel to the bottom through the large particle matrix, in accordance with $P(\Delta z_s|\phi)$. The second feature is possibly linked to the large particles having a maximum segregation speed at an intermediate concentration.

Theoretical comparison.—Current approaches to modeling size segregation use an advection-diffusion equation for ϕ [39]:

$$\frac{\partial \phi}{\partial t} + \mathrm{div}(\phi \mathbf{u}) - \frac{\partial}{\partial z}(qF(\phi)) = \frac{\partial}{\partial z}\left(D\frac{\partial \phi}{\partial z}\right), \quad (1)$$

where $\mathbf{u}$ is the bulk velocity field, $q = q(\omega\gamma_0, g)$ is the mean segregation speed, g is gravity, D is the diffusivity, and $F(\phi)$ is the flux function, which determines the dependence of the segregation flux on ϕ. The simplest flux function has a quadratic form

$$F(\phi) = \phi(1-\phi). \quad (2)$$

This is employed in a number of models [12–14] and is symmetric about $\phi = 0.5$, dictating that small and large particles behave identically, but in opposite directions. Recently, asymmetric flux functions were introduced by Ref. [40] with the simplest being a cubic form

$$F(\phi) = A_\kappa \phi(1-\phi)(1-\kappa\phi), \quad (3)$$

where asymmetry parameter $0 \le \kappa < 1$, and normalization constant A_κ gives the same amplitude as the symmetric flux function. The applied shear gives a velocity profile $\mathbf{u} = (u(z,t), 0, 0)$. In combination with the lateral spatial uniformity of ϕ, this means that the transport term in Eq. (1) is zero. Equation (1) reduces to

$$\frac{\partial \phi}{\partial \hat{t}} - \frac{\partial}{\partial \hat{z}}(S_r F(\phi)) = \frac{\partial}{\partial \hat{z}}\left(D_r \frac{\partial \phi}{\partial \hat{z}}\right), \quad (4)$$

where $\hat{z} = z/A$, and $S_r = qT/A$, $D_r = DT/A^2$ are nondimensional segregation and diffusive-remixing coefficients, respectively. The symmetric and asymmetric models were least squares fitted to the data in Fig. 2(b) to obtain $S_r = 0.016$ for the symmetric model and $\kappa = 0.89$, $S_r = 0.030$ for the asymmetric model. Integrating Eq. (4) gives the ϕ evolution in Figs. 5(b) and 5(c). Qualitatively, Fig. 5(c) reproduces the experimental result on some critical points: (i) the difference in time between the arrival of small particles at the bottom and large particles at the top of the flow; (ii) the collective rising of large particles; and (iii) a lower ϕ in the bottom half of the flow near the end of the experiment, indicating that some large particles are still inside the small particle matrix, segregating very slowly. These features are not found in the symmetric result in Fig. 5(b). The theoretical displacements per cycle are given by

$$|\Delta\hat{z}_l| = S_r \frac{F(\phi)}{1-\phi}, \qquad |\Delta\hat{z}_s| = S_r \frac{F(\phi)}{\phi}, \quad (5)$$

and are shown alongside the experimental data in Figs. 4(c) and 4(d). The trend is clearly better predicted by the asymmetric flux, which is able to reproduce both the peak in $|\langle\Delta z_l\rangle|$ around $\phi = 0.5$ and the nonlinear decrease of $|\langle\Delta z_s\rangle|$. We attribute the discrepancy of $|\langle\Delta z_s\rangle|$ at low ϕ to tracking errors, when small particles move more than their radius and their displacement is not recorded, thereby lowering the measured value.

Discussion.—We analyze particle motion in a segregating bidisperse mixture under oscillatory shear and discover an underlying asymmetry in the behavior of large and small particles. The small particle motion is steplike, falling down through the large particle matrix typically one layer at a time. On the other hand, the large particle motion is smoother but slower, and linked to the scale of rearrangements of the surrounding small particles. The asymmetric motion of the large and small particles combine to give a characteristic dependence of the particle segregation speeds on the local volume fraction. Large particles segregate slower in the presence of many small particles, while small particles segregate faster in the presence of many large particles. We also observe that large particles move quickest when close to other large particles at intermediate concentrations, a process reminiscent of a collective motion [41]. The underlying asymmetry also manifests at meso and bulk scales. In the development of $\phi(z,\hat{t})$, small particles reach the bottom of the flow faster than large particles reach the top. The segregation time increases linearly when a mixture contains a larger fraction of small particles. Although there is no direct evidence that the observed asymmetry persists for continuous shear, Staron and Phillips [20] report that the segregation time under steady shear also increases linearly with the total concentration of small particles. These insights give a new understanding of segregation in sheared systems, with the dynamic behavior of two species being inherently different.

Models for segregation have typically considered the motion of the large and small grains to be identical. However, an experimentally determined cubic flux [40] brings asymmetric behavior for the two species and gives good agreement on both particle and bulk scales. This draws parallels with the use of asymmetric flux functions to model asymmetry in sedimentation [42], traffic flows [43,44], and diffusion across membranes [45]. For example, in the sedimentation of suspensions, particles settle faster when traveling together, but the settling velocity goes to zero more rapidly than a linear decrease at high concentrations [42]. Similarly, the velocity of cars in traffic approaches zero nonlinearly at high car densities [44]. The commonality between these processes is their discrete nature, but interestingly, size segregation is the only process that consists of two discrete species.

Further work is needed to analyze particle scale motion for continuously sheared flows, e.g., down chutes and within rotating drums, to determine whether asymmetry persists and what form the segregation flux takes. The distinct segregation dynamics of the two species also leads to questions as to a possible relation with other dynamic processes such as dynamic heterogeneity [46].

The authors would like to acknowledge enlightening discussions with Marco Ramaioli, Karen Daniels, Anthony Thornton, and Matthias Schröter, as well as technical and analytical assistance from Justine Caillet. Financial support for this work came from the Swiss SNF Grant No. 200021-149441 and NERC Grants No. NER/A/S/2003/00439 and No. NE/E003206/1, as well as EPSRC Grants No. EP/I019189/1, No. EP/M022447/1 and No. EP/K00428X/1.

*christophe.ancey@epfl.ch
†kasper.vandervaart@epfl.ch

[1] I. S. Aranson and L. S. Tsimring, *Granular Patterns* (Oxford University Press, New York, 2008).
[2] J. M. Ottino and D. V. Khakhar, Annu. Rev. Fluid Mech. **32**, 55 (2000).
[3] D. Pihler-Puzović and T. Mullin, Proc. R. Soc. A **469**, 20130203 (2013).
[4] S. C. Williams, Powder Technol. **2**, 13 (1968).
[5] J. Johanson, Chem. Eng. **85**, 183 (1978).
[6] T. Shinbrot and F. J. Muzzio, Phys. Today **53**, 25 (2000).
[7] R. M. Iverson, Rev. Geophys. **35**, 245 (1997).
[8] C. G. Johnson, B. P. Kokelaar, R. M. Iverson, M. Logan, R. G. LaHusen, and J. M. N. T. Gray, J. Geophys. Res. **117**, 013301 (2012).
[9] D. M. Palladino and G. A. Valentine, J. Volcanol. Geotherm. Res. **69**, 343 (1995).
[10] J. McElwaine and K. Nishimura, in *IUTAM Symposium on Segregation in Granular Flows*, edited by A. D. Rosato and D. L. Blackmore (Springer, Netherlands, 2000), Vol. 81 of Solid Mechanics and Its Applications, p. 81.
[11] J. Bridgwater, W. Foo, and D. Stephens, Powder Technol. **41**, 147 (1985).
[12] J. M. N. T. Gray and A. R. Thornton, Proc. R. Soc. A **461**, 1447 (2005).
[13] L. B. H. May, L. A. Golick, K. C. Phillips, M. Shearer, and K. E. Daniels, Phys. Rev. E **81**, 051301 (2010).
[14] Y. Fan, C. P. Schlick, P. B. Umbanhowar, J. M. Ottino, and R. M. Lueptow, J. Fluid Mech. **741**, 252 (2014).
[15] B. Marks, P. Rognon, and I. Einav, J. Fluid Mech. **690**, 499 (2012).
[16] K. M. Hill and S. D. Tan, J. Fluid Mech. **756**, 54 (2014).
[17] J. Bridgwater, Particuology **8**, 563 (2010).
[18] A. Thornton, T. Weinhart, S. Luding, and O. Bokhove, Int. J. Mod. Phys. C **23**, 1240014 (2012).
[19] Y. Fan, P. B. Umbanhowar, J. M. Ottino, and R. M. Lueptow, Proc. R. Soc. A **469**, 20130235 (2013).
[20] L. Staron and J. Phillips, Phys. Fluids **26**, 033302 (2014).
[21] S. B. Savage and C. K. K. Lun, J. Fluid Mech. **189**, 311 (1988).
[22] J. Vallance and S. Savage, in *IUTAM Symposium on Segregation in Granular Materials*, edited by A. D. Rosato and D. L. Blackmore (Springer, Netherlands, 2000), Vol. 81 of Solid Mechanics and Its Applications, p. 31.
[23] S. Wiederseiner, N. Andreini, G. Epely-Chauvin, G. Moser, M. Monnereau, J. M. N. T. Gray, and C. Ancey, Phys. Fluids **23**, 013301 (2011).
[24] L. A. Golick and K. E. Daniels, Phys. Rev. E **80**, 042301 (2009).
[25] S. McDonald, D. Harris, and P. Withers, Int. J. Material Res. **103**, 162 (2012).
[26] J. A. Dijksman, F. Rietz, K. A. Lőrincz, M. van Hecke, and W. Losert, Rev. Sci. Instrum. **83**, 011301 (2012).
[27] S. Wiederseiner, N. Andreini, G. Epely-Chauvin, and C. Ancey, Exp. Fluids **50**, 1183 (2011).
[28] M. Herrera, S. McCarthy, S. Slotterback, E. Cephas, W. Losert, and M. Girvan, Phys. Rev. E **83**, 061303 (2011).
[29] S. Slotterback, M. Mailman, K. Ronaszegi, M. van Hecke, M. Girvan, and W. Losert, Phys. Rev. E **85**, 021309 (2012).
[30] M. Harrington, J. H. Weijs, and W. Losert, Phys. Rev. Lett. **111**, 078001 (2013).
[31] A. M. Scott and J. Bridgwater, Ind. Eng. Chem. Fundam. **14**, 22 (1975).
[32] C. Cassar, M. Nicolas, and O. Pouliquen, Phys. Fluids **17**, 103301 (2005).
[33] M. D. Shattuck, R. A. Ingale, and P. M. Reis, AIP Conf. Proc. **1145**, 43 (2009).
[34] T. Weinhart, R. Hartkamp, A. R. Thornton, and S. Luding, Phys. Fluids **25**, 070605 (2013).
[35] J. R. Royer and P. M. Chaikin, Proc. Natl. Acad. Sci. U.S.A. **112**, 49 (2015).
[36] A. Jha, J. Gill, and V. Puri, Part. Sci. Technol. **26**, 482 (2008).
[37] Y. Fan and K. M. Hill, New J. Phys. **13**, 095009 (2011).
[38] The ratio S_r/D_r is found by least squares matching the steady end state.
[39] J. M. N. T. Gray, P. Gajjar, and B. P. Kokelaar, C. R. Phys. **16**, 73 (2015).
[40] P. Gajjar and J. M. N. T. Gray, J. Fluid Mech. **757**, 297 (2014).
[41] T. Vicsek and A. Zafeiris, Phys. Rep. **517**, 71 (2012).
[42] G. Batchelor, J. Fluid Mech. **52**, 245 (1972).
[43] M. J. Lighthill and G. B. Whitham, Proc. R. Soc. A **229**, 317 (1955).
[44] 75 Years of the Fundamental Diagram for Traffic Flow Theory: Greenshields Symposium, No. E-C149 in Transportation Research Circular (Transportation Research Board of the National Academies, Washington, DC, 2011).
[45] N. Packard and R. Shaw, Working Paper, Santa Fe Institution, Santa Fe Institute, 13100 Hyde Park Road, Santa Fe, New Mexico 87501, USA (2004), http://www.santafe.edu/media/workingpapers/04-12-040.pdf.
[46] R. Candelier, O. Dauchot, and G. Biroli, Phys. Rev. Lett. **102**, 088001 (2009).

3.2 Additional theoretical material

This section provides further material to explain the how the segregation model of chapter 2 was used to the derive the results presented in the preceding paper "Underlying Asymmetry within Particle Size Segregation".

Experimental observations from the shearbox apparatus indicate that the particle-particle contacts are the dominant factor in determining the particle dynamics, drawing similarities with dense granular flows (Ancey *et al.*, 1999; GDR Midi, 2004; Cassar *et al.*, 2005). The continuum segregation equation, derived in chapter 2 for dense granular flows, was therefore considered to be suitable for modelling segregation in this environment. As a result of the velocity field $\boldsymbol{u} = (u(z,t),0,0)$, and the lateral spatial uniformity of the concentration field, the full segregation equation (1.12) reduces to

$$\frac{\partial \phi}{\partial t} - \frac{\partial}{\partial z}\big(qF(\phi)\big) = \frac{\partial}{\partial z}\left(D\,\frac{\partial \phi}{\partial z}\right), \tag{3.1}$$

where the function $F(\phi)$ explicitely describes the concentration dependence. Non-dimensionalising time t by the the period T, and the vertical height z by the maximum amplitude A gives

$$\frac{\partial \phi}{\partial \hat{t}} - \frac{\partial}{\partial \hat{z}}\big(S_r F(\phi)\big) = \frac{\partial}{\partial \hat{z}}\left(D_r\,\frac{\partial \phi}{\partial \hat{z}}\right), \tag{3.2}$$

where $\hat{z} = z/A$ and $\hat{t} = t/T$. The non-dimensional segregation and diffusive remixing coefficients are $S_r = qT/A$ and $D_r = DT/A^2$ respectively. As there is no motion of the particles across the base ($\hat{z} = 0$) or across the surface of the flow ($\hat{z} = 1$), a no-flux boundary condition may be applied

$$S_r F(\phi) + D_r \frac{\partial \phi}{\partial \hat{z}} = 0 \qquad (\hat{z} = 0, 1). \tag{3.3}$$

The segregation flux function $F(\phi)$ is assumed to take the cubic form

$$F(\phi) = A_\kappa \phi(1-\phi)(1-\kappa\phi), \tag{3.4}$$

where the asymmetry parameter is $0 \leqslant \kappa \leqslant 1$, and the normalisation constant

$$A_\kappa = \frac{27\kappa^2}{4\big(-2\kappa^3 + 3\kappa^2 + 3\kappa - 2 + 2(\kappa^2 - \kappa + 1)^{3/2}\big)} \tag{3.5}$$

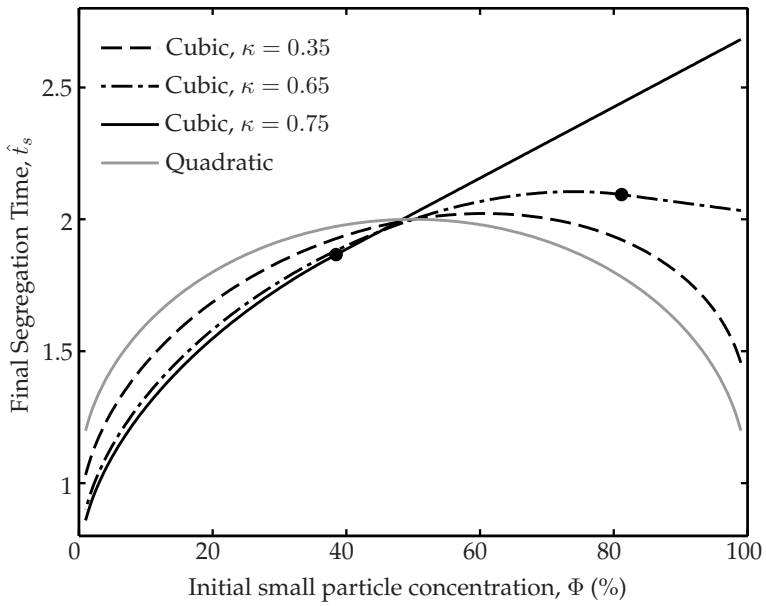

Figure 3.1: The final segregation time $\hat{t}_s$ as a function of the initial small particle concentration. These were derived from the exact solutions to equation (3.6) under the non-diffuse limit $D_r = 0$, with $S_r = 1$. The quadratic flux (3.10), shown with a grey solid line, has a parabolic-like dependence on the initial concentration Φ, that is symmetric about $\Phi = 50\%$. The maximum segregation time also occurs at $\Phi = 50\%$. For asymmetric convex flux functions, with $0 \leqslant \kappa \leqslant 0.5$, the dependence is still parabolic-like, except that the maximum segregation time occurs at a concentration Φ that is increased towards $\Phi = 100\%$. For example, the black dashed line shows the dependence for $\kappa = 0.35$. For convex cubic flux functions with values of the asymmetry parameter $0.5 < \kappa \leqslant 1$ there are different behaviours depending on Φ in relation to the critical initial small particle concentration Φ_c, shown with black markers. As can be seen for the curves $\gamma = 0.65$ and $\gamma = 0.75$, shown with black dash-dotted lines and black solid lines respectively, small initial concentrations $\Phi \leqslant \Phi_c$ share the parabolic-like dependence of the non-convex fluxes. However, for higher initial concentrations, $\Phi > \Phi_c$, there is a linear dependence on the initial concentration. As the asymmetry parameter is increased, Φ_c decreases, meaning the linear behaviour becomes dominant.

gives the same maximum amplitude of 1/4 as for the quadratic flux function. This is the simplest member of the family of functions described in section 3 of chapter 2, and is entirely equivalent to the cubic function used there, except that the asymmetry parameter in this case is κ rather than γ.

3.2.1 Final segregation time

As explained in chapter 2, the theoretical limit $D_r = 0$ provides a useful simplification since it allows the effects of the asymmetry to be evaluated. In this limit,

equation (3.2) becomes

$$\frac{\partial \phi}{\partial \hat{t}} - \frac{\partial}{\partial \hat{z}}\big(S_r F(\phi)\big) = 0. \tag{3.6}$$

This equation is the same as the steady-state velocity-independent segregation equation (4.3)* of chapter 2, with $\hat{t}$ in place of ξ and $\hat{z}$ in place of ψ. Thus the segregation time in this system is entirely equivalent to the final segregation distance examined in chapter 2. In particular, the results of section 6 from chapter 2 can be used to predict the segregation time of a normally graded initial particle distribution as a function of the initial small particle concentration $\Phi = 1 - \psi_{\mathsf{A}}$, where ψ_{A} is the initial interface height between the large and small particles. Using equation (6.10)* of chapter 2 for the final segregation distance ξ_{F}, the final segregation time $\hat{t}_s$ for a convex cubic flux with $0 \leqslant \kappa \leqslant 0.5$ is given by

$$\hat{t}_s = \frac{\Phi}{S_r A_\kappa \phi_{\mathsf{F}}^2 (1 + \kappa - 2\kappa\phi_{\mathsf{F}})}, \tag{3.7}$$

where concentration ϕ_{F} is defined by

$$\frac{\Phi}{1-\Phi} = \frac{\phi_{\mathsf{F}}^2 (1 + \kappa - 2\kappa\phi_{\mathsf{F}})}{(1-\phi_{\mathsf{F}})^2 (1 - 2\kappa\phi_{\mathsf{F}})}. \tag{3.8}$$

As shown in figure 11 of chapter 2, the solution structure for convex flux functions with $0.5 < \kappa \leqslant 1$ can change depending on the initial interface height ψ_{A}. Thus the critical initial small particle concentration Φ_c at which the two solutions change is given by equation (6.26)* of chapter 2, namely

$$1 - \Phi_c = \frac{8\kappa^3 - 12\kappa^2 + 6\kappa - 1}{11\kappa^3 - 19\kappa^2 + 11\kappa - 2}. \tag{3.9}$$

When $\Phi \leqslant \Phi_c$, the final segregation time is given by equation (3.7) above. However, when $\Phi > \Phi_c$, the final segregation time is given by equations (6.24)* and (6.25)* of chapter 2, noting that $\Phi = 1 - \psi_{\mathsf{A}}$.

The equivalent result for the quadratic flux $F(\phi) = \phi(1-\phi)$ can be found in equation (3.16) of Thornton *et al.* (2006),

$$\hat{t}_s = \frac{1}{S_r}\big(\sqrt{1-\Phi} + \sqrt{\Phi}\big)^2. \tag{3.10}$$

This result is recovered from equations (3.7–3.8) in the limit $\kappa \to 0$. As shown in figure 3.1 with the grey solid line, the final segregation time $\hat{t}_s$ for the quadratic flux (3.10) has a parabolic like-dependence on the initial concentration Φ, with the

maximum segregation time occurring for $\Phi = 50\%$. The segregation time for convex flux functions (3.7), with low values of the asymmetry parameter κ, has a similar dependence, except an asymmetry is introduced with the maximum segregation time shifted further towards $\Phi = 100\%$. This can be seen for $\gamma = 0.35$ with the black dashed line. At higher values of the asymmetry parameter $0.5 < \kappa \leqslant 1$, when the flux function is non-convex, there are two different behaviours that are dependent on the initial small particle concentration Φ. At low initial small particle concentrations, $\Phi \leqslant \Phi_c$, the dependence is parabolic-like, and qualitatively similar to the dependence for the convex flux function. At higher concentrations $\Phi > \Phi_c$, however, there is a linear dependence between the final segregation time $\hat{t}_s$ and the initial small particle concentration Φ. The linear dependence is due to the influence of the decreasing large particle velocity in the limit as the small particle concentration ϕ tends toward unity. Figure 3.1 shows the dependencies for $\kappa = 0.65$ and $\kappa = 0.75$, shown with black dash-dotted lines and black solid lines respectively. The values of Φ_c are indicated with black markers for both of these values of κ. As the asymmetry parameter κ is increased, the critical initial concentration Φ_c (3.9) decreases, and so the linear behaviour becomes dominant. It is worthwhile to note that Staron & Phillips (2014) reported a linear relationship between the segregation time and the total concentration of small particles in their discrete particles simulations of a two-dimensional chute flow.

A least squares fit was performed on the experimental data shown in figure 2 of the paper to determine $S_r = 0.016$ for the quadratic flux, and $S_r = 0.030$, $\kappa = 0.89$ for the cubic flux.

3.2.2 Steady state balance between segregation and diffusive remixing

The segregating flow governed by equation (3.2) tends to a steady state, in which there is a balance between segregation that acts to separate the constituents, and diffusive remixing that acts to reduce concentration gradients at the interface between the constituents. In this steady state, the non-dimensional segregation equation

(3.2) reduces to

$$-\frac{\partial}{\partial \hat{z}}\big(S_r F(\phi)\big) = \frac{\partial}{\partial \hat{z}}\left(D_r \frac{\partial \phi}{\partial \hat{z}}\right) \qquad (0 < \hat{z} < 1), \tag{3.11}$$

with the no-flux boundary condition (3.3) at $\hat{z} = 0, 1$. Following Gray & Chugunov (2006), integrating (3.11) with respect to $\hat{z}$ shows that the normal flux $S_r F(\phi) + D_r \partial\phi/\partial\hat{z}$ is equal to a constant across the depth of the flow. The boundary condition (3.11) has the exact same form, implying that this constant is zero, and so

$$S_r F(\phi) + D_r \frac{\partial \phi}{\partial \hat{z}} = 0 \qquad (0 \leqslant \hat{z} \leqslant 1). \tag{3.12}$$

This ODE can be integrated by separating variables, giving

$$\hat{z} = C - \frac{D_r}{S_r} \int \frac{1}{F(\phi)}\, \mathrm{d}\phi, \tag{3.13}$$

where C is a constant of integration. Using the cubic flux (3.4), this gives

$$\hat{z} = \begin{cases} C - \dfrac{D_r}{S_r} \dfrac{1}{A_\kappa(1-\kappa)} \ln\left(\dfrac{\phi^{(1-\kappa)}(1-\kappa\phi)^\kappa}{(1-\phi)}\right) & (\hat{z} \neq 1) \\ C - \dfrac{D_r}{S_r} \dfrac{1}{A_\kappa} \left(\ln\left(\dfrac{\phi}{1-\phi}\right) + \dfrac{1}{1-\phi}\right) & (\hat{z} = 1) \end{cases}, \tag{3.14}$$

whilst Gray & Chugunov (2006) previously derived the equivalent result for the quadratic flux as

$$\hat{z} = C - \frac{D_r}{S_r} \ln\left(\frac{\phi}{1-\phi}\right). \tag{3.15}$$

As explained in Wiederseiner *et al.* (2011) and Gray & Ancey (2015), constant C may be determined by imposing an integral constraint. Integrating the segregation equation (3.2) across the flow depth and applying the no-flux boundary condition implies that the integral

$$I = \int_0^1 \phi\, \mathrm{d}\hat{z} \tag{3.16}$$

is independent of time $\hat{t}$. In particular, this means that I is equal to the initial small particle concentration Φ. For the particular case of the quadratic flux, it is possible to invert the steady state for the quadratic flux (3.15) to give $\phi = \phi(\hat{z}, C)$. The integration constant C can be found by evaluating I, giving $\phi = \phi(\hat{z}, \Phi)$. This is not, however, possible in the general case because of the complex dependence $\hat{z} = \hat{z}(\phi)$. Instead, Gray & Ancey (2015) showed that it is possible to reverse the direction of integration in (3.16) by defining an extended solution

$$\hat{z}_e = \max(0, \min(1, \hat{z})), \tag{3.17}$$

giving the alternative expression for I

$$I = \int_0^1 \hat{z}_e \, \mathrm{d}\phi. \tag{3.18}$$

This integral can be numerically evaluated through quadrature, and the constant of integration C found through iteration.

The experimental data shown in figure 5 of the paper can be seen to tend towards a steady state after $\hat{t} = 100$. This steady state was least squares fitted with the quadratic and cubic steady state expressions, (3.15) and (3.14) respectively, to give $S_r/D_r = 20.9$ for the quadratic and $S_r/D_r = 29.6$ for the cubic. Note that the value of $\kappa = 0.89$ determined from the segregation time (§ 3.2.1) was used for the asymmetry parameter.

4. Asymmetric breaking size-segregation waves in dense granular free-surface flows

---

This chapter is a copy of an article titled "*Asymmetric breaking size-segregation waves in dense granular free-surface flows*" by P. Gajjar, K. van der Vaart, A. R. Thornton, C. G. Johnson, C. Ancey and J. M. N. T. Gray. The article was published in volume 794 of the Journal of Fluid Mechanics (2016), on pages 460–505. The first page shows the front cover on which the article featured. Permission for reproduction granted by Cambridge University Press. The digital object identifier (DOI) for this article is http://dx.doi.org/10.1017/jfm.2016.170.

CAMBRIDGE
UNIVERSITY PRESS

10 May 2016

Journal of Fluid Mechanics

VOLUME 794

J. Fluid Mech. (2016), *vol.* 794, *pp.* 460–505.

doi:10.1017/jfm.2016.170

Asymmetric breaking size-segregation waves in dense granular free-surface flows

P. Gajjar[1,†], K. van der Vaart[2], A. R. Thornton[3], C. G. Johnson[1], C. Ancey[2] and J. M. N. T. Gray[1]

[1]School of Mathematics and Manchester Centre for Nonlinear Dynamics, University of Manchester, Manchester M13 9PL, UK

[2]Environmental Hydraulics Laboratory, École Polytechnique Fédérale de Lausanne, Écublens, 1015 Lausanne, Switzerland

[3]Multi-Scale Mechanics Group, MESA+, University of Twente, The Netherlands

(Received 23 July 2015; revised 23 December 2015; accepted 27 February 2016)

Debris and pyroclastic flows often have bouldery flow fronts, which act as a natural dam resisting further advance. Counter intuitively, these resistive fronts can lead to enhanced run-out, because they can be shouldered aside to form static levees that self-channelise the flow. At the heart of this behaviour is the inherent process of size segregation, with different sized particles readily separating into distinct vertical layers through a combination of kinetic sieving and squeeze expulsion. The result is an upward coarsening of the size distribution with the largest grains collecting at the top of the flow, where the flow velocity is greatest, allowing them to be preferentially transported to the front. Here, the large grains may be overrun, resegregated towards the surface and recirculated before being shouldered aside into lateral levees. A key element of this recirculation mechanism is the formation of a breaking size-segregation wave, which allows large particles that have been overrun to rise up into the faster moving parts of the flow as small particles are sheared over the top. Observations from experiments and discrete particle simulations in a moving-bed flume indicate that, whilst most large particles recirculate quickly at the front, a few recirculate very slowly through regions of many small particles at the rear. This behaviour is modelled in this paper using asymmetric segregation flux functions. Exact non-diffuse solutions are derived for the steady wave structure using the method of characteristics with a cubic segregation flux. Three different structures emerge, dependent on the degree of asymmetry and the non-convexity of the segregation flux function. In particular, a novel ‘lens-tail’ solution is found for segregation fluxes that have a large amount of non-convexity, with an additional expansion fan and compression wave forming a ‘tail’ upstream of the ‘lens’ region. Analysis of exact solutions for the particle motion shows that the large particle motion through the ‘lens-tail’ is fundamentally different to the classical ‘lens’ solutions. A few large particles starting near the bottom of the breaking wave pass through the ‘tail’, where they travel in a region of many small particles with a very small vertical velocity, and take significantly longer to recirculate.

† Email address for correspondence: parmesh.gajjar@alumni.manchester.ac.uk

Key words: granular media, mixing, pattern formation

1. Introduction

Debris and pyroclastic flow deposits often show evidence of bouldery fronts that have a high proportion of large particles (e.g. Sharp & Nobles 1953; Johnson 1970, 1984; Takahashi 1980; Costa & Williams 1984; Pierson 1986; Iverson 2014; Turnbull, Bowman & McElwaine 2015). Figure 1 shows large boulders deposited at the front of a debris flow in Arizona, USA. These large grains tend to be more resistive to downslope motion than the fines, and consequentially have a significant influence on the overall flow dynamics by acting as a 'dam' that resists the flow behind (Pierson 1986). The advancing, more mobile, fine grains from within the interior of the flow (Major & Iverson 1999) shoulder the large particles at the front to the sides (Johnson *et al.* 2012), forming coarse-grained levees that channelise the flow. The inside of this channel is lined by a layer of deposited fine grains, further reducing the friction and increasing the run-out distance (Kokelaar *et al.* 2014). All of this behaviour is readily reproduced in both large- and small-scale experiments (Iverson & Vallance 2001; Iverson *et al.* 2010; Johnson *et al.* 2012). In particular, Pouliquen, Delour & Savage (1997) observed that the interaction of the resistive front with the mobile interior also causes a lateral instability where the flow-front fingers and breaks into a number of different confining channels (Sharp & Nobles 1953; Pouliquen *et al.* 1997; Woodhouse *et al.* 2012). The development of the bouldery fronts is thus key to understanding how segregation feeds back on the bulk flow field.

A key component within the formation of coarse-grained fronts and lateral levees is the inherent process of size segregation that is common to all polydisperse granular media. Whilst flowing, granular mixtures dilate sufficiently to allow the flow to act like a sieve that naturally sorts the different sized constituents. Small gaps in the grain matrix allow the finer grains to preferentially percolate downwards under gravity, whilst there is a return flow of coarse grains towards the surface. The exact mechanism for the rising of large grains is under investigation (van der Vaart *et al.* 2015), although the net result is an upward coarsening in the particle-size distribution that is often called inverse grading. For example, a bidisperse mixture containing just two grain sizes would separate into two separate layers in the absence of diffusion, with the large particles on top of the small ones, as shown in figure 2(*a*). The surface layers have the highest velocities, and so the larger particles are transported to the front of the flow. These coarse grains may then be pushed *en masse* at the front if massive enough (Pouliquen & Vallance 1999), or otherwise may be overrun by the advancing flow. They are able to rise up back towards the surface as they are resegregated, creating a complex recirculating motion that connects the upstream inversely graded body of the flow to the coarse-rich flow front. As more large grains are supplied towards the front, the coarse-grained margin grows in size, with the interface propagating forward at a slower speed than the advancing front (Gray & Kokelaar 2010*a*,*b*). The front may obtain a steady size in two dimensions if there is no further upstream supply of large particles, or alternatively, if the upstream supply of large particles is matched by the rate of deposition on the lower basal surface (Gray & Ancey 2009). The front may also obtain a finite-size steady state in three

FIGURE 1. Photograph of the front of a debris flow that has stopped in the channel of Rattlesnake Creek, Arizona, USA. The large boulders seen here in the front are typical of many debris and pyroclastic flows, with larger particles segregating upwards to the faster moving surface layers and preferentially transported towards the front, where they accumulate. Photo courtesy of C. Magirl and USGS.

dimensions by shouldering the large grains, transported to the front, laterally outwards to the sides to produce static coarse-grained levees (Johnson *et al.* 2012; Kokelaar *et al.* 2014).

1.1. *Recirculating particle motion*

The first real insights into the structure of the recirculation zone were provided by Pouliquen *et al.* (1997) and Pouliquen & Vallance (1999), who used a moving camera to approximately measure the lateral recirculating motion of a line of large black crushed fruit stones placed on the surface of a flow of translucent glass beads. Their observations, however, lacked spatial resolution, and further direct experimental observation of the recirculation has been challenging due to its complex time dependence. The recirculation zone propagates quickly downstream at speed u_{wave} as the front advances forward at speed u_{front}, meaning that there is the difficulty of capturing the motion using a camera moving with the recirculation zone. Long chutes are also required before a steady recirculation regime emerges.

An alternative approach is to use the moving-bed flume set-up shown in figure 3, that is similar to that used by Davies (1990). The flume is 104 cm in length with a rough 10 cm wide upward moving conveyor belt positioned between the four stationary vertical walls. The inclination of the channel was set at 19.8° to establish a uniform flow height along the channel. Higher or lower angles were found to

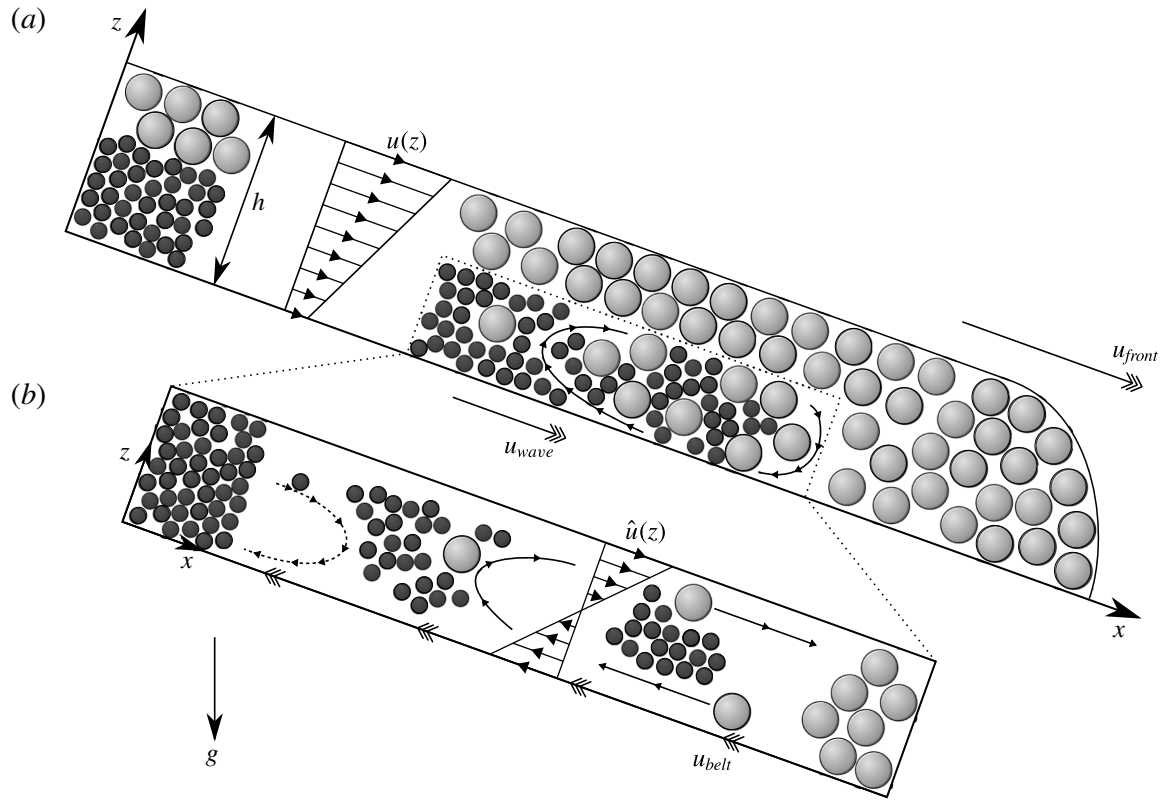

FIGURE 2. (*a*) A vertical section through a steadily propagating avalanche travelling down an inclined plane. In the body of the flow, the large grains segregate to the upper layers, where the velocity $u(z)$ is greatest, and hence are transported towards the front of the avalanche, where they are overrun, resegregated upwards and recirculated to form a coarse-rich particle front. A complex recirculating motion is created that links the vertically segregated flow in the rear of the avalanche from the coarse-grained front, with the recirculating region known as a 'breaking size-segregation wave' (Thornton & Gray 2008). Although the front increases in size as more large particles are supplied from the inversely graded flow upstream, the recirculation region shown with dotted lines reaches a steady structure that travels at the average speed u_{wave}. (*b*) A convenient way of studying this steady recirculation regime is to use a moving-bed flume, which can establish a steady motion within a short chute length. The belt moves upstream at a speed u_{belt}, driving an upstream flow in the lowest layers, whilst the upper layers move downstream under gravity. This generates a net velocity profile $\hat{u}(z) = u(z) - u_{wave}$ and is the same as examining the recirculation zone within (*a*) from a frame advecting at speed u_{wave}. There is no upstream supply of large particles in this configuration (*b*), and so, provided that the segregation and diffusion rates are constant (Thornton & Gray 2008), it is mathematically equivalent to the subset of figure (*a*) marked by the dotted lines. Large particles rise towards the surface, and are sheared towards the downstream end of the flume. Some large grains are driven back upstream by the belt, segregate back towards the surface and are recirculated.

cause an accumulation towards the front or rear of the channel, respectively. The belt moves upstream at a velocity $u_{belt} = 72$ mm s^{-1}. This generates the experimental configuration shown schematically in figure 2(*b*), where the lower layers of the flow are forced upstream by the belt, while the upper layers move downstream under gravity. While this flow is not itself inversely graded, it is mathematically equivalent to the section of an inversely graded avalanche shown in figure 2(*a*), provided that the segregation and diffusion rates are constant (Thornton & Gray 2008). The absence

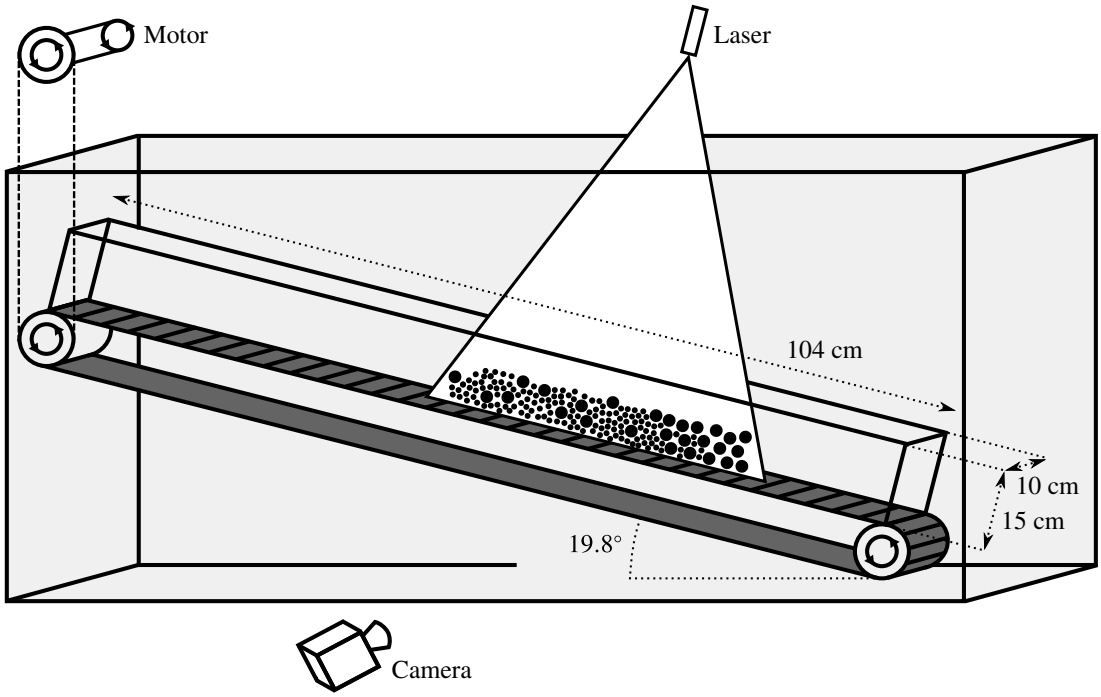

FIGURE 3. A schematic diagram of the moving-bed flume set-up. The flume is 104 cm in length and 15 cm high, with a rough 10 cm wide conveyor belt at the base that moves upstream at velocity $u_{belt} = 72$ mm s^{-1}. This generates the flow configuration sketched in figure 2(*b*), with the particles in the lower layers of the flow forced upstream by the belt, whilst those in the upper layers of the flow move downstream under gravity. The entire set-up is submerged in a larger tank containing a mixture of benzyl-alcohol and ethanol. This acted as the index matched interstitial fluid, and had a viscosity $\mu = 3$ mPa s and fluid density of 995 kg m^{-3}. The motor unit was mounted outside of the tank and drove the belt through a chain mechanism. A dye (rhodamine) was added to the fluid and the flow illuminated with a laser sheet of wavelength 532 nm. A camera positioned at one of the glass side walls captured the temporal evolution, with particles appearing as dark circles. The diameters of these circles could be tracked in time to determine whether the particle was small or large. An example snapshot at one moment in time, and the time-averaged concentration fields are shown in figure 6.

of the layer of large particles also allows a steady state to develop within the experimental configuration. Both the experimental configuration and the full problem are assumed to be two-dimensional, meaning that there are no side-wall effects. Just as in the full problem, the large grains in the experimental configuration (figure 2*b*) initially segregate upwards and are sheared towards the downstream end of the flume, as shown in the normal exposure photograph in figure 4(*a*). However, the motion of the belt forces some large grains to be carried upstream, where they subsequently lie below small grains. The large grains resegregate upwards, and once they reach the surface, they are carried back towards the downstream end of the flume. The oblique view in figure 5 looking upstream from the end of the flume clearly shows the accumulated large particles, and resembles the bouldery front shown in figure 1. This moving-bed flume allows the structure of the steady recirculation regime to be examined in greater detail. For example, the long time exposure photograph in 4(*b*), taken with an exposure time of 133 s, illustrates the time-averaged concentration field of the recirculation zone.

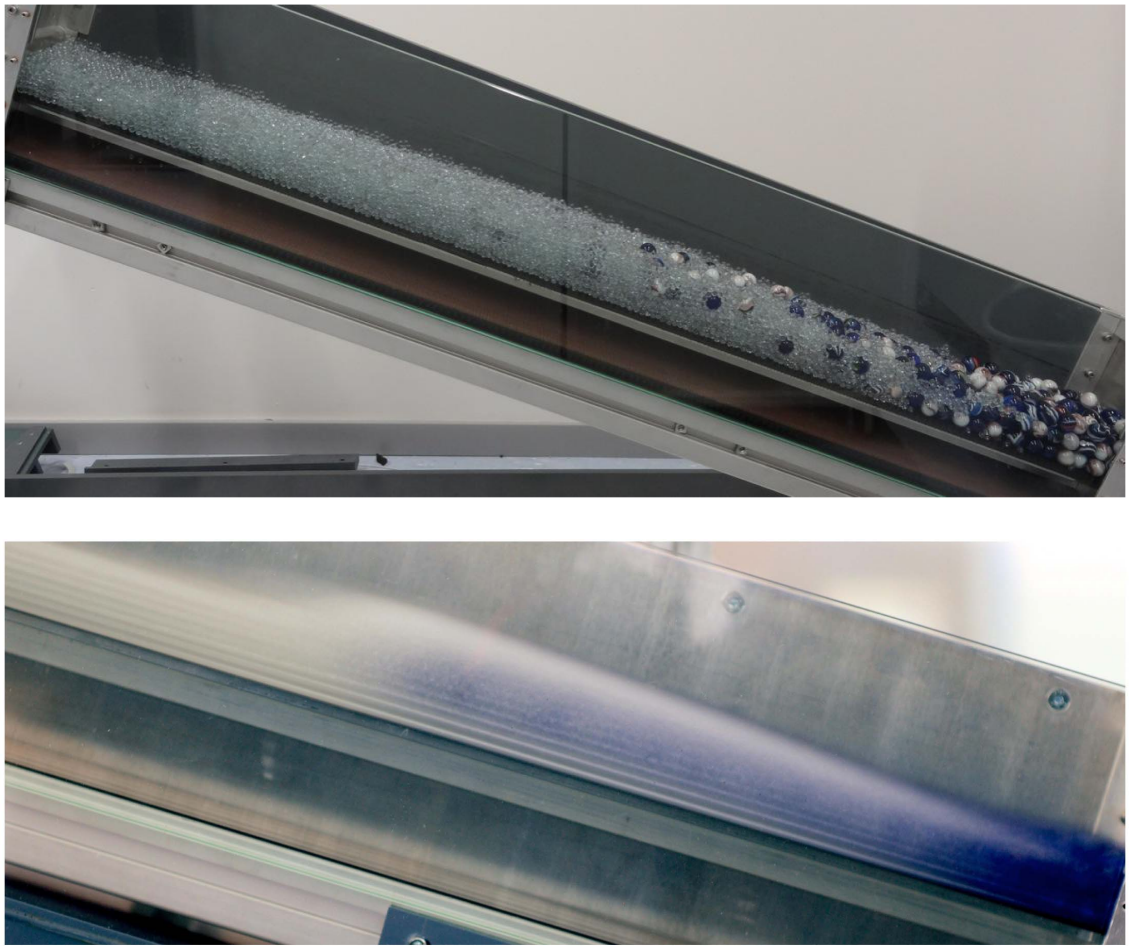

FIGURE 4. Photographs showing the steady recirculation regime established within the 104 cm long moving-bed flume set-up sketched in figure 3. The particle diameters were 5 and 14 mm. The normal exposure photograph (*a*) shows the large blue and white marbles collecting towards the right, forming a coarse-rich flow region at the downstream end of the flume, whilst the long exposure photograph (*b*) shows a time-averaged concentration field and the structure of the breaking size-segregation wave. An exposure time of 133 s was used to capture (*b*).

The individual motion of the particles on the centre line was revealed using refractive index matched scanning ('RIMS': Wiederseiner *et al.* 2011*a*; Dijksman *et al.* 2012; van der Vaart *et al.* 2015). Spherical borosilicate glass beads of density 2230 kg m^{-3} and diameters 14 and 5 mm were used, with the volume ratio of large particles to small particles being 2 : 5. As shown in figure 3, the entire flume set-up was submerged in a tank containing a mixture of benzyl-alcohol and ethanol, which acted as the index matched interstitial fluid of viscosity $\mu = 3$ mPa s, with a fluid density of 995 kg m^{-3}. The motor unit for the belt was positioned outside of the tank and drove the belt through a system of chains. A fluorescent dye (rhodamine) was added to the liquid, which was excited by a laser sheet of wavelength 532 nm in a thin plane parallel to the flow direction. As the particles contain no dye, they appear as dark circles on a bright background. The result is a cross-sectional image of the interior of the flow, which is captured through the glass side wall using a high-speed camera. The laser and camera were positioned to capture the section of the flow containing the recirculation zone. The dark circles are tracked over time, with the minimum and maximum diameters used to determine whether that circle

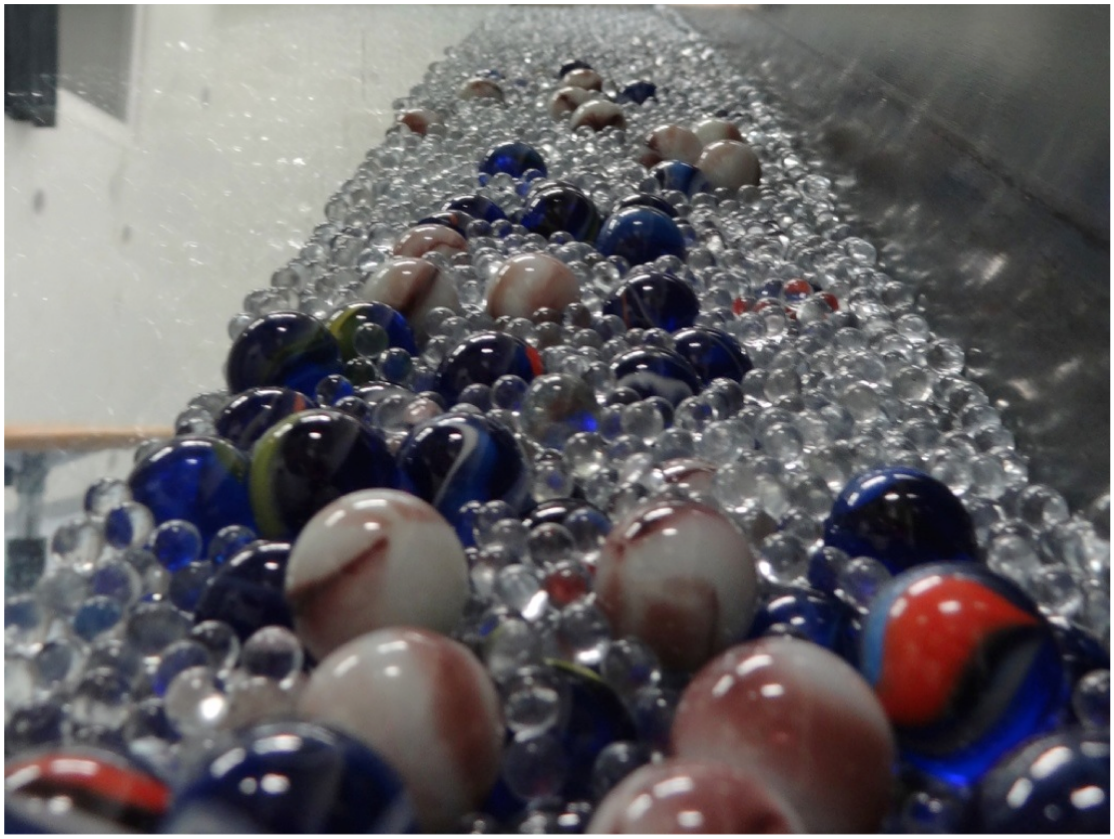

FIGURE 5. An oblique upstream view from the surface of steady-state coarse-rich front established in the moving-bed flume of figure 3. The large blue and white marbles congregate towards the front of the picture, with the smaller clear glass beads towards the rear.

corresponds to a small or large particle. The large size ratio between the grains minimised identification errors, although there was a small possibility that a large particle may be mistaken for a small particle. This, however, would only happen if the particle was sliced close to its edge and never moved closer to the plane of the laser. A typical snapshot of the particle motion is shown in figure 6(*a*), where it can be seen that there are a few large particles in regions of many small particles at the upstream (left) end of the flow. These large particles are seen to move very slowly, compared with the majority of the large particles which recirculate very quickly towards the front. Figure 6(*c*) shows a time-averaged concentration plot, which was averaged over a 40 min period, with 1 image taken every 2 s. The slow movement of the large particles through the upstream region of small particles lowers the concentration there, and causes the 'white' 'tail'-like region.

It is worthwhile considering what influence the interstitial fluid has on the particle behaviour. The presence of a fluid (rather than air) not only modifies the interstitial pore pressures, but also couples the stress carried by the particles to that carried by the fluid flowing through gaps in the grain matrix (Iverson & LaHusen 1989; Iverson 1997, 2005). This coupling is particularly significant in unsteady flows, since local changes in the particle volume fraction allow large excess pore pressures to develop, which in turn feedback on the granular motion (du Pont *et al.* 2003; Muite, Hunt & Joseph 2004; Pailha, Nicolas & Pouliquen 2008; Pailha & Pouliquen 2009). However, for steady, dense granular flows such as those sketched in figure 2, the large number of particle–particle contacts mean that frictional interactions are still dominant in

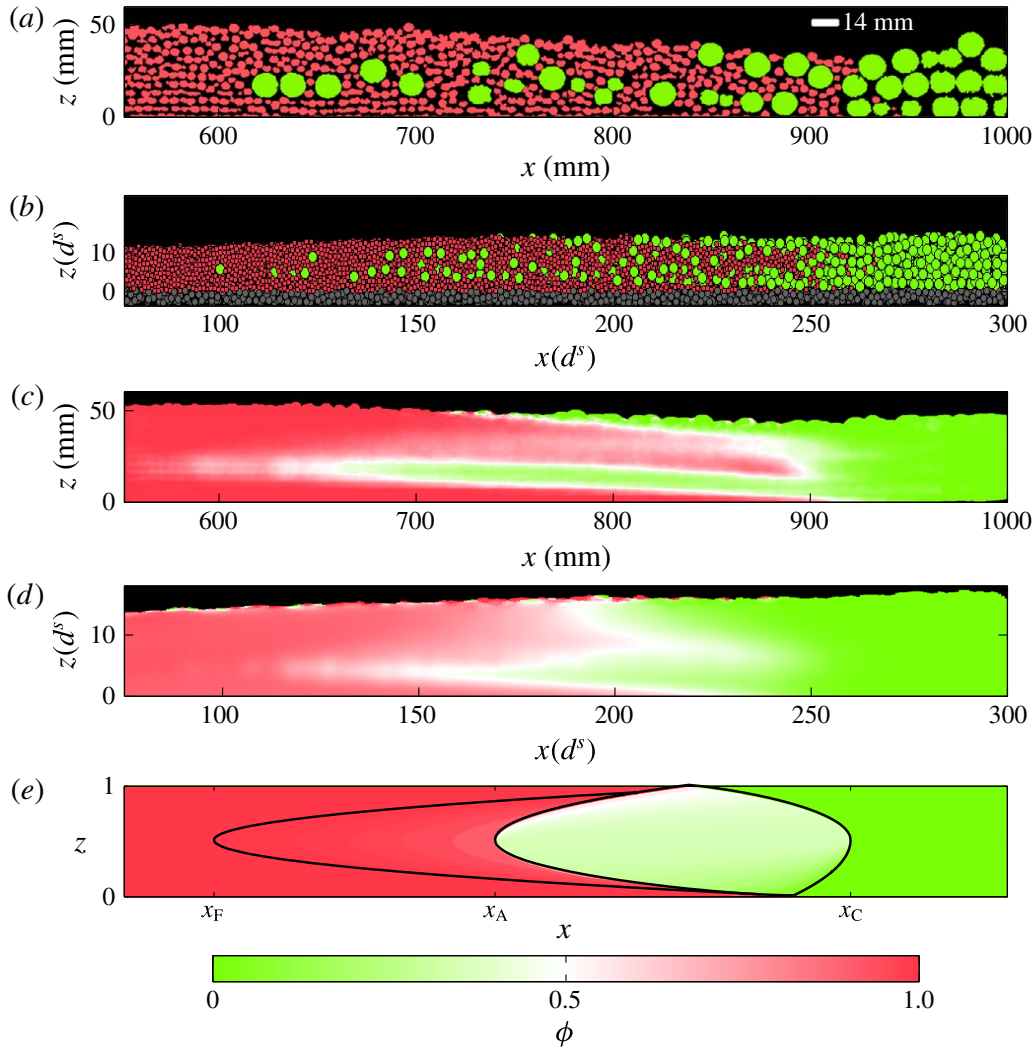

FIGURE 6. (*a*) An experimental snapshot of the recirculation zone, captured using the moving-bed flume of figure 3 with refractive index matched scanning. The white label indicates the length scale of 14 mm. (*b*) Structure of the recirculation zone found using DPM simulations. The fixed base particles are shown in grey. Both the experimental and simulation results show several large particles positioned towards the rear, where they are surrounded by many small particles. These large particles are seen to move very slowly, and take a long time to recirculate. (*c*) Shows the experimental time-averaged concentration field, which was produced by averaging the individual particle positions over a 40 min period, with 1 image every 2 s. The time-averaged concentration field for the simulations was produced by coarse graining all of the particle positions from 749 subsequent time frames, and is shown in (*d*). Both of the time-averaged concentration plots indicate a 'tail' upstream, where the concentration is lower due to the slow motion of a few large grains. This is similar to asymmetric behaviour observed within a linear shear cell (van der Vaart *et al.* 2015), and motivates a continuum breaking wave structure with an asymmetric flux function, shown in (*e*) for a cubic flux. The solid lines mark the boundaries of the recirculation zone, with two distinct 'lens' and 'tail' regions (see § 2). The downstream 'lens' region with a strong green hue is where most of the large particles recirculate, whilst the red hue of the upstream 'tail' region shows how only a few large particles recirculate through that area. The theory does not account for spatial velocity variations, diffusive remixing or differential particle friction, and finite-size effects are also significant. These may all contribute to the difference in the 'tail' structure between the theory and the experiments and simulations. Without calibrating the segregation flux for this particular flow regime, it is remarkable that the asymmetric flux produces a 'tail' region, and it is of interest to further understand the asymmetric breaking-wave structure and particle recirculation within it. In all of the above plots, the lower belt moves from right to left, with gravity acting to cause particles to flow downstream towards the right.

determining the rheological behaviour (Ancey, Coussot & Evesque 1999) even when an interstitial fluid is present. Cassar, Nicolas & Pouliquen (2005) showed that, in steady flows submerged in water, at least 75 % of the overburden pressure is borne by the contact network. They also showed that the same rheology used to describe dense steady aerial flows (GDR Midi 2004) also applies to immersed flows, with the interstitial fluid changing the time scale of the particle rearrangements. This is consistent with the experimental results of Vallance & Savage (2000) and the theory of Thornton, Gray & Hogg (2006) who both showed that the role of the interstitial fluid in flows containing different sized constituents is to modify the segregation time scales. These results would suggest that the physical phenomena observed in the experiments above, with a few large particles recirculating very slowly in regions of small particles, are indicative an underlying asymmetry in the particle motion that occurs whether the flow is dry or submerged. Further experimental work, using techniques such as X-ray tomography (e.g. McDonald, Harris & Withers 2012), is needed to compare the particle scale dynamics in dry flows with those containing an interstitial fluid.

Discrete particle method (DPM) simulations of a moving bed-flume set-up were also performed using the MercuryDPM code (`MercuryDPM.org`; Thornton *et al.* 2013*a*,*b*). A dry bidisperse mixture of spherical particles was used, with all of the particles of the same (non-dimensional) density $\rho^* = \pi/6$, but of two different (non-dimensional) diameters, $d^s = 1$ and $d^l = 2.4$, for small and large particles, respectively. All of the simulation parameters were non-dimensionalised so that $g = 1$. A frictional spring-dashpot model (Cundall & Strack 1979; Weinhart *et al.* 2012) with linear elastic and linear dissipative contributions was used for both the normal and tangential forces. The tangential force models the effects of particle surface roughness, and its spring stiffness was taken to be $2/7$ of the spring stiffness for the normal direction. The tangential force also truncates so that it is always less than $1/2$ of the normal force. The particles all had the same coefficient of restitution $r_c = 0.1538$, which was chosen to be less than typical known values for glass ($\sim$0.9) in order to model the dissipative effects of the interstitial fluid removing energy from the system. The contact time for all head on collisions was fixed at 0.0054, with the collision properties chosen to be different for small/small, small/large and large/large collisions so that both the contact time and the coefficient of restitution were the same even in the mixed case. Further details of the precise DPM implementation may be found in Thornton *et al.* (2012*b*) and Weinhart *et al.* (2012). The simulations were conducted in a box of length $300d^s$ with fixed end walls and width $8.4d^s$. The side walls were periodic in order to bring the simulations closer to the assumptions of the analytic model in figure 2(*b*), which is two-dimensional and has no side-wall effects. A small inclined wall was placed between the base and the vertical upstream wall in order to prevent small particles being crushed by the wall or shooting away from it. This was seen to only affect the dynamics very close to the wall, and did not affect the recirculation zone. A rough moving base was created in several steps. Firstly, particles of diameter $d^b = 1.7$ were stuck randomly to a horizontal plate. Particles of diameter d^b were slowly dropped onto this plate and allowed to settle. Once a thick layer of height $12d^b$ was produced, a slice of particles was taken whose centres lay between $9.3d^b$ and $11d^b$. These particles were endowed with infinite mass and inclined at an angle of 23° to form the base for the moving-bed flume simulations. The layer is thick enough to ensure that no flowing particles can fall through the rough base during the simulations. More details of this base creation process can be found in Weinhart *et al.* (2012) whereas a detailed description of different bed creation methods and their effect on the

macroscopic friction experienced by the flow can be found in Thornton *et al.* (2012*a*). Before each time step $\Delta t = 10^{-4}\sqrt{d^s/g}$, the base was moved upstream by a distance $u_{belt}\Delta t = 1.5 \times 10^{-4} d^s$. The system was allowed to evolve until a steady recirculation zone was formed.

Figure 6(*b*) shows a snapshot from the simulations, which have a very similar structure to the experimental results: most large particles recirculate quickly at the front but a few large particles recirculate slowly at the rear. This behaviour is also evident in the time- and width-averaged concentration plot shown in figure 6(*d*), which was produced by employing the micro–macro coarse-graining technique (Goldhirsch 2010; Weinhart *et al.* 2013) on the individual particle positions from 749 subsequent time steps. The new extension by Tunuguntla, Thornton & Weinhart (2015), based on a mixture theory formulation (Morland 1992), allowed the (partial) densities for the bulk (ρ), small (ρ^s) and large particles (ρ^l) to be separately extracted, with the small particle concentration defined as ρ^s/ρ, i.e. the local small particle material density over the local granular material density. The coarse-graining method used two-dimensional Gaussian functions at each of the particle positions and generated the continuum field at every point in space; however, for ease of computing, the data is shown on a 250×250 grid. As was seen in the experimental concentration field in figure 6(*c*), the slow moving large particles have lowered the upstream concentration and produced a white 'tail' protruding backwards from the main region of recirculation. This qualitative similarity between the concentration field of the simulations that were laterally periodic (figure 6*d*) and the concentration field of the experiments (figure 6*c*) indicates that there are only minimal effects arising from the side walls and justifies the two-dimensional approximation of the analytic solution. Dry simulations, using a much higher restitution coefficient, also gave a similar concentration field, indicating that the behaviour is not an artefact of the presence of the fluid nor the exact particle properties. Despite the fact that no attempt was made to calibrate the simulations and experiments, both show very similar behaviour using different sized particles in different sized flumes. The presence of the 'tail', in which large particles recirculate very slowly through regions of many small particles, points towards a fundamental asymmetry in the interactions between the large and small particles. Recently, van der Vaart *et al.* (2015) uncovered a similar asymmetry in a linear shear cell, and showed how the asymmetry could be modelled using a continuum approach.

1.2. *Continuum segregation equation for bidisperse mixtures*

Non-dimensional continuum models for segregation in bidisperse mixtures (e.g. Bridgwater, Foo & Stephens 1985; Savage & Lun 1988; Bridgwater 1994; Dolgunin & Ukolov 1995; Gray & Thornton 2005; Gray & Chugunov 2006; Thornton *et al.* 2006; May, Shearer & Daniels 2010) all share a similar advection–diffusion structure

$$\frac{\partial \phi}{\partial t} + \nabla \cdot (\phi \boldsymbol{u}) - \frac{\partial}{\partial z}(S_r F(\phi)) = \frac{\partial}{\partial z}\left(D_r \frac{\partial \phi}{\partial z}\right), \tag{1.1}$$

where the z coordinate is the upward pointing normal to the flume bed, the x coordinate points down the flume and the y coordinate points horizontally across the flume bed. The bulk velocity field $\boldsymbol{u} = (u, v, w)$ has components in the above directions, the small particle concentration is ϕ, and S_r and D_r are the non-dimensional segregation and diffusive-remixing coefficients, respectively. As the typical length

and height of the avalanche are L and H, and magnitudes of the downstream and segregation velocities are U and Q, the non-dimensional segregation coefficient $S_r = QL/(HU)$ represents the ratio of the typical segregation time scale Q/H to the typical downstream transport time scale U/L. Similarly, the non-dimensional diffusion coefficient $D_r = DL/(H^2U)$ represents the ratio of the typical diffusion time scale D/H^2 to the typical downstream transport time scale U/L, with D being the diffusivity between the two particle species. The large particle concentration is $1-\phi$ since the solids volume fraction is assumed to be uniform and constant throughout the flowing layer (Rognon *et al.* 2007). The first term on the left-hand side in (1.1) describes the temporal evolution, whilst the second term describes the advection with the bulk flow. The segregation is captured by the third term, with $F(\phi)$ the segregation flux and the negative sign indicating that there is a net motion of small particles downwards. The segregation flux is often assumed to be the product of the small and large particle concentrations,

$$F(\phi) = \phi(1-\phi), \tag{1.2}$$

and has the property that segregation ceases when the concentration reaches zero (pure large phase) or unity (pure small phase). The right-hand side of equation (1.1) reduces the sharp concentration shocks that develop between the two species, and models the diffusion of one species into the other that results from the random-walk-like behaviour of the grains. In many flows, this is small compared to the segregation (Gray & Hutter 1997; Dasgupta & Manna 2011; Wiederseiner *et al.* 2011*b*; Thornton *et al.* 2012*b*) and so the non-diffuse solution in which $D_r = 0$ is a useful approximation, with (1.1) reducing to a scalar hyperbolic equation. A full review of the derivation, history and applications of (1.1) can be found in Gray, Gajjar & Kokelaar (2015).

1.3. *Asymmetry between large and small particle motion*

Recent experiments by Golick & Daniels (2009) and van der Vaart *et al.* (2015) have uncovered an underlying asymmetry in the behaviour of large and small grains during segregation, with a characteristic dependence on the local relative volume fraction of small particles. Within their annular ring shear experiments, Golick & Daniels (2009) inferred that large particles were segregating very slowly in regions of many small particles, but were not able to further explain this observation. Using a classical linear shear cell (Bridgwater 1976) and the 'refractive index matched scanning technique' (Wiederseiner *et al.* 2011*a*; Dijksman *et al.* 2012), experiments by van der Vaart *et al.* quantified on both bulk and particle scales how large particles rise slower in regions of many small particles compared to small particles percolating down through a region of many large particles. They also showed that the large particle velocity displayed a peak at approximately $\phi = 0.55$, proving that the coarse grains rise quickest as a group. Gajjar & Gray (2014) showed that the normal constituent velocities associated with the segregation equation (1.1) are

$$w^l(\phi) = w + S_r\frac{F(\phi)}{1-\phi}, \qquad w^s(\phi) = w - S_r\frac{F(\phi)}{\phi}, \tag{1.3a,b}$$

with both velocities uniquely determined by the geometry of the flux function $F(\phi)$ at every concentration ϕ. The velocity of the large particles $w^l(\phi)$ (1.3*a*) is directly proportional to the gradient of the chord, namely the gradient of the straight line segment (Clapham & Nicholson 2009), joining (1, 0) with $(\phi, F(\phi))$. Similarly, the

velocity of the small particles $w^s(\phi)$ is directly proportional to the gradient of the chord joining $(0, 0)$ with $(\phi, F(\phi))$. A pair of these two chords for $\phi = \phi_{max}$ are shown in figure 7(*b*). Since the quadratic segregation flux (1.2) utilised by many segregation models is symmetric about $\phi = 0.5$ (figure 7*a*), it gives linear segregation velocities for the large and small grains

$$w^l(\phi) = w + S_r\phi, \quad w^s(\phi) = w - S_r(1-\phi). \tag{1.4a,b}$$

The maxima of these velocities are equal in magnitude (figure 7*c*), and so (1.2) is unable to capture the asymmetry measured by van der Vaart *et al.* (2015). In order to model the asymmetric behaviour between large and small grains, Gajjar & Gray (2014) introduced a new class of flux functions with the following properties: (i) $F(\phi)$ is skewed towards $\phi = 0$, with a maximum occurring at $0 < \phi_{max} < 1/2$; (ii) $F(\phi)$ is normalised to have the same amplitude as the quadratic flux (1.2); and (iii) $F(\phi)$ has at most one inflexion point ϕ_{inf} in the interval $(\phi_{max}, 1)$. Although there are other ways of normalising the class of flux functions, e.g. by the area, there were no qualitative differences between the different methods. The simplest flux function fitting all of the above requirements is the cubic form

$$F(\phi) = A_\gamma\phi(1-\phi)(1-\gamma\phi), \tag{1.5}$$

where γ is the asymmetry parameter and A_γ is a normalisation constant. Note that the limit $\gamma \to 0$ of (1.5) recovers the symmetric quadratic flux (1.2). For small amounts of asymmetry, $0 \leqslant \gamma \leqslant 0.5$, $F(\phi)$ is convex up (Clapham & Nicholson 2009), whilst for greater amounts of asymmetry $0.5 < \gamma \leqslant 1$, $F(\phi)$ is non-convex with a single inflexion point

$$\phi_{inf} = \frac{1+\gamma}{3\gamma}. \tag{1.6}$$

As shown in figure 7(*c*), the cubic functions (1.5) are able to reproduce the asymmetric behaviour that a small particle will percolate down more quickly at low ϕ (figure 7*e*) than a large particle rises upwards at high ϕ (figure 7*g*). In addition, figure 7(*b*) shows how the presence of an inflexion point (1.6) means that the chord joining $(\phi, F(\phi))$ with $(1, 0)$ initially has an increasing gradient as ϕ increases from 0 to ϕ_{M}, and a decreasing gradient thereafter. Thus, the non-convex flux functions display a maximum in the large particle velocity at an intermediate concentration ϕ_{M} (figure 7*f*). This behaviour will be known as the *collective motion* of the large particles.

Gajjar & Gray (2014) were able to examine the influence of asymmetry on the segregation process by constructing exact solutions to the non-diffuse ($D_r = 0$) hyperbolic segregation equation (1.1) using the method of characteristics (e.g. Whitham 1974; Billingham & King 2001). Concentration ϕ is constant along characteristic curves, which are also simply known as characteristics. The characteristics combine to form distinct features in the solution, such as rarefaction fans, shocks, semi-shocks and compressions, with physical definitions of these features provided in appendix A. Characteristics may diverge and form an expansion fan, with a smoothly varying concentration field, or converge and form a shock with a sharp jump in concentration from the rearward ($-$) side to the forward ($+$) side. The propagation of the shock surface $z_s(t, x, y)$ is governed by

$$\frac{\partial z_s}{\partial t} + u\frac{\partial z_s}{\partial x} + v\frac{\partial z_s}{\partial y} - w = -S_r\frac{[\![F(\phi)]\!]}{[\![\phi]\!]}, \tag{1.7}$$

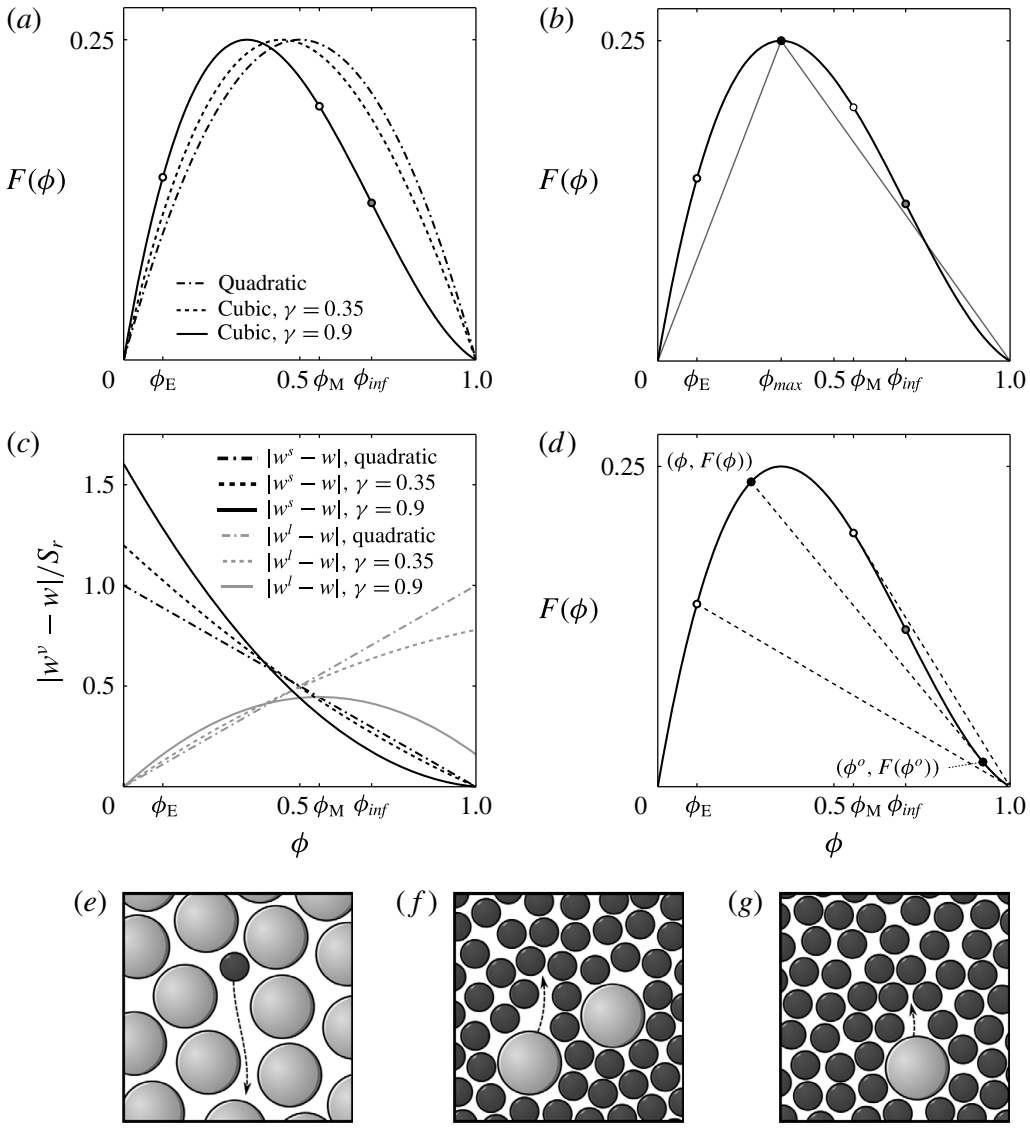

FIGURE 7. There is an intrinsic geometric relationship between the segregation flux $F(\phi)$ shown in (a), and its segregation velocities w^{ν} (1.3) shown in (c). At any concentration ϕ, the gradient of the chords (straight line segment) joining $(\phi, F(\phi))$ with $(1, 0)$ and $(0, 0)$ are proportional to the velocities (1.3) of the large and small particles, respectively. These chords are illustrated in (b) for $\phi = \phi_{max} = \phi_{\mathrm{R}}$. The quadratic flux (1.2) is symmetric about $\phi = 0.5$, and thus gives linear segregation velocities (1.4) that have the same magnitude. The cubic flux is skewed towards $\phi = 0$ with a maximum occurring at $0 < \phi_{max} = \phi_{\mathrm{R}} < 1/2$, and is normalised by (2.8) to have the same amplitude as the quadratic flux. This gives asymmetric segregation velocities, with a single small particle (e) having a greater velocity that a single large particle (g). For higher amounts of asymmetry, measured by the asymmetry parameter γ, the cubic flux has an inflexion point at $\phi_{inf} = (1 + \gamma)/3\gamma$. It is this inflexion point which causes the large particle velocity to have a peak at an intermediate concentration ϕ_{M}, with large particles moving quickest when in close proximity to other large particles (f). (d) The image point ϕ^o (1.8) of concentration ϕ is defined as the point at which the gradient of the tangent to the flux function $F'(\phi^o)$ is equal to the gradient of the chord joining ϕ to ϕ^o on F. These pairs of concentrations $\{\phi, \phi^o\}$ (filled black circles) cause the formation of semi-shocks, where only the characteristics of concentration ϕ collide with shock on one side, whilst the characteristics of concentration ϕ^o lie tangential to the shock on the other side. Two pairs of concentrations $\{1, 1^o = \phi_{\mathrm{M}}\}$, and $\{\phi_{\mathrm{E}}, \phi_{\mathrm{E}}^o = 1\}$ (open circles) are particularly important in the solutions, with the chords tangential at $\phi = \phi_{\mathrm{M}}$ and $\phi = 1$ respectively. Note that the segregation flux in (b) and (d) is the cubic flux (1.5) with $\gamma = 0.9$.

with 'jump' brackets $[\![f]\!] = f^+ - f^-$ denoting the discontinuity in f across the shock (Gray, Shearer & Thornton 2006). Note that the right-hand side of (1.7) is proportional to the gradient of the chord on flux $F(\phi)$ between $\phi = \phi^-$ and $\phi = \phi^+$ (Gajjar & Gray 2014). The characteristics usually collide with both sides of a shock, but the non-convex cubic flux functions give rise to a special type of shock, known as a semi-shock (Rhee, Aris & Amundson 1986), where characteristics only collide with one side of the shock and are tangential to it on the other. The image point ϕ^o of concentration ϕ is defined as the point at which the gradient of the tangent to the flux function $F'(\phi^o)$ is equal to the gradient of the chord joining ϕ to ϕ^o on F, with the shock condition (1.7) giving the relation

$$F'(\phi^o) = \frac{F(\phi) - F(\phi^o)}{\phi - \phi^o}. \tag{1.8}$$

By this definition, the characteristics of concentration ϕ^o lie tangential to the shock, whilst the characteristics of concentration ϕ collide with the other side. For the cubic flux function (1.5), the relationship (1.8) between concentrations ϕ and ϕ^o simplifies to

$$\phi^o = \frac{1}{2}\left(\frac{1+\gamma}{\gamma} - \phi\right). \tag{1.9}$$

An example pair of concentrations $\{\phi, \phi^o\}$ is shown with closed black circles in figure 7(*d*). It is possible that the characteristics of concentration ϕ^o may collide with another semi-shock; characteristics of concentration $(\phi^o)^o = \phi^{oo}$ would lie tangential to this semi-shock on the other side. An example of the relationship between ϕ, ϕ^o and ϕ^{oo} is illustrated in figure 8. Two pairs of concentrations $\{1, 1^o = \phi_M\}$, and $\{\phi_E, \phi_E^o = 1\}$ are of particular importance in the exact solutions, with

$$1^o = \phi_M = \frac{1}{2\gamma} \quad \text{and} \quad \phi_E = \frac{1-\gamma}{\gamma}, \tag{1.10a,b}$$

using the short hand notation $1^o = \phi^o|_{\phi=1}$. As shown by the open circles in figure 7(*d*), the chord between $(\phi_M, F(\phi_M))$ and $(1, 0)$ is tangential to the segregation flux F at $\phi = \phi_M$, whilst the chord between $(\phi_E, F(\phi_E))$ and $(1, 0)$ is tangential to F at $\phi = 1$. Concentration ϕ_M has the physical significance that it is the concentration at which the large particles reach their maximum velocity and is important in the solution structure described in § 2.2, whilst concentration ϕ_E is important in the structure described in § 2.3, and determines which of the two non-convex solutions is formed.

Tunuguntla, Bokhove & Thornton (2014) showed that asymmetry causes the distance for complete segregation of an initially homogeneous mixture to become dependent on the initial conditions, and Gajjar & Gray (2014) specifically found the distance to be dependent on the inflow concentration, with a higher proportion of fines increasing the final segregation distance. In addition, the decreasing large particle velocity at higher concentrations causes semi-shocks to form, where large particles take longer to rise to the upper layer. This creates a stronger dependence of the final segregation distance on the inflow concentration for both homogeneous and normally graded inflow profiles, similar to the linear relationship reported by both Staron & Phillips (2014) and van der Vaart *et al.* (2015). In particular, van der Vaart *et al.* (2015) were able to fit their data to a non-convex cubic flux with $\gamma = 0.89$, which also matched their experimental observation of a peak in the large particle velocity around $\phi = 0.55$. It is also interesting that asymmetric segregation flux functions arise naturally in the work of Gray & Ancey (2015), which extends the model of Gray & Chugunov (2006) to account for differences in both particle size and particle density.

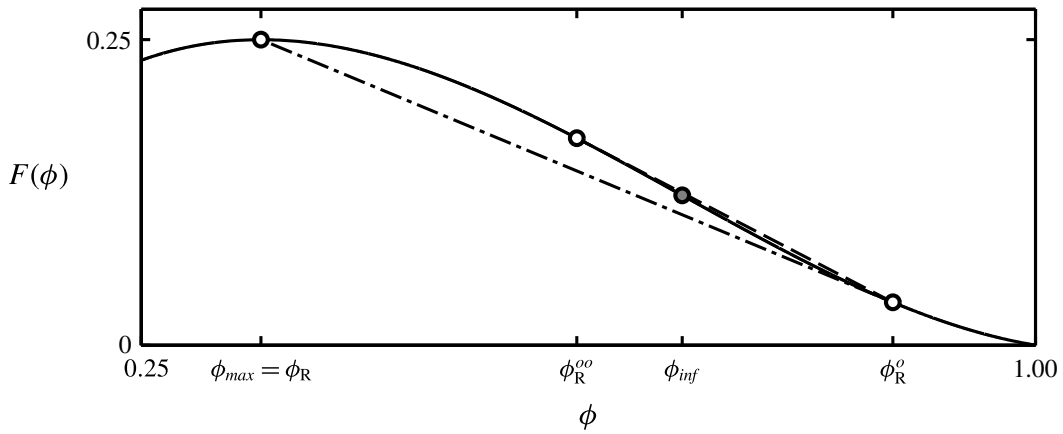

FIGURE 8. A sketch showing the relationship between ϕ_R, ϕ_R^o and $(\phi_R^o)^o = \phi_R^{oo}$ for the cubic flux with $\gamma = 0.9$ (see (1.5)). The dash-dotted line shows that the chord joining ϕ_R to ϕ_R^o is tangential to the flux function at ϕ_R^o, whilst the dashed line shows that the chord joining ϕ_R^o with ϕ_R^{oo} is tangential to the flux function at ϕ_R^{oo}. These points are important in the construction of the 'lens-tail' structure in § 2.3.

1.4. *Breaking size-segregation waves*

One of the strengths of the continuum theory is its ability to reveal the structure and development of the recirculation zone that plays a vital role in the formation of bouldery fronts (Thornton & Gray 2008; Gray & Ancey 2009; Johnson *et al.* 2012). The simplest recirculation structure arises in the case of steady uniform flow (Pouliquen 1999*b*; Rognon *et al.* 2007; Forterre & Pouliquen 2008), in which the flow thickness h is constant. The combination of the propensity of the avalanche to form an upward coarsening size distribution through particle size segregation and the shear profile

$$\boldsymbol{u} = (u(z), 0, 0), \tag{1.11}$$

means that a monotonically decreasing interface separating large particles above from small particles below (figure 9*a*) will continually steepen as fine grains are sheared over the top of coarse grains (figure 9*b*). The interface eventually breaks in finite time (figure 9*c*, Gray *et al.* 2006), forming a recirculation zone (figure 9*d*) in which the large grains lying immediately below small grains are resegregated back towards the surface, and then swept downstream by the shear velocity (Thornton & Gray 2008; Gray & Kokelaar 2010*a*,*b*). The similarity with classical breaking waves formed when an air–water interface steepens and breaks (Basco 1985; Shand 2009) led Thornton & Gray (2008) to refer to the propagating recirculation zone as a breaking size-segregation wave.

The bulk velocity field (1.11) implies that the segregation equation (1.1) reduces to

$$\frac{\partial \phi}{\partial t} + \frac{\partial}{\partial x}(\phi u(z)) - \frac{\partial}{\partial z}(S_r F(\phi)) = 0. \tag{1.12}$$

Numerical solutions to (1.12) using a simple TVD Lax–Friedrichs shock-capturing finite volume scheme (Yee 1989; Tóth & Odstrčil 1996; LeVeque 2002) show that the breaking size-segregation wave initially has a complex structure (figure 9*d*) that oscillates back and forth in time like a spinning rugby ball (Thornton & Gray 2008). Exact solutions for the structure have only been derived for the early stages of wave

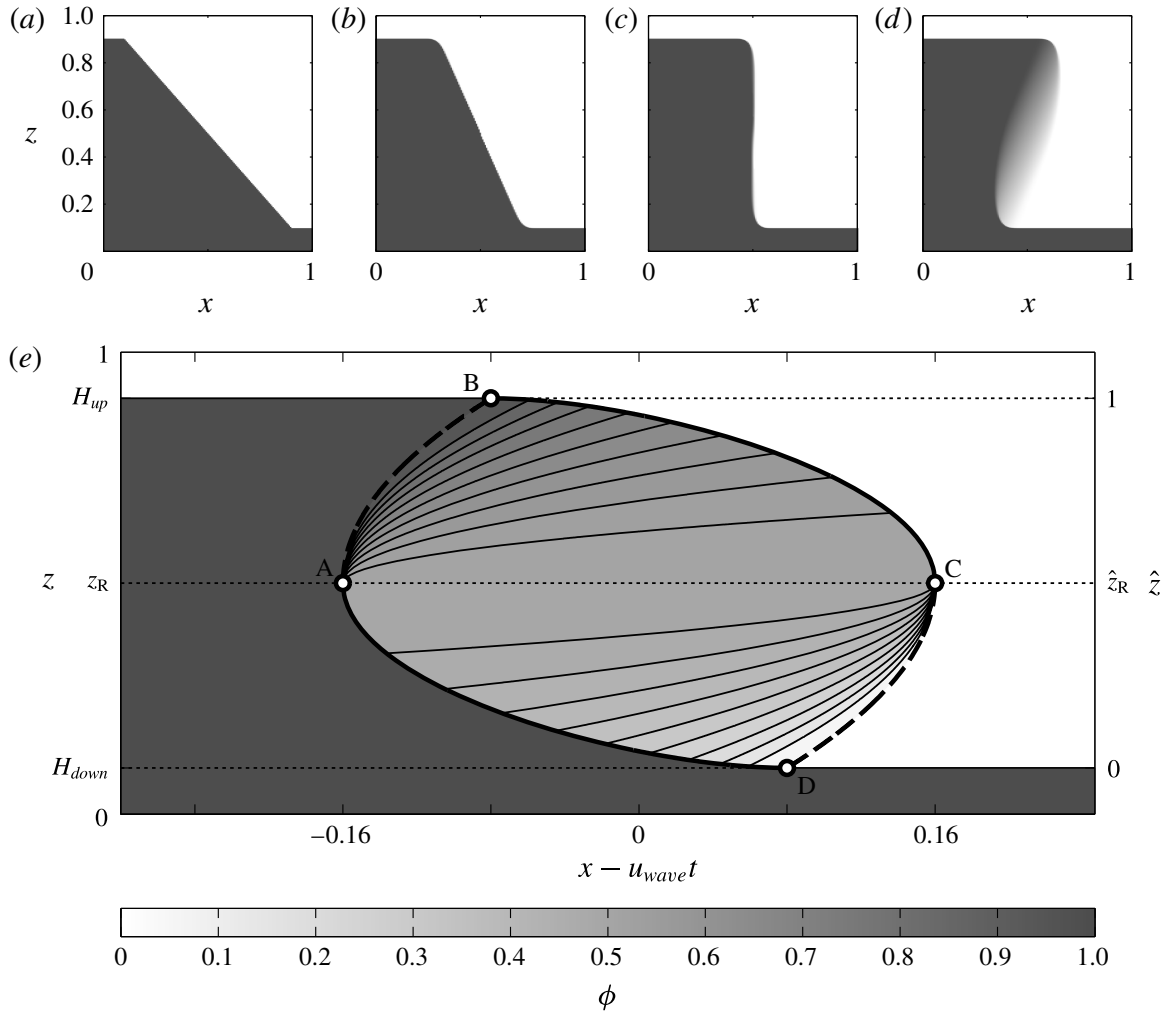

FIGURE 9. Numerical solutions of the segregation equation (1.12) in a steady uniform flow with a quadratic flux (1.2) show that a monotonically decreasing interface between large and small grains (*a*) continually steepens in time ($t = 0.0$) (*b*) as small particles are sheared over the top of large particles ($t = 0.5$). This interface breaks in finite time ($t = 1.0$) (*c*) and forms a recirculation zone ($t = 1.5$) (*d*), in which the large particles rise upwards towards the surface as they are resegregated before being sheared back towards the front. The recirculating zone has a complex 'breaking-wave' structure that oscillates in time, however the oscillations exponentially decay and the structure tends towards a steady state. (*e*) The steady breaking wave (Thornton & Gray 2008) for the quadratic flux function (1.2) exists between the vertical heights $H_{down} = 0.1$ and $H_{up} = 0.9$, and consists of two expansion fans and two concentration shocks arranged in a 'lens'-like structure. The two expansion fans are ABCA centred at point A and CDAC centred at point C, with individual characteristic curves shown with thin solid lines. The edge of the expansion fans are the $\phi = 1$ and $\phi = 0$ characteristics, which lie along AB and CD, respectively, and are shown with thick dashed lines. The two shocks are BC and DA, and are shown with thick solid lines. However, this structure is unable to replicate the slow movement of large particles upstream of the main recirculation region that was seen in figure 6.

breaking (McIntyre *et al.* 2007), however, the simulations show that oscillations are transient and exponentially decay, with the structure tending towards a steady state. Thornton & Gray (2008) generated an exact solution for the steady wave with the quadratic flux (1.2). As shown in figure 9(*e*), it consists of two expansion fans and two concentration shocks arranged in a 'lens'-like structure. In general, the breaking

wave forms between the two vertical heights $z = H_{down}$ and $z = H_{up}$, and propagates at a speed u_{wave} that is equal to the mean speed between these heights,

$$u_{wave} = \frac{1}{H_{up} - H_{down}} \int_{H_{down}}^{H_{up}} u(z)\, \mathrm{d}z. \tag{1.13}$$

Note that the recirculation zone within the moving-belt flume in § 1.1 occupies the entire height, hence $H_{down} = 0$ and $H_{up} = 1$. Since the velocity $u(z)$ is monotonically increasing, the breaking wave propagates faster than the basal velocity but slower than both the surface velocity and the front velocity u_{front} (Gray & Ancey 2009). At a height $z = z_{\mathrm{R}}$, the bulk velocity is equal to u_{wave}. Above z_{R}, $u(z) > u_{wave}$, and so material is swept towards the breaking wave from the left, whilst for $z < z_{\mathrm{R}}$, $u(z) < u_{wave}$ and so material flows towards the breaking wave from the right. The change in flow direction relative to the 'lens' at $z = z_{\mathrm{R}}$ is crucial, and thus both expansion fans are initiated at this height, centred at points A and C. The $\phi = 1$ characteristic lies between points A and B, whilst the $\phi = 0$ characteristic lies between points C and D. Two concentration shocks join point B with C and point D with A, respectively. Although the upper portion of the 'lens' ABCA contains lower concentrations than the lower portion of the 'lens' CDAC, the positions of the characteristics, expansion fans and shocks are rotationally invariant about the centre of the lens. This is a direct result of the symmetry of the quadratic flux (1.2) about $\phi = 0.5$.

Gray & Ancey (2009) derived the structure of the steady-state recirculation zone in a non-uniform depositing flow that was reconstructed from a travelling wave solution to the depth-averaged avalanche equations (Savage & Hutter 1989; Pouliquen 1999*a*,*b*; Wieland, Gray & Hutter 1999; Gray, Tai & Noelle 2003). They found that the breaking wave also consisted of two expansion fans and two shocks arranged in a 'lens', but surrounding a central 'eye' of constant concentration. The wave is located at a unique position behind the flow front and determines the concentration deposited within the basal layer. The model was able to qualitatively describe the features of their experimental two-dimensional depositing flow constrained by lateral side walls, namely the coarse-grained flow front, the rapidly moving large particles on the surface and the static layer of coarse grains at the base sandwiching an intermediate layer of fine grains. The experiments, were, however, too grainy to resolve the finer structure of the breaking wave.

In the absence of the two-dimensional side-wall restrictions, Johnson *et al.* (2012) numerically solved for the structure of the recirculation zone on the centreline of a three-dimensional front, which has a more elaborate 'breaking-wave structure'. Numerical solutions suggest that both the characteristic curves and the particle paths continually spiral inwards, because of the sidewards advection of mass into the lateral levees. The exact analytic structure of the three-dimensional recirculation zone is still proving illusive.

Figure 6(*e*) shows a breaking-wave structure using the simple asymmetric cubic model (1.5) from § 1.3. As with the structure of the symmetric flux in figure 9, the asymmetric wave also has a 'lens'-like structure towards the downstream end. The asymmetry also causes a new upstream 'tail' to be produced, through which a few large particles recirculate slowly. Although this behaviour is very similar to the individual particle motion observed in experiments and simulations in § 1.1, the shape and structure of the 'tail' region are qualitatively different. There are a number of other factors present within the moving-bed flume set-up used in both the experiments

and simulations that are unaccounted for by the simple theory. Streamwise spatial variations in the velocity field, diffusive remixing and the differential friction of the two particles on the moving base may all have an influence on the 'tail' shape. The size of the system and finite-size effects may also contribute to the discrepancy in the 'tail' structure. Further experimental work and extensive simulations are currently being conducted in order to understand more about the slow particle movement through the 'tail'. Nevertheless, without any knowledge of the exact shape of the segregation flux function in this environment (Gajjar & Gray 2014), the fact that a simple asymmetric cubic flux produces a 'tail' means that it is of interest to understand the derivation and particle paths. This paper examines the effect of an asymmetric segregation flux function (Gajjar & Gray 2014; van der Vaart *et al.* 2015) on both the structure of a two-dimensional breaking size-segregation wave, and the particle recirculation within it.

2. Steady-state structure of the travelling breaking wave

The simplest steady-state breaking wave occurs under steady uniform flow (§ 1.4), and exists between the vertical heights $z = H_{down}$ and $z = H_{up}$. The wave propagates forwards with velocity u_{wave}, and it is convenient to transfer to a (Lagrangian) reference frame translating with the recirculation zone by employing the change of variables

$$\hat{t} = \frac{S_r}{H_{up} - H_{down}}\, t, \quad \hat{x} = \frac{S_r}{H_{up} - H_{down}}(x - u_{wave}\, t), \quad \hat{z} = \frac{z - H_{down}}{H_{up} - H_{down}}. \quad (2.1a\text{–}c)$$

At steady state, the wave is stationary in this frame. The wave has also conveniently been stretched to lie between $\hat{z} = 0$ and $\hat{z} = 1$, whilst the S_r parameter dependence has been removed. The segregation equation (1.12) becomes a simple quasi-linear equation

$$\hat{u}\frac{\partial \phi}{\partial \hat{x}} - \frac{\partial}{\partial \hat{z}} F(\phi) = 0, \quad (2.2)$$

where the relative velocity $\hat{u} = u - u_{wave}$. Equations (1.11) and (2.1) also simplify the shock condition (1.7) to give

$$\hat{u}\frac{\partial \hat{z}_s}{\partial \hat{x}} = -\frac{[\![F(\phi)]\!]}{[\![\phi]\!]}. \quad (2.3)$$

Equation (2.2) may be solved using the method of characteristics (e.g. Whitham 1974). The analysis is simplified by mapping to velocity-integrated coordinates (ξ, ψ)

$$\xi = \hat{x}, \quad \psi(\hat{z}) = \int_0^{\hat{z}} \hat{u}(\hat{z}')\, \mathrm{d}\hat{z}'. \quad (2.4a,b)$$

Under this transformation, (2.2) becomes

$$\frac{\partial \phi}{\partial \xi} - \frac{\partial}{\partial \psi} F(\phi) = 0, \quad (2.5)$$

with the concentration ϕ taking the constant value ϕ_λ on straight line characteristics of gradient

$$\frac{\partial \psi}{\partial \xi} = -F'(\phi_\lambda) = -A_\gamma\left(3\gamma\phi_\lambda^2 - 2(1+\gamma)\phi_\lambda + 1\right). \quad (2.6)$$

The shock condition (2.3) also reduces to

$$\frac{\mathrm{d}\psi}{\mathrm{d}\xi} = -\frac{[\![F(\phi)]\!]}{[\![\phi]\!]}. \tag{2.7}$$

Transformation (2.4) splits the domain into two sections, which are separated by the no-mean-flow line $\hat{z} = \hat{z}_{\mathrm{R}}$. In the lower domain, ψ decreases from $\psi = 0$ at $z = 0$ to $\psi = \psi_{\mathrm{R}} < 0$ at $\hat{z} = \hat{z}_{\mathrm{R}}$, with both the bulk flow and time-like direction to the left, whilst in the upper domain ψ increases from $\psi = \psi_{\mathrm{R}}$ at $\hat{z} = \hat{z}_{\mathrm{R}}$ to $\psi = 0$ at $\hat{z} = 1$, with the bulk flow and time-like direction to the right. The characteristics in each domain can be calculated independently, with the concentrations matched across $\hat{z} = \hat{z}_{\mathrm{R}}$.

For the cubic flux (1.5), the characteristics form three distinct breaking-wave structures for different values of asymmetry parameter γ, as shown in figure 10. A 'lens'-like structure (figure 10*a*) that is very similar to that of Thornton & Gray (2008) is formed for convex flux functions with low amounts of asymmetry ($\gamma \leqslant 0.5$). The only differences between the two structures are that the top of the convex 'lens' is shifted to the right because of large particles rising at a slower rate than the percolating fines, and that the structures are no longer rotationally invariant. The symmetric structure of Thornton & Gray (2008) is, however, recovered in the limit $\gamma \to 0$. The new 'lens' structure derivation presented here is implicit in terms of the small particle concentration ϕ, and so is valid for not only the quadratic (1.2) and cubic fluxes (1.5), but also other convex asymmetric flux functions such as those of Marks, Rognon & Einav (2012) and Tunuguntla *et al.* (2014). A second 'lens'-like structure (figure 10*b*) is formed for non-convex flux functions with low amounts of asymmetry ($0.5 < \gamma \leqslant \Gamma$ where $\Gamma = (5 + \sqrt{5})/10$). The top of the 'lens' is shifted further to the right as compared to the convex lens, and an additional semi-shock is found in the upper region. A new 'lens-tail' structure (figure 10*c*) arises for larger amounts of asymmetry ($\Gamma < \gamma \leqslant 1$). There is a large difference between the speeds of large and small particles, and additionally collective motion is observed, where large particles preferentially rise together in a group (van der Vaart *et al.* 2015). These combine to produce an additional 'tail'-like region to the left of the 'lens' where a few large particles rise very slowly and are swept a long way downstream. Each of these structures is examined in more detail below.

2.1. *Convex 'lens' structure*

First consider the 'lens' structure of the convex flux when $\gamma \leqslant 0.5$. The 'lens' is formed from two shocks BC and DA and two expansion fans ABCA and CDAC, as shown in figure 10(*a*) for $\gamma = 0.35$. The front of the breaking wave is positioned at ξ_{C}, and as $F'(\phi_{max}) = 0$, the $\phi = \phi_{max}$ characteristic is horizontal along the no-mean-flow line $\hat{z} = \hat{z}_{\mathrm{R}}$. Concentration ϕ_{max} will thus be known as ϕ_{R} throughout the remainder of this paper. Note that the definition of the asymmetric flux function in § 1.3 implies that

$$F(\phi_{\mathrm{R}}) = 1/4. \tag{2.8}$$

Within the lower domain $\hat{z} < \hat{z}_{\mathrm{R}}$, rarefaction fan CDAC is centred at point C with concentrations in the range $[0, \phi_{\mathrm{R}}]$. From (2.6), each characteristic of the rarefaction fan is given by

$$\psi = \psi_{\mathrm{R}} - F'(\phi)(\xi - \xi_{\mathrm{C}}). \tag{2.9}$$

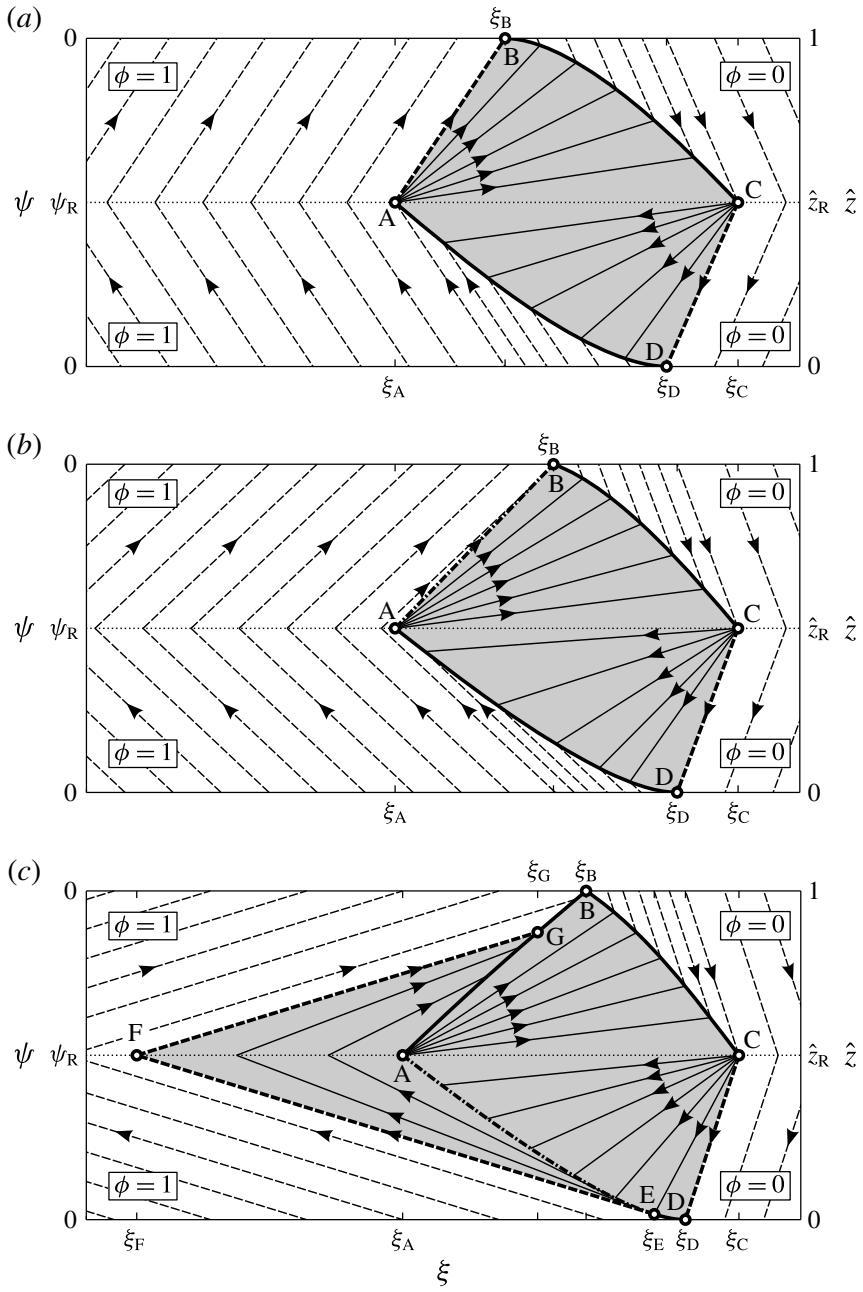

FIGURE 10. Schematic diagrams of the exact solutions to illustrate the breaking-wave structures. The characteristic curves are shown in transformed coordinates (ξ, ψ), with transformation (2.4) splitting the domain into two regions separated by the no-mean-flow line $\hat{z} = \hat{z}_R$, $\psi = \psi_R$. In the lower region ($\hat{z} < \hat{z}_R$), the bulk flow and the time-like direction are both to the left, whilst in the upper region ($\hat{z} > \hat{z}_R$), they are both to the right. Three different breaking-wave structures are formed for different values of the asymmetry parameter γ. A 'lens'-like structure is formed for both convex flux functions, $0 < \gamma \leqslant 0.5$, and non-convex flux functions with $0.5 < \gamma \leqslant \Gamma$, as shown for $\gamma = 0.35$ and $\gamma = 0.65$ in (*a*) and (*b*), respectively. The difference between the two is that the outer characteristic of the rarefaction fan AB becomes a semi-shock with non-convex flux functions in (*b*). A 'lens-tail' structure is formed for higher values of asymmetry, $\Gamma < \gamma \leqslant 1$, as shown for $\gamma = 0.9$ in (*c*). The characteristics of the pure phases of large and small particles are shown with thin dashed straight lines, whilst the characteristics within the breaking wave are shown with thin solid straight lines. Thick solid lines indicate shocks, thick dash-dot lines represent a semi-shock whilst thick dashed straight lines mark the edge of an expansion fan or compression wave. None of the above structures with $\gamma > 0$ have rotational symmetry about the centre of the lens. Contoured plots of these solutions are shown in figure 12, in physical (x, z) coordinates.

The $\phi = 0$ characteristic CD separates the breaking wave from the region of large particles downstream, and reaches the bottom of the wave at point D, where $\psi = 0$ and $\xi = \xi_{\mathrm{D}}$

$$\xi_{\mathrm{D}} = \xi_{\mathrm{C}} + \frac{\psi_{\mathrm{R}}}{F'(0)}. \tag{2.10}$$

A sharp concentration shock DA separates the breaking wave ($\phi^- = \phi$) from the upstream region of small particles ($\phi^+ = 1$), with gradient given by (2.7)

$$\frac{\mathrm{d}\psi}{\mathrm{d}\xi} = \frac{F(\phi)}{1-\phi}. \tag{2.11}$$

Following Gajjar & Gray (2014), a differential equation governing the downstream position of shock DA may be derived in terms of the small particle concentration ϕ. Using the chain rule, the shock gradient (2.11) may be written as

$$\frac{\mathrm{d}\psi}{\mathrm{d}\phi} = \frac{F(\phi)}{1-\phi}\frac{\mathrm{d}\xi}{\mathrm{d}\phi}. \tag{2.12}$$

The rarefaction characteristics (2.9) which govern the concentration on the lower side of the shock ($\phi^- = \phi$) may be differentiated with respect to ϕ to give

$$\frac{\mathrm{d}\psi}{\mathrm{d}\phi} = -F''(\phi)(\xi - \xi_{\mathrm{C}}) - F'(\phi)\frac{\mathrm{d}}{\mathrm{d}\phi}(\xi - \xi_{\mathrm{C}}). \tag{2.13}$$

Equating (2.12) and (2.13) yields an ordinary differential equation (ODE) for the shock path DA, which may be written as

$$\frac{\mathrm{d}}{\mathrm{d}\phi}\left[\big(F(\phi) + (1-\phi)F'(\phi)\big)\,(\xi - \xi_{\mathrm{C}})\right] = 0. \tag{2.14}$$

The above sequence of steps to combine (2.9) and (2.11) into (2.14) is important and will be used throughout this paper to derive equations for shocks and particle paths. Shock DA starts from point D where $\phi = 0$, and so (2.14) can be integrated to give the implicit position of the shock as

$$\xi = \xi_{\mathrm{C}} + \frac{\psi_{\mathrm{R}}}{F(\phi) + (1-\phi)F'(\phi)}, \tag{2.15}$$

where the concentration $\phi \in [0, \phi_{\mathrm{R}}]$ in the rarefaction fan is used to parametrise the shock path, and the height $\psi = \psi(\phi, \xi)$ is given by (2.9). When $\phi = \phi_{\mathrm{R}}$, shock DA meets the no-mean-velocity line $\hat{z} = \hat{z}_{\mathrm{R}}$ at point A, where $\psi = \psi_{\mathrm{R}}$ and $\xi = \xi_{\mathrm{A}}$

$$\xi_{\mathrm{A}} = \xi_{\mathrm{C}} + \frac{\psi_{\mathrm{R}}}{F(\phi_{\mathrm{R}})}. \tag{2.16}$$

There is also a rarefaction fan ABCA centred at point A in the upper domain ($\hat{z} > \hat{z}_{\mathrm{R}}$), with characteristics

$$\psi = \psi_{\mathrm{R}} - F'(\phi)(\xi - \xi_{\mathrm{A}}), \tag{2.17}$$

for $\phi \in [\phi_R, 1]$. The $\phi = 1$ characteristic AB separates the left-hand edge of the breaking wave from the small particle region upstream and reaches the top at point B, where $\psi = 0$ and

$$\xi = \xi_B = \xi_A + \frac{\psi_R}{F'(1)}. \tag{2.18}$$

Shock BC exists between points B and C, and separates the rarefaction fan characteristics within the breaking wave ($\phi^- = \phi$) from the pure large particle phase downstream ($\phi^+ = 0$). Combining (2.7) and (2.17) in the same manner as (2.9) and (2.11) above yields the governing differential equation for the streamwise shock position

$$\frac{\mathrm{d}}{\mathrm{d}\phi}\Big[\big(F(\phi) - \phi F'(\phi)\big)\,(\xi - \xi_A)\Big] = 0, \tag{2.19}$$

which may be integrated with the initial condition that the shock starts from point B (where $\psi = 0$ and $\phi = 1$) to give the implicit downstream position of the shock as

$$\xi = \xi_A - \frac{\psi_R}{F(\phi) - \phi F'(\phi)}. \tag{2.20}$$

This is valid for concentrations in the range $\phi \in [\phi_R, 1]$, with the height of the shock given by (2.17). Shock BC propagates downwards until $\phi = \phi_R$, where it meets the no-mean-flow line $\hat{z} = \hat{z}_R$ at point C with downstream coordinate

$$\xi_C = \xi_A - \frac{\psi_R}{F(\phi_R)}. \tag{2.21}$$

This is consistent with (2.16), closing the structure of the breaking wave.

As the asymmetric flux functions are normalised through (2.8) so that their maximum value is the same as that of the quadratic flux, (2.16) and (2.21) imply that the 'lens' has a constant length of $-4\psi_R$, which is identical to Thornton & Gray (2008). However, the result of the asymmetry is that both points B and D are shifted to the right as compared to the quadratic flux. This means that the characteristics in the upper and lower portions of the 'lens' are no longer rotationally invariant about the centre of the lens.

2.2. *Non-convex 'lens' structure*

The 'lens' structure for asymmetric flux functions with small amounts of non-convexity, $0.5 < \gamma \leqslant \Gamma$, is similar to the convex 'lens' structure of § 2.1. However, as explained in § 1.3, the non-convexity causes the large particles to display collective motion, with the maximum large particle velocity occurring at concentration ϕ_M. This causes a slight difference in the upper domain, and an example of the structure is shown in figure 10(*b*) for $\gamma = 0.65$. The characteristics of the rarefaction fan ABCA still satisfy (2.17), but for $\phi \in [\phi_R, \phi_M]$. A semi-shock AB now separates the rarefaction fan from the small particle region upstream, and is equivalent to the $\phi = \phi_M$ characteristic. Point B thus has downstream position

$$\xi_B = \xi_A + \frac{\psi_R}{F'(\phi_M)}, \tag{2.22}$$

which is shifted even further to the right. Shock BC still satisfies (2.20), but with concentrations in the range $\phi \in [\phi_R, \phi_M]$. The remainder of the structure is the same as § 2.1 and the length of the 'lens' remains unaffected.

2.3. *'Lens-tail' structure*

For larger amounts of asymmetry, $\Gamma < \gamma \leqslant 1$, the greater difference between the maximum speeds of large and small particles and the collective motion of coarse grains combine to produce a new 'lens-tail' structure, shown in figure 10(*c*) for $\gamma = 0.9$. The structure shares some similarities with the structure for normally graded inflow with an asymmetric flux derived by Gajjar & Gray (2014). A rarefaction fan CDEAC occurs in the lower domain, with characteristics given by (2.9) for $\phi \in [0, \phi_R]$. However, the upstream region of small particles ($\phi^+ = 1$) is separated from the rarefaction fan ($\phi^- = \phi$) by a shock DE, together with a semi-shock EA that lies adjacent to a non-centred expansion fan EFAE. This non-centred expansion fan forms the lower portion of the 'tail'. Shock DE satisfies (2.15), but with $\phi \in [0, \phi_E]$ where ϕ_E is defined in (1.10*b*). Point E has coordinates (ξ_E, ψ_E) given by (2.15) with $\phi = \phi_E$

$$\xi_E = \xi_C + \frac{\psi_R}{F(\phi_E) + (1-\phi_E)F'(\phi_E)} = \xi_C + \frac{\psi_R \gamma^2}{A_\gamma (2\gamma - 1)^3}, \tag{2.23a}$$

$$\psi_E = \psi_R - F'(\phi_E)(\xi_E - \xi_C) = \psi_R \frac{(1-\gamma)^2(3\gamma - 1)}{(2\gamma - 1)^3}. \tag{2.23b}$$

Semi-shock EA separates each rarefaction characteristic $\phi^- = \phi$ in CDEFC from its image point concentration characteristic $\phi^+ = \phi^o$ in EAFE. Using the definition of the image point concentration ϕ^o (1.9), the shock gradient (2.7) and the equation of the rarefaction characteristics (2.9) can be manipulated in a similar manner to (2.9) and (2.11) to give a first-order differential equation for the semi-shock path

$$\frac{1}{\xi - \xi_C}\frac{\mathrm{d}\xi}{\mathrm{d}\phi} = \frac{F''(\phi)}{F'(\phi^o) - F'(\phi)} = -\frac{8\gamma}{3\gamma\phi - (1+\gamma)}. \tag{2.24}$$

For the cubic flux, this equation is separable and can be integrated exactly given that the semi-shock starts from point E

$$\xi_{EA} = \xi_C + \frac{\psi_R \gamma^2}{A_\gamma}\left(\frac{256}{(2\gamma-1)\big(3\gamma\phi - (1+\gamma)\big)^8}\right)^{1/3}, \tag{2.25a}$$

$$\psi_{EA} = \psi_R - F'(\phi)(\xi_{EA}(\phi) - \xi_C), \tag{2.25b}$$

with concentration $\phi \in [\phi_E, \phi_R]$. Point A lies at the end of the semi-shock (2.25) on the no-mean-flow line $\hat{z} = \hat{z}_R$ with $\phi = \phi_R$, and thus has downstream coordinate

$$\xi_A = \xi_C + \frac{\psi_R \gamma^2}{A_\gamma}\left(\frac{256}{(2\gamma-1)(\gamma^2 - \gamma + 1)^4}\right)^{1/3}. \tag{2.26}$$

Each of the image point concentration ϕ^o characteristics on the forward side (upstream side as the time-like direction is to the left) of the semi-shock EA lies locally tangential and forms a non-centred expansion fan in EAFE. Each characteristic has equation

$$\psi - \psi_{EA}(\phi) = -F'(\phi^o)\big(\xi - \xi_{EA}(\phi)\big), \tag{2.27}$$

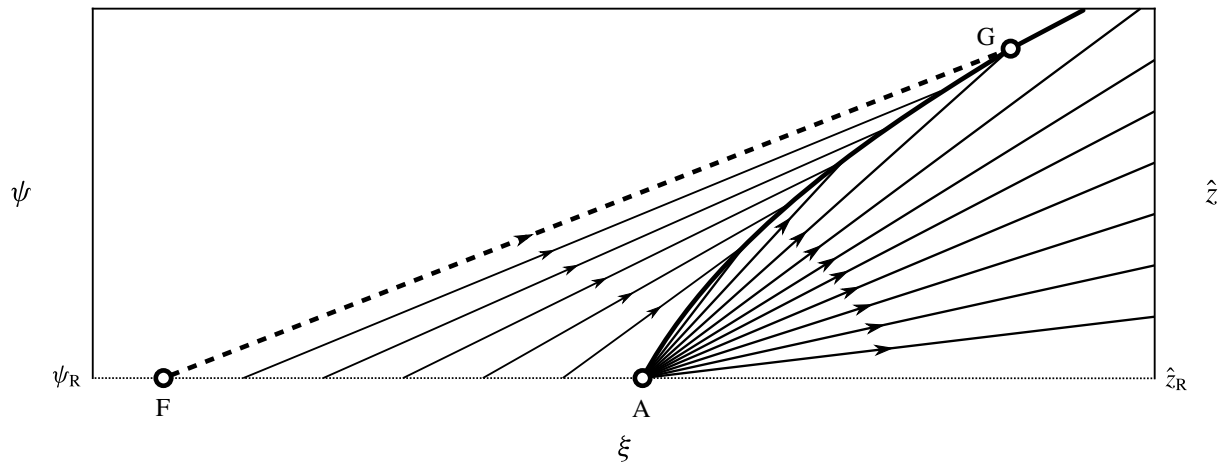

FIGURE 11. A sketch of the upper part of the 'lens-tail' structure, where compression wave FAGF interacts with the rarefaction fan centred at A to form shock AG. The concentration change along either side of the shock is governed by (2.32), whilst the shock position is given by (2.31). Note that the diagram is not to scale and that FG is not tangential at G.

upon which the concentration has a constant value of ϕ^o with $\phi \in [\phi_E, \phi_R]$. The characteristics each meet the no-mean-flow line at $\xi_{FA}(\phi)$, which is given by equating (2.25) and (2.27) with $\psi = \psi_R$

$$\xi_{FA} = \xi_C - \frac{\psi_R \gamma}{F'(\phi^o)} \left(\frac{4}{(2\gamma - 1)(3\gamma\phi - (1+\gamma))^2} \right)^{1/3}, \quad \phi \in [\phi_E, \phi_R]. \tag{2.28}$$

Point F is the furthest upstream part of the breaking wave and is given by the ϕ_E^o characteristic that is tangential at point E,

$$\xi_F = \xi_C + \frac{\psi_R \gamma}{A_\gamma (2\gamma - 1)(1 - \gamma)}. \tag{2.29}$$

The solution in the upper domain ($\hat{z} > \hat{z}_R$) matches the lower domain ($\hat{z} < \hat{z}_R$) along the no-mean-flow line $\psi = \psi_R$. As $F'(\phi_R) = 0$, the ϕ_R characteristic lies horizontally between points C and A and gives concentration $\phi = \phi_R$, whilst (2.28) governs the concentration between A and F. A characteristic of concentration ϕ^o emanates into the upper region from each point between F and A

$$\psi = \psi_R - F'(\phi^o)\left(\xi - \xi_{FA}(\phi)\right), \tag{2.30}$$

with $\phi \in [\phi_E, \phi_R]$ implying that $\phi_R^o \leqslant \phi^o \leqslant 1$. The ϕ_R^o characteristic originates from A, whilst the $\phi = 1$ characteristic originates from F. All the characteristics form a compression wave FGAF (Whitham 1974; Rhee *et al.* 1986); each characteristic has a steeper gradient than the characteristic immediately to its left, as shown in figure 11. This is the upper portion of the 'tail' region. The 'lens' region is formed from an expansion fan AGBCA centred at A whose characteristics are given by (2.17) with $\phi_R \leqslant \phi \leqslant \phi_R^{oo}$. These rarefaction characteristics collide with the compression wave characteristics (2.30) to form a shock AG. A full derivation of the governing equations

for the shock is provided in appendix B. The shock coordinates are given implicitly given by

$$\xi_{\mathrm{AG}}(\phi_{left},\phi_{right}) = \frac{F'(\phi_{left})\tilde{\xi}_{\mathrm{FA}}(\phi_{left}) - F'(\phi_{right})\xi_{\mathrm{F}}}{F'(\phi_{left}) - F'(\phi_{right})}, \tag{2.31a}$$

$$\psi_{\mathrm{AG}}(\phi_{left},\phi_{right}) = \psi_{\mathrm{R}} - \frac{F'(\phi_{left})F'(\phi_{right})}{F'(\phi_{left}) - F'(\phi_{right})}\left(\tilde{\xi}_{\mathrm{FA}}(\phi_{left}) - \xi_{\mathrm{F}}\right), \tag{2.31b}$$

where $\xi_{\mathrm{FA}}(\phi) = \tilde{\xi}_{\mathrm{FA}}(\phi^o)$, and concentrations ϕ_{left} and ϕ_{right} on the left (upstream) and right (downstream) sides of the shock are related by

$$\frac{\mathrm{d}\phi_{right}}{\mathrm{d}\phi_{left}} = \frac{F(\phi_{left}) - F(\phi_{right}) - (\phi_{left}-\phi_{right})F'(\phi_{right})}{F(\phi_{left}) - F(\phi_{right}) - (\phi_{left}-\phi_{right})F'(\phi_{left})} \times \left[\frac{F'(\phi_{right})F''(\phi_{left})}{F'(\phi_{left})F''(\phi_{right})} - \frac{F'(\phi_{left}) - F'(\phi_{right})}{F''(\phi_{right})}\frac{\tilde{\xi}'_{\mathrm{FA}}(\phi_{left})}{\tilde{\xi}_{\mathrm{FA}}(\phi_{left}) - \xi_{\mathrm{F}}}\right]. \tag{2.32}$$

The shock entropy condition (Oleinik 1959; Rhee *et al.* 1986; Gajjar & Gray 2014) requires that AG must initially start tangential to the rarefaction fan, and as $\phi_{left} = \phi^o_{\mathrm{R}}$ at point A, (1.9) implies that $\phi_{right} = (\phi^o_{\mathrm{R}})^o = \phi^{oo}_{\mathrm{R}}$ at this point. The relationship between ϕ_{R}, ϕ^o_{R} and ϕ^{oo}_{R} is illustrated in figure 8. Equation (2.32) may be numerically integrated from $\phi_{left} = \phi^o_{\mathrm{R}}$ to $\phi_{left} = 1$ to give $\phi_{right} = \phi_{\mathrm{G}}$ at point G and the coordinates $(\xi_{\mathrm{G}}, \psi_{\mathrm{G}})$ of point G are given by (2.31). Shock GB separates the upstream region of pure small particles ($\phi^- = 1$) from the rarefaction fan in the 'lens' region ($\phi^+ = \phi$). Combining (2.7) and (2.17) using the chain rule shows that GB satisfies

$$\frac{\mathrm{d}}{\mathrm{d}\phi}\left[\left(F(\phi) + (1-\phi)F'(\phi)\right)(\xi - \xi_{\mathrm{A}})\right] = 0. \tag{2.33}$$

The shock starts from point G, and hence (2.33) can be integrated to give

$$\xi_{\mathrm{GB}} = \xi_{\mathrm{A}} + \frac{F(\phi_{\mathrm{G}}) + (1-\phi_{\mathrm{G}})F'(\phi_{\mathrm{G}})}{F(\phi) + (1-\phi)F'(\phi)}(\xi_{\mathrm{G}} - \xi_{\mathrm{A}}), \tag{2.34a}$$

$$\psi_{\mathrm{GB}} = \psi_{\mathrm{R}} - F'(\phi)\left(\xi_{\mathrm{GB}}(\phi) - \xi_{\mathrm{A}}\right), \tag{2.34b}$$

with $\phi \in [\phi_{\mathrm{B}}, \phi_{\mathrm{G}}]$. A final shock BC satisfying (2.19) separates the downstream region of large particles ($\phi^+ = 0$) from the rarefaction fan ($\phi^- = \phi$). Shock BC must meet the no-mean-flow line at C, where $\phi = \phi_{\mathrm{R}}$, and since $\xi_{\mathrm{C}} - \xi_{\mathrm{A}}$ is given by (2.26), equation (2.19) can be integrated to give

$$\xi_{\mathrm{BC}} = \xi_{\mathrm{A}} - \frac{\mathscr{G}}{F(\phi) - \phi F'(\phi)} = \xi_{\mathrm{A}} - \frac{\mathscr{G}}{A_\gamma \phi^2(1+\gamma-2\gamma\phi)}, \tag{2.35a}$$

$$\psi_{\mathrm{BC}} = \psi_{\mathrm{R}} - \frac{F'(\phi)\mathscr{G}}{F(\phi) - \phi F'(\phi)}, \tag{2.35b}$$

with $\phi \in [\phi_R, \phi_B]$ and

$$\mathscr{G} = (\xi_C - \xi_A)F(\phi_R) = \frac{\xi_C - \xi_A}{4} = \frac{\psi_R \gamma^2}{A_\gamma}\left(\frac{4}{(2\gamma-1)(\gamma^2-\gamma+1)^4}\right)^{1/3}. \tag{2.36}$$

The shock reaches the top of the 'lens' at point B where $\psi = 0$, and hence (2.35) determines both ϕ_B and ξ_B.

A requirement for the 'lens-tail' solution to form is that point E must reside in the lower domain, which occurs when $\phi_E < \phi_R$. Instead, if $\phi_E > \phi_R$, then point E would lie in the upper domain and shock DE would continue up to the no-mean-flow line, forming the non-convex 'lens' structure of § 2.2. The transition between the 'lens' solution and the 'lens-tail' solution thus occurs when point E lies on the no-mean-flow line $\psi = \psi_R$, i.e. when $\phi_R = \phi_E$. The definition $F'(\phi_R) = 0$ implies that for the cubic flux (1.5)

$$\phi_R = \frac{1+\gamma \pm \sqrt{\gamma^2-\gamma+1}}{3\gamma}, \tag{2.37}$$

and equating this with ϕ_E (1.10*b*) gives the quadratic equation

$$5\gamma^2 - 5\gamma + 1 = 0. \tag{2.38}$$

As the cubic flux (1.5) is non-convex when $\gamma > 0.5$, the transition between the non-convex 'lens' and 'lens-tail' solutions takes place at the larger of the two roots of (2.38), namely

$$\gamma = \Gamma = (5+\sqrt{5})/10. \tag{2.39}$$

2.4. *Solution in physical coordinates*

Following Thornton & Gray (2008), transformations (2.1) and (2.4) from (x, z) to (ξ, ψ) coordinates mean that the steady-state structures shown in figure 10 describe all of the breaking size-segregation waves that develop under steady uniform flow. They are valid for waves that exist between all vertical heights H_{down} and H_{up}, for any constant segregation number S_r and for any monotonically increasing velocity profile $u(z)$. For example, consider the simple linear velocity profile,

$$u = \alpha + 2(1-\alpha)z, \quad 0 \leqslant \alpha < 1, \tag{2.40}$$

where α is the parameter that controls the amount of shear across the layer. The case of $\alpha = 0$ represents simple shear with zero basal velocity, whilst $\alpha = 1$ corresponds to plug flow. Not only is this the simplest non-trivial velocity field that highlights all the major features of the breaking-wave structure, but it is also a good leading-order approximation to the velocity field measured in the (shallow) moving-bed flume experiments of § 1.1. From (1.13), the breaking wave travels downstream with velocity

$$u_{wave} = \alpha + (1-\alpha)(H_{up} + H_{down}), \tag{2.41}$$

and so the relative downstream velocity $\hat{u}$ becomes

$$\hat{u} = (1-\alpha)(H_{up} - H_{down})(2\hat{z} - 1). \tag{2.42}$$

The no-mean-flow line $\hat{z}_R = 1/2$ lies halfway between the vertical heights H_{down} and H_{up} in untransformed variables. Transformation (2.4) means that z and ψ have a quadratic relation,

$$\psi = (1-\alpha)(H_{up} - H_{down})(\hat{z}^2 - \hat{z}), \tag{2.43}$$

with the transformed no-mean-flow line $\psi_R = -(1-\alpha)(H_{up} - H_{down})/4$. Inverting equation (2.43) gives $\hat{z}$ as a function of ψ, with the positive and negative roots for the upper and lower regions, respectively. Figure 12 shows the steady breaking waves in physical coordinates for linear shear with $\alpha = 0.5$, $S_r = 1$, $H_{up} = 0.9$ and $H_{down} = 0.1$ for $\gamma = 0.35$, 0.65 and 0.9 in (a), (b) and (c) respectively.

2.5. *Comparison with solution for the quadratic flux*

The asymmetric cubic flux function (1.5) leads to a number of differences in the structures shown in figure 12 and that of the quadratic flux function (1.2) shown in figure 9(*e*). The two 'lens'-like structures in figure 12(*a*,*b*) have a strong similarity to the symmetric 'lens' structure. As the normalisation of the flux function (2.8) implies that (2.21) is independent of γ, the 'lens' length is identical to the quadratic 'lens' length $(1-\alpha)(H_{up} - H_{down})^2/S_r$. However, with an asymmetric flux, the 'lens' structures have no rotational symmetry. The asymmetry also means the maximum rise velocity of large particles is less than the maximum percolation velocity of fines, causing point B to lie further downstream. When $\Gamma < \gamma \leqslant 1$, a few large particles surrounded by many fines rise very slowly, and so are swept a long way downstream before recirculating. This causes the additional 'tail'-like region, and substantially increases the length of the breaking wave. The colour map shows how the concentration in the 'tail' is very similar to $\phi = 1$ of the surrounding region of pure small particles, reflecting the very small number of large particles that circulate slowly through this region. Most of the large particles still rise at a moderate speed through the 'lens' region; however, the small particles percolate down very quickly. This leaves a higher concentration of coarse grains in the middle of the 'lens', shown by a stronger green hue. Interestingly, the length of this 'lens' region in the 'lens-tail' structure remains very close to the length of the 'lens' structures. Comparing (2.26) with (2.16) shows that the length of the 'lens' within the 'lens-tail' structure is, at most, only 9 % less than the length of the 'lens' structure.

3. Recirculating particle motion through the breaking wave

The recirculating motion of the grains can be understood by examining the particle paths as they pass through the breaking wave. Following Thornton *et al.* (2006) and Thornton & Gray (2008), the particle paths of the large (superscript l) and small grains (superscript s) are given by

$$\frac{\mathrm{d}x^\nu}{\mathrm{d}t} = u^\nu, \quad \frac{\mathrm{d}z^\nu}{\mathrm{d}t} = w^\nu, \quad (\nu = l, s). \tag{3.1a,b}$$

The normal constituent velocities w^ν are given by (1.3) and the downstream constituent velocities are assumed to be equal to the downstream bulk velocity (1.11), $u^s = u^l = u$. Eliminating the time dependence from (3.1) and employing the non-dimensionalisation (2.1) gives the non-dimensional particle paths

$$\hat{u}(\hat{z})\frac{\mathrm{d}\hat{z}^\nu}{\mathrm{d}\hat{x}^\nu} = \hat{w}^\nu(\phi), \quad (\nu = l, s), \tag{3.2}$$

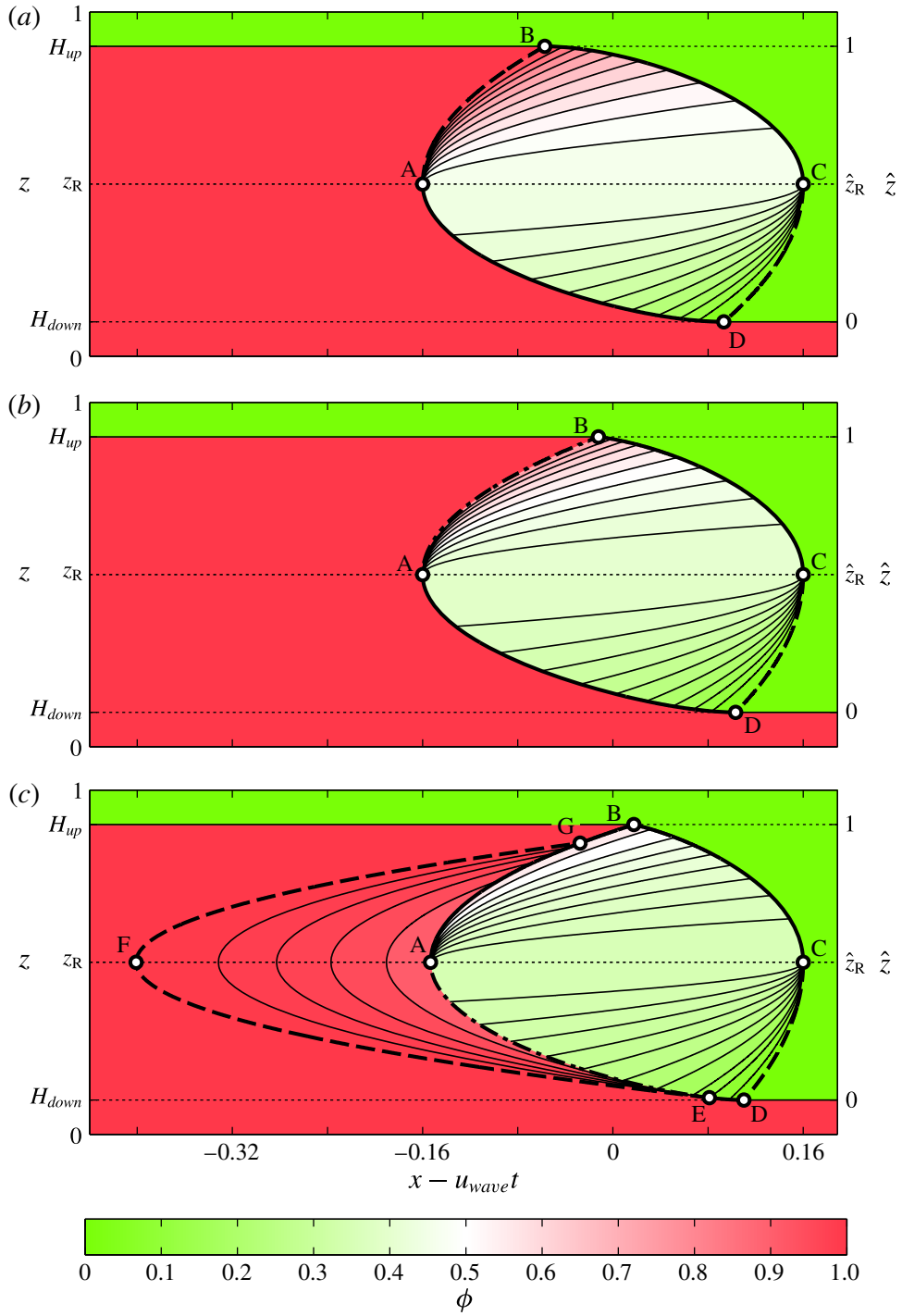

FIGURE 12. The breaking wave that develops between $H_{up} = 0.9$ and $H_{down} = 0.1$ is shown in physical coordinates (x, z) in a frame translating with velocity u_{wave} (1.13). The bulk velocity $u(z)$ follows a linear shear profile (2.40) with $\alpha = 0.5$. The three different structures that arise for the asymmetric cubic flux (1.5) with $S_r = 1$ are shown in (*a–c*) for $\gamma = 0.35$, 0.65 and 0.9, respectively. The asymmetry in the large and small particle velocities that result from the asymmetric flux function causes point B to be swept further downstream in the two 'lens'-like structures (*a*) and (*b*) compared to the symmetric quadratic flux shown in figure 9(*e*). These asymmetric velocities are even more significant in (*c*), where the slow rise rate of large particles surrounded by many fines means that some large particles are swept a long way upstream before recirculating. This results in the 'tail' region EFGAE. The concentration map reflects how only a small number of large particles recirculate through this region. Most large particles still rise at a moderate velocity, and recirculate in the 'lens' region.

which simplify further in velocity-averaged coordinates (2.4) to give

$$\frac{\mathrm{d}\psi^l}{\mathrm{d}\xi^l} = \frac{F(\phi)}{1-\phi}, \quad \frac{\mathrm{d}\psi^s}{\mathrm{d}\xi^s} = -\frac{F(\phi)}{\phi}. \tag{3.3a,b}$$

The concentration fields derived in § 2 can be used with (3.3) to calculate the particle paths through each of the breaking-wave structures.

3.1. *Recirculation through the 'lens' structures*

First consider the recirculation through a breaking wave with a convex 'lens' structure when $\gamma \leqslant 0.5$. Suppose a small particle starts at a height $\hat{z}^s_{enter} > \hat{z}_{\mathrm{R}}$, equivalent to transformed height ψ^s_{enter}. The small grains are moving faster than the breaking wave in the upper region, and so they are swept downstream to the right before crossing AB and entering the 'lens' at downstream distance

$$\xi^s_{enter} = \xi_{\mathrm{A}} + \frac{\psi^s_{enter} - \psi_{\mathrm{R}}}{F'(1)}. \tag{3.4}$$

Although the local small particle velocity is given by (3.3*b*), the local concentration changes through the rarefaction fan ABCA according to characteristics (2.17). These characteristics may be differentiated with respect to ϕ as in (2.13), whilst the chain rule may be used to write the small particle velocity (3.3*b*) in a similar manner to (2.12). Combining these equations shows that the small particle motion through the upper part of the 'lens' is governed by ODE (2.19), with ξ^s instead of ξ. As the small particle enters the 'lens' at ξ^s_{enter} (3.4) when $\phi = 1$, the motion through ABCA is given by

$$\xi^s = \xi_{\mathrm{A}} + \frac{\psi^s_{enter} - \psi_{\mathrm{R}}}{F(\phi) - \phi F'(\phi)}, \tag{3.5}$$

with $\phi \in [\phi_{\mathrm{R}}, 1]$. The small particle continues along this path until it crosses the no-mean-flow line AC at

$$\xi^s_{\mathrm{AC}} = \xi_{\mathrm{A}} + \frac{\psi^s_{enter} - \psi_{\mathrm{R}}}{F(\phi_{\mathrm{R}})} = \xi_{\mathrm{A}} + 4(\psi^s_{enter} - \psi_{\mathrm{R}}), \tag{3.6}$$

with the last equation a result of the normalisation (2.8). The motion through the lower region CDAC is similarly governed by velocity (3.3*b*) and characteristics (2.9), which combine to give the differential equation

$$\frac{\mathrm{d}}{\mathrm{d}\phi}\left[\big(F(\phi) - \phi F'(\phi)\big)\,(\xi^s - \xi_{\mathrm{C}})\right] = 0. \tag{3.7}$$

Since the small particle crosses the no-mean-flow line at $\xi^s = \xi^s_{\mathrm{AC}}$ when $\phi = \phi_{\mathrm{R}}$, equations (2.21), (3.6) and (3.7) imply that the motion through the lower region CDAC is given by

$$\xi^s = \xi_{\mathrm{C}} + \frac{\psi^s_{enter}}{F(\phi) - \phi F'(\phi)}, \tag{3.8}$$

with $\phi \in [\phi^s_{\mathrm{DA}}, \phi_{\mathrm{R}}]$. The small particle exits the breaking wave across DA, with equations (2.9), (2.15) and (3.8) giving both the concentration ϕ^s_{DA} and the exit height ψ^s_{DA}.

Similarly, consider a large particle that starts in the lower region at a height $\hat{z}^l = \hat{z}^l_{enter} < \hat{z}_R$, corresponding to $\psi^l = \psi^l_{enter}$. The large particles initially move slower than the breaking wave, and so are swept upstream to the left until they meet CD at distance

$$\xi^l_{enter} = \xi_C + \frac{\psi_R - \psi^l_{enter}}{F'(0)}. \tag{3.9}$$

The concentration within the lower part of the 'lens' CDAC is governed by characteristics (2.9) whilst the local velocity is given by (3.3*a*); these combine to give differential equation (2.14) with ξ^l replacing ξ. With the initial condition $\phi = 0$ at $\xi^l = \xi^l_{enter}$, the large particle path through CDAC is given by

$$\xi^l = \xi_C + \frac{\psi_R - \psi^l_{enter}}{F(\phi) + (1-\phi)F'(\phi)}. \tag{3.10}$$

Each large particle crosses the no-mean-flow line AC at distance

$$\xi^l_{AC} = \xi_C + \frac{\psi_R - \psi^l_{enter}}{F(\phi_R)} = \xi_C + 4(\psi_R - \psi^l_{enter}). \tag{3.11}$$

In the upper part of the 'lens', characteristics (2.17) govern the concentration at a point (ξ, ψ), and can be combined with (3.3*a*) to give a governing differential equation that resembles (2.14)

$$\frac{\mathrm{d}}{\mathrm{d}\phi}\left[\left(F(\phi) + (1-\phi)F'(\phi)\right)(\xi^l - \xi_A)\right] = 0. \tag{3.12}$$

The initial condition that $\phi = \phi_R$ at $\xi^l = \xi^l_{AC}$, along with (2.21) and (3.11) give the large particle path through ABCA as

$$\xi^l = \xi_A - \frac{\psi^l_{enter}}{F(\phi) + (1-\phi)F'(\phi)}, \tag{3.13}$$

where $\phi \in [\phi_R, \phi^l_{BC}]$. The large particle exits the breaking wave by crossing shock BC when $\phi = \phi^l_{BC}$ and $\xi^l = \xi^l_{BC}$. These are found by equating (2.20) and (3.13), with the exit height $\psi^l = \psi^l_{BC}$ given by (2.17). After exiting the breaking wave, the large particles continue to move downstream at a constant height ψ^l_{BC}.

The particle paths through the non-convex 'lens' structure that forms for $0.5 < \gamma \leqslant \Gamma$ are identical to the above, except that the small particles enter the breaking wave by crossing semi-shock AC (2.17) when $\phi = \phi_M$ (1.10*a*). Thus, the distance ξ^s_{enter} at which they first enter the 'lens' is given by

$$\xi^s_{enter} = \xi_A - \frac{\psi^s_{enter} - \psi_R}{F'(\phi_M)}, \tag{3.14}$$

whilst equation (3.5) governing the motion of the small particles through the upper region is valid for $\phi \in [\phi_R, \phi_M]$.

The small particle paths are parameterised by ψ^s_{enter}, and are given implicitly by (3.4) or (3.14) (for $\gamma \leqslant 0.5$ and $0.5 < \gamma \leqslant \Gamma$ respectively), (3.5), (3.6) and (3.8), whilst the large particle paths are parameterised by ψ^l_{enter} and are given by (3.9)–(3.13). The paths can be transformed back from velocity averaged (ξ, ψ) variables to physical (x, z) variables using the results of § 2.4, and are shown in figure 13(*a*,*b*) for $\gamma = 0.35$ and $\gamma = 0.65$, respectively.

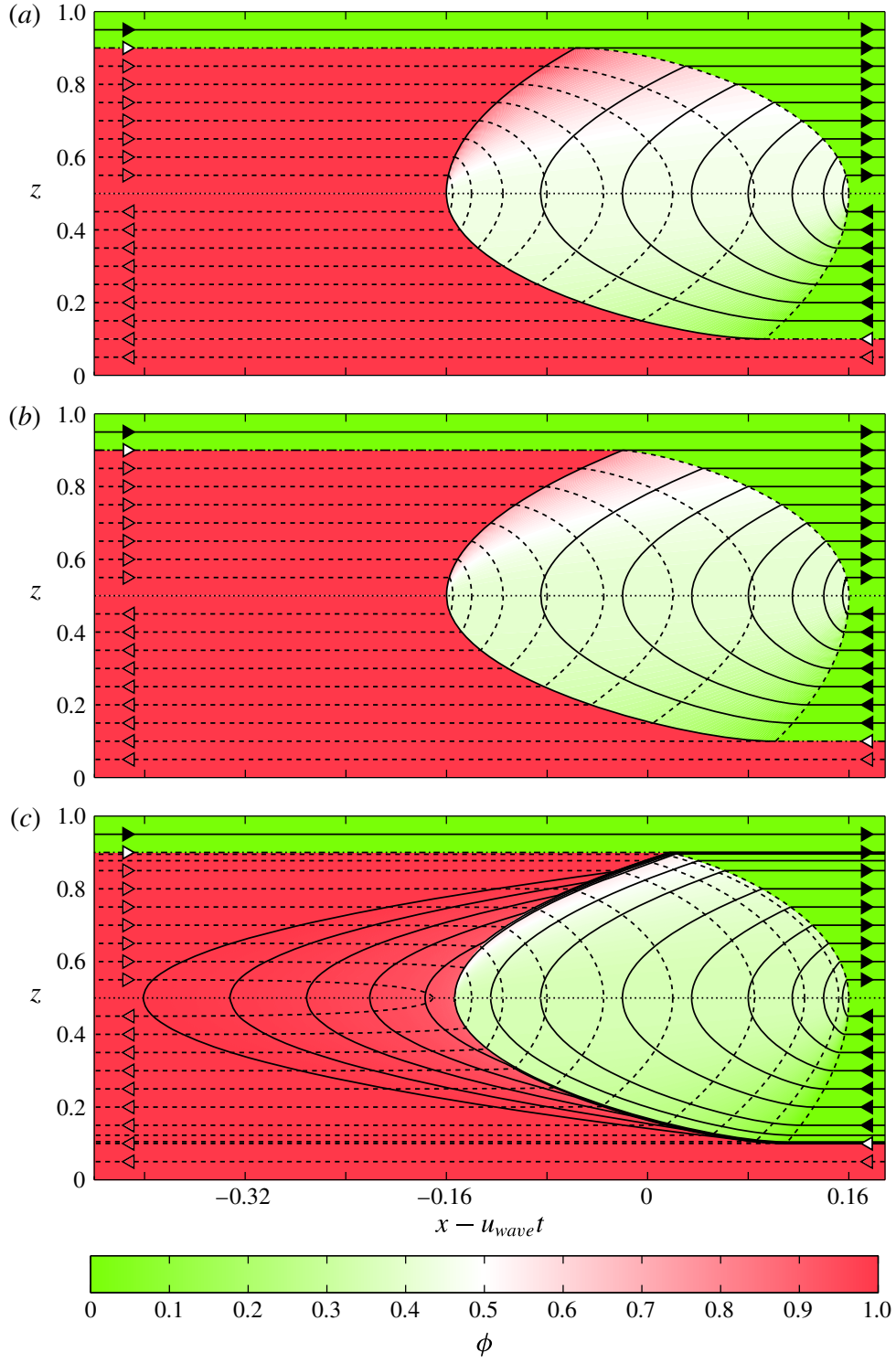

FIGURE 13. The particle paths within the breaking wave are shown superimposed on top of the concentration field for each of the cases in figure 12. The large particles are shown using a solid line with a black arrow, whilst the small particles are shown using a dashed line with a red arrow. The dash-dot line with white arrows shows the upstream and downstream shocks where large particles propagate along the upper side and small particles propagate along the lower side. The boundary of the breaking wave, where particles recirculate between the vertical heights H_{up} and H_{down}, is defined by the highest small particle path and lowest large particle path.

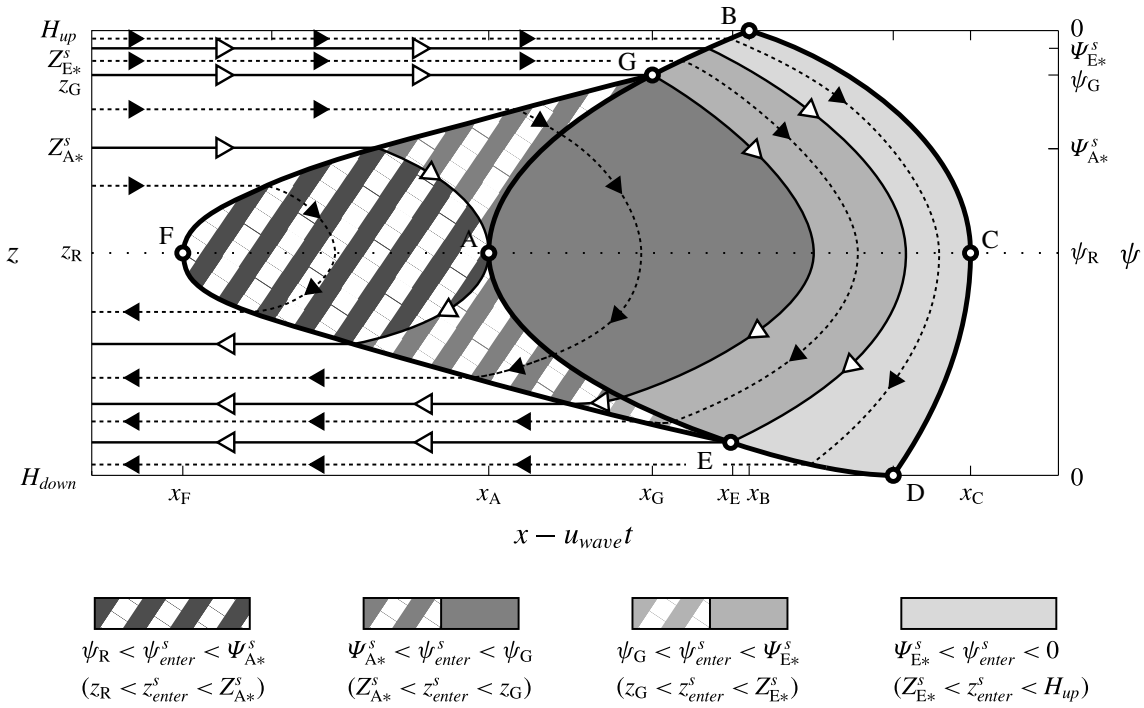

FIGURE 14. A sketch showing how the small particles may pass through different parts of the 'lens-tail' structure depending on their initial starting height (not to scale). There are two critical heights Ψ^s_{A*} and Ψ^s_{E*}, corresponding to physical heights $Z^s_{A*} = z(\Psi^s_{A*})$ and $Z^s_{E*} = z(\Psi^s_{E*})$, which define small particle paths that pass through points A and E, respectively. These paths, along with the path passing through point G, are shown with thin solid lines and white arrows. The small particles starting at an initial height $\Psi^s_{E*} \leqslant \psi^s_{enter} < 0$ (physical height $Z^s_{E*} \leqslant z^s_{enter} < H_{up}$) just pass through the 'lens', whilst those starting at an initial height $\psi_G \leqslant \psi^s_{enter} < \Psi^s_{E*}$ (physical height $z_G \leqslant z^s_{enter} < Z^s_{E*}$) pass through the 'lens' and the lower portion of the 'tail'. Small grains starting at $\Psi^s_{A*} \leqslant \psi^s_{enter} < \psi_G$ (physical height $Z^s_{A*} \leqslant z^s_{enter} < z_G$) pass through the upper portion of the 'tail', the 'lens' and the lower portion of the 'tail'. Finally, small grains starting closest to the no-mean-flow line $\psi_R < \psi^s_{enter} < \Psi^s_{A*}$ (at physical heights $z_R < z^s_{enter} < Z^s_{A*}$) only recirculate through the 'tail' region. The 'lens' and 'tail' regions are shown with solid colour and cross-shading, respectively, whilst sample particle paths starting at each of these heights are shown using thin dashed lines with black arrows. The thick solid lines mark the boundaries of the breaking wave.

3.2. *Recirculation through the 'lens-tail' structure*

Just like the recirculation within the 'lens' structure, the small particle (superscript s) motion is parameterised by ψ^s_{enter}. As summarised in figure 14, the initial starting height ψ^s_{enter} determines whether the small grains may pass through only the 'lens', both the 'lens' and 'tail' regions, or just through the 'tail'. The small particles starting at a height $\Psi^s_{E*} \leqslant \psi^s_{enter} < 0$ would cross shock GB at downstream distance ξ^s_{GB}, recirculate through the 'lens' and exit the breaking wave across DE. Solving $\psi_{GB} = \psi^s_{enter}$ in (2.34) gives the position ξ^s_{GB} at which the particle enters the breaking wave, and the concentration ϕ^s_{GB} on the downstream side of shock GB at this point. The motion through the upper portion of the 'lens' AGBCA is governed by (2.19), with ξ^s replacing ξ. This can be integrated subject to $\xi^s = \xi^s_{GB}$ at $\phi = \phi^s_{GB}$ to give

$$\xi^s = \xi_A + \frac{F(\phi^s_{GB}) - \phi^s_{GB}F'(\phi^s_{GB})}{F(\phi) - \phi F'(\phi)}(\xi^s_{GB} - \xi_A), \tag{3.15}$$

where $\phi \in [\phi_R, \phi^s_{GB}]$ and height ψ^s is given by (2.17). The particles cross the no-mean-flow line AC at a distance ξ^s_{AC}, given by $\phi = \phi_R$ in (3.15). This provides the initial condition for (3.7), governing the motion through the lower part of the 'lens' CDEFC, which integrates to give

$$\xi^s = \xi_C + \frac{\frac{1}{4}(\xi^s_{AC} - \xi_C)}{F(\phi) - \phi F'(\phi)}, \tag{3.16}$$

with the concentration ϕ in the range $\phi \in [\phi^s_{DE}, \phi_R]$. The particles exit the breaking wave across shock DE at downstream distance ξ^s_{DE}, which is found by equating (3.16) with (2.15). This also gives the concentration ϕ^s_{DE}, with the exit height ψ^s_{DE} given by (2.9).

As shown in figure 14, there is a critical initial height Ψ^s_{E*} from which a small particle passes through point E. It is calculated by equating $\xi^s = \xi_E$ in (3.16) and substituting back into (3.15) and (2.17). Small grains starting below Ψ^s_{E*} at an initial height $\psi_G \leqslant \psi^s_{enter} < \Psi^s_{E*}$ enter the 'lens' across GB, travel through the 'lens' according to (2.19) and (3.16), before passing through the lower part of the 'tail' and exiting the breaking wave across EF. The small particle crosses from the 'lens' to the 'tail' at $(\xi^s_{EA}, \psi^s_{EA})$ when $\phi = \phi^s_{EA}$, which are given by equating (3.16) with (2.25). The lower portion of the 'tail' EAFE is spanned by characteristics (2.27) of concentration ϕ^o; following Gajjar & Gray (2014), these may be implicitly differentiated with respect to ϕ^o

$$\frac{\mathrm{d}\psi}{\mathrm{d}\phi^o} - \frac{\mathrm{d}\psi_{EA}}{\mathrm{d}\phi^o} = -F''(\phi^o)\xi - F'(\phi^o)\frac{\mathrm{d}\xi}{\mathrm{d}\phi^o} + \frac{\mathrm{d}}{\mathrm{d}\phi^o}\big(F'(\phi^o)\xi_{EA}(\phi)\big), \tag{3.17}$$

and combined with (3.3*b*) using the chain rule to give the inhomogeneous first-order differential equation

$$\frac{\mathrm{d}}{\mathrm{d}\phi^o}\Big(\big(F(\phi^o) - \phi^o F'(\phi^o)\big)\,\xi^s\Big) = -\phi^o\frac{\mathrm{d}}{\mathrm{d}\phi^o}\Big(\psi_{EA} + F'(\phi^o)\xi_{EA}(\phi)\Big). \tag{3.18}$$

Integrating by parts with the initial condition $\phi = \phi^s_{EA}$ at $\xi^s = \xi^s_{EA}$ gives

$$\xi^s = \xi_C + \frac{g_1(\phi^s_{EA})(\xi^s_{EA} - \xi_C) + g_2(\phi) - g_2(\phi^s_{EA})}{g_1(\phi)}, \tag{3.19a}$$

$$\psi^s = \psi_{EA}(\phi) - F'(\phi^o)(\xi^s(\phi) - \xi_{EA}(\phi)), \tag{3.19b}$$

where $\phi \in [\phi_E, \phi^s_{EA}]$ and the functions $g_1(u)$, $g_2(u)$ are defined as

$$g_1(u) = \frac{A_\gamma}{4\gamma}u(1 + \gamma - \gamma u)^2, \tag{3.20a}$$

$$g_2(u) = \psi_R\gamma\left(\frac{4}{2\gamma - 1}\right)^{1/3} u\big(3\gamma u - (1 + \gamma)\big)^{-2/3}. \tag{3.20b}$$

The final height $\psi^s_{exit} = \psi^s_{EF}$ at which these small particles exit the breaking wave is given by $\phi = \phi_E$ in (3.19).

Small particles starting below ψ_G will first enter the breaking wave across FG at a distance

$$\xi^s_{FG} = \xi_F + \frac{\psi_R - \psi^s_{enter}}{F'(1)}, \tag{3.21}$$

and travel through the upper portion of the 'tail' FGAF where the concentration is given by characteristics (2.30). In a similar fashion to (3.17) above, these can be combined with (3.3*b*) to give the inhomogeneous differential equation

$$\frac{\mathrm{d}}{\mathrm{d}\phi^o}\Big(\big(F(\phi^o)-\phi^o F'(\phi^o)\big)\,\xi^s\Big)=-\phi^o\frac{\mathrm{d}}{\mathrm{d}\phi^o}\Big(F'(\phi^o)\xi_{\mathrm{FA}}(\phi)\Big). \tag{3.22}$$

This is closely related to (3.18), and integrating by parts with the initial condition $\xi^s=\xi^s_{\mathrm{FG}}$ at $\phi=\phi_{\mathrm{E}}$ gives an almost identical form to (3.19*a*) for the ξ coordinate

$$\xi^s = \xi_{\mathrm{C}}+\frac{g_1(\phi_{\mathrm{E}})(\xi^s_{\mathrm{FG}}-\xi_{\mathrm{C}})+g_2(\phi)-g_2(\phi_{\mathrm{E}})}{g_1(\phi)}, \tag{3.23a}$$

$$\psi^s = \psi_{\mathrm{R}}-F'(\phi^o)(\xi^s(\phi)-\xi_{\mathrm{FA}}(\phi)). \tag{3.23b}$$

Whether or not a small particle will travel through the 'lens' region is governed by a second critical initial height $\Psi^s_{\mathrm{A}*}$, at which a small particle passes through point A. Small particles starting above this critical height, $\Psi^s_{\mathrm{A}*}<\psi^s_{enter}\leqslant\psi_{\mathrm{G}}$ will pass through the upper portion of the 'tail' FGAF following (3.23), with $\phi\in[\phi_{\mathrm{E}},\,\phi^s_{\mathrm{AG}}]$. Concentration ϕ^s_{AG} and coordinates $(\xi^s_{\mathrm{AG}},\,\psi^s_{\mathrm{AG}})$ where the particle crosses AG can be found by equating (3.23) with a numerical form of (2.31) and (2.32). The equivalent concentration to ϕ^s_{AG} on the right-hand side of shock AG, at $\xi=\xi^s_{\mathrm{AG}}$ provides the initial condition for the motion through the upper part of the 'lens' FGBCA given by (2.19). The particles then pass across AC into the lower 'lens' and 'tail' regions and then exit across EF.

The small particles starting below the critical height $\Psi^s_{\mathrm{A}*}$ at $\psi_{\mathrm{R}}<\psi^s_{enter}\leqslant\Psi^s_{\mathrm{A}*}$ do not pass through the 'lens', but just recirculate within the 'tail'. Their motion through the upper portion of the 'tail' FGAF is given by (3.23) with $\phi\in[\phi_{\mathrm{E}},\,\phi^s_{\mathrm{FA}}]$ until they cross FA at ξ^s_{FA}. Concentration ϕ^s_{FA} and position ξ^s_{FA} are both found by solving $\psi^s=\psi_{\mathrm{R}}$ in (3.23), and provide the initial condition for (3.18) in the lower portion of the 'tail'. The particle path replicates (3.19) with ϕ^s_{FA} and ξ^s_{FA} replacing ϕ^s_{EA} and ξ^s_{EA}, and concentration ϕ in the range $\phi^s_{\mathrm{FA}}\leqslant\phi\leqslant\phi_{\mathrm{E}}$. As previously, the particle exits the breaking wave across EF at a final height ψ^s_{EF}.

Figure 15 shows how the initial starting height of the large particles (superscript l) also determines which parts of the breaking wave they pass through. All the large particles start in the lower domain at a height $\psi_{\mathrm{R}}<\psi^l_{enter}<0$ (with $\hat{z}<\hat{z}_{\mathrm{R}}$) and travel upstream at this height before meeting CD at distance $\xi^l_{enter}=\xi^l_{\mathrm{CD}}$ given by (3.9). Upon entering the breaking wave, the large particles circulate through the lower portion of the 'lens' CDEAC following (3.10). Most of the coarse grains cross AC at a distance ξ^l_{AC} given by (3.11), with the particle passing through point A (i.e. $\xi^l_{\mathrm{AC}}=\xi_{\mathrm{A}}$) defining a critical height $\Psi^l_{\mathrm{A}*}$

$$\Psi^l_{\mathrm{A}*}=\psi_{\mathrm{R}}+\tfrac{1}{4}(\xi_{\mathrm{C}}-\xi_{\mathrm{A}}). \tag{3.24}$$

Most of the large particles initially start above this critical height, $\psi_{\mathrm{R}}<\psi^l_{enter}<\Psi^l_{\mathrm{A}*}$, cross AC and follow paths in the upper portion of the 'lens' governed by (3.12). The initial condition that $\xi^l=\xi^l_{\mathrm{AC}}$ when $\phi=\phi_{\mathrm{R}}$ gives the path through the upper portion of the 'lens' AGBCA as

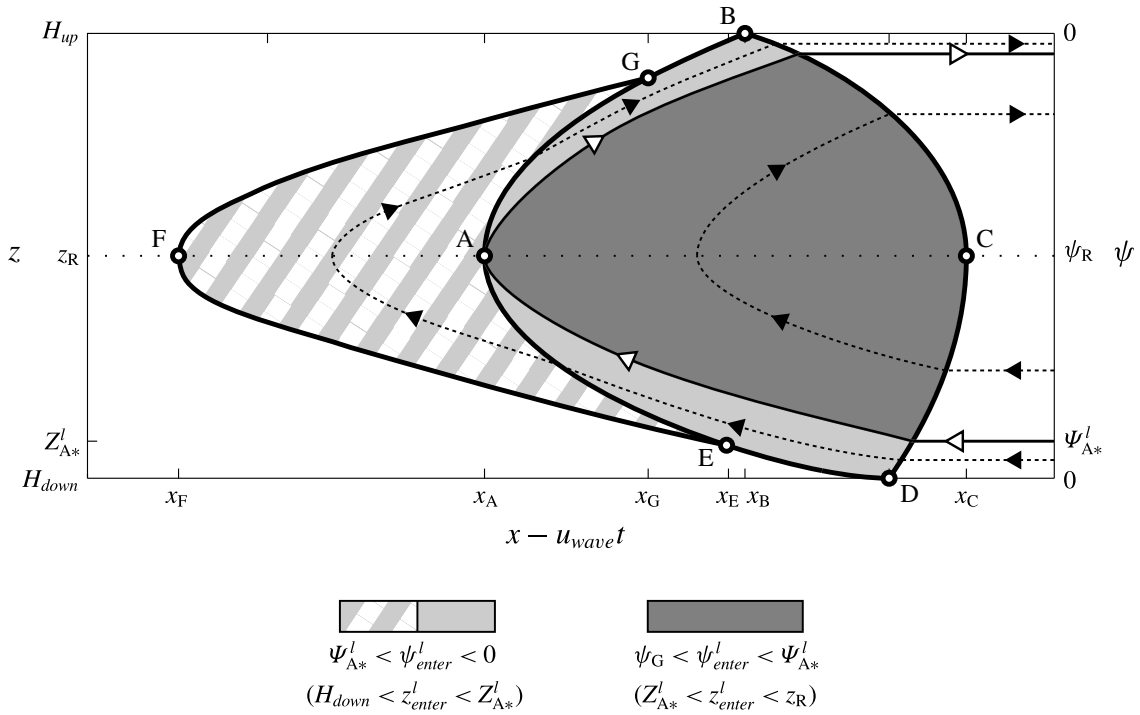

FIGURE 15. A sketch showing how the large particles may pass through different parts of the 'lens-tail' structure depending on their initial starting height (not to scale). All of the large grains pass through the 'lens' region (shown with solid colour), but the large grains starting below the critical height Ψ^l_{A*} also pass through the 'tail' region (cross-shaded). Critical height Ψ^l_{A*} corresponds to the physical height $Z^l_{A*} = z(\Psi^l_{A*})$. Two particle paths are shown with thin dashed lines and black arrows, whilst the particle path for the critical height Ψ^l_{A*}, which passes through point A, is shown with a thin solid line and white arrows. The structure of the breaking wave is shown with thick solid lines.

$$\xi^l = \xi_A + \frac{\psi_R - \psi^l_{enter} + \frac{1}{4}(\xi_C - \xi_A)}{F(\phi) + (1-\phi)F'(\phi)}, \tag{3.25a}$$

$$\psi^l = \psi_R - F'(\phi)(\xi^l - \xi_A). \tag{3.25b}$$

However, there are a few large particles that start below the critical height $\Psi^l_{A*} < \psi^l_{enter} < 0$, and cross EA into the 'tail' region. Their initial motion through the 'lens' CDEAC is given by (3.10) with $\phi \in [0, \phi^l_{EA}]$, where concentration ϕ^l_{EA} and the point of crossing $(\xi^l_{EA}, \psi^l_{EA})$ are found by equating (3.10) with (2.25). As with the small particles, the motion of the large particles through the lower part of the 'tail' EAFE is governed by characteristics (2.27) and local velocity (3.3*a*), which combine to give the governing differential equation

$$\frac{\mathrm{d}}{\mathrm{d}\phi^o}\left((F(\phi^o) + (1-\phi^o)F'(\phi^o))\,\xi^l\right) = (1-\phi^o)\frac{\mathrm{d}}{\mathrm{d}\phi^o}(\psi_{EA} + F'(\phi^o)\xi_{EA}(\phi)). \tag{3.26}$$

This can be integrated by parts with $\xi^l = \xi^l_{EA}$ at $\phi = \phi^l_{EA}$ to give

$$\xi^l = \xi_C + \frac{g_3(\phi^l_{EA})(\xi^l_{EA} - \xi_C) + g_4(\phi) - g_4(\phi^l_{EA})}{g_3(\phi)}, \tag{3.27a}$$

$$\psi^l = \psi_{EA}(\phi) - F'(\phi^o)(\xi^l(\phi) - \xi_{EA}(\phi)), \tag{3.27b}$$

where $\phi \in [\phi^l_{\rm FA}, \phi^l_{\rm EA}]$ and functions $g_3(u)$, $g_4(u)$ are defined as

$$g_3(u) = \frac{A_\gamma}{4\gamma}(1-u)(1-\gamma-\gamma u)^2, \tag{3.28a}$$

$$g_4(u) = \psi_{\rm R}\gamma\left(\frac{4}{2\gamma-1}\right)^{1/3}(1-u)\big(3\gamma u-(1+\gamma)\big)^{-2/3}. \tag{3.28b}$$

The coarse grains meet the no-mean-flow line FA at streamwise distance $\xi^l_{\rm FA}$ and concentration $\phi=\phi^l_{\rm FA}$, which are found from (3.27*b*) by solving $\psi^l=\psi_{\rm R}$. The motion through the upper 'lens' is governed by a similar differential equation to (3.26)

$$\frac{\rm d}{{\rm d}\phi^o}\Big(\big(F(\phi^o)+(1-\phi^o)F'(\phi^o)\big)\,\xi^l\Big) = (1-\phi^o)\frac{\rm d}{{\rm d}\phi^o}\Big(F'(\phi^o)\xi_{\rm FA}(\phi)\Big), \tag{3.29}$$

with $\phi=\phi^l_{\rm FA}$ at $\xi^l=\xi^l_{\rm FA}$ giving

$$\xi^l = \xi_{\rm C} + \frac{g_3(\phi^l_{\rm FA})(\xi^l_{\rm FA}-\xi_{\rm C})+g_4(\phi)-g_4(\phi^l_{\rm FA})}{g_3(\phi)}, \tag{3.30a}$$

$$\psi^l = \psi_{\rm R} - F'(\phi^o)(\xi^l(\phi)-\xi_{\rm FA}(\phi)). \tag{3.30b}$$

These grains then cross shock AG at point $(\xi^l_{\rm AG}, \psi^l_{\rm AG})$, and move through the upper portion of the 'lens' AGBCA following

$$\xi^l = \xi_{\rm A} + \frac{F(\phi^l_{\rm AG})+(1-\phi^l_{\rm AG})F'(\phi^l_{\rm AG})}{F(\phi)+(1-\phi)F'(\phi)}(\xi^l_{\rm AG}-\xi_{\rm A}), \tag{3.31a}$$

$$\psi^l = \psi_{\rm R} - F'(\phi)(\xi^l(\phi)-\xi_{\rm A}), \tag{3.31b}$$

where $\phi^l_{\rm AG}$ is the concentration on the right-hand side of shock AG at $(\xi^l_{\rm AG}, \psi^l_{\rm AG})$. The particles finally cross BC at $(\xi^l_{\rm BC}, \psi^l_{\rm BC})$ and exit the breaking wave at this height.

Like the recirculation in the 'lens', the small and large particle paths are parameterised by ψ^s_{enter} and ψ^l_{enter}, respectively. The critical heights $\Psi^s_{\rm E*}$, $\Psi^s_{\rm A*}$ and $\Psi^l_{\rm A*}$ determine which of the 'lens' and 'tail' regions the particles pass through. A typical set of paths through the 'lens-tail' structure is shown in figure 13(*c*) for $\gamma=0.9$. Despite the 'tail' region, the paths of the small particles through the 'lens-tail' structure are qualitatively similar to the paths through the 'lens' shown in figures 13(*a*,*b*). However the additional motion of the large particles through the 'tail' region means that these paths are very different to previous cases. It is useful to analyse this further by calculating the recirculation times.

3.3. *Recirculation times*

Using the particle paths calculated in §§ 3.1 and 3.2, it is possible to numerically calculate the recirculation times for large and small particles to travel through the domain shown in figure 13. Small particles start at $x=-0.44$ in the upper domain $z>z_{\rm R}$ and travel downstream towards the breaking wave. They recirculate within the breaking wave, before travelling upstream and exiting across $x=-0.44$ in the lower domain $z<z_{\rm R}$. Despite the presence of the 'tail' region, there is no qualitative difference between the small particle recirculation times in any of the solutions. The large particles start at $x=0.1888$ in the lower domain and travel upstream.

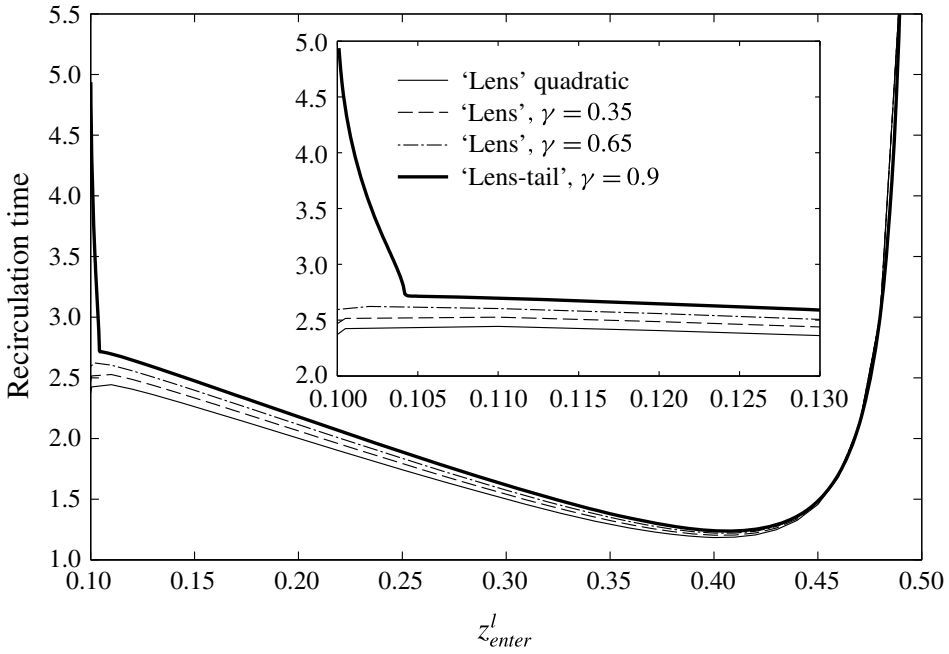

FIGURE 16. Recirculation time for large particles to travel through the region shown in figure 13. The particles start in the lower domain, downstream of the breaking wave at $x = 0.1888$. In a frame translating with the breaking wave, the particles are swept upstream towards the wave, recirculate within the wave, before travelling downstream back to $x = 0.1888$. The recirculation time increases significantly as z^l_{enter} approaches 0.5 since the horizontal velocity $\hat{u}(z)$ tends to zero. The recirculation time also increases significantly for the 'lens-tail' structure as $z^l_{enter} \to H_{down} = 0.1$ (inset), with large particles recirculating very slowly through the 'tail' region at the rear. This behaviour is unique to the 'lens tail' and it not found for any of the 'lens' structures.

They recirculate in the breaking wave, before travelling back downstream and exiting the region in the upper domain at $x = 0.1888$. The recirculation times for these paths are shown in figure 16. The recirculation time tends to infinity as $z^l_{enter} \to 0.5$ for all the structures, since $\hat{u}(z)$ tends towards zero in this limit. The large particles spend an increasing amount of time travelling upstream towards the breaking wave and travelling downstream back towards $x = 0.1888$ after recirculating. However, the 'lens-tail' structure also shows an increase in the recirculation time in the limit $z^l_{enter} \to H_{down}$, with large particles starting close to $H_{down} = 0.1$ passing through the 'tail'. The concentration in the 'tail' is very close to $\phi = 1$, hence (1.3*a*) implies that the vertical velocity is very low. Close to the no-mean-flow line $z = z_R$, the horizontal velocity $\hat{u}(z)$ is very close to zero, so the large particles take a long time recirculating through the 'tail'. Although there is a smooth transition between the path length of a particle starting above $Z^l_{A*} = z(\Psi^l_{A*})$ and travelling through just the 'lens', and a particle starting below Z^l_{A*} that passes through both the 'lens' and 'tail', there is a sharp change in the velocity of the latter particle as it crosses EA. This causes the large increase in the recirculation time at $z = 0.1042$, with the large particle at this height passing through both the 'lens' and 'tail' regions.

4. Conclusions

Debris and pyroclastic flows typically exhibit large particle-rich fronts, which can be shouldered aside to form levees that laterally confine the flow and enhance its run out. The coarse grain fronts are able to exist and grow because of a complex recirculation

zone just upstream of the front, which are known as a 'breaking size-segregation wave'. The recirculation zone is established because particle-size segregation enables overrun large particles to rise back up into the faster moving parts of the flow near the surface, whilst enabling the small particles that are sheared over the top of the large to percolate back down into the slower parts of the flow. The primary aim of this paper has been to examine exact solutions for the structure of the breaking wave using a continuum model with an asymmetric cubic segregation flux (1.5). The cubic flux is parameterised by a single parameter γ which controls the difference between the maximum speed of a single small particle falling through a region of many large particles and the speed of a large particle rising through a region of many small grains (Gajjar & Gray 2014; van der Vaart *et al.* 2015). For $0 \leqslant \gamma \leqslant 0.5$, the segregation flux is convex (up), whilst for $0.5 < \gamma \leqslant 1$, it is non-convex, with the non-convexity allowing semi-shocks to form.

The method of characteristics is used to derive three fundamentally different solution structures shown in figures 10 and 12, which are dependent on the amount of asymmetry γ. Convex flux functions ($0 \leqslant \gamma \leqslant 0.5$) give rise to a 'lens'-like solution formed of two shocks and two expansion fans. This is very similar to the 'lens' solution of Thornton & Gray (2008); however, there is no rotational symmetry about the centre of the 'lens', and point B at the top of the breaking wave lies further downstream. Non-convex flux functions with a small amount of asymmetry ($0.5 < \gamma \leqslant \Gamma = (5+\sqrt{5})/10$) also give a 'lens' solution, with the only difference being that a semi-shock AB separates the upper expansion fan from the upstream region of small particles, causing the top of the wave to lie even further downstream. Although the structure of the 'lens' is affected by the amount of asymmetry, the 'lens' has a constant length of $-4\psi_{\mathrm{R}}$, irrespective of γ. The transformed no-mean-flow height ψ_{R} is only dependent on the velocity profile $u(z)$ and the vertical height of the wave $H_{up} - H_{down}$, meaning that the length of the 'lens' solution is independent of the segregation flux. The length is thus the same in both the convex and non-convex cases, and is equal to the length of the breaking wave for the quadratic flux (Thornton & Gray 2008). The combination of higher amounts of asymmetry and the collective motion of large particles for $\Gamma < \gamma \leqslant 1$ produces a new 'lens-tail' structure. The 'tail' is formed by an additional expansion and compression wave upstream of the 'lens', and significantly increases the total length of the breaking wave. However the length of 'lens' region in the 'lens-tail' structure remains very close to the length of the 'lens' in the other solutions, i.e. $-4\psi_{\mathrm{R}}$.

The precise asymmetric segregation flux must still be determined for the recirculating chute flow regime, but the results of this paper provide the general framework for deriving the breaking-wave structure. The three structures presented would be qualitatively the same for other (non-cubic) flux functions that satisfy the conditions of § 1.3; namely that $F(\phi)$ has a maximum at $\phi_{max} = \phi_{\mathrm{R}}$, with $0 < \phi_{max} < 1/2$ and $F(\phi_{max})$, and that F has at most one inflexion point in the interval $(\phi_{max}, 1)$. The derivation of the structures is given in a general form, and may be extended to other flux functions. For example, the derivation of the convex 'lens' structure in § 2.1 is more general than that of Thornton & Gray (2008), and can be applied directly to other convex (non-cubic) flux functions, such as the asymmetric flux functions presented by Marks *et al.* (2012) and Tunuguntla *et al.* (2014). The non-convex 'lens' (§ 2.2) would also apply directly to non-convex functions in which ϕ_{E} (1.10*b*) is greater than ϕ_{R}. Non-convex functions with $\phi_{\mathrm{E}} < \phi_{\mathrm{R}}$ would produce a 'lens-tail' solution that is qualitatively similar to figure 12(*c*). The analysis would also follow directly up to (2.24), with numerical integration needed for (2.24)–(2.36).

The particle paths were calculated implicitly in terms of the local concentration ϕ and are shown in figure 13. The small and large particle paths are parameterised by the initial starting heights ψ^s_{enter} and ψ^l_{enter}, with figures 14 and 15 illustrating the three critical heights $\Psi^s_{\mathrm{E}*}$, $\Psi^s_{\mathrm{A}*}$ and $\Psi^l_{\mathrm{A}*}$ for the 'lens-tail' structure that determine which of the 'lens' and 'tail' regions the particles pass through. Small particles starting above $Z^s_{\mathrm{E}*} = z(\Psi^s_{\mathrm{E}*})$ and small particles starting below $Z^s_{\mathrm{A}*} = z(\Psi^s_{\mathrm{A}*})$ pass through only the 'lens' and 'tail' regions, respectively, whilst small particles starting in $Z^s_{\mathrm{A}*} \leqslant z^s_{enter} \leqslant Z^s_{\mathrm{E}*}$ pass through both the 'lens' and 'tail' regions. Some small particles are able to recirculate only in the 'tail' region, but the large particles always travel through the 'lens' region. The majority of the large particles start above $Z^l_{\mathrm{A}*} = z(\Psi^l_{\mathrm{A}*})$ and just travel through the 'lens', but a few large particles start below this height, and also pass through the 'tail' in addition to the lens. It is the motion of these large particles which has a significant effect on the recirculation time shown in figure 16. Although the recirculation time tends to infinity for large particles starting near the no-mean-flow line $z = z_{\mathrm{R}}$, the motion of large particles through the 'tail' in the 'lens-tail' structure also increases the recirculation time significantly for particles starting close to $z = H_{down}$, with the velocity in the 'tail' near the no-mean-flow line close to zero in both the normal and downstream components.

It was exactly this kind of behaviour that was observed in both the moving-bed flume experiments and numerical discrete particle method simulations in § 1.1. Whilst most large particles recirculated quickly at the front, a few large particles recirculated much more slowly through regions of many small particles upstream, creating a 'tail'-like region. The correspondence between this behaviour and the new 'lens-tail' structure for the asymmetric cubic flux (1.5) in figure 6 shows that the flux function of van der Vaart *et al.* (2015) gives qualitative agreement in a very different physical environment, with their reported value of $\gamma = 0.89$ producing a 'lens-tail' solution. As the asymmetry is essential for producing a 'tail', this paper, therefore, provides further physical evidence for the asymmetry between large and small particle segregation speeds, and shows how an asymmetric continuum model with a cubic flux (Gajjar & Gray 2014; van der Vaart *et al.* 2015) captures all of the essential behaviour. The similarity between the physical experiments and numerical simulations shows that MercuryDPM could be a valuable tool in future research. Extensive experimental and numerical work is currently under way to analyse the particle motion within the breaking wave, which may also help to answer some wider segregation questions that remain unanswered in this framework. For instance, the robustness of the 'lens'-length $(1-\alpha)(H_{up} - H_{down})^2/S_r$ in all three structures suggests that the recirculating motion in a moving-bed flume could be a useful method of examining how the non-dimensional segregation coefficient S_r varies with particle-size ratio. Although this relationship has been deduced from DPM simulations (Thornton *et al.* 2012*b*), an experimental verification is still lacking.

Acknowledgements

This research was supported by EPSRC Doctoral Training Grant EP/K502947/1, EPSRC research grants EP/I019189/1, EP/K00428X/1 and EP/M022447/1, NERC grant NE/K003011/1, and Royal Society grant WM150058, along with Swiss SNF grant no. 200021-149441. P.G. also acknowledges support from the Margaret Elizabeth Lee Fellowship. J.M.N.T.G. is a Royal Society Wolfson Research Merit Award holder and an EPSRC Established Career Fellow.

Appendix A. Features of hyperbolic solutions

This appendix describes some of the features found in solutions to hyperbolic equations. For further general information on hyperbolic equations, the reader is referred to Rhee *et al.* (1986), whilst in particular Gajjar & Gray (2014) provides further details of deriving exact solutions to segregation problems. Solutions may be constructed using the method of characteristics (Whitham 1974; Billingham & King 2001), where the concentration ϕ is constant along characteristic curves, otherwise known as characteristics. Comparing the (quasi-linear) segregation (2.2),

$$\hat{u}\frac{\partial \phi}{\partial \hat{x}} - \frac{\partial}{\partial \hat{z}}F(\phi) = 0, \tag{A 1}$$

with the full derivative of ϕ with respect to an arbitrary variable s

$$\frac{\mathrm{d}\phi}{\mathrm{d}s} = \frac{\mathrm{d}\hat{x}}{\mathrm{d}s}\frac{\partial \phi}{\partial \hat{x}} + \frac{\mathrm{d}\hat{z}}{\mathrm{d}s}\frac{\partial \phi}{\partial \hat{z}}, \tag{A 2}$$

implies that the concentration ϕ is constant along characteristics curves given by

$$\frac{\mathrm{d}\hat{x}}{\mathrm{d}s} = \hat{u}, \quad \frac{\mathrm{d}\hat{z}}{\mathrm{d}s} = -F'(\phi). \tag{A 3a,b}$$

These characteristics become straight lines under the transformation to depth-averaged velocity (ξ, ψ) coordinates (2.4)

$$\xi = \hat{x}, \quad \psi(\hat{z}) = \int_0^{\hat{z}} \hat{u}(\hat{z}')\,\mathrm{d}\hat{z}', \tag{A 4a,b}$$

with concentration ϕ equal to ϕ_λ along lines with constant gradient (2.6)

$$\frac{\partial \psi}{\partial \xi} = -F'(\phi_\lambda) = -A_\gamma\left(3\gamma\phi_\lambda^2 - 2(1+\gamma)\phi_\lambda + 1\right). \tag{A 5}$$

Note that (ξ, ψ) coordinates are also streamfunction coordinates (Gray & Ancey 2009). As shown in figure 17(*a*) characteristics of different concentrations may collide, leading to the formation of a shock. The shock has gradient (2.7)

$$\frac{\mathrm{d}\psi}{\mathrm{d}\xi} = -\frac{[\![F(\phi)]\!]}{[\![\phi]\!]}, \tag{A 6}$$

with the 'jump' brackets $[\![f]\!] = f^+ - f^-$ mathematically representing the physical jump in concentration across the interface that is pictured in figure 17(*b*). Figure 17(*c*) shows how characteristics may diverge away from each other in a rarefaction fan. Physically, this leads to a smoothly varying concentration field, as shown in figure 17(*d*). Non-convex flux functions also give rise to a 'semi-shock' structure, in which characteristics lie parallel to the shock on one side, but collide with it on the other. One such 'semi-shock' is pictured in figure 17(*e*), with figure 17(*f*) showing how there is a smooth variation in the concentration between ϕ_R and ϕ_M, before a sharp jump in the concentration from $\phi = \phi_\mathrm{M}$ to $\phi = 1$. Finally, characteristics may also converge towards each other, without colliding, leading to the formation of a compression wave (figure 17*g*). This also leads to a smoothly varying concentration field, as shown in figure 17(*h*). These hyperbolic features are, however, idealised solutions to the full segregation equation. The stochastic, random-walk nature of particle motion in real world flows causes diffusive remixing between the two species that smooths over any sharp discontinuities in concentration that occur at shocks (Gray & Chugunov 2006; Gray *et al.* 2015).

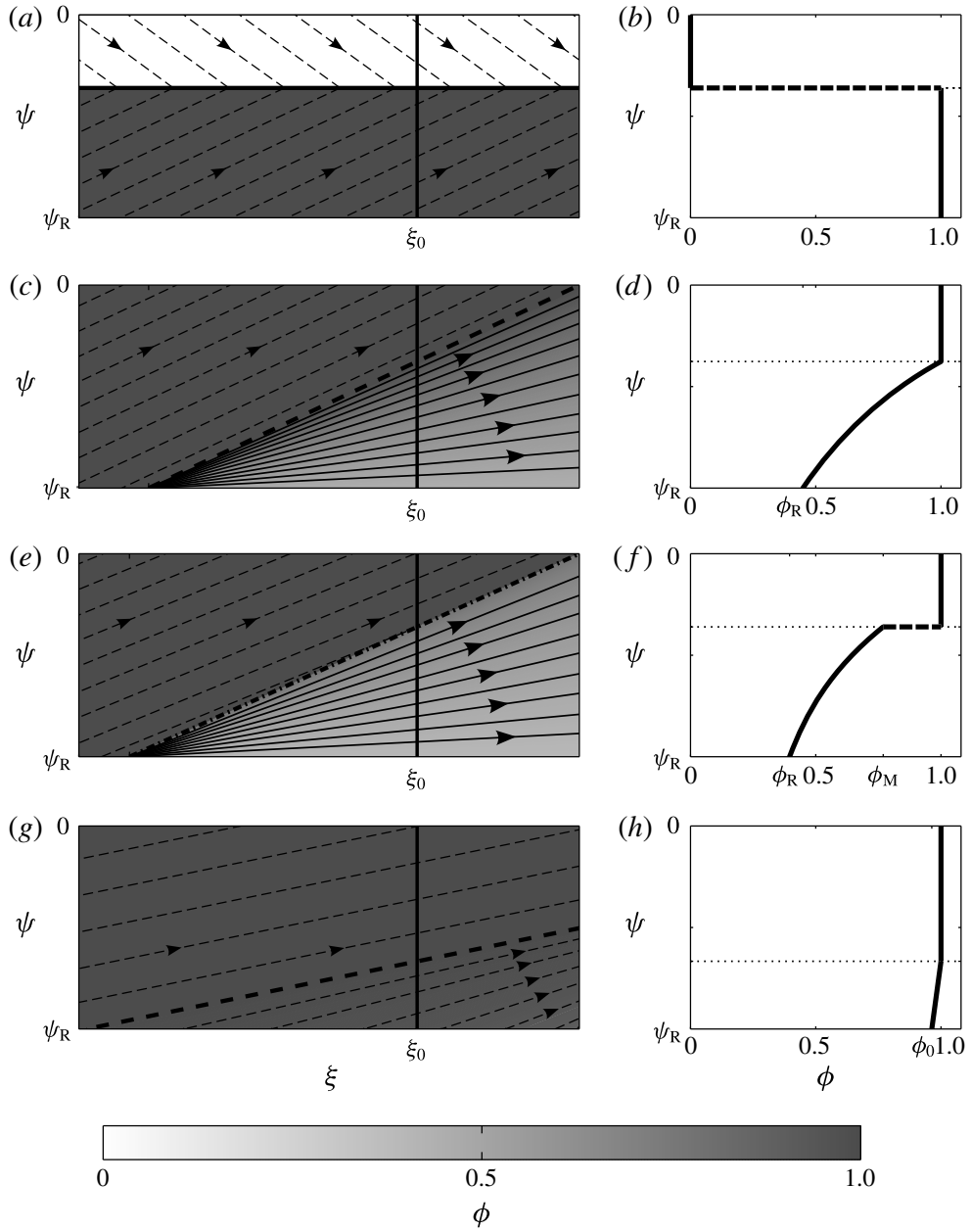

FIGURE 17. Exact solutions to hyperbolic equations may be constructed using the method of characteristics. Solutions are constructed by determining the position of characteristics, or lines upon which the concentration ϕ is constant, with figures (*a*,*c*,*e*,*g*) showing the solutions in (ξ, ψ) coordinates. These solutions may be physically visualised by plotting the concentration ϕ as a function of the height ψ at a particular downstream position ξ_0, with sketches shown in figures (*b*,*d*,*f*,*h*). Characteristics may collide and form a shock (*a*), which physically corresponds to a sharp jump in the concentration from $\phi = 1$ below the shock to $\phi = 0$ above the shock (*b*). Characteristics may diverge in a rarefaction fan (*c*), giving a smoothly varying concentration field from $\phi = \phi_R$ to $\phi = 1$ (*d*). Non-convex segregation flux functions give rise to semi-shocks, with characteristics lying parallel to the semi-shock on the lower side, but colliding with it on the upper side (*e*). There is a smoothly varying concentration field between $\phi = \phi_R$ and $\phi = \phi_M$, with a sharp jump in the concentration from $\phi = \phi_M$ to $\phi = 1$ at the height of the semi-shock (*f*). Characteristics may also converge to form a compression wave (*g*), which also leads to a smoothly varying concentration field (*h*) from $\phi = \phi_0$ to $\phi = 1$.

Appendix B. Derivation of equations governing shock AG

Following Rhee *et al.* (1986), this appendix derives governing equations for the shock AG, as the concentration changes along both sides of the shock. The compression wave to the left of shock AG has characteristics of concentration ϕ_{left} given by (2.30)

$$\psi = \psi_{\mathrm{R}} - F'(\phi_{left})\big(\xi - \tilde{\xi}_{\mathrm{FA}}(\phi_{left})\big), \tag{B 1}$$

where $\tilde{\xi}_{\mathrm{FA}}(\phi^o) = \xi_{\mathrm{FA}}(\phi)$. The rarefaction fan (2.17) to the right of shock AG has characteristics of concentration ϕ_{right},

$$\psi = \psi_{\mathrm{R}} - F'(\phi_{right})(\xi - \xi_{\mathrm{F}}), \tag{B 2}$$

whilst the shock condition (2.7) governs the gradient of AG

$$\frac{\mathrm{d}\psi}{\mathrm{d}\xi} = c(\phi_{left}, \phi_{right}) = -\frac{F(\phi_{left}) - F(\phi_{right})}{\phi_{left} - \phi_{right}}. \tag{B 3}$$

Treating ϕ_{left} and ϕ_{right} as independent variables and using the chain rule gives

$$\frac{\mathrm{d}\psi}{\mathrm{d}\xi} = c(\phi_{left}, \phi_{right}) = \frac{\dfrac{\partial\psi}{\partial\phi_{left}} + \dfrac{\partial\psi}{\partial\phi_{right}}\dfrac{\mathrm{d}\phi_{right}}{\mathrm{d}\phi_{left}}}{\dfrac{\partial\xi}{\partial\phi_{left}} + \dfrac{\partial\xi}{\partial\phi_{right}}\dfrac{\mathrm{d}\phi_{right}}{\mathrm{d}\phi_{left}}}, \tag{B 4}$$

which, after rearranging, implies that

$$\frac{\mathrm{d}\phi_{right}}{\mathrm{d}\phi_{left}} = -\frac{c(\phi_{left}, \phi_{right})\dfrac{\partial\xi}{\partial\phi_{left}} - \dfrac{\partial\psi}{\partial\phi_{left}}}{c(\phi_{left}, \phi_{right})\dfrac{\partial\xi}{\partial\phi_{right}} - \dfrac{\partial\psi}{\partial\phi_{right}}}. \tag{B 5}$$

The compression wave and the rarefaction fan meet at the shock, and so (B 1) and (B 2) govern both the height ψ_{AG} and downstream position ξ_{AG} of the shock

$$\xi_{\mathrm{AG}}(\phi_{left}, \phi_{right}) = \frac{F'(\phi_{left})\tilde{\xi}_{\mathrm{FA}}(\phi_{left}) - F'(\phi_{right})\xi_{\mathrm{F}}}{F'(\phi_{left}) - F'(\phi_{right})}, \tag{B 6a}$$

$$\psi_{\mathrm{AG}}(\phi_{left}, \phi_{right}) = \psi_{\mathrm{R}} - \frac{F'(\phi_{left})F'(\phi_{right})}{F'(\phi_{left}) - F'(\phi_{right})}\big(\tilde{\xi}_{\mathrm{FA}}(\phi_{left}) - \xi_{\mathrm{F}}\big). \tag{B 6b}$$

Differentiating (B 6) gives

$$\frac{\partial\xi_{\mathrm{AG}}}{\partial\phi_{left}} = -\frac{F'(\phi_{right})F''(\phi_{left})}{\big(F'(\phi_{left}) - F'(\phi_{right})\big)^2}\big(\tilde{\xi}_{\mathrm{FA}}(\phi_{left}) - \xi_{\mathrm{F}}\big) + \frac{F'(\phi_{left})}{F'(\phi_{left}) - F'(\phi_{right})}\tilde{\xi}'_{\mathrm{FA}}(\phi_{left}), \tag{B 7}$$

$$\frac{\partial\xi_{\mathrm{AG}}}{\partial\phi_{right}} = \frac{F'(\phi_{left})F''(\phi_{right})}{\big(F'(\phi_{left}) - F'(\phi_{right})\big)^2}\big(\tilde{\xi}_{\mathrm{FA}}(\phi_{left}) - \xi_{\mathrm{F}}\big), \tag{B 8}$$

$$\frac{\partial\psi_{\mathrm{AG}}}{\partial\phi_{left}} = \frac{\big(F'(\phi_{right})^2\big)F''(\phi_{left})}{\big(F'(\phi_{left}) - F'(\phi_{right})\big)^2}\big(\tilde{\xi}_{\mathrm{FA}}(\phi_{left}) - \xi_{\mathrm{F}}\big) - \frac{F'(\phi_{left})F'(\phi_{right})}{F'(\phi_{left}) - F'(\phi_{right})}\tilde{\xi}'_{\mathrm{FA}}(\phi_{left}), \tag{B 9}$$

$$\frac{\partial \psi_{AG}}{\partial \phi_{right}} = -\frac{(F'(\phi_{left}))^2 F''(\phi_{right})}{(F'(\phi_{left}) - F'(\phi_{right}))^2}(\tilde{\xi}_{FA}(\phi_{left}) - \xi_F), \tag{B 10}$$

which may be substituted into (B 5) to give (2.32)

$$\frac{\mathrm{d}\phi_{right}}{\mathrm{d}\phi_{left}} = \frac{c(\phi_{left}, \phi_{right}) + F'(\phi_{right})}{c(\phi_{left}, \phi_{right}) + F'(\phi_{left})} \times \left\{ \frac{F'(\phi_{right})F''(\phi_{left})}{F'(\phi_{left})F''(\phi_{right})} - \frac{F'(\phi_{left}) - F'(\phi_{right})}{F''(\phi_{right})} \frac{\tilde{\xi}'_{FA}(\phi_{left})}{\tilde{\xi}_{FA}(\phi_{left}) - \xi_F} \right\}. \tag{B 11}$$

As $\xi_{FA}(\phi) = \tilde{\xi}_{FA}(\phi^o)$, (2.28) and (1.9) for the cubic flux function give

$$\tilde{\xi}_{FA}(\phi) = \xi_C - \frac{\psi_R \gamma}{F'(\phi)((2\gamma - 1)(1 + \gamma - 3\gamma\phi)^2)^{1/3}}, \tag{B 12}$$

$$\frac{\partial \tilde{\xi}_{FA}(\phi)}{\partial \phi} = \psi_R \gamma \frac{F''(\phi)(1 + \gamma - 3\gamma\phi) - 2\gamma F'(\phi)}{(F'(\phi))^2((2\gamma - 1)(1 + \gamma - 3\gamma\phi)^5)^{1/3}}. \tag{B 13}$$

Equations (B 12) and (B 13) may be used with (B 11) to numerically solve for the changing concentration along the shock path.

REFERENCES

ANCEY, C., COUSSOT, P. & EVESQUE, P. 1999 A theoretical framework for granular suspensions in a steady simple shear flow. *J. Rheol.* **43** (6), 1673–1699.

BASCO, D. 1985 A qualitative description of wave breaking. *J. Waterways Port Coast. Ocean Div. ASCE* **111** (2), 171–188.

BILLINGHAM, J. & KING, A. C. 2001 *Wave Motion*. Cambridge University Press.

BRIDGWATER, J. 1976 Fundamental powder mixing mechanisms. *Powder Technol.* **15**, 215–236.

BRIDGWATER, J. 1994 Mixing and segregation mechanisms in particle flow. In *Granular Matter* (ed. A. Mehta), pp. 161–193. Springer.

BRIDGWATER, J., FOO, W. & STEPHENS, D. 1985 Particle mixing and segregation in failure zones – theory and experiment. *Powder Technol.* **41**, 147–158.

CASSAR, C., NICOLAS, M. & POULIQUEN, O. 2005 Submarine granular flows down inclined planes. *Phys. Fluids* **17** (10), 103301.

CLAPHAM, C. & NICHOLSON, J. 2009 *The Concise Oxford Dictionary of Mathematics*. Oxford University Press.

COSTA, J. E. & WILLIAMS, G. 1984 Debris flow dynamics. *Tech. Rep.* 84–606. (videotape) US Geological Survey.

CUNDALL, P. A. & STRACK, O. D. L. 1979 A discrete numerical model for granular assemblies. *Gèotechnique* **29** (1), 47–65.

DASGUPTA, P. & MANNA, P. 2011 Geometrical mechanism of inverse grading in grain-flow deposits: an experimental revelation. *Earth-Sci. Rev.* **104** (1–3), 186–198.

DAVIES, T. R. H. 1990 Debris-flow surges – experimental simulation. *J. Hydrol. NZ.* **29**, 18–46.

DIJKSMAN, J. A., RIETZ, F., LORINCZ, K. A., VAN HECKE, M. & LOSERT, W. 2012 Invited article: refractive index matched scanning of dense granular materials. *Rev. Sci. Instrum.* **83** (1), 011301.

DOLGUNIN, V. N. & UKOLOV, A. A. 1995 Segregation modelling of particle rapid gravity flow. *Powder Technol.* **83**, 95–103.

FORTERRE, Y. & POULIQUEN, O. 2008 Flows of dense granular media. *Annu. Rev. Fluid Mech.* **40** (1), 1–24.

GAJJAR, P. & GRAY, J. M. N. T 2014 Asymmetric flux models for particle-size segregation in granular avalanches. *J. Fluid Mech.* **757**, 297–329.

GDR MIDI 2004 On dense granular flows. *Eur. Phys. J.* E **14**, 341–365.

GOLDHIRSCH, I. 2010 Stress, stress asymmetry and couple stress: from discrete particles to continuous fields. *Granul. Matt.* **12** (3), 239–252.

GOLICK, L. A. & DANIELS, K. E. 2009 Mixing and segregation rates in sheared granular materials. *Phys. Rev.* E **80** (4), 042301.

GRAY, J. M. N. T. & ANCEY, C. 2009 Segregation, recirculation and deposition of coarse particles near two-dimensional avalanche fronts. *J. Fluid Mech.* **629**, 387–423.

GRAY, J. M. N. T. & ANCEY, C. 2015 Particle-size and -density segregation in granular free-surface flows. *J. Fluid Mech.* **779**, 622–668.

GRAY, J. M. N. T. & CHUGUNOV, V. A. 2006 Particle-size segregation and diffusive remixing in shallow granular avalanches. *J. Fluid Mech.* **569**, 365–398.

GRAY, J. M. N. T, GAJJAR, P. & KOKELAAR, P. 2015 Particle-size segregation in dense granular avalanches. *C. R. Physique* **16** (1), 73–85.

GRAY, J. M. N. T. & HUTTER, K. 1997 Pattern formation in granular avalanches. *Contin. Mech. Thermodyn.* **9**, 341–345.

GRAY, J. M. N. T. & KOKELAAR, B. P. 2010*a* Erratum large particle segregation, transport and accumulation in granular free-surface flows – erratum. *J. Fluid Mech.* **657**, 539.

GRAY, J. M. N. T. & KOKELAAR, B. P. 2010*b* Large particle segregation, transport and accumulation in granular free-surface flows. *J. Fluid Mech.* **652**, 105–137.

GRAY, J. M. N. T., SHEARER, M. & THORNTON, A. R. 2006 Time-dependent solutions for particle-size segregation in shallow granular avalanches. *Proc. R. Soc. Lond.* A **462**, 947–972.

GRAY, J. M. N. T., TAI, Y. C. & NOELLE, S. 2003 Shock waves, dead-zones and particle-free regions in rapid granular free-surface flows. *J. Fluid Mech.* **491**, 161–181.

GRAY, J. M. N. T. & THORNTON, A. R. 2005 A theory for particle size segregation in shallow granular free-surface flows. *Proc. R. Soc. Lond.* A **461**, 1447–1473.

IVERSON, R. M. 1997 The physics of debris-flows. *Rev. Geophys.* **35**, 245–296.

IVERSON, R. M. 2005 Regulation of landslide motion by dilatancy and pore pressure feedback. *J. Geophys Res. Earth* **110** (F2), F02015.

IVERSON, R. M. 2014 Debris flows: behaviour and hazard assessment. *Geol. Today* **30** (1), 15–20.

IVERSON, R. M. & LAHUSEN, R. G. 1989 Dynamic pore-pressure fluctuations in rapidly shearing granular materials. *Science* **246** (4931), 796–799.

IVERSON, R. M., LOGAN, M., LAHUSEN, R. G. & BERTI, M. 2010 The perfect debris flow? Aggregated results from 28 large-scale experiments. *J. Geophys. Res.* **115**, F03005.

IVERSON, R. M. & VALLANCE, J. W. 2001 New views of granular mass flows. *Geology* **29** (2), 115–118.

JOHNSON, A. M. 1970 *Physical Processes in Geology*. Freeman, Cooper & Company.

JOHNSON, A. M. 1984 Debris flows. In *Slope Instability*. Wiley.

JOHNSON, C. G., KOKELAAR, B. P., IVERSON, R. M., LOGAN, M., LAHUSEN, R. G. & GRAY, J. M. N. T. 2012 Grain-size segregation and levee formation in geophysical mass flows. *J. Geophys. Res.* **117**, F01032.

KOKELAAR, B. P., GRAHAM, R. L., GRAY, J. M. N. T. & VALLANCE, J. W. 2014 Fine-grained linings of leveed channels facilitate runout of granular flows. *Earth Planet. Sci. Lett.* **385**, 172–180.

LEVEQUE, R. J. 2002 *Finite Volume Methods for Hyperbolic Problems*. Cambridge University Press.

MAJOR, J. J. & IVERSON, R. M. 1999 Debris-flow deposition: effects of pore-fluid pressure and friction concentrated at flow margins. *Geol. Soc. Am. Bull.* **111** (10), 1424–1434.

MARKS, B., ROGNON, P. & EINAV, I. 2012 Grainsize dynamics of polydisperse granular segregation down inclined planes. *J. Fluid Mech.* **690**, 499–511.

MAY, L. B. H., SHEARER, M. & DANIELS, K. E. 2010 Scalar conservation laws with nonconstant coefficients with application to particle size segregation in granular flow. *J. Nonlinear Sci.* **20** (6), 689–707.

McDONALD, S., HARRIS, D. & WITHERS, P. 2012 In situ x-ray microtomography study of the movement of a granular material within a die. *Intl J. Mater. Res.* **103** (2), 162–169.

McINTYRE, M., ROWE, E., SHEARER, M., GRAY, J. M. N. T. & THORNTON, A. R. 2007 Evolution of a mixing zone in granular avalanches. *Appl. Math. Res. Express* **2007**, abm008.

MORLAND, L. W. 1992 Flow of viscous fluids through a porous deformable matrix. *Surv. Geophys.* **13** (3), 209–268.

MUITE, B. K., HUNT, M. L. & JOSEPH, G. G. 2004 The effects of a counter-current interstitial flow on a discharging hourglass. *Phys. Fluids* **16** (9), 3415–3425.

OLEINIK, O. A. 1959 Uniqueness and stability of the generalized solution of the cauchy problem for a quasi-linear equation. *Usp. Mat. Nauk* **14**, 165–170.

PAILHA, M., NICOLAS, M. & POULIQUEN, O. 2008 Initiation of underwater granular avalanches: influence of the initial volume fraction. *Phys. Fluids* **20** (11), 111701.

PAILHA, M. & POULIQUEN, O. 2009 A two-phase flow description of the initiation of underwater granular avalanches. *J. Fluid Mech.* **633**, 115–135.

PIERSON, T. C. 1986 Flow behavior of channelized debris flows, Mount St. Helens, Washington. In *Hillslope Processes* (ed. A. D. Abrahams), pp. 269–296. Allen and Unwin.

DU PONT, S. COURRECH, GONDRET, P., PERRIN, B. & RABAUD, M. 2003 Granular avalanches in fluids. *Phys. Rev. Lett.* **90**, 044301.

POULIQUEN, O. 1999*a* On the shape of granular fronts down rough inclined planes. *Phys. Fluids* **11** (7), 1956–1958.

POULIQUEN, O. 1999*b* Scaling laws in granular flows down rough inclined planes. *Phys. Fluids* **11** (3), 542–548.

POULIQUEN, O., DELOUR, J. & SAVAGE, S. B. 1997 Fingering in granular flows. *Nature* **386**, 816–817.

POULIQUEN, O. & VALLANCE, J. W. 1999 Segregation induced instabilities of granular fronts. *Chaos* **9** (3), 621–630.

RHEE, H. K., ARIS, R. & AMUNDSON, N. R. 1986 *First-order Partial Differential Equations: Volume 1 Theory and Applications of Single Equations*. Prentice-Hall.

ROGNON, P. G., ROUX, J. N., NAAIM, M. & CHEVOIR, F. 2007 Dense flows of bidisperse assemblies of disks down an inclined plane. *Phys. Fluids* **19** (5), 058101.

SAVAGE, S. B. & HUTTER, K. 1989 The motion of a finite mass of granular material down a rough incline. *J. Fluid Mech.* **199**, 177–215.

SAVAGE, S. B. & LUN, C. K. K. 1988 Particle size segregation in inclined chute flow of dry cohesionless granular solids. *J. Fluid Mech.* **189**, 311–335.

SHAND, T. D. 2009 The effect of wave grouping on shoaling and breaking processes. PhD thesis, Civil & Environmental Engineering, Faculty of Engineering, University of New South Wales.

SHARP, R. P. & NOBLES, L. H. 1953 Mudflow of 1941 at Wrightwood, Southern California. *Geol. Soc. Am. Bull.* **64** (5), 547–560.

STARON, L. & PHILLIPS, J. C. 2014 Segregation time-scale in bi-disperse granular flows. *Phys. Fluids* **26** (3), 033302.

TAKAHASHI, T. 1980 Debris flow on prismatic open channel. *J Hydraul. Div. ASCE* **106** (3), 381–396.

THORNTON, A. R. & GRAY, J. M. N. T. 2008 Breaking size-segregation waves and particle recirculation in granular avalanches. *J. Fluid Mech.* **596**, 261–284.

THORNTON, A. R., GRAY, J. M. N. T. & HOGG, A. J. 2006 A three-phase mixture theory for particle size segregation in shallow granular free-surface flows. *J. Fluid Mech.* **550**, 1–25.

THORNTON, A. R., KRIJGSMAN, D., FRANSEN, R., GONZALEZ, S., TUNUGUNTLA, D., TEN VOORTWIS, A., LUDING, S., BOKHOVE, O. & WEINHART, T. 2013*a* Mercury-DPM: fast particle simulations in complex geometries. *Newsl. EnginSoft Year 10* **1**, 48–53.

THORNTON, A. R., KRIJGSMAN, D., TE VOORTWIS, A., OGARKO, V., LUDING, S., FRANSEN, R., GONZALEZ, S. I., BOKHOVE, O., IMOLE, O. & WEINHART, T. 2013*b* A review of recent work on the Discrete Particle Method at the University of Twente: an introduction to the open- source package MercuryDPM. In *Proceedings of DEM6 – 6th International Conference on Discrete Particle Method.*

THORNTON, A. R., WEINHART, T., LUDING., S. & BOKHOVE, O. 2012*a* Frictional dependence of shallow-granular flows from discrete particle simulations. *Eur. Phys. J.* E **35** (12), 127.

THORNTON, A. R., WEINHART, T., LUDING, S. & BOKHOVE, O. 2012*b* Modeling of particle size segregation: calibration using the discrete particle method. *Intl J. Mod. Phys.* C **23** (8), 1240014.

TÓTH, G. & ODSTRČIL, D. 1996 Comparison of some flux corrected transport and total variation diminishing numerical schemes for hydrodynamic and magnetohydrodynamic problems. *J. Comput. Phys.* **128** (1), 82–100.

TUNUGUNTLA, D., BOKHOVE, O. & THORNTON, A. R. 2014 A mixture theory for size and density segregation in shallow granular free-surface flows. *J. Fluid Mech.* **749**, 99–112.

TUNUGUNTLA, D., THORNTON, A. R. & WEINHART, T. 2015 From discrete elements to continuum fields: extension to bidisperse systems. *Comput. Part. Mech.* 1–17; doi:10.1007/s40571-015-0087-y.

TURNBULL, B., BOWMAN, E. T. & MCELWAINE, J. N. 2015 Debris flows: experiments and modelling. *C. R. Physique* **16** (1), 86–96.

VAN DER VAART, K., GAJJAR, P., EPELY-CHAUVIN, G., ANDREINI, N., GRAY, J. M. N. T. & ANCEY, C. 2015 Underlying asymmetry within particle size segregation. *Phys. Rev. Lett.* **114**, 238001.

VALLANCE, J. W. & SAVAGE, S. B. 2000 Particle segregation in granular flows down chutes. In *IUTAM Symposium on Segregation in Granular Materials* (ed. A. D. Rosato & D. L. Blackmore). Kluwer.

WEINHART, T., HARTKAMP, R., THORNTON, A. R. & LUDING, S. 2013 Coarse-grained local and objective continuum description of three-dimensional granular flows down an inclined surface. *Phys. Fluids* **25** (7), 070605.

WEINHART, T., THORNTON, A. R., LUDING, S. & BOKHOVE, O. 2012 Closure relations for shallow granular flows from particle simulations. *Granul. Matt.* **14** (4), 531–552.

WHITHAM, G. B. 1974 *Linear and Nonlinear Waves*. John Wiley.

WIEDERSEINER, S., ANDREINI, N., EPELY-CHAUVIN, G. & ANCEY, C. 2011*a* Refractive-index and density matching in concentrated particle suspensions: a review. *Exp. Fluids* **50** (5), 1183–1206.

WIEDERSEINER, S., ANDREINI, N., EPELY-CHAUVIN, G., MOSER, G., MONNEREAU, M., GRAY, J. M. N. T. & ANCEY, C. 2011*b* Experimental investigation into segregating granular flows down chutes. *Phys. Fluids* **23**, 013301.

WIELAND, M., GRAY, J. M. N. T. & HUTTER, K. 1999 Channelised free surface flow of cohesionless granular avalanches in a chute with shallow lateral curvature. *J. Fluid Mech.* **392**, 73–100.

WOODHOUSE, M. J., THORNTON, A. R., JOHNSON, C. G., KOKELAAR, B. P. & GRAY, J. M. N. T. 2012 Segregation-induced fingering instabilities in granular free-surface flows. *J. Fluid Mech.* **709**, 543–580.

YEE, H. C. 1989 A class of high resolution explicit and implicit shock-capturing methods. *Tech Rep.* NASA-TM-101088. NASA Ames Research Center, NASA Ames Research Center; Moffett Field, CA, United States, doc ID: 19890016281.

5. RADIAL MONODISPERSE FINGERING

This chapter describes some preliminary work on granular flow in a conical geometry. A cone set-up was originally designed to produce a rotationally symmetric version of the segregation fingering patterns shown in figure 1.4. However, the initial prototype experiments suggested that the geometry creates interesting patterns with even monodisperse grains. A larger, precise experiment was designed, and some early results are presented here.

5.1 Experiments in a conical geometry

5.1.1 Experimental methodology

A precise, axisymmetric cone of basal radius 446.4 mm, height 244.4 mm and inclination angle $\zeta = 28.6^{\circ}$ was created by gluing concentric PVC rings of decreasing diameter, and tapering the side using a large lathe. The distance from the cone apex to the basal perimeter was 508.4 mm. A metal bar of diameter 20 mm was attached at the apex of the cone to provide support for the cylindrical hopper and gate. A perspex cylinder with an outer diameter of 63 mm diameter and inner diameter of 57 mm was screwed onto the metal bar to create the hopper for the granular material. A slightly larger 79 mm outer diameter cylinder was mounted on the outside of the hopper as a spring loaded release gate. The bottom edge of this cylinder was tapered at the same angle as the cone so that it could sit flush with the surface of the cone. A metal bracket fixed onto the central metal bar controlled the upwards travel distance of the gate, G_t. The height of this bracket could be adjusted in order to set the volume flux Q exiting from the gate. The base of the cone was made rough by fixing a monolayer of particles to the bed in a multi-stage process. Firstly double sided tape was stuck onto the base of the cone. Next, duck-tape (strong fabric tape)

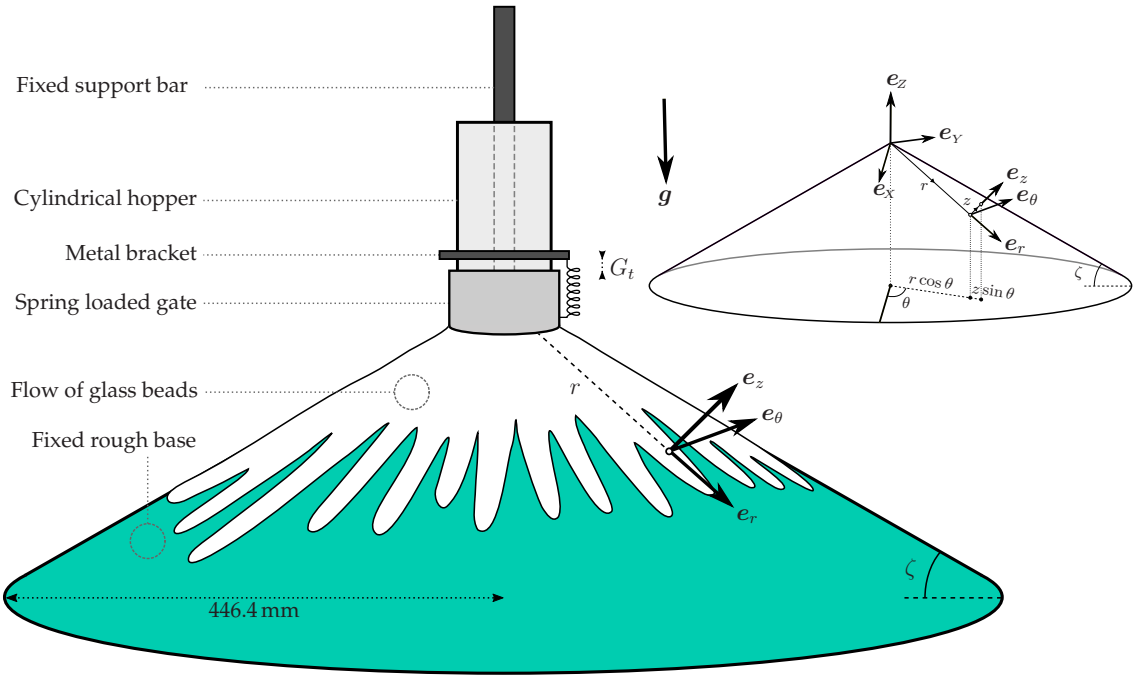

Figure 5.1: Sketch diagram showing the experimental set-up and the conical coordinate system (inset). A solid PVC cone was constructed of basal radius 446.4 mm and inclination angle $\zeta = 28.6^\circ$. A monolayer of 'deco' beads of diameter $750 - 1000\,\mu$m were glued onto the surface of the cone to create a rough frictional base. The cylindrical hopper was mounted on the central bracket, with a spring-loaded gate allowing the $200 - 250\,\mu$m glass beads to flow over the cone. The height of the metal bracket could be adjusted to change the travel of the gate G_t, and hence the initial flux released from the hopper Q. The glass beads spread steadily over the surface of the cone before splitting into a regular pattern of fingers at a critical radius r_{crit}. This flow is best described using the orthogonal conical coordinate system (r, θ, z) shown in the inset, with r the radial distance from the apex of the cone to the point down the length of the cone, θ the axial rotation around the cone, and z the distance normal to the cone surface. The unit basis vectors in this coordinate system are $\{\boldsymbol{e}_r, \boldsymbol{e}_\theta, \boldsymbol{e}_z\}$, with $\boldsymbol{e}_r$ pointing radially down the surface of the cone, $\boldsymbol{e}_\theta$ pointing around the cone at a constant radial distance, and $\boldsymbol{e}_z$ normal to the cone surface. These unit vectors are a series of two rotations (5.1) of a standard Cartesian coordinate system (X, Y, Z) that is fixed at the apex of the cone with unit vectors $\{\boldsymbol{e}_X, \boldsymbol{e}_Y, \boldsymbol{e}_Z\}$. The transformation of Cartesian vector components (X, Y, Z) to conical coordinates is given by (5.5).

Flow material	Grain type	Spherical glass beads
	Grain size	$200 - 250\,\mu\mathrm{m}$, sieved
	Colour	Clear
	Manufacturer	Wheelabrator Plus
	Product name	'Vaquashene'
Basal material	Bead type	Spherical glass beads with thin coloured metal coating
	Bead size	$750 - 1000\,\mu\mathrm{m}$
	Colour	Turquoise
	Manufacturer	Sigmund Lindner GmbH
	Product name	'Deco beads'
Flow parameters	Inclination angle	$\zeta = 28.6°$
	Initial fill volume	$500\,\mathrm{cm}^3$
	Flowing volume fraction[1]	$\nu = 0.55$
Basal friction parameters[2]	Lower flow angle	$\zeta_1 = 23.25°$
	Upper flow angle	$\zeta_2 = 33.69°$
	h_{start} angle parameter	$\zeta_3 = 25.21°$
	Empirical length scale	$\mathscr{L} = 0.50\,\mathrm{mm}$
	Typical grain size	$d = 0.225\,\mathrm{mm}$
	Empirical constant[3]	$\beta = 0.136$
Critical heights	Flow stop height	$h_{stop}(\zeta) = 0.52\,\mathrm{mm}$
	Flow start height	$h_{start}(\zeta) = 1.09\,\mathrm{mm}$

Table A: A summary of the important experimental and modelling parameters that were held constant for the runs listed in table B. Notes: [1]The solids volume fraction of the flowing material ν was assumed to be 0.55. [2]The basal friction parameters were determined by measuring the thickness of the deposit left at different angles $h_{stop}(\zeta)$ and the angle needed for stationary material to be remobilised $\zeta_{start}(h)$. See Pouliquen & Forterre (2002) and Edwards & Gray (2014) for further details. [3]The empirical constant β is taken to be equal to 0.136 for glass beads, regardless of the roughness conditions (Pouliquen, 1999).

was stuck onto the double sided tape, with the sticky side facing upwards. A single layer of $750-1000\,\mu\mathrm{m}$ diameter turquoise 'deco' beads (glass beads with a very thin coloured metal surface manufactured by Sigmund Lindner GmbH) were attached to the sticky tape. Finally, the beads were fixed in place by applying a very thin layer of a water-glue solution to the surface. The glue solution filled in some of the gaps between the beads, and prevented beads from being dislodged after multiple experiments. A sketch of the experimental configuration is shown in figure 5.1, and a summary of the important parameters is provided in table A.

Before each experiment, the travel distance of the gate G_t was set by fixing the metal bracket a distance G_t above the top edge of the gate. The flux Q was measured by filming the decreasing level of the grains in the hopper over time. A scale on the side of the hopper allowed the change in volume to be identified, with the change in time determined from the video. The gate was held down next to the surface of the cone whilst the hopper was filled with $500\,\mathrm{cm}^3$ of $200-250\,\mu\mathrm{m}$ sieved spherical glass beads. Upon releasing the gate, the spring-mechanism would make it quickly move vertically upwards by the preset distance G_t, opening a gap of $G_o = G_t \cos\zeta$ between the basal surface and the bottom tapered edge of the gate. The grains could then flow out of the hopper with constant flux Q. A number of experiments were performed with different fluxes Q, as summarised in table B. The experimental results were seen to be extremely sensitive to the basal friction, and so a vacuum cleaner was used to remove any residual grains from the base after each run. Comments on the sensitivity of the results to the basal friction are made in § 5.1.4.

5.1.2 A radial fingering instability

The typical behaviour of the experiments can be seen in the overhead photographs in figure 5.2: the flow initially spreads radially in a circular manner, before splitting into a series of individual channels. This remarkable fingering pattern is a contrast to flow on a planar chute, where the flow is steady with a constant velocity and uniform height provided the inclination angle is between ζ_1 and ζ_2 and the initial flow height $h > h_{start}$. In addition, Pouliquen & Vallance (1999) showed that the propagating front of such a flow is stable with respect to transverse perturbations, and remains straight as it moves downstream. Figure 5.3(*a*) shows a space-time plot

Run Number	Flux ($cm^3\ s^{-1}$)	Critical Radius r_{crit} (mm)	No. Fingers	Marker
26	12.97	126.8 ± 15	43	○
27	13.20	147.0 ± 15	44	×
30	11.93	156.4 ± 10	44	□
31	12.55	158.7 ± 15	46	◇
32	11.38	147.4 ± 10	41	△
33	11.83	146.0 ± 10	42	▽
34	18.05	190.0 ± 10	52	☆
35	18.41	194.8 ± 10	51	○
36	19.22	191.0 ± 10	52	×
37	19.68	187.5 ± 10	50	□
38	14.93	178.3 ± 15	47	◇
39	15.17	177.7 ± 10	50	△
41	15.14	179.0 ± 10	49	☆
42	16.41	192.2 ± 10	49	○
43	15.78	159.7 ± 10	40	×
44	20.84	195.0 ± 15	47	□
45	21.32	201.2 ± 10	52	◇
46	20.38	196.2 ± 15	49	△
47	32.11	241.5 ± 10	61	▽
48	34.67	259.0 ± 10	62	☆
49	34.83	254.0 ± 10	64	○
50	22.69	209.2 ± 10	56	×
51	24.56	232.8 ± 10	58	□
52	23.48	222.4 ± 10	56	◇
59	31.98	280.0 ± 25	66	▽
60	32.82	268.8 ± 15	63	☆
61	31.30	285.6 ± 10	62	○
63	27.58	223.8 ± 15	58	×
64	28.10	245.0 ± 10	59	□
66	35.16	272.5 ± 10	69	◇
67	34.83	280.8 ± 15	69	△
68	34.67	284.8 ± 10	64	▽
69	34.83	281.7 ± 10	64	☆

Table B: A list of the runs using monodisperse grains that are plotted in figures 5.8, 5.10 and 5.11.

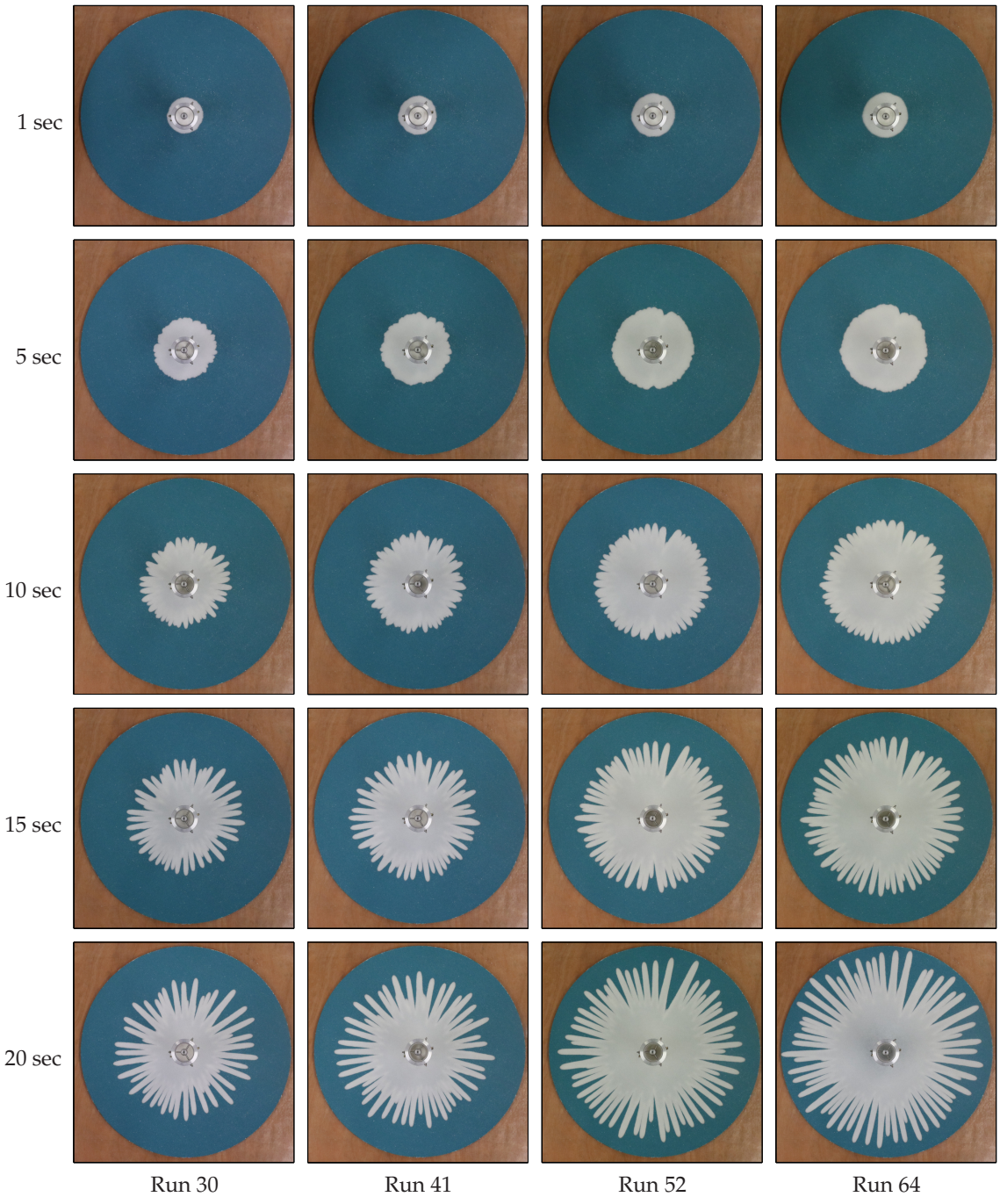

Figure 5.2: A series of overhead photographs showing how the flow evolves after it exits from the gate. Photographs are shown at 1, 5, 10, 15 and 20 seconds after the gate was released, for runs 30, 41, 52 and 64 from table B. Photographs from top to bottom are in order of increasing time, whilst those from left to right are from experiments with increasing flux. As would be expected, the runs with larger fluxes spread further in a given time. Contour plots showing the temporal evolution of the propagating front are shown in figures 5.4–5.7 for these runs.

for a planar chute that was constructed by taking the middle column of pixels from a series of overhead pictures taken at 100 frames per second, and laying them side-by-side to give the downstream $x - x_0$ with time t. Distance x_0 is the downstream distance at the top of picture. The light coloured area to the right of the picture is the granular material, with the straight leading edge between the light and dark regions indicating that the front propagates downstream at a constant speed of 0.148 m/s. The chute was inclined at $\zeta = 28.6°$, the same inclination angle as the cone, and the gate opening height was $G_o = 2.63\,\mathrm{mm}$. The equivalent space-time plot for the cone, with the same gate opening height, is shown in figure 5.3(*b*). The front initially starts from the gate at $r = r_0$ at 0.148 m/s, which is shown with the dashed black line. However, the curved profile shows that the front slows as it moves downstream. This observation that the granular flow slows as it spreads radially is similar to the radial spreading of other liquids, for example the axisymmetric spreading of gravity-currents (e.g. Huppert & Simpson, 1980; Huppert, 1982; Takagi & Huppert, 2010).

The temporal evolution can be seen in further detail in contour plots of the propagating front presented in figures 5.4–5.7. The front of the flow in each photograph was found by contouring the red channel of the image, and contours were plotted at 0.5 second intervals for the first 20 seconds after the gate was released. The contours initially have a circular shape as the granular material spreads radially, and progressively become closer together as the flow slows down. It can also be seen that the circular shaped contours of the radial spreading regime become subject to small axial perturbations long before the flow is seen to develop a pronounced fingering pattern. These small perturbations could be due to inhomogeneities in the bed, with small gaps between the fixed beads causing small perturbations to the flow height. The small perturbations could also be due to inhomogeneity in the filling of the hopper and the subsequent release. The role of these perturbations on the fingering pattern will be discussed further in § 5.3.3. Other observations that can be taken from these contour plots are that: 1) The contours are further apart for later runs that have higher fluxes, showing that the front velocity increases with the initial flux; 2) The fingering pattern develops at larger radii for higher fluxes.

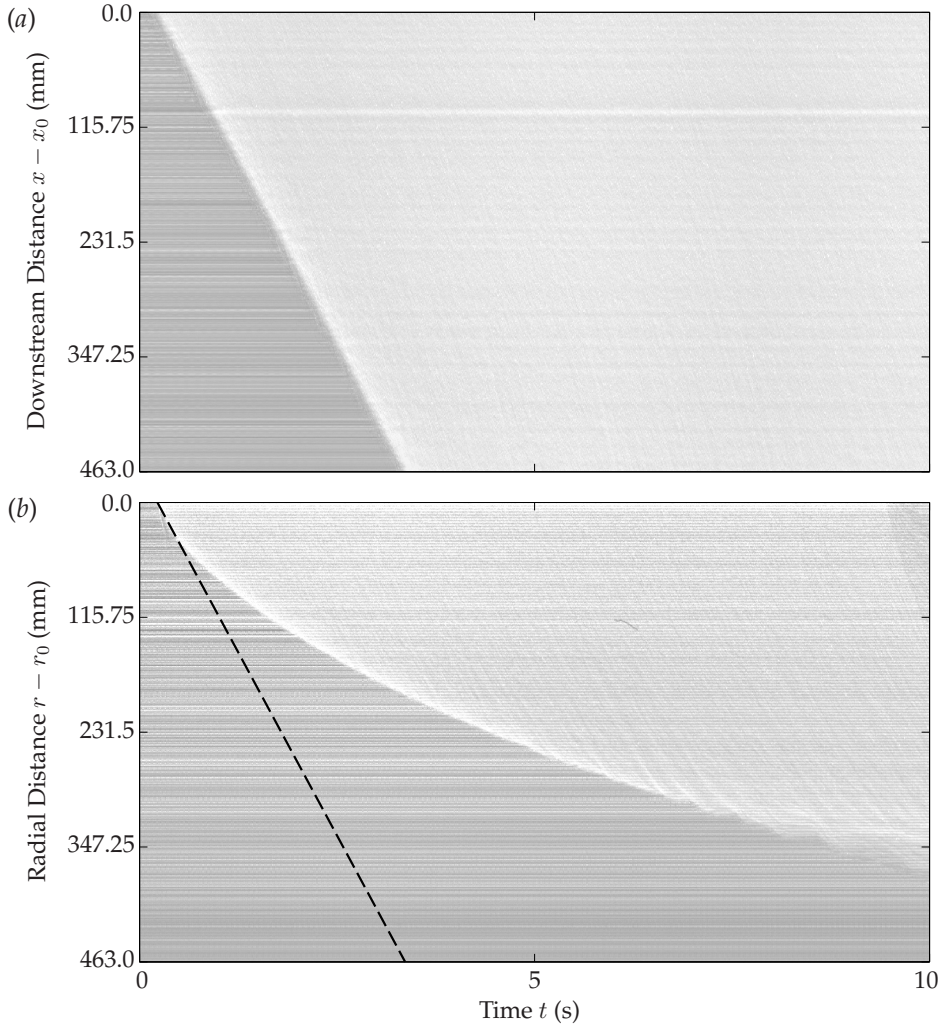

Figure 5.3: Space-time plots showing the propagation of the flow front over time. Each plot is constructed by taking the middle column of pixels from a series of overhead pictures and laying them size-by-side to give the downstream position ($x - x_0$ and $r - r_0$ for the planar chute and cone, respectively) as a function of time t. Constant x_0 corresponds to an arbitrary downstream distance, whilst r_0 is the radius at which the flow exits the cylindrical hopper. Horizontal lines indicate stationary grains. (*a*) For a planar chute, inclined at an angle $\zeta = 28.6°$ with an initial gate opening height of $G_o = 2.63\,\mathrm{mm}$, the diagonal line indicates that the front propagates at a steady speed of 0.148 m/s. (*b*) In the conical geometry, the front initially starts at propagating at the same speed as the chute. The constant speed of 0.148 m/s is shown by the diagonal dashed black line. However, as the front moves radially downstream, it slows down as a result of the radial spreading. The gate opening for the cone was also $G_o = 2.63\,\mathrm{mm}$.

This latter observation will be analysed in further detail in the following section by examining the onset of the fingering instability.

5.1.3 The onset of the fingering instability

The onset of the fingering instability can be analysed by comparing the outermost edge of the flow with a circular front. The same procedure as figures 5.4–5.7 was used to find the edge of the flow, namely a single contour was found in the red channel of the image. A circle was fitted to this edge, and the perimeter of the fitted circle was compared to the actual perimeter of flow front. As shown in figure 5.8(*a*) for run 64, the ratio of the actual perimeter to the fitted circle perimeter is initially constant in region I as the flow spreads radially. This constant ratio is shown with the grey horizontal dashed line. After the onset of the fingering instability in region II, the development of individual channels causes the actual flow perimeter to be much larger than the fitted circle perimeter. The ratio diverges away from the constant value, with the increasing perimeter causing the ratio to increase as the flow advances. The transition between the two regions occurs at a critical radius r_{crit}, which is shown with the solid black marker. The critical radius is identified as the first point at which the ratio diverges away from the constant value, with the error shown with the vertical black dotted lines. The dynamics for all of the runs in table B are plotted in figure 5.8(*b*), and share the same typical behaviour as in (*a*): All of the runs display an initial constant ratio between the flow front perimeter and the fitted circle perimeter, before the ratio diverges after the flow has fingered and developed channels.

One might expect the constant ratio to be close to unity, however a simple scaling argument is able give an approximation for the ratio. As sketched in figure 5.9, the discrete nature of grains at the edge of the flow would increase the observed perimeter. The number of grains of diameter d that can fit around a circle of radius r is $N = 2\pi r/d$. Each of these grains contributes a semi circular length of $\pi d/2$, and so the total perimeter length is $N\pi d/2 = \pi^2 r$. Dividing this by the perimeter of a fitted circle $2\pi r$ gives a ratio of $\pi/2 \approx 1.6$, which is very close to that observed in figure 5.8. Whilst this could be a plausible explanation for the ratio lying in the range $(1.5, 2)$, the extra perimeter length provided by individual grains may not be

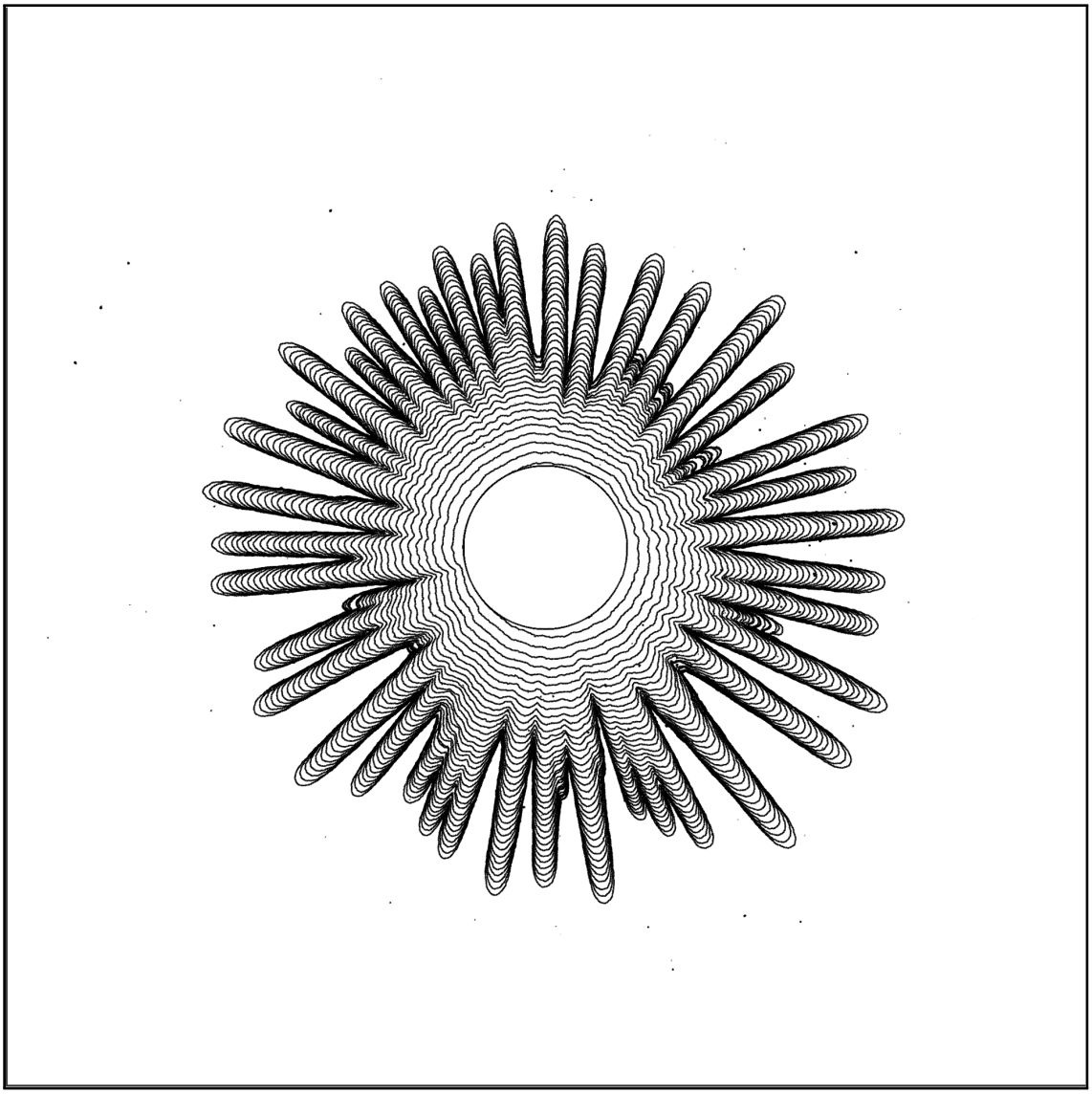

Figure 5.4: The temporal evolution can be visualised by plotting the outer most edge of the flow at specific time intervals. The first 20 seconds of the evolution of run 30 are shown; the inner most contour is 0.5 sec after the gate has been released, and all subsequent contours follow at 0.5 sec intervals. The edges of the flow were found by contouring the red-channel of the photographs. Similar contour plots for runs 41, 52 and 64 can be seen in figures 5.5, 5.6 and 5.7 respectively.

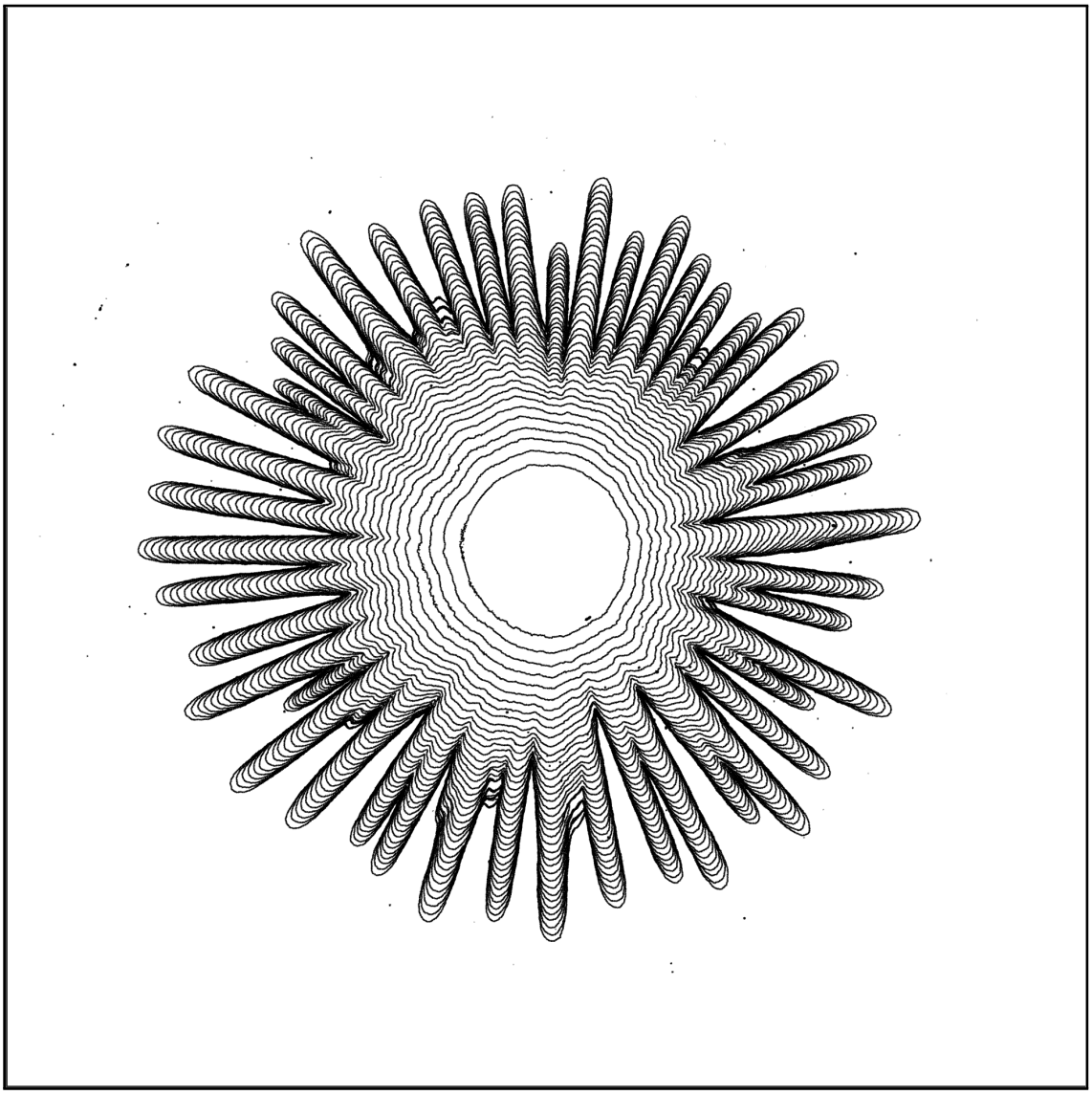

Figure 5.5: Temporal evolution contours for the first 20 seconds of run 41. The inner most contour is 0.8 sec after the gate has been released, and all subsequent contours follow at 0.5 sec intervals. Similar contour plots for runs 30, 52 and 64 can be seen in figures 5.4, 5.6 and 5.7 respectively.

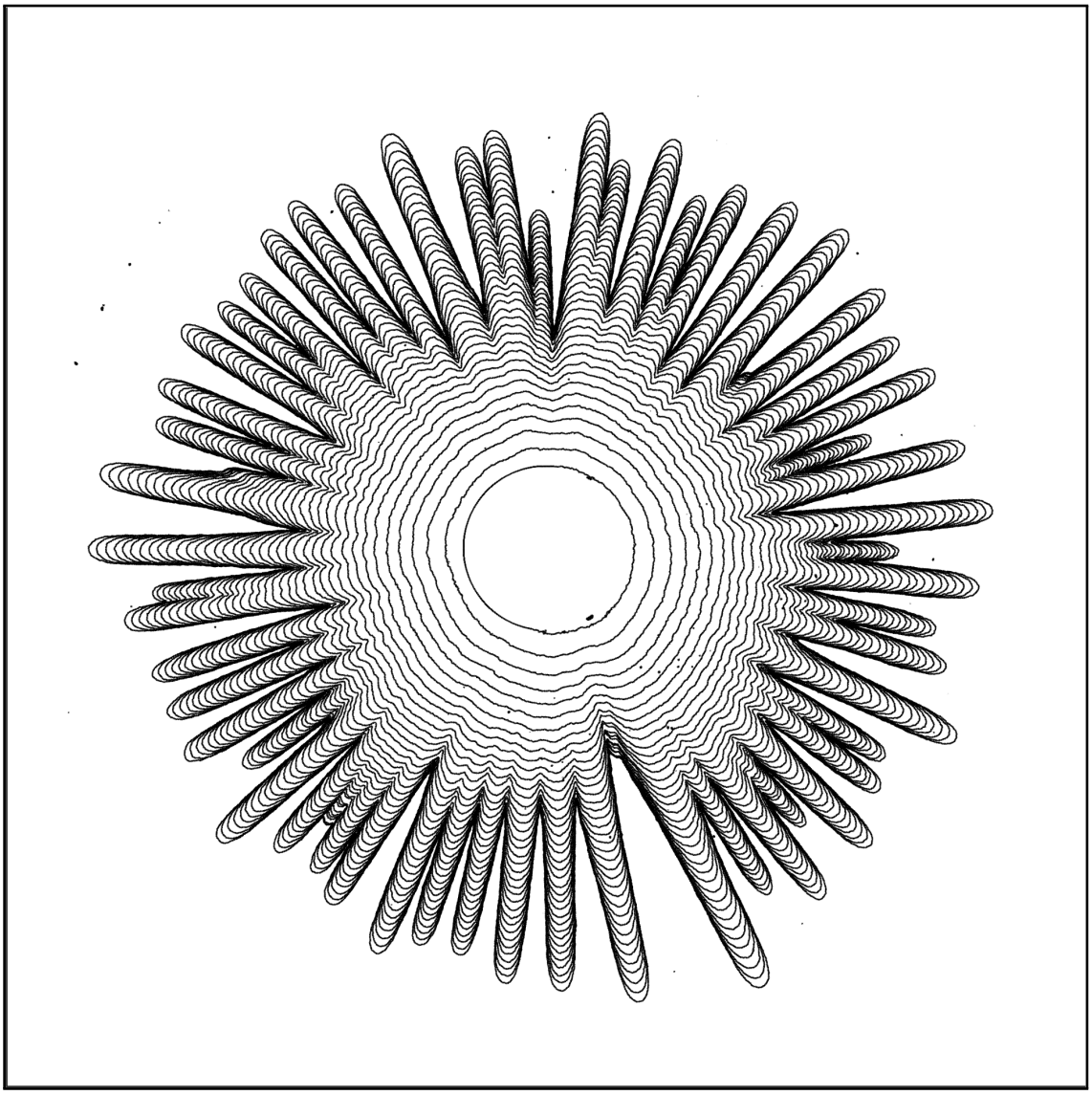

Figure 5.6: Temporal evolution contours for the first 20 seconds of run 52. The inner most contour is 0.5 sec after the gate has been released, and all subsequent contours follow at 0.5 sec intervals. Similar contour plots for runs 30, 41 and 64 can be seen in figures 5.4, 5.5 and 5.7 respectively.

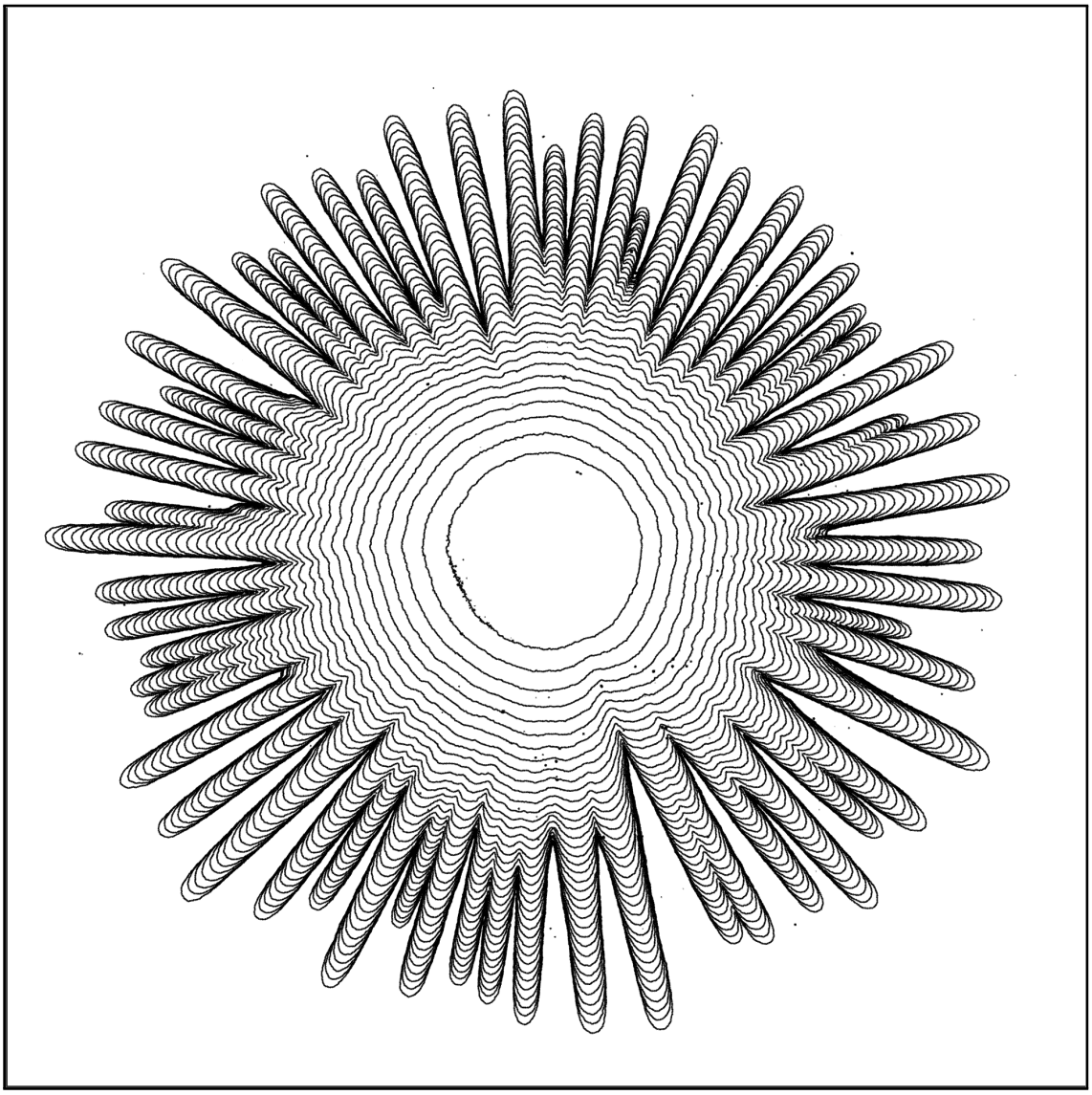

Figure 5.7: Temporal evolution contours for the first 20 seconds of run 64. The inner most contour is 0.8 sec after the gate has been released, and all subsequent contours follow at 0.5 sec intervals. Similar contour plots for runs 30, 41 and 52 can be seen in figures 5.4, 5.5 and 5.6 respectively.

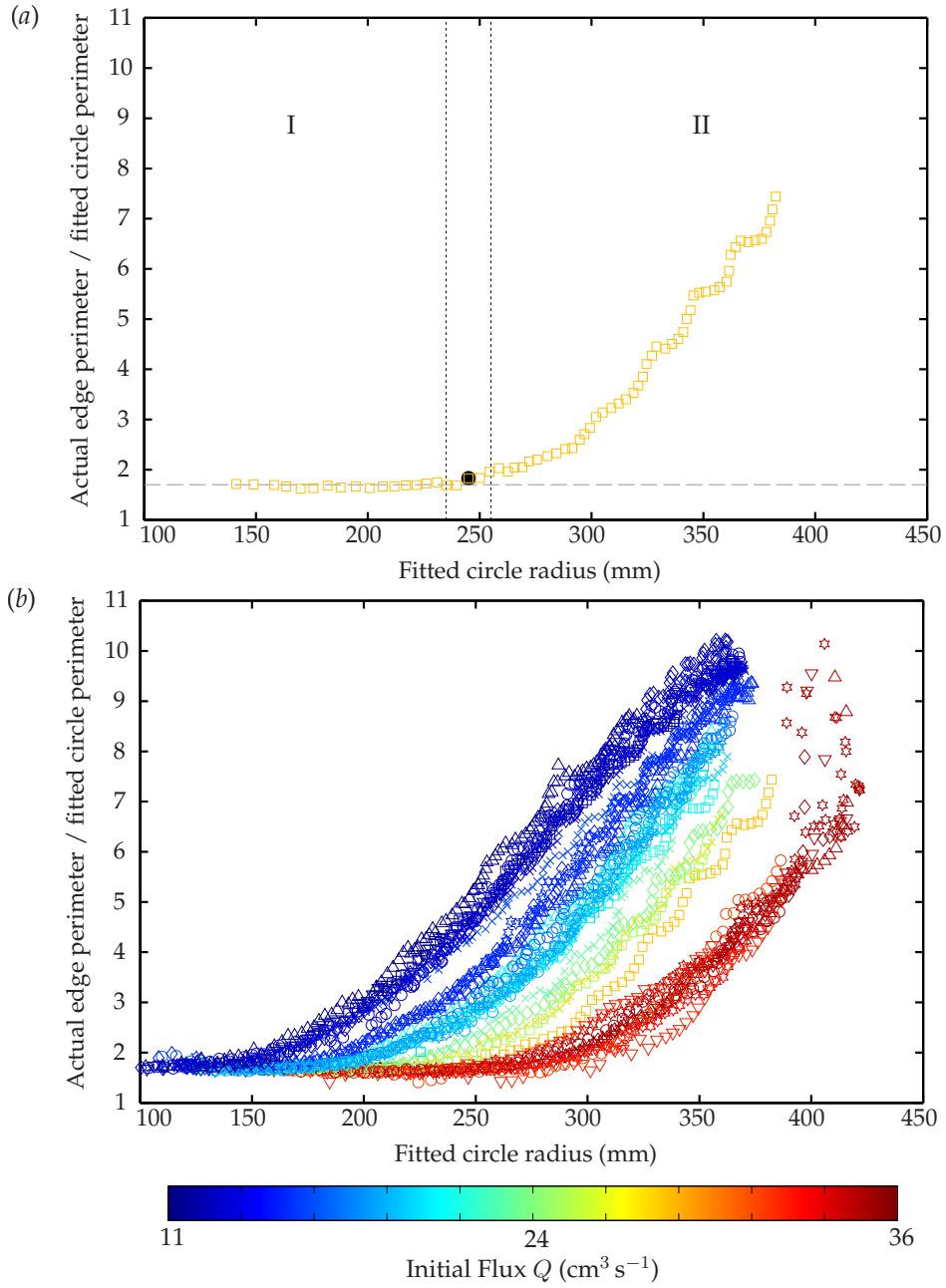

Figure 5.8: The fingering dynamics can be analysed by fitting a circle to the edge of the flow, and examining the ratio of the flow edge perimeter to the fitted circle perimeter. (*a*) The flow dynamics for run 64 illustrate the general behaviour. The ratio of the actual flow perimeter to the fitted circle perimeter is constant in region I where the flow spreads radially. However, the ratio diverges in region II when the flow fingers, with the perimeter increasing due to the development of individual channels. The transition between the two regions occurs at a critical radius r_{crit}. This is shown with a solid black marker, and the error in identifying r_{crit} is shown with the vertical dotted lines. (*b*) Each of the runs in table B is plotted with the markers coloured by the flux value of that run. It can be seen that all the runs initially display a constant ratio where the flow spreads radially, before the ratio diverges when the flow fingers and splits into channels. As the flux increases, it can be seen that the critical radius r_{crit} also increases.

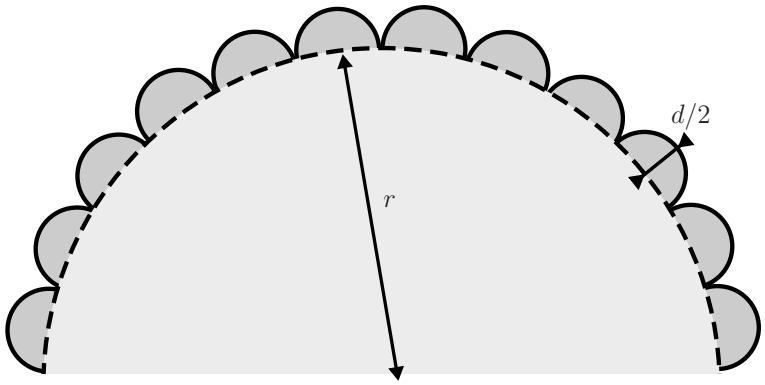

Figure 5.9: A sketch showing how edge length of discrete grains (of diameter d) may increase the perimeter length above that of a circle circumference (of radius r). The perimeter length is shown with a solid black line, and a typical circle perimeter is shown with a dashed line. The ratio of the perimeter length to the fitted circle length would be $\pi/2 \approx 1.6$, and independent of the radius r. This is very close to the constant ratio seen in figure 5.8.

detectable from the overhead images. Tests also showed that different circle fitting algorithms gave different constant ratio values. Thus, the depature away from a unit ratio could be from the combined errors of the edge detection and circle fitting algorithms. The circle fitting is also more accurate for larger radii, and hence, for some runs, there is a slight decrease in the ratio in region I once the radius is greater than 200 mm. It can be seen that the transition from region I to region II occurs at larger radii for higher fluxes; this suggests an increasing relationship between r_{crit} and the flux Q. This relationship can clearly be seen in figure 5.10, where the critical radius r_{crit} is plotted against the flux Q for each run. The data are strongly indicative of a linear relationship, with the least squares regression fit $r_{crit} = kQ + e$ giving the dimensional constants $k = 5.49\,\mathrm{cm^{-2}\,s}$ and $e = 86\,\mathrm{mm}$. This quantifies the previous observation that as the flux increases, the flow spreads further before fingering and splitting into channels.

5.1.4 The number of fingers and the finger width

Figure 5.11 is a plot of the number of fingers against the initial flux Q, for all of the runs in table B. There appears to be a linear relationship, with a least squares regression fit giving a gradient of $9.7 \times 10^5\,\mathrm{m^{-3}}\,s$ and an offset $+31.8$. For each of the runs in table B, the images did not have a high enough pixel resolution to accurately determine the finger width. However, the width was physically measured in a set

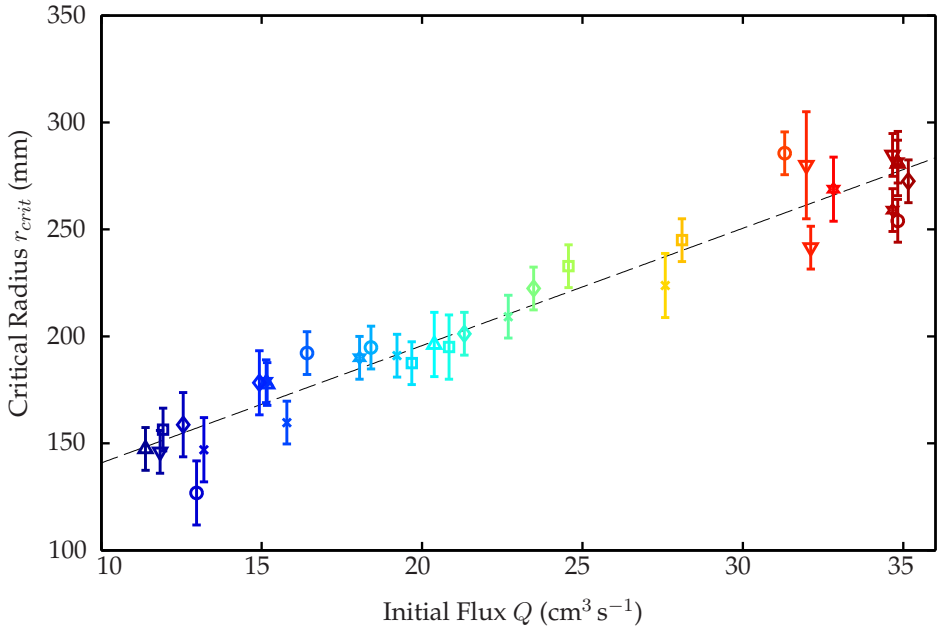

Figure 5.10: The initial flux Q has a linear relationship with the critical radius r_{crit}. The dashed black line is the least squares regression fit $r_{crit} = kQ + e$, where $k = 5.49\,\mathrm{cm}^{-2}\,\mathrm{s}$ and $e = 86\,\mathrm{mm}$. Each of the runs from table B have the same colours and markers as in figure 5.8.

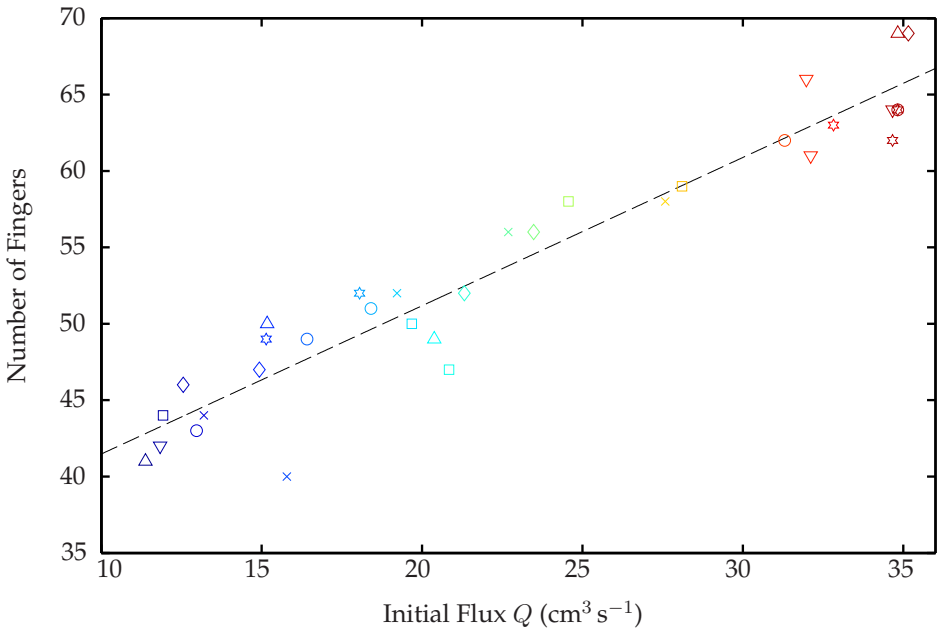

Figure 5.11: The number of fingers appears to scale linearly with the initial flux Q. The dashed black line is the least squares regression fit with gradient $9.7 \times 10^5\,\mathrm{m}^{-3}\,s$ and offset $+31.8$. Each of the runs from table B have the same colours and markers as in figure 5.8.

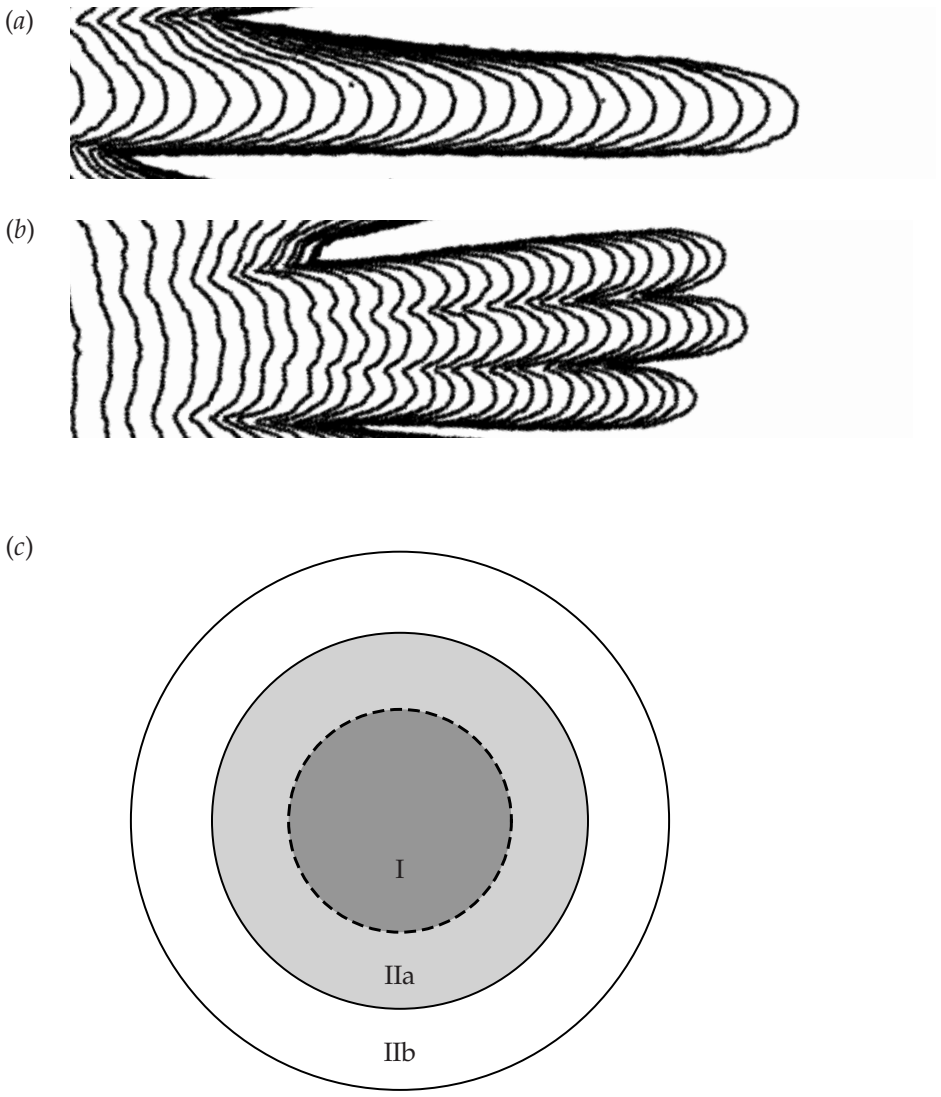

Figure 5.12: Individual channels have a series of mechanisms for readjusting the width once an initial channel is formed. (*a*) A channel may itself narrow, or (*b*) it could split again to form several new channels with smaller widths. Both of these examples are taken from the contour plot of run 64 in figure 5.7. Overall, the flow may thus behave something like the sketch shown in (*c*). The flow initially spreads in an axisymmetric manner in region I, before becoming unstable at the thick dashed line. Once an initial channel has been formed, the channels transition and re-adjust in region IIa until they find their stable width. In region IIb, the flow remains in its stable channels. Regions IIa and IIb are indistinguishable from each other when examining the ratio of actual perimeter to fitted perimeter in figure 5.8(*a*).

Run Number	Flux ($cm^3\,s^{-1}$)	No. Developed Channels	Mean Finger Width (mm)	Standard Deviation (mm)
5	15.28	62	19.0	3.06
6	15.39	62	17.8	3.67
7	14.97	61	18.6	2.10
8	23.16	55	17.3	4.77
9	23.65	57	17.2	4.52
10	23.65	49	18.3	4.46
11	24.17	45	17.8	4.88
12	12.85	55	17.6	1.93
13	12.74	55	18.4	2.52
14	12.60	55	17.9	3.20
23	7.12	49	17.2	1.48
24	7.21	48	17.4	1.75

Table C: A list of runs used to measure the finger width of developed channels.

of earlier runs directly on the cone surface. In order to get a consistent measurement of the channel width, the measurement was taken at the edge of the cone for any developed channels than flowed over the edge. Any finger that stopped on the cone was not measured. The results are summarised in table C and appear to show that the finger width has a constant value $\sim 18\,\mathrm{mm}$. Note that the number of developed channels is recorded in C, as opposed to the total number of fingers in B. Further work is required to see whether these channels widths are stable, or whether they gradually widen (or narrow) in time (Félix & Thomas, 2004; Deboeuf *et al.*, 2006; Takagi *et al.*, 2011).

It was observed that the finger width and the number of fingers were sensitive to the basal friction. In a few runs where residual grains were left on the cone surface, the number of fingers was observed to (marginally) increase. Residual grains would decrease the basal friction, suggesting that the number of fingers increases with lower basal friction. These runs also had a greater variability in the finger width, but this may be due to presence/absence of residual grains at different points on the surface. Further work is needed to quantify the sensitivity to the basal friction; however, changing the fixed particle base on the cone is not a trivial undertaking!

Due to the low pixel resolution of the images, further work is needed to accurately determine the wavelength of the initial instability, possibly using a modulated inflow (Malloggi *et al.*, 2006). However, there appears to be a non-trivial

relationship between the initial instability wavelength and the width of a stable developed channel. As can be seen in the contour plots in figures 5.4–5.7, individual channels have a series of mechanisms for re-adjusting the width once an initial channel has been formed. Two examples from the contour plots of run 64 are shown in figures 5.12(*a*,*b*), where it can be seen that a channel may narrow (*a*), or it may split again to form a number of smaller channels (*b*). This suggests that the overall flow may behave like the sketch in figure 5.12(*c*). The flow initially spreads in an axisymmetric manner in region I, before becoming unstable and fingering at the thick dashed line. The channels then undergo a series of adjustments in region IIa to find their stable width, before flowing steadily down the stable developed channels in region IIb. The two latter regions are indistinguishable from each other in region II described in figure 5.8(*a*), and hence they are labelled as IIa and IIb. Analysing these re-adjustment mechanisms using a high speed camera could potentially uncover new secrets about the ability of granular systems to naturally form patterns (Aranson & Tsimring, 2008).

5.2 Modelling granular flow in a conical geometry

Dense granular flows can be mathematically described using continuum mass and momentum equations with a $\mu(I)$-rheology. It is, therefore, necessary to transfer the vector equations (1.1)–(1.2) to an appropriate coordinate system for the conical geometry. Readers who are familiar with conical curvilinear coordinate systems may skip direct to § 5.3.

5.2.1 An orthogonal conical coordinate system

The flow in this geometry is best described using a conical coordinate system (r, θ, z), in which r is the radial distance from the apex of the cone to the point measured down the inclined slope of the cone, θ is the axial rotation around the cone, and z is the vertical height normal to the cone surface. As shown in figure 5.1, the orthogonal unit basis vectors in this coordinate system are $\{\boldsymbol{e}_r, \boldsymbol{e}_\theta, \boldsymbol{e}_z\}$. These are an adaptation of standard cylindrical polars but with $\boldsymbol{e}_r$ pointing radially down the surface

of the cone, $\boldsymbol{e}_\theta$ pointing around the cone at a constant radial distance, and $\boldsymbol{e}_z$ pointing normally to the cone surface. For a comprehensive explanation of orthogonal curvilinear coordinate systems, the reader is referred to the texts by Happel & Brenner (1965) or Ruban & Gajjar (2014). The conical unit vectors may be transformed from the unit basis vectors $\{\boldsymbol{e}_X, \boldsymbol{e}_Y, \boldsymbol{e}_Z\}$ of a Cartesian coordinate system (X, Y, Z) fixed at the apex of the cone through a series of two rotations: 1) A rotation of the Cartesian unit vectors through an angle of θ about the Z plane, followed by; 2) a rotation through the constant angle ζ about the Y plane. The entire transformation may be expressed using rotation matrices,

$$\begin{pmatrix} \boldsymbol{e}_r \\ \boldsymbol{e}_\theta \\ \boldsymbol{e}_z \end{pmatrix} = \begin{pmatrix} \cos\zeta & 0 & -\sin\zeta \\ 0 & 1 & 0 \\ \sin\zeta & 0 & \cos\zeta \end{pmatrix} \begin{pmatrix} \cos\theta & \sin\theta & 0 \\ -\sin\theta & \cos\theta & 0 \\ 0 & 0 & 1 \end{pmatrix} \begin{pmatrix} \boldsymbol{e}_X \\ \boldsymbol{e}_Y \\ \boldsymbol{e}_Z \end{pmatrix}, \tag{5.1}$$

which quickly allows the conical basis vectors to be given in terms of Cartesian basis vectors,

$$\boldsymbol{e}_r = +\cos\zeta\cos\theta\,\boldsymbol{e}_X + \cos\zeta\sin\theta\,\boldsymbol{e}_Y - \sin\zeta\,\boldsymbol{e}_Z, \tag{5.2a}$$

$$\boldsymbol{e}_\theta = -\sin\theta\,\boldsymbol{e}_X + \cos\theta\,\boldsymbol{e}_Y \tag{5.2b}$$

$$\boldsymbol{e}_z = +\sin\zeta\cos\theta\,\boldsymbol{e}_X + \sin\zeta\sin\theta\,\boldsymbol{e}_Y + \cos\zeta\,\boldsymbol{e}_Z, \tag{5.2c}$$

and the Cartesian basis vectors to be given in terms of the conical basis vectors

$$\boldsymbol{e}_X = +\cos\zeta\cos\theta\,\boldsymbol{e}_r - \sin\theta\,\boldsymbol{e}_\theta + \sin\zeta\cos\theta\,\boldsymbol{e}_z, \tag{5.3a}$$

$$\boldsymbol{e}_Y = +\cos\zeta\sin\theta\,\boldsymbol{e}_r + \cos\theta\,\boldsymbol{e}_\theta + \sin\zeta\sin\theta\,\boldsymbol{e}_z, \tag{5.3b}$$

$$\boldsymbol{e}_Z = -\sin\zeta\,\boldsymbol{e}_r + \cos\zeta\,\boldsymbol{e}_z. \tag{5.3c}$$

Since the slope inclination ζ is fixed, it can be seen that the only non-zero derivatives of the conical basis vectors are

$$\frac{\partial \boldsymbol{e}_r}{\partial\theta} = \cos\zeta\,\boldsymbol{e}_\theta, \qquad \frac{\partial \boldsymbol{e}_\theta}{\partial\theta} = -\cos\zeta\,\boldsymbol{e}_r - \sin\zeta\,\boldsymbol{e}_z, \qquad \frac{\partial \boldsymbol{e}_z}{\partial\theta} = \sin\zeta\,\boldsymbol{e}_\theta. \tag{5.4a–c}$$

For every point in space $\boldsymbol{r} = \boldsymbol{r}(X, Y, Z) = \boldsymbol{r}(r, \theta, z)$, the Cartesian (X, Y, Z) position vector components are related to (r, θ, z) by

$$X = (r\cos\zeta + z\sin\zeta)\cos\theta, \tag{5.5a}$$

$$Y = (r\cos\zeta + z\sin\zeta)\sin\theta, \tag{5.5b}$$

$$Z = -r\sin\zeta + z\cos\zeta, \tag{5.5c}$$

where $r\cos\zeta + z\sin\zeta$ is the projection of the point onto the plane at the base of the cone, and θ is the rotation from the X-axis. Calculating the partial derivatives $\partial\boldsymbol{r}/\partial r$, $\partial\boldsymbol{r}/\partial\theta$ and $\partial\boldsymbol{r}/\partial z$ from (5.5) gives the scale factors

$$\hat{h}_r = 1, \qquad \hat{h}_\theta = \mathcal{M} = r\cos\zeta + z\sin\zeta, \qquad \hat{h}_z = 1, \tag{5.6a–c}$$

and the conical basis vectors (5.2). The scale factors in (5.6) resemble those of cylindrical polars, with the adaptation $r\cos\zeta + z\sin\zeta$ due to the slope. Any vector, for example the velocity $\boldsymbol{u}$, can be expressed in conical coordinates with components (u_r, u_θ, u_z)

$$\boldsymbol{u} = u_r\boldsymbol{e}_r + u_\theta\boldsymbol{e}_\theta + u_z\boldsymbol{e}_z. \tag{5.7}$$

5.2.2 Vector operators

Using the scale factors (5.6), the differential operator ∇ in conical coordinates is given by

$$\nabla = \boldsymbol{e}_r\frac{\partial}{\partial r} + \frac{1}{\mathcal{M}}\boldsymbol{e}_\theta\frac{\partial}{\partial\theta} + \boldsymbol{e}_z\frac{\partial}{\partial z}. \tag{5.8}$$

The gradient of a scalar field, say the pressure p, is thus given by

$$\nabla p = \boldsymbol{e}_r\frac{\partial p}{\partial r} + \frac{1}{\mathcal{M}}\boldsymbol{e}_\theta\frac{\partial p}{\partial\theta} + \boldsymbol{e}_z\frac{\partial p}{\partial z}. \tag{5.9}$$

Taking the vector dot product of operator (5.8) with $\boldsymbol{u}$ (5.7), and utilising the basis vector derivatives (5.4) and orthogonality, implies that the divergence of $\boldsymbol{u}$ is given by

$$\nabla\cdot\boldsymbol{u} = \frac{\partial u_r}{\partial r} + \frac{1}{\mathcal{M}}\frac{\partial u_\theta}{\partial\theta} + \frac{u_r\cos\zeta}{\mathcal{M}} + \frac{u_z\sin\zeta}{\mathcal{M}} + \frac{\partial u_z}{\partial z}. \tag{5.10}$$

Similarly, the vector gradient dyadic $\nabla\boldsymbol{u}$ can be shown from first principles to be

$$\nabla\boldsymbol{u} = \left(\boldsymbol{e}_r\frac{\partial}{\partial r} + \frac{1}{\mathcal{M}}\boldsymbol{e}_\theta\frac{\partial}{\partial\theta} + \boldsymbol{e}_z\frac{\partial}{\partial z}\right)\left(u_r\boldsymbol{e}_r + u_\theta\boldsymbol{e}_\theta + u_z\boldsymbol{e}_z\right), \tag{5.11}$$

$$= d_{ij}\boldsymbol{e}_i\boldsymbol{e}_j \qquad (i,j = r,\theta,z) \tag{5.12}$$

where the indices i, j are summed over r, θ, z. Note that the expression $\boldsymbol{ab}$ is the second order tensor that results from the dyadic product of vectors $\boldsymbol{a}$ and $\boldsymbol{b}$. The

coefficients d_{ij} are given by

$$\left.\begin{aligned} d_{rr} &= \frac{\partial u_r}{\partial r}, \qquad d_{r\theta} = \frac{\partial u_\theta}{\partial r}, \qquad d_{rz} = \frac{\partial u_z}{\partial r}, \\ d_{\theta r} &= \frac{1}{\mathcal{M}}\frac{\partial u_r}{\partial \theta} - \frac{u_\theta \cos\zeta}{\mathcal{M}}, \\ d_{\theta\theta} &= \frac{1}{\mathcal{M}}\frac{\partial u_\theta}{\partial \theta} + \frac{u_r \cos\zeta}{\mathcal{M}} + \frac{u_z \sin\zeta}{\mathcal{M}}, \\ d_{\theta z} &= \frac{1}{\mathcal{M}}\frac{\partial u_z}{\partial \theta} - \frac{u_\theta \sin\zeta}{\mathcal{M}} \\ d_{zr} &= \frac{\partial u_r}{\partial z}, \qquad d_{z\theta} = \frac{\partial u_\theta}{\partial z}, \qquad d_{zz} = \frac{\partial u_z}{\partial z}. \end{aligned}\right\} \tag{5.13}$$

Equations (5.7), (5.12) and (5.13) may be combined to give

$$\begin{aligned} \boldsymbol{u}\cdot\nabla\boldsymbol{u} \quad = \quad & \boldsymbol{e}_r\left(u_r\frac{\partial u_r}{\partial r} + \frac{u_\theta}{\mathcal{M}}\frac{\partial u_r}{\partial \theta} - \frac{u_\theta^2\cos\zeta}{\mathcal{M}} + u_z\frac{\partial u_r}{\partial z}\right) \\ & + \boldsymbol{e}_\theta\left(u_r\frac{\partial u_\theta}{\partial r} + \frac{u_\theta}{\mathcal{M}}\frac{\partial u_\theta}{\partial \theta} + \frac{u_\theta u_r\cos\zeta}{\mathcal{M}} + \frac{u_\theta u_z\sin\zeta}{\mathcal{M}} + u_z\frac{\partial u_\theta}{\partial z}\right) \\ & + \boldsymbol{e}_z\left(u_r\frac{\partial u_z}{\partial r} + \frac{u_\theta}{\mathcal{M}}\frac{\partial u_z}{\partial \theta} - \frac{u_\theta^2\sin\zeta}{\mathcal{M}} + u_z\frac{\partial u_z}{\partial z}\right). \end{aligned} \tag{5.14}$$

Finally, following Happel & Brenner (1965), the divergence of a dyadic $\mathbf{S} = S_{ij}\boldsymbol{e}_i\boldsymbol{e}_j$ (in which i, j are summed over r, θ, z) may be derived as

$$\begin{aligned} \nabla\cdot\mathbf{S} \quad = \quad & \boldsymbol{e}_r\left(\frac{1}{\mathcal{M}}\left\{\frac{\partial}{\partial r}(S_{rr}\mathcal{M}) + \frac{\partial}{\partial\theta}S_{\theta r} + \frac{\partial}{\partial z}(S_{zr}\mathcal{M})\right\} - \frac{S_{\theta\theta}\cos\zeta}{\mathcal{M}}\right) \\ & + \boldsymbol{e}_\theta\left(\frac{1}{\mathcal{M}}\left\{\frac{\partial}{\partial r}(S_{r\theta}\mathcal{M}) + \frac{\partial}{\partial\theta}S_{\theta\theta} + \frac{\partial}{\partial z}(S_{z\theta}\mathcal{M})\right\}\right. \\ & \qquad \left. + \frac{S_{\theta r}\cos\zeta}{\mathcal{M}} + \frac{S_{\theta z}\sin\zeta}{\mathcal{M}}\right) \\ & + \boldsymbol{e}_z\left(\frac{1}{\mathcal{M}}\left\{\frac{\partial}{\partial r}(S_{rz}\mathcal{M}) + \frac{\partial}{\partial\theta}S_{\theta z} + \frac{\partial}{\partial z}(S_{zz}\mathcal{M})\right\} - \frac{S_{\theta\theta}\sin\zeta}{\mathcal{M}}\right). \end{aligned} \tag{5.15}$$

5.2.3 Governing equations

The dense granular flow is described by the mass and momentum conservation equations (1.1) and (1.2). Assuming that the density ρ is constant means that (1.1) reduces to a divergence free velocity field, $\nabla\cdot\boldsymbol{u} = 0$. Thus, equation (5.10) implies that

$$0 = \frac{\partial u_r}{\partial r} + \frac{1}{\mathcal{M}}\frac{\partial u_\theta}{\partial\theta} + \frac{u_r\cos\zeta}{\mathcal{M}} + \frac{u_z\sin\zeta}{\mathcal{M}} + \frac{\partial u_z}{\partial z}. \tag{5.16}$$

Consequentially, $\boldsymbol{u}\cdot\nabla\boldsymbol{u}$ may be written in conservative form as

$$\begin{aligned}\nabla\cdot(\boldsymbol{u}\otimes\boldsymbol{u}) = {} & \boldsymbol{e}_r\left(\frac{1}{\mathcal{M}}\frac{\partial}{\partial r}(u_r^2\mathcal{M}) + \frac{1}{\mathcal{M}}\frac{\partial(u_ru_\theta)}{\partial\theta} + \frac{1}{\mathcal{M}}\frac{\partial(u_ru_z\mathcal{M})}{\partial z} - \frac{u_\theta^2\cos\zeta}{\mathcal{M}}\right)\\ & + \boldsymbol{e}_\theta\left(\frac{1}{\mathcal{M}}\frac{\partial}{\partial r}(u_ru_\theta\mathcal{M}) + \frac{1}{\mathcal{M}}\frac{\partial u_\theta^2}{\partial\theta} + \frac{1}{\mathcal{M}}\frac{\partial}{\partial z}(u_\theta u_z\mathcal{M}) + \frac{u_ru_\theta\cos\zeta}{\mathcal{M}}\right)\\ & + \boldsymbol{e}_z\left(\frac{1}{\mathcal{M}}\frac{\partial}{\partial r}(u_ru_z\mathcal{M}) + \frac{1}{\mathcal{M}}\frac{\partial(u_\theta u_z)}{\partial\theta} + \frac{1}{\mathcal{M}}\frac{\partial}{\partial z}(u_z^2\mathcal{M}) - \frac{u_\theta^2\sin\zeta}{\mathcal{M}}\right).\end{aligned} \tag{5.17}$$

From (5.12) and (5.13), the symmetric strain rate tensor $\mathbf{D} = D_{ij}\boldsymbol{e}_i\boldsymbol{e}_j$ (1.4) has components

$$\left.\begin{aligned} D_{rr} &= \frac{\partial u_r}{\partial r}, \qquad & D_{zz} &= \frac{\partial u_z}{\partial z}\\ D_{\theta\theta} &= \frac{1}{\mathcal{M}}\frac{\partial u_\theta}{\partial\theta} + \frac{u_r\cos\zeta}{\mathcal{M}} + \frac{u_z\sin\zeta}{\mathcal{M}},\\ D_{r\theta} &= D_{\theta r} = \frac{1}{2}\left(\frac{\partial u_\theta}{\partial r} + \frac{1}{\mathcal{M}}\frac{\partial u_r}{\partial\theta} - \frac{u_\theta\cos\zeta}{\mathcal{M}}\right),\\ D_{rz} &= D_{zr} = \frac{1}{2}\left(\frac{\partial u_z}{\partial r} + \frac{\partial u_r}{\partial z}\right),\\ D_{\theta z} &= D_{z\theta} = \frac{1}{2}\left(\frac{1}{\mathcal{M}}\frac{\partial u_z}{\partial\theta} - \frac{u_\theta\sin\zeta}{\mathcal{M}} + \frac{\partial u_\theta}{\partial z}\right),\end{aligned}\right\} \tag{5.18}$$

which link to the deviatoric stress $\boldsymbol{\tau}$ through the constitutive relation (1.3). The gravitational vector $\boldsymbol{g}$ points vertically down, and so $\boldsymbol{g} = -g\boldsymbol{e}_z$, where the gravitational acceleration constant $g = 9.81\,\mathrm{ms}^{-2}$. Using (5.3c),

$$\boldsymbol{g} = g\sin\zeta\boldsymbol{e}_r - g\cos\zeta\boldsymbol{e}_z. \tag{5.19}$$

Through equations (5.9), (5.15), (5.17), and (5.19), the radial component of the momentum equation (1.2) can be written as

$$\begin{aligned}&\rho\left(\frac{\partial u_r}{\partial t} + \frac{1}{\mathcal{M}}\frac{\partial}{\partial r}(u_r^2\mathcal{M}) + \frac{1}{\mathcal{M}}\frac{\partial}{\partial\theta}(u_ru_\theta) + \frac{1}{\mathcal{M}}\frac{\partial}{\partial z}(u_ru_z\mathcal{M}) - \frac{u_\theta^2\cos\zeta}{\mathcal{M}}\right)\\ &\quad = -\frac{\partial p}{\partial r} + \rho g\sin\zeta + \frac{1}{\mathcal{M}}\frac{\partial}{\partial r}(\tau_{rr}\mathcal{M}) + \frac{1}{\mathcal{M}}\frac{\partial}{\partial\theta}\tau_{\theta r} + \frac{1}{\mathcal{M}}\frac{\partial}{\partial z}(\tau_{zr}\mathcal{M}) - \frac{\tau_{\theta\theta}\cos\zeta}{\mathcal{M}}.\end{aligned} \tag{5.20}$$

Similarly, the axial component of the momentum equation is

$$\begin{aligned}&\rho\left(\frac{\partial u_\theta}{\partial t} + \frac{1}{\mathcal{M}}\frac{\partial}{\partial r}(u_ru_\theta\mathcal{M}) + \frac{1}{\mathcal{M}}\frac{\partial}{\partial\theta}u_\theta^2 + \frac{1}{\mathcal{M}}\frac{\partial}{\partial z}(u_\theta u_z\mathcal{M}) + \frac{u_ru_\theta\cos\zeta}{\mathcal{M}}\right)\\ &\quad = -\frac{1}{\mathcal{M}}\frac{\partial p}{\partial\theta} + \frac{1}{\mathcal{M}}\frac{\partial}{\partial r}(\tau_{r\theta}\mathcal{M}) + \frac{1}{\mathcal{M}}\frac{\partial}{\partial\theta}\tau_{\theta\theta} + \frac{1}{\mathcal{M}}\frac{\partial}{\partial z}(\tau_{z\theta}\mathcal{M}) + \frac{\tau_{\theta z}\sin\zeta}{\mathcal{M}} + \frac{\tau_{\theta r}\cos\zeta}{\mathcal{M}}.\end{aligned} \tag{5.21}$$

whilst the normal momentum balance is

$$\rho\left(\frac{\partial u_z}{\partial t}+\frac{1}{\mathcal{M}}\frac{\partial}{\partial r}(u_r u_z\mathcal{M})+\frac{1}{\mathcal{M}}\frac{\partial}{\partial\theta}(u_\theta u_z)+\frac{1}{\mathcal{M}}\frac{\partial}{\partial z}(u_z^2\mathcal{M})-\frac{u_\theta^2\sin\zeta}{\mathcal{M}}\right) \tag{5.22}$$

$$=-\frac{\partial p}{\partial z}-\rho g\cos\zeta+\frac{1}{\mathcal{M}}\frac{\partial}{\partial r}(\tau_{rz}\mathcal{M})+\frac{1}{\mathcal{M}}\frac{\partial}{\partial\theta}\tau_{\theta z}+\frac{1}{\mathcal{M}}\frac{\partial}{\partial z}(\tau_{zz}\mathcal{M})-\frac{\tau_{\theta\theta}\sin\zeta}{\mathcal{M}}.$$

5.2.4 Boundary conditions

The mass and momentum equations, (5.16) and (5.20)–(5.22), are supplemented by kinematic and dynamic boundary conditions at the surface $z=s(r,\theta,t)$ and base $b=z(r,\theta,t)$ of the flow. The surface and basal interfaces are given by

$$F^s=z-s(r,\theta,t),\qquad F^b=b(r,\theta,t)-z. \tag{5.23a,b}$$

The unit vectors normal to these interfaces are given by

$$\boldsymbol{n}^s=\frac{\nabla F^s}{|\nabla F^s|},\qquad \boldsymbol{n}^b=\frac{\nabla F^b}{|\nabla F^b|}. \tag{5.24a,b}$$

The kinematic boundary condition implies that particles on the surface stay on the surface, and similarly for the base, i.e.

$$\frac{\mathrm{D}F^s}{\mathrm{D}t}=\frac{\partial F^s}{\partial t}+\boldsymbol{u}^s\cdot\nabla F^s=0,\qquad \frac{\mathrm{D}F^b}{\mathrm{D}t}=\frac{\partial F^b}{\partial t}+\boldsymbol{u}^b\cdot\nabla F^b=0, \tag{5.25a,b}$$

where $\boldsymbol{u}^s=(u_r^s,u_\theta^s,u_z^s)$ and $\boldsymbol{u}^b=(u_r^b,u_\theta^b,u_z^b)$ are the surface and basal velocities, respectively. Using the scalar gradient (5.9), this implies that

$$-\frac{\partial s}{\partial t}-u_r^s\frac{\partial s}{\partial r}-\frac{1}{\mathcal{M}}u_\theta^s\frac{\partial s}{\partial\theta}+u_z^s=0,\qquad (z=s), \tag{5.26a}$$

$$\frac{\partial b}{\partial t}+u_r^b\frac{\partial b}{\partial r}+\frac{1}{\mathcal{M}}u_\theta^b\frac{\partial b}{\partial\theta}-u_z^b=0,\qquad (z=b). \tag{5.26b}$$

The free-surface is assumed to be stress-free,

$$\mathbf{S}^s\cdot\boldsymbol{n}^s=0, \tag{5.27}$$

where $\mathbf{S}=-p\mathbf{I}+\boldsymbol{\tau}$ is the sum total of both the isotropic pressure and the deviatoric stress, and $\mathbf{I}$ is the identity matrix. In particular, in the radial and normal directions, this gives

$$p\frac{\partial s}{\partial r}-\tau_{rr}\frac{\partial s}{\partial r}-\tau_{r\theta}\frac{1}{\mathcal{M}}\frac{\partial s}{\partial\theta}+\tau_{rz}=0, \tag{5.28a}$$

$$-p-\tau_{zr}\frac{\partial s}{\partial r}-\tau_{z\theta}\frac{1}{\mathcal{M}}\frac{\partial s}{\partial\theta}+\tau_{zz}=0, \tag{5.28b}$$

with all of the quantities evaluated at $z = s$. At the base, the frictional balance is

$$\mathbf{S}^b \cdot \boldsymbol{n}^b = \left(\boldsymbol{n}^b \cdot \mathbf{S}^b \cdot \boldsymbol{n}^b\right)\left(\frac{\boldsymbol{u}^b}{|\boldsymbol{u}^b|} + \boldsymbol{n}^b\right). \tag{5.29}$$

5.2.5 Non-dimensional scaling

It is useful to non-dimensionalise the lengths using a typical radial distance R and a typical flow height H, with the ratio $\epsilon = H/R$ indicating the shallowness of the flow

$$r = R\tilde{r}, \quad z = \epsilon R\tilde{z}, \quad \mathcal{M} = R(\tilde{r}\cos\zeta + \epsilon\tilde{z}\sin\zeta) = R\tilde{\mathcal{M}}. \tag{5.30a–c}$$

The radial and axial velocities u_r and u_θ are assumed to scale with the gravity wave speed $\sqrt{gH}$; the mass balance equation (5.16) provides the scaling for u_z. Thus

$$(u_r, u_\theta, u_z) = \sqrt{gH}(\tilde{u}_r, \tilde{u}_\theta, \epsilon\tilde{u}_z) \qquad t = \frac{R}{\sqrt{gH}}\,\tilde{t}, \tag{5.31a,b}$$

where $\tilde{t}$ is the non-dimensional time. Applying scalings (5.30) and (5.31) to (5.18) implies that

$$\left.\begin{aligned}
D_{rr} &= \epsilon\sqrt{\frac{g}{H}}\frac{\partial\tilde{u}_r}{\partial\tilde{r}}, & D_{zz} &= \epsilon\sqrt{\frac{g}{H}}\frac{\partial\tilde{u}_z}{\partial\tilde{z}} \\
D_{\theta\theta} &= \epsilon\sqrt{\frac{g}{H}}\left(\frac{1}{\tilde{\mathcal{M}}}\frac{\partial\tilde{u}_\theta}{\partial\theta} + \frac{\tilde{u}_r\cos\zeta}{\tilde{\mathcal{M}}} + \epsilon\frac{\tilde{u}_z\sin\zeta}{\tilde{\mathcal{M}}}\right), \\
D_{r\theta} &= D_{\theta r} = \frac{1}{2}\epsilon\sqrt{\frac{g}{H}}\left(\frac{\partial\tilde{u}_\theta}{\partial\tilde{r}} + \frac{1}{\tilde{\mathcal{M}}}\frac{\partial\tilde{u}_r}{\partial\theta} - \frac{\tilde{u}_\theta\cos\zeta}{\tilde{\mathcal{M}}}\right), \\
D_{rz} &= D_{zr} = \frac{1}{2}\sqrt{\frac{g}{H}}\left(\epsilon^2\frac{\partial\tilde{u}_z}{\partial\tilde{r}} + \frac{\partial\tilde{u}_r}{\partial\tilde{z}}\right), \\
D_{\theta z} &= D_{z\theta} = \frac{1}{2}\sqrt{\frac{g}{H}}\left(\epsilon\frac{1}{\tilde{\mathcal{M}}}\frac{\partial\tilde{u}_z}{\partial\theta} - \epsilon\frac{\tilde{u}_\theta\sin\zeta}{\tilde{\mathcal{M}}} + \frac{\partial\tilde{u}_\theta}{\partial\tilde{z}}\right),
\end{aligned}\right\} \tag{5.32}$$

The trace of $\mathbf{D}$ scales as

$$\operatorname{tr}\mathbf{D}^2 = D_{rr}^2 + D_{\theta\theta}^2 + D_{zz}^2 + 2(D_{r\theta}^2 + D_{rz}^2 + D_{\theta z}^2) = 2(D_{rz}^2 + D_{\theta z}^2) + \mathcal{O}(\epsilon^2), \tag{5.33}$$

and hence

$$\|\mathbf{D}\| = \sqrt{D_{rz}^2 + D_{\theta z}^2} + \mathcal{O}(\epsilon). \tag{5.34}$$

Combining (5.32) and (5.34) gives the non-dimensionalisation

$$\begin{aligned}
&(D_{rr}, D_{\theta\theta}, D_{zz}, D_{r\theta}, D_{rz}, D_{\theta z}, \|\mathbf{D}\|) \\
&\qquad = \sqrt{\frac{g}{H}}\left(\epsilon\tilde{D}_{rr}, \epsilon\tilde{D}_{\theta\theta}, \epsilon\tilde{D}_{zz}, \epsilon\tilde{D}_{r\theta}, \tilde{D}_{rz}, \tilde{D}_{\theta z}, \|\tilde{\mathbf{D}}\|\right).
\end{aligned} \tag{5.35}$$

Using the fact that $\boldsymbol{\tau} = \mu(I)p\mathbf{D}/\|\mathbf{D}\|$ (1.3) and $p \sim \rho g H$,

$$(p, \tau_{rr}, \tau_{\theta\theta}, \tau_{zz}, \tau_{r\theta}, \tau_{rz}, \tau_{\theta z}, \boldsymbol{\tau}) = \rho g H(\tilde{p}, \epsilon\tilde{\tau}_{rr}, \epsilon\tilde{\tau}_{\theta\theta}, \epsilon\tilde{\tau}_{zz}, \epsilon\tilde{\tau}_{r\theta}, \tilde{\tau}_{rz}, \tilde{\tau}_{\theta z}, \tilde{\boldsymbol{\tau}}). \tag{5.36}$$

The mass balance equation (5.16) can now be non-dimensionalised through equations (5.30) and (5.31) to give

$$0 = \frac{\partial \tilde{u}_r}{\partial \tilde{r}} + \frac{1}{\tilde{\mathcal{M}}}\frac{\partial \tilde{u}_\theta}{\partial \theta} + \frac{\tilde{u}_r \cos\zeta}{\tilde{\mathcal{M}}} + \epsilon\frac{\tilde{u}_z \sin\zeta}{\tilde{\mathcal{M}}} + \frac{\partial \tilde{u}_z}{\partial \tilde{z}}. \tag{5.37}$$

In addition to equations (5.20)–(5.22), equations (5.35)–(5.36) help to non-dimensionalise the radial momentum equation

$$\begin{aligned}\epsilon\left(\frac{\partial \tilde{u}_r}{\partial \tilde{t}} + \frac{1}{\tilde{\mathcal{M}}}\frac{\partial}{\partial \tilde{r}}(\tilde{u}_r^2\tilde{\mathcal{M}}) + \frac{1}{\tilde{\mathcal{M}}}\frac{\partial}{\partial \theta}(\tilde{u}_r\tilde{u}_\theta) + \frac{1}{\tilde{\mathcal{M}}}\frac{\partial}{\partial \tilde{z}}(\tilde{u}_r\tilde{u}_z\tilde{\mathcal{M}}) - \frac{\tilde{u}_\theta^2\cos\zeta}{\tilde{\mathcal{M}}}\right)\\ = -\epsilon\frac{\partial \tilde{p}}{\partial \tilde{r}} + \sin\zeta + \epsilon^2\frac{1}{\tilde{\mathcal{M}}}\frac{\partial}{\partial \tilde{r}}(\tilde{\tau}_{rr}\tilde{\mathcal{M}})\\ + \epsilon^2\frac{1}{\tilde{\mathcal{M}}}\frac{\partial}{\partial \theta}\tilde{\tau}_{\theta r} + \frac{1}{\tilde{\mathcal{M}}}\frac{\partial}{\partial \tilde{z}}(\tilde{\tau}_{zr}\tilde{\mathcal{M}}) - \epsilon^2\frac{\tilde{\tau}_{\theta\theta}\cos\zeta}{\tilde{\mathcal{M}}}.\end{aligned} \tag{5.38}$$

Similarly, the non-dimensional axial momentum equation is

$$\begin{aligned}\epsilon\left(\frac{\partial \tilde{u}_\theta}{\partial \tilde{t}} + \frac{1}{\tilde{\mathcal{M}}}\frac{\partial}{\partial \tilde{r}}(\tilde{u}_r\tilde{u}_\theta\tilde{\mathcal{M}}) + \frac{1}{\tilde{\mathcal{M}}}\frac{\partial}{\partial \theta}\tilde{u}_\theta^2 + \frac{1}{\tilde{\mathcal{M}}}\frac{\partial}{\partial \tilde{z}}(\tilde{u}_\theta\tilde{u}_z\tilde{\mathcal{M}}) + \frac{\tilde{u}_r\tilde{u}_\theta\cos\zeta}{\tilde{\mathcal{M}}}\right)\\ = -\epsilon\frac{1}{\tilde{\mathcal{M}}}\frac{\partial \tilde{p}}{\partial \theta} + \epsilon^2\frac{1}{\tilde{\mathcal{M}}}\frac{\partial}{\partial \tilde{r}}(\tilde{\tau}_{r\theta}\tilde{\mathcal{M}}) + \epsilon^2\frac{1}{\tilde{\mathcal{M}}}\frac{\partial}{\partial \theta}\tilde{\tau}_{\theta\theta}\\ + \frac{1}{\tilde{\mathcal{M}}}\frac{\partial}{\partial \tilde{z}}(\tilde{\tau}_{z\theta}\tilde{\mathcal{M}}) + \epsilon\frac{\tilde{\tau}_{\theta r}\cos\zeta}{\tilde{\mathcal{M}}} + \epsilon\frac{\tilde{\tau}_{\theta z}\sin\zeta}{\tilde{\mathcal{M}}},\end{aligned} \tag{5.39}$$

and the non-dimensional normal momentum equation is

$$\begin{aligned}\epsilon\left(\epsilon\frac{\partial \tilde{u}_z}{\partial \tilde{t}} + \epsilon\frac{1}{\tilde{\mathcal{M}}}\frac{\partial}{\partial \tilde{r}}(\tilde{u}_r\tilde{u}_z\tilde{\mathcal{M}}) + \epsilon\frac{1}{\tilde{\mathcal{M}}}\frac{\partial}{\partial \theta}(\tilde{u}_\theta\tilde{u}_z) + \epsilon\frac{1}{\tilde{\mathcal{M}}}\frac{\partial}{\partial \tilde{z}}(\tilde{u}_z^2\tilde{\mathcal{M}}) - \frac{\tilde{u}_\theta^2\sin\zeta}{\tilde{\mathcal{M}}}\right)\\ = -\frac{\partial \tilde{p}}{\partial \tilde{z}} - \cos\zeta + \epsilon\frac{1}{\tilde{\mathcal{M}}}\frac{\partial}{\partial \tilde{r}}(\tilde{\tau}_{rz}\tilde{\mathcal{M}})\\ + \epsilon\frac{1}{\tilde{\mathcal{M}}}\frac{\partial}{\partial \theta}\tilde{\tau}_{\theta z} + \epsilon\frac{1}{\tilde{\mathcal{M}}}\frac{\partial}{\partial \tilde{z}}(\tilde{\tau}_{zz}\tilde{\mathcal{M}}) - \epsilon^2\frac{\tilde{\tau}_{\theta\theta}\sin\zeta}{\tilde{\mathcal{M}}}.\end{aligned} \tag{5.40}$$

Assuming that the surface and basal interface positions (s, b) scale like z, i.e. $(s, b) = R(\epsilon\tilde{s}, \epsilon\tilde{b})$, the stress-free boundary conditions (5.28) become

$$\epsilon\tilde{p}\frac{\partial \tilde{s}}{\partial \tilde{r}} - \epsilon^2\tilde{\tau}_{rr}\frac{\partial \tilde{s}}{\partial \tilde{r}} - \epsilon^2\tilde{\tau}_{r\theta}\frac{1}{\tilde{\mathcal{M}}}\frac{\partial \tilde{s}}{\partial \theta} + \tilde{\tau}_{rz} = 0, \tag{5.41a}$$

$$-\tilde{p} - \epsilon\tilde{\tau}_{zr}\frac{\partial \tilde{s}}{\partial \tilde{r}} - \epsilon\tilde{\tau}_{z\theta}\frac{1}{\tilde{\mathcal{M}}}\frac{\partial \tilde{s}}{\partial \theta} + \epsilon\tilde{\tau}_{zz} = 0, \tag{5.41b}$$

with all of the quantities evaluated at $\tilde{z} = \tilde{s}$. Finally, the kinematic boundary conditions (5.26) at the surface and base of the flow become

$$-\frac{\partial \tilde{s}}{\partial \tilde{t}} - \tilde{u}_r^s \frac{\partial \tilde{s}}{\partial \tilde{r}} - \frac{1}{\tilde{\mathcal{M}}} \tilde{u}_\theta^s \frac{\partial \tilde{s}}{\partial \theta} + \tilde{u}_z^s = 0, \qquad (\tilde{z} = \tilde{s}), \tag{5.42a}$$

$$\frac{\partial \tilde{b}}{\partial \tilde{t}} + \tilde{u}_r^b \frac{\partial \tilde{b}}{\partial \tilde{r}} + \frac{1}{\tilde{\mathcal{M}}} \tilde{u}_\theta^b \frac{\partial \tilde{b}}{\partial \theta} - \tilde{u}_z^b = 0, \qquad (\tilde{z} = \tilde{b}). \tag{5.42b}$$

5.3 Steady axisymmetric flow

5.3.1 A Bagnold velocity profile

Consider the case of steady axisymmetric flow, in which $\tilde{u}_\theta = 0$ and all of the temporal and axial derivatives are zero. It is assumed that the flow is shallow, so that $\epsilon = H/R \ll 1$. The leading order, $\mathcal{O}(1)$, terms from normal momentum equation (5.40) imply that

$$\frac{\partial \tilde{p}}{\partial \tilde{z}} = -\cos\zeta. \tag{5.43}$$

The leading order balance from the normal component of the stress-free surface (5.41a) implies that $\tilde{p} = 0$ at $\tilde{z} = \tilde{s}$, and thus the pressure is lithostatic throughout the depth

$$\tilde{p} = (\tilde{s} - \tilde{z})\cos\zeta. \tag{5.44}$$

From (5.38), the leading order balance shows that

$$\frac{1}{\tilde{\mathcal{M}}} \frac{\partial}{\partial \tilde{z}} (\tilde{\tau}_{zr} \tilde{\mathcal{M}}) = -\sin\zeta. \tag{5.45}$$

As (5.30c) implies that $\tilde{\mathcal{M}} = \tilde{r} + \mathcal{O}(\epsilon)$, and the leading order balance from (5.41) gives that $\tilde{\tau}_{zr} = 0$ on $\tilde{z} = \tilde{s}$, it can be seen that

$$\tilde{\tau}_{zr} = (\tilde{s} - \tilde{z})\sin\zeta. \tag{5.46}$$

Interestingly, at leading order, the flow over a cone is the same as for flow down a planar chute, and the subsequent derivation is the same as for planar chute flow (e.g. Andreotti *et al.*, 2013; Gray & Edwards, 2014). For axisymmetric flow, (5.32) and (5.34) imply that

$$\tilde{D}_{zr} = \frac{1}{2}\frac{\partial \tilde{u}_r}{\partial \tilde{z}} + \mathcal{O}(\epsilon^2), \qquad \|\tilde{\mathbf{D}}\| = \frac{1}{2}\frac{\partial \tilde{u}_r}{\partial \tilde{z}} + \mathcal{O}(\epsilon), \tag{5.47a,b}$$

and hence (1.3) implies that

$$\tilde{\tau}_{zr} = \mu(I)\,\tilde{p}\,\mathrm{sgn}\left(\frac{\partial \tilde{u}_r}{\partial \tilde{z}}\right). \tag{5.48}$$

Assuming $\partial\tilde{u}_r/\partial\tilde{z}$ to be positive, the combination of (5.44) and (5.46) imply that

$$\mu(I) = \tan\zeta. \tag{5.49}$$

Since the inclination angle of the cone ζ is constant, this implies that the inertial number $I = I_\zeta$ is constant,

$$I_\zeta = I_0\left(\frac{\tan\zeta - \tan\zeta_1}{\tan\zeta_2 - \tan\zeta}\right), \tag{5.50}$$

where ζ_1 and ζ_2 are the minimum and maximum angles for steady uniform flow, and I_0 is the constant defined in (1.6b). In non-dimensional variables, the definition of I (1.6a) becomes

$$I = \frac{2\|\tilde{\mathbf{D}}\|\tilde{d}}{\sqrt{\tilde{p}\nu}}, \tag{5.51}$$

where ν is the solids volume fraction and $\tilde{d} = \epsilon d$ is the (non-dimensional) typical grain size. The combination of (5.44) and (5.47) gives the ordinary differential equation

$$\frac{\partial\tilde{u}_r}{\partial\tilde{z}} = \frac{I_\zeta\sqrt{\nu\cos\zeta}}{\tilde{d}}(\tilde{s}-\tilde{z})^{1/2}, \tag{5.52}$$

which integrates to show that the leading order radial velocity $\tilde{u}_r$ obeys a Bagnold velocity profile (Bagnold, 1954)

$$\tilde{u}_r = \frac{2I_\zeta}{3\tilde{d}}\sqrt{\nu\cos\zeta}\left(\tilde{h}^{3/2} - (\tilde{s}-\tilde{z})^{3/2}\right), \tag{5.53}$$

where $\tilde{h} = \tilde{s} - \tilde{b}$ is the depth of the flow.

5.3.2 Spreading dynamics

The spreading dynamics are controlled by the mass balance equation (5.37); at leading order, under the assumption of an axisymmetric flow, this becomes

$$\frac{1}{\tilde{\mathcal{M}}}\frac{\partial}{\partial\tilde{r}}(\tilde{u}_r\tilde{\mathcal{M}}) + \frac{\partial\tilde{u}_z}{\partial\tilde{z}} = 0. \tag{5.54}$$

With the aid of the kinematic conditions (5.42), equation (5.54) may be depth-averaged from $\tilde{z} = \tilde{b}$ to $\tilde{z} = \tilde{s}$ to give

$$\frac{\partial}{\partial\tilde{r}}(\tilde{r}\bar{\tilde{u}}_r\tilde{h}) = 0, \tag{5.55}$$

where $\bar{\tilde{u}}_r = (1/\tilde{h}) \int_{\tilde{z}=\tilde{b}}^{\tilde{z}=\tilde{s}} \tilde{u}_r(\tilde{z})\,\mathrm{d}\tilde{z}$ is the depth integrated velocity. From the Bagnold velocity profile (5.53), $\bar{\tilde{u}}_r$ may be explicitly calculated to be

$$\bar{\tilde{u}}_r = \tilde{U}_0\,\tilde{h}^{3/2}, \tag{5.56}$$

with

$$\tilde{U}_0 = \frac{2I_\zeta}{5\tilde{d}}\sqrt{\nu\cos\zeta}. \tag{5.57}$$

Integrating (5.55) implies that

$$\tilde{Q}_0 = \tilde{r}\bar{\tilde{u}}_r\tilde{h}, \tag{5.58}$$

with $\tilde{Q}_0 = \tilde{Q}/2\pi$ the (non-dimensional) initial flux per unit radian. Combining equations (5.56) and (5.58) gives the flow depth $\tilde{h}$ and depth averaged radial velocity $\bar{\tilde{u}}_r$ as functions of $\tilde{r}$

$$\tilde{h} = \left(\frac{\tilde{Q}_0}{\tilde{U}_0}\right)^{2/5}\tilde{r}^{-2/5}, \qquad \bar{\tilde{u}}_r = \left(\tilde{U}_0^2\tilde{Q}_0^3\right)^{1/5}\tilde{r}^{-3/5}. \tag{5.59a,b}$$

The (non-dimensional) Froude number Fr is the ratio of the depth averaged velocity $\bar{u}_r$ to the gravity wave speed $\sqrt{gh\cos\zeta}$, and can be shown to scale as

$$Fr = \frac{1}{\sqrt{\cos\zeta}}\left(\tilde{U}_0^3\tilde{Q}_0^2\right)^{1/5}\tilde{r}^{-2/5}. \tag{5.60}$$

The Froude number is important in determining the basal friction law, with (1.5) valid for $Fr \geqslant \beta$; if the Froude number drops below this value then the extended friction formulation of Forterre & Pouliquen (2003) must be assumed. For the remainder of the analysis it is assumed that $Fr \geqslant \beta$.

5.3.3 A critical height and radius for fingering

Section 5.1.3 revealed a linear relationship between the flux Q and the critical fingering radius r_{crit}. This relationship can be deduced from the leading order spreading dynamics of § 5.3.2 by assuming that the onset of fingering occurs at a critical height $\hat{h}_{crit}$. From (5.56), the critical velocity when $\tilde{h} = \tilde{h}_{crit}$ is

$$\bar{\tilde{u}}_r|_{crit} = \tilde{U}_0\,\tilde{h}_{crit}^{3/2}, \tag{5.61}$$

and so (5.58) implies that

$$\tilde{Q}_0 = \left(\tilde{U}_0\tilde{h}_{crit}^{5/2}\right)\tilde{r}_{crit}. \tag{5.62}$$

As the quantities in the brackets on the right hand side are constant, $\tilde{Q}_0 \propto \tilde{r}_{crit}$. In dimensional variables, this means that

$$Q = \left(2\pi U_0 h_{crit}^{5/2}\right) r_{crit}. \tag{5.63}$$

There are a few reasons why the theory predicts a directly proportional relationship between the flux Q and the critical radius r_{crit}, but the experimental results of § 5.1.3 give an offset of $e = 86\,\mathrm{mm}$. The most significant error is likely to come from the edge detection and circle fitting algorithms. As can be seen in the contour plots in figures 5.4–5.7, the front appears to show small perturbations even whilst the overall front shape is still roughly circular. Although these small perturbations may develop and cause the front to become non-circular, the perturbations would remain undetected by the current algorithms until they are sufficiently large. The result is that current experimental techniques may only detect the onset of fingering after it has actually happened, and thus predict the critical radius r_{crit} to be further downstream that the theoretical value. The second reason contributing to the offset may be the jamming around the gate that means zero flux at zero radius is impractical in the experiments. At gate travel distances below $G_t = 1.5\,\mathrm{mm}$, corresponding to a gate opening of $G_o = 1.32\,\mathrm{mm}$ and a flux of $Q = 7\,\mathrm{cm^3\,s^{-1}}$, mass did not flow uniformly out of the hopper because of localised jamming. Despite the difference in the offset e between the theory and experiments, if it assumed that the constant of proportionality k is the same, then h_{crit} can be determined as

$$h_{crit} = (2\pi k U_0)^{2/5} = 1.10\,\mathrm{mm}. \tag{5.64}$$

The parameters used to calculate U_0 are given in table A. The above value of h_{crit} is very close to the experimentally determined value of $h_{start}(28.6°) = 1.09\,\mathrm{mm}$ for the glass beads and base used in the experiments. Whilst the flow will stop when it reaches a height of $h_{stop}(28.6°) = 0.52\,\mathrm{mm}$, any stopped material must attain a height of h_{start} before it is remobilised. It is still an open question as to why h_{start} may be the critical height for the flow, and what physical mechanism is at work such that it is this height which causes the instability. One possible explanation could be based on the work of Malloggi *et al.* (2006), who noticed that when the flowing height is between h_{start} and h_{stop}, there is a metastable regime in which the flow front is

unstable to transverse perturbations. By using a modulated initial condition, they showed that small perturbations to the front would coarsen and develop into a fingering pattern. As granular material on a planar chute inclined between ζ_1 and ζ_2 flows steadily at a constant height (Pouliquen, 1999), it becomes difficult to obtain the metastable regime between h_{start} and h_{stop}. Although the initial flow height is much higher than h_{start}, the radial spreading in the conical set-up causes the flow to thin according to (5.59a). Once the flow has spread and thinned such that the height drops below h_{start}, the propagating front would be unstable to the small axial perturbations observed in figures 5.4–5.7. These small perturbations would coarsen, causing the flow front to finger and develop individual channels. Whilst this could be a plausible explanation, further work is needed to confirm this hypothesis.

5.4 A depth-averaged rheological model

A recent depth-averaged version of the $\mu(I)$-rheology (Gray & Edwards, 2014) has been shown to accurately model the dynamics of both roll-wave instabilities (Razis *et al.*, 2014) and erosion-deposition waves (Edwards & Gray, 2014). The two-dimensional generalisation (Baker *et al.*, 2016) was also shown to predict the velocity-profile scalings and flux to channel-width relationship. The key component behind the formulation of this depth averaged $\mu(I)$-rheology model was the Bagnold velocity profile, and since it was shown in § 5.3.1 that the leading order velocity profile in conical coordinates is also Bagnold, the depth-averaged model could be extended to this geometry. The fact that the depth-averaged leading order mass balance (5.58) alone is able to predict the linear relationship between the flux and the critical radius lends promise that the complete depth-averaged model is able to capture all of the subtle dynamics of this geometry.

By defining the depth-average $\overline{f}$ of a quantity f to be its average across the depth of the flow $h = s - b$,

$$\overline{f} = \frac{1}{h}\int_b^s f \,\mathrm{d}z, \tag{5.65}$$

the mass and momentum equations (1.1)-(1.2) can be depth-averaged to give

$$\frac{\partial h}{\partial t} + \nabla\cdot(h\bar{\boldsymbol{u}}) = 0, \tag{5.66}$$

$$\frac{\partial}{\partial t}(h\bar{\boldsymbol{u}}) + \nabla\cdot(\chi h\bar{\boldsymbol{u}}\otimes\bar{\boldsymbol{u}}) + \nabla\left(\frac{1}{2}gh^2\cos\zeta\right) = gh\boldsymbol{S} + \frac{1}{\rho}\nabla\cdot(h\bar{\boldsymbol{\tau}}). \tag{5.67}$$

The depth-averaging operation flattens the coordinate system to just (r,θ) space, and so $\bar{\boldsymbol{u}} = (\bar{u}_r, \bar{u}_\theta)$ with the gradient operator reducing to

$$\nabla = \boldsymbol{e}_r\frac{\partial}{\partial r} + \frac{1}{\mathcal{M}}\boldsymbol{e}_\theta\frac{\partial}{\partial\theta}. \tag{5.68}$$

The shape factor χ links the depth-average of products of velocities to the product of depth-averaged velocities $\overline{\boldsymbol{u}\boldsymbol{u}} = \chi\bar{\boldsymbol{u}}\bar{\boldsymbol{u}}$, and is dependent on the vertical velocity profile. Savage & Hutter (1989) showed that $\chi = 6/5$ for a parabolic velocity profile, Pouliquen & Forterre (2002) showed that $\chi = 4/3$ for a linear velocity profile with no basal slip (5.81) whilst Börzsönyi *et al.* (2008) showed that $\chi = 5/4$ for a Bagnold profile (5.53). All of these values are close to 1, and Pouliquen & Forterre (2002) showed that numerical simulations of slow granular flows are insensitive to the particular value of χ chosen. As depatures away from unity cause problems in handling grain-free regions (Hogg & Pritchard, 2004), it is assumed here for simplicity that $\chi = 1$ (e.g. Savage & Hutter, 1989; Gray *et al.*, 1999, 2003; Baker *et al.*, 2016). The source term $\boldsymbol{S}$ (not to be confused with the stress $\mathbf{S}$) is the result of gravity and basal friction (5.29)

$$\boldsymbol{S} = \cos\zeta\left(\tan\zeta - \mu_b\frac{\bar{u}_r}{\|\bar{\boldsymbol{u}}\|}\right)\boldsymbol{e}_r - \cos\zeta\mu_b\frac{\bar{u}_\theta}{\|\bar{\boldsymbol{u}}\|}\boldsymbol{e}_\theta. \tag{5.69}$$

Finally, Baker *et al.* (2016) assumed that the depth-averaged deviatoric stress $\bar{\boldsymbol{\tau}}$ scales as

$$h\bar{\boldsymbol{\tau}} = \rho\,\upsilon\,h^{3/2}\bar{\mathbf{D}}, \tag{5.70}$$

with the depth-averaged strain rate tensor $\bar{\mathbf{D}}$ equal to

$$\bar{\mathbf{D}} = \frac{1}{2}\left(\nabla\bar{\boldsymbol{u}} + \nabla\bar{\boldsymbol{u}}^{\mathrm{T}}\right), \tag{5.71}$$

and the depth-averaged viscosity coefficient υ given by

$$\upsilon = \frac{2\mathscr{L}\sqrt{g}}{9\beta}\frac{\sin\zeta}{\sqrt{\cos\zeta}}\left(\frac{\mu_2 - \tan\zeta}{\tan\zeta - \mu_1}\right). \tag{5.72}$$

The relevant components for the 2-D quantities can be deduced from equations (5.15), (5.17) and (5.18) by ignoring any terms with a z component. Strictly speaking, since $\mathcal{M}$ includes z dependence, any products of quantities with $\mathcal{M}$ would need to have their depth-averaged product evaluated explicitly. For example $\overline{Mu}$ would need to be calculated and related back to $\overline{M}$ and $\bar{u}$ to close the model. The mathematical complexity of this increases greatly. Motivated by the shallow water approximation in which $\epsilon = H/R \ll 1$, equation (5.30c) implies that $\mathcal{M} = r\cos\zeta + \mathcal{O}(\epsilon)$. Since the z dependence lies at a higher order, it is therefore assumed for the sake of simplicity and mathematical tractability that $\mathcal{M} = r\cos\zeta$. Putting all of this together, the depth-averaged mass equation (5.66) in component form becomes:

$$\frac{\partial h}{\partial t} + \frac{1}{r}\frac{\partial}{\partial r}(r\bar{u}_r h) + \frac{1}{r\cos\zeta}\frac{\partial}{\partial \theta}(\bar{u}_\theta h) = 0. \tag{5.73}$$

The radial component of the depth averaged momentum equation (5.67) becomes

$$\begin{aligned}
&\frac{\partial}{\partial t}(h\bar{u}_r) + \frac{1}{r}\frac{\partial}{\partial r}(r\bar{u}_r^2 h) + \frac{1}{r\cos\zeta}\frac{\partial}{\partial \theta}(\bar{u}_r\bar{u}_\theta h) - \frac{\bar{u}_\theta^2 h}{r} + \frac{\partial}{\partial r}\left(\frac{1}{2}gh^2\cos\zeta\right) \\
&\quad = hg\cos\zeta\left(\tan\zeta - \mu_b\frac{\bar{u}_r}{\|\bar{\boldsymbol{u}}\|}\right) + \frac{1}{r}\frac{\partial}{\partial r}\left(\upsilon h^{3/2} r\frac{\partial \bar{u}_r}{\partial r}\right) \\
&\qquad + \frac{1}{r\cos\zeta}\frac{\partial}{\partial\theta}\left(\frac{1}{2}\upsilon h^{3/2}\left(\frac{\partial\bar{u}_\theta}{\partial r} + \frac{1}{r\cos\zeta}\frac{\partial\bar{u}_r}{\partial\theta} - \frac{\bar{u}_\theta}{r}\right)\right) \\
&\qquad - \frac{\upsilon h^{3/2}}{r}\left(\frac{1}{r\cos\zeta}\frac{\partial\bar{u}_\theta}{\partial\theta} + \frac{\bar{u}_r}{r}\right).
\end{aligned} \tag{5.74}$$

Finally, the axial component of the momentum equation (5.67) becomes

$$\begin{aligned}
&\frac{\partial}{\partial t}(h\bar{u}_\theta) + \frac{1}{r}\frac{\partial}{\partial r}(r\bar{u}_r\bar{u}_\theta h) + \frac{1}{r\cos\zeta}\frac{\partial}{\partial\theta}(\bar{u}_\theta^2 h) + \frac{\bar{u}_r\bar{u}_\theta h}{r} + \frac{1}{r\cos\zeta}\frac{\partial}{\partial\theta}\left(\frac{1}{2}gh^2\cos\zeta\right) \\
&\quad = -hg\cos\zeta\mu_b\frac{\bar{u}_\theta}{\|\bar{\boldsymbol{u}}\|} + \frac{1}{r}\frac{\partial}{\partial r}\left(\upsilon h^{3/2} r\left(\frac{\partial\bar{u}_\theta}{\partial r} + \frac{1}{r\cos\zeta}\frac{\partial\bar{u}_r}{\partial\theta} - \frac{\bar{u}_\theta}{r}\right)\right) \\
&\qquad + \frac{1}{r\cos\zeta}\frac{\partial}{\partial\theta}\left(\upsilon h^{3/2}\left(\frac{1}{r\cos\zeta}\frac{\partial\bar{u}_\theta}{\partial\theta} + \frac{\bar{u}_r}{r}\right)\right) \\
&\qquad + \frac{1}{2}\frac{\upsilon h^{3/2}}{r}\left(\frac{\partial\bar{u}_\theta}{\partial r} + \frac{1}{r\cos\zeta}\frac{\partial\bar{u}_r}{\partial\theta} - \frac{\bar{u}_\theta}{r}\right).
\end{aligned} \tag{5.75}$$

Rather than assuming the tensorial form of the depth-averaged equations (5.66)–(5.67), the above equations (5.73)–(5.75) can be derived directly from first principles by depth-averaging (5.16) and (5.20)–(5.21). As these depth-averaged equations in

conical geometry follow naturally from the work in §§ 5.2.1 and 5.2.2, they are stated here for completeness. It is hoped that time-dependent solutions to these equations will be able to model this radial monodisperse fingers and give further insight into the physical mechanisms at work. However, such numerical simulations lie beyond the scope of this thesis.

5.5 Bidisperse segregation patterns on a cone

The cone set-up was originally designed to study radial segregation patterns, and so it is interesting to observe how a bidisperse mixture flows in this geometry. A mixture containing 70% of $200-250\,\mu\mathrm{m}$ spherical glass beads and 30% of $300-425\,\mu\mathrm{m}$ of angular Carborundum grains was prepared and loaded into the hopper, following the procedure outlined in § 5.1. The gate travel was $G_t = 2.0\,\mathrm{mm}$ giving a gate opening of $G_o = 1.76\,\mathrm{mm}$. The flux was not recorded for this experiment; however it is expected to be similar to monodisperse runs 30 and 41 (table B) which had gate travel values of $G_t = 1.8\,\mathrm{mm}$ and $G_t = 2.1\,\mathrm{mm}$ respectively. Six overhead photographs are presented in figure 5.13, showing the evolution of the flow at 1, 5, 10, 15, 20 and 25 seconds after the gate has been released. The close-up view in figure 5.14 shows that the bidisperse fingers on a cone also have coarse grained levees, large-particle rich fronts and a channel lining containing less frictional fine grains. These were also characteristic features of the channels produced through segregation on a planar chute in figure 1.4. However, in the conical geometry, the spreading and thinning of the flow also promotes the fingering instability. The additional thinning mechanism means that the channels are more prone to tip-splitting than the planar chute. As compared to the monodisperse fingers in figure 5.2 which were caused by thinning alone, the additional segregation mechanism causes the bidisperse flow to finger at an earlier time and smaller critical radius than the monodisperse flows.

Woodhouse *et al.* (2012) recently developed a model for bidisperse fingers using the depth-averaged mass and momentum equations (5.66)–(5.67), together with a depth averaged segregation equation (Gray & Kokelaar, 2010). Whilst their results

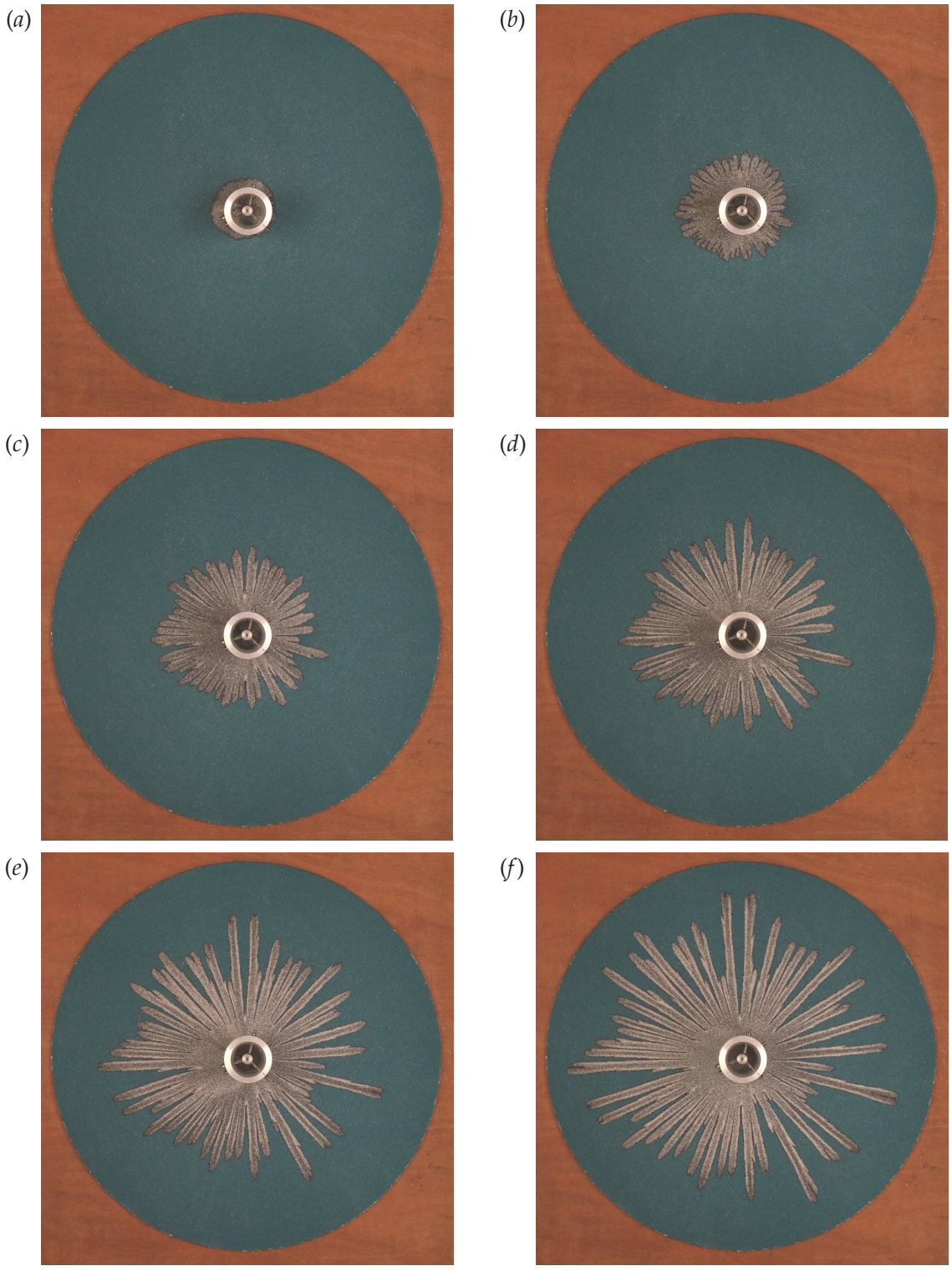

Figure 5.13: A series of overhead photographs showing how a bidisperse flow evolves after it exits from the gate. The bidisperse mixture contained 70% of $200 - 250\,\mu\mathrm{m}$ spherical glass beads and 30% of $300 - 425\,\mu\mathrm{m}$ of angular Carborundum grains. Panels (*a*)-(*f*) show the flow at 1, 5, 10, 15, 20 and 25 seconds after the gate was released, respectively. The gate travel G_t and gate-opening G_o were $2.0\,\mathrm{mm}$ and $1.76\,\mathrm{mm}$. Compared to the monodisperse flows in figure 5.2, the bidisperse mixture develops a pronounced fingering pattern within 5 seconds, at a much smaller critical radius. This is a result of both thinning and segregation promoting the fingering instability.

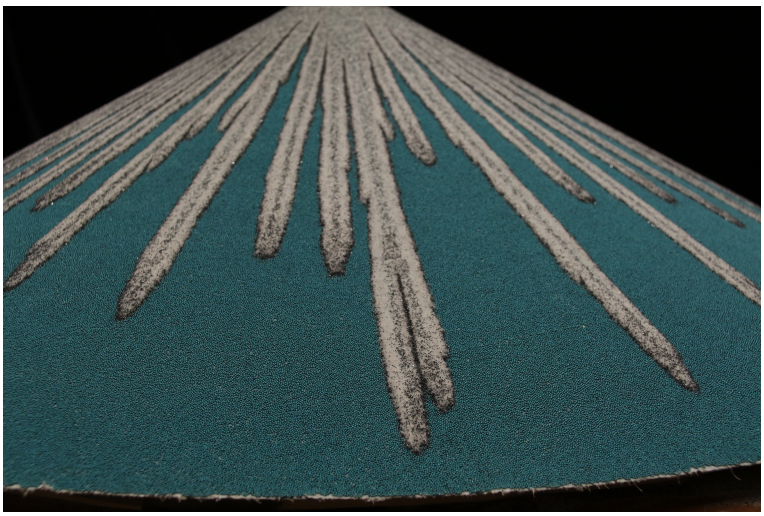

Figure 5.14: Fingers produced from a bidisperse mixture on a cone share the same characteristics as the fingering-channels produced on a planar chute shown in figure 1.4, namely coarse grained levees, large-particle rich fronts and a channel-lining containing less frictional small grains.

looked promising, the wavelength was grid-dependent. Work is now under way to use the depth-averaged $\mu(I)$-rheology to set the wavelength (Gray *et al.*, 2015).

The segregation equation (1.12) in conical co-ordinates takes the form

$$\frac{\partial \phi}{\partial t} + \frac{1}{\mathcal{M}}\frac{\partial}{\partial r}\left(\phi u_r \mathcal{M}\right) + \frac{1}{\mathcal{M}}\frac{\partial}{\partial \theta}\left(\phi u_\theta\right) + \frac{1}{\mathcal{M}}\frac{\partial}{\partial z}\left(\phi u_z \mathcal{M}\right) - \frac{\partial}{\partial z}\left(\tilde{F}(\phi)\right) = \frac{\partial}{\partial z}\left(D\frac{\partial \phi}{\partial z}\right), \quad (5.76)$$

where ϕ is the small particle concentration. This may be depth-averaged through the depth-averaging operation (5.65) to give

$$\frac{\partial}{\partial t}\left(\bar{\phi}h\right) + \frac{1}{r}\frac{\partial}{\partial r}\left(r\overline{\phi u_r}h\right) + \frac{1}{r\cos\zeta}\frac{\partial}{\partial \theta}\left(\overline{\phi u_\theta}h\right) - \phi\left[\frac{\partial s}{\partial t} + u_r^s\frac{\partial s}{\partial r} + \frac{1}{\mathcal{M}}u_\theta^s\frac{\partial s}{\partial \theta} - u_z^s\right]$$
$$+\phi\left[\frac{\partial b}{\partial t} + u_r^b\frac{\partial b}{\partial r} + \frac{1}{\mathcal{M}}u_\theta^b\frac{\partial b}{\partial \theta} - u_z^b\right] + \left[\tilde{F}(\phi) - D\frac{\partial \phi}{\partial z}\right]_{z=b}^{z=s} = 0, \quad (5.77)$$

where $\bar{\phi}$ is the depth-averaged concentration of small particles and $\overline{\phi u_r}$, $\overline{\phi u_\theta}$ are the depth-averaged fluxes of small particles in the radial and axial directions. The first two square brackets disappear due to the kinematic boundary conditions at the surface and base of the flow (5.26), whilst the third square bracket also vanishes as a result of zero flux at the surface and base of the flow (3.3). Thus

$$\frac{\partial}{\partial t}\left(\bar{\phi}h\right) + \frac{1}{r}\frac{\partial}{\partial r}\left(r\overline{\phi u_r}h\right) + \frac{1}{r\cos\zeta}\frac{\partial}{\partial \theta}\left(\overline{\phi u_\theta}h\right) = 0, \quad (5.78)$$

Following Gray & Kokelaar (2010), a number of assumptions allow the model to be closed by relating $\bar{\phi}$, $\overline{\phi u_r}$, and $\overline{\phi u_\theta}$ to the depth-averaged concentration $\bar{\phi}$ and

the depth averaged velocity $\overline{\boldsymbol{u}}$. Firstly, the avalanche is assumed to be inversely graded, with large particles above the small particles. This assumption is holds if the length scale for complete segregation is much less than the typical length scale of the avalanche R. The interface between the two particles is assumed to lie at $z = l$, i.e.

$$\phi = \begin{cases} 0 & l \leqslant z \leqslant s, \\ 1 & b \leqslant z < l. \end{cases} \tag{5.79}$$

Thus the depth-integrated concentration $\overline{\phi}$ can be calculated to be

$$\overline{\phi}h = \int_b^s \phi \, \mathrm{d}z = \int_b^l \mathrm{d}z = l - b = \eta. \tag{5.80}$$

Whilst the actual flow was shown to follow a Bagnold velocity profile, the simplifying assumption is made that the velocity $\boldsymbol{u}$ scales linearly with the depth

$$\boldsymbol{u} = \alpha\overline{\boldsymbol{u}} + 2(1-\alpha)\overline{\boldsymbol{u}}\left(\frac{z-b}{h}\right). \tag{5.81}$$

The parameter α controls the amount of shear across the layer, with $\alpha = 0$ corresponding to simple shear and $\alpha = 1$ giving plug flow. This assumption captures the leading order behaviour, and greatly simplifies the analysis. Using (5.81), the depth-averaged radial concentration flux $\overline{\phi u_r}$ can be calculated to be

$$\begin{aligned} \overline{\phi u_r}h = \int_b^s \phi u_r \, \mathrm{d}z &= \int_b^l \alpha\overline{u}_r + 2(1-\alpha)\overline{u}_r\left(\frac{z-b}{h}\right) \mathrm{d}z \\ &= \overline{u}_r\eta - (1-\alpha)\left(1-\frac{\eta}{h}\right)\overline{u}_r\eta. \end{aligned} \tag{5.82}$$

Similarly, the depth-averaged axial concentration flux can be calculated to be

$$\overline{\phi u_\theta}h = \overline{u}_\theta\eta - (1-\alpha)\left(1-\frac{\eta}{h}\right)\overline{u}_\theta\eta. \tag{5.83}$$

Substituting (5.82) and (5.83) into the depth-averaged segregation equation (5.78) gives

$$\begin{aligned} 0 = \frac{\partial}{\partial t}\left(\overline{\phi}h\right) + \frac{1}{r}\frac{\partial}{\partial r}\left(r\left\{\overline{u}_r\eta - (1-\alpha)\left(1-\frac{\eta}{h}\right)\overline{u}_r\eta\right\}\right) \\ + \frac{1}{r\cos\zeta}\frac{\partial}{\partial\theta}\left(\overline{u}_\theta\eta - (1-\alpha)\left(1-\frac{\eta}{h}\right)\overline{u}_\theta\eta\right). \end{aligned} \tag{5.84}$$

Gray & Kokelaar (2010) named this the 'large particle transport equation' since it preferentially transports large particles to the front of the flow. A concentration-averaged basal friction coefficient

$$\mu = \mu^l(1-\overline{\phi}) + \mu^s\overline{\phi} \tag{5.85}$$

allows (5.84) to be coupled with the depth averaged mass and momentum equations (5.73)–(5.75). In the above equation, μ^l and μ^s are independent basal friction coefficients for the large and small phases respectively, with $\mu^l > \mu^s$ required for a frictional front and fingering instability to develop. If numerical simulations of monodisperse flows on a cone prove successful, then the system of equations (5.73)–(5.75), & (5.84) could be used for simulating bidisperse flows in this geometry.

5.6 Discussion and future work

This chapter has presented some early experimental results from granular flow over a conical surface, along with a continuum model in a orthogonal conical coordinate system. The experiments show that the flow initially spreads radially, before developing a beautiful fingering pattern. This fingering pattern is a contrast to flow on a inclined plane, which has a steady velocity and uniform height with a stable front that propagates as a straight line. As a result of the radial spreading in the conical geometry, the velocity of the flow front decreases as it moves downstream. The theory also predicts that the flow thins as it spreads. The critical fingering radius r_{crit} can be seen to scale linearly with the initial flux Q; this relationship is also found through a depth-averaged model at leading order. In addition, the depth-averaged model suggests that the critical height at which the flow starts to develop fingers is $h_{crit} = 1.10\,\mathrm{mm}$, which is within experimental error of $h_{start} = 1.09\,\mathrm{mm}$. Although the exact cause of the fingering instability is currently unknown, one possible explanation is that the flow becomes unstable to small perturbations once the flow height has thinned below h_{start}. The small axial perturbations that can be seen in figures 5.4–5.7 could then coarsen and develop into a full fingering pattern. However, further work is needed to confirm this hypothesis. Firstly a laser profilometer could be used to provide experimental validation of the thinning law predicted by (5.59a). Secondly, perturbations could be introduced to the flow at points where the height is below h_{start} to determine whether the instability grows or decays away. If these techniques do confirm the above hypothesis, the fundamental question still remains as to the physical mechanism(s) causing the granular front to become unstable at heights below h_{start}. Image analysis using images from a very high speed

camera, or colour-change experiments in which a batch of coloured grains is introduced during the flow may provide some insights. Numerical simulations of the full depth-averaged equations (5.66)–(5.75) may also be a valuable tool.

Further work is also needed to understand the transition region between the initial fingering instability, and the development of channels that appear to have a constant width. Are the width of the developed channels really constant, or do they creep in time? Do more pronounced levees form as there is a larger mass flux through the fingers? What sets the width of a stable channel? And finally, what fundamental physical mechanism causes the initial fingers to re-adjust into these stable channels? All of these questions are still open and could potentially illuminate new secrets behind the behaviour of granular materials.

The fact that a monodisperse material can develop fingering patterns similar to those observed through segregation in figure 1.4 highlights the complex nature of the $\mu(I)$-rheology. Yet, whilst many advances have been made in our understanding of monodisperse flows, the rheology of bidisperse and polydisperse materials is still an open question. Since the rheology has such an important influence on the flow dynamics, further work in this area may uncover behaviour that is just as significant as the segregation process.

6. CONCLUSION

Size-segregation is an important process within dense granular flows that occur in both geophysical and industrial environments. This natural sorting by size of the constituents is not only problematic in industry, where a homogeneous mixing is often desired, but also increases the destructive ability of natural avalanches by playing a crucial role in the formation of coarse-grained levees that allow the flow to travel over larger distances and at higher velocities. Understanding segregation is thus of widespread importance, and this thesis has extended a continuum model for segregation in dense granular flows. The major contribution of this work has been to examine the influence of the local concentration field on segregation of a bidisperse mixture; in particular, modelling the physical observations that a small particle percolates downwards through a region of many large particles at a faster rate than a large particle rises upwards through a region of many small particles.

Chapter 2, the paper titled *"Asymmetric flux models for particle-size segregation in granular avalanches"*, is a theoretical study that introduces a revised model, which takes into account the observations of an asymmetry between the segregation of small particles surrounded by many large particles and large particles surrounded by many small particles. A detailed derivation of the governing (bidisperse) segregation equation is presented, which is used throughout the thesis. The paper also introduces a new general class of asymmetric flux functions, which have the property that their maximum amplitude is skewed towards lower concentrations of small particles. The flux functions are also normalised to have the same amplitude as the symmetric quadratic flux function, and may either be convex or non-convex with a single inflexion point. With this new class of flux functions, the maximum velocity of the small particles is increased above that obtained with the symmetric quadratic flux, but the maximum velocity of the large particles is decreased. This

entire class of general flux functions is, therefore, able to capture the behaviour that large particles segregate in regions of many small particles at a slower rate than a small particle segregating in regions of many large particles. The simplest member of this class of flux functions is the simple cubic family of flux functions with a single asymmetry parameter. This is used to match against experimental data in chapter 3, and is also used to derive breaking wave structures in chapter 4. Chapter 2 also introduces the method of characteristics, that can be used to derive solutions to the hyperbolic segregation equation in the limit of no diffusive remixing. Although this limit is a theoretical simplification, it is useful in assessing the effects of the asymmetric concentration dependence on the segregation. The remainder of the chapter derives exact solutions for the cases of a homogeneous inflow and a normally graded inflow, with small particles initially above the large. These exact solutions demonstrate that the asymmetry causes the maximum segregation distance for a homogeneous inflow to become dependent on the initial inflow concentration, with flows containing a higher proportion of small particles taking a larger distance to completely segregate. The exact solution for the normally graded inflow shows that the ratio of the distances for the first small particle to reach the base, and the first large particle to reach the surface, becomes dependent on the strength of asymmetry parameter.

Chapter 3, the letter titled *Underlying Asymmetry within Particle Size Segregation*, used a classical shearbox set-up and the refractive index-matched scanning technique to experimentally study segregation dynamics on bulk and particle scales, and compare it with the theoretical model derived in chapter 2. The asymmetry between the small and large particle velocities is quantified, with a single small particle segregating through regions of large particles three times faster than a single large particle segregating in regions of small particles. The single small particle also exhibits a step-like motion as it falls downwards through layers of large particles, whilst the motion of a single large particle motion is smoother, and likely to be linked to the rearrangements of the surrounding small particles. Large particles are also seen to move quickest when they are close to other large particles at an intermediate concentration. Measurements of the final segregation time, mean displacement per cycle and the bulk concentration show very good agreement with

the continuum segregation using a asymmetric cubic segregation flux function. Not only does this provide experimental evidence for the asymmetric model, but it also opens up parallels with other processes such as sedimentation and traffic flow where asymmetric fluxes are commonly employed.

Segregation in natural granular avalanches can create a complex recirculation motion: large particles that segregate to the top of the flow are transported towards the front, where they are overrun and then re-segregated upwards. Chapter 4, the paper titled *"Asymmetric breaking size-segregation waves in dense granular free-surface flows"* analyses the asymmetric particle motion within this recirculation zone. A moving bed flume was used to create a (mathematically) equivalent configuration to the avalanche recirculation, and both experiments and discrete particle simulations in this set-up revealed that, whilst the majority of large particles recirculate very quickly towards the front of the flow, a few large particles travel very slowly towards the rear and take a long time to recirculate. The asymmetric segregation flux model in the non-diffuse hyperbolic limit is used to derive structures for this recirculation zone that are known as "breaking-waves size-segregation waves". Compared to previous solutions using a symmetric quadratic flux (Thornton & Gray, 2008), the non-convex asymmetric flux functions can produce a new 'lens-tail' structure, in which a few large particles recirculate very slowly towards the rear of the flow. These particles are shown to take longer to recirculate, and also increase the length of the breaking wave region.

Whilst the work in this thesis has analysed and experimentally validated a theory for segregation in dense granular flows using asymmetric flux functions, a few questions still remain open with regards to the model. Firstly, although the cubic flux gives good quantitative agreement in a shearbox environment, the precise form of the asymmetric flux function may depend on the exact flow configuration. The amount of asymmetry may also be linked to the size ratio between the constituents, with larger size differences exhibiting greater asymmetry. A firm understanding of these parts of the model would allow this theory to be used confidently as a predictive tool.

The results of chapter 5 provide an important illustration of the context to the entire segregation model. Granular materials are known to have a complex rheological behaviour, with monodisperse flows described by a $\mu(I)$-rheology. The rheology is linked closely to the basal friction through two angles, ζ_1 and ζ_2, which are the angles at which a material starts to flow and starts to accelerate, respectively. Between these angles, and provided the height is greater than the critical height h_{start}, a monodisperse flow down an inclined plane will flow steadily with a constant speed and uniform height. Previous authors (Malloggi *et al.*, 2006) found a metastable region with heights between h_{stop} and h_{start} in which the flow front was unstable to transverse perturbations. Whilst the authors acknowledged that accessing this metastable regime can be problematic, the novel experiments in this chapter in a conical geometry force the flow to consistently thin. It was seen that at a critical height very close to h_{start}, the steady flow splits into a number of regular fingers. The only difference between a flow down a chute, and the flow on the cone is the slowing and thinning, implying that the frontal instability is solely due to the rheology in the region where the height is less than h_{start}. These results demonstrate the importance of the rheology for monodisperse flows, and yet, the rheology of bidisperse or polydisperse materials still remains poorly understood. For example, it is still not known how segregation, or the local particle concentration, changes the rheology of the flow, or even whether the local rheology of the flow changes the local segregation rate? At particle-scales, the rheology of a dense granular flow and the segregation are both intrinsically linked to the inter-particle contacts and the grain matrix, and so it is likely that they are both inter-related in some manner. Limited work has been performed in identifying a possible inertial number for polydisperse flows (Rognon *et al.*, 2007; Tripathi & Khakhar, 2011), but an extensive evaluation for this is required. Such an inertial number may provide one way of linking segregation and rheology.

Considering figure 6 in chapter 4, there are quite a few factors which may contribute to the differences between the time-averaged concentration plots of the experiments and DEM simulations, and the theoretical breaking wave. Local shear-rates, height dependence and finite grain sizes may all be factors in the difference. However the complex link between rheology and segregation may also have an

important role to play, and could potentially link all of these factors together. Currently, segregation theories tend to isolate individual factors such as the shear-rate, height dependence and concentration dependence and examine their influence. However, all the processes are likely to be inter-linked with the poly-disperse rheology. Thus a holistic approach to modelling segregation that is formulated around the rheology might result in the most accurate theory.

BIBLIOGRAPHY

ANCEY, C., COUSSOT, P. & EVESQUE, P. 1999 A theoretical framework for granular suspensions in a steady simple shear flow. *J. Rheol.* **43** (6), 1673–1699.

ANDREOTTI, B., FORTERRE, Y. & POULIQUEN, O. 2013 *Granular Media: Between Fluid and Solid*. Cambridge University Press.

ARANSON, I. S. & TSIMRING, L. S. 2008 *Granular Patterns*. Oxford University Press.

BAGNOLD, R. A. 1954 Experiments on gravity-free dispersion of large solid spheres in a newtonian fluid under shear. *Proc. Roy. Soc. Lond. A* **225**, 49–63.

BAKER, J. L., BARKER, T. & GRAY, J. M. N. T. 2016 A two-dimensional depth-averaged $\mu(I)$-rheology for dense granular avalanches. *J. Fluid Mech.* **787**, 367–395.

BARKER, T., SCHAEFFER, D. G., BOHORQUEZ, P. & GRAY, J. M. N. T. 2015 Well-posed and ill-posed behaviour of the $\mu(I)$-rheology for granular flow. *J. Fluid Mech.* **779**, 794–818.

BARTELT, P. & MCARDELL, B. W. 2009 Granulometric investigations of snow avalanches. *J. Glaciol.* **55** (193), 829–833.

BATCHELOR, G. K. 1967 *An Introduction to Fluid Dynamics*. Cambridge, UK: Cambridge University Press.

BIDE, T., BROWN, T. J., HOBBS, S. F. & IDOINE, N. 2014 United Kingdom Minerals Yearbook. Minerals and Waste Programme Open Report OR/15/043. British Geological Survey, Keyworth, Nottingham.

BÖRZSÖNYI, T., HALSEY, T. C. & ECKE, R. E. 2008 Avalanche dynamics on a rough inclined plane. *Phys. Rev. E* **78**, 011306.

BOURNE, J. R. 1964 The mixing of powders, pastes, and non-newtonian fluids. *The Chemical Engineer* **181**, 202–216.

BRIDGWATER, J. 1976 Fundamental powder mixing mechanisms. *Powder Technol.* **15**, 215–236.

BRIDGWATER, J. 1994 Mixing and segregation mechanisms in particle flow. In *Granular Matter* (ed. A. Mehta), pp. 161–193. Springer New York.

BRIDGWATER, J., FOO, W. & STEPHENS, D. 1985 Particle mixing and segregation in failure zones - theory and experiment. *Powder Technol.* **41**, 147–158.

CAMPBELL, C. S. 1990 Rapid granular flows. *Ann. Rev. Fluid Mech.* **2** (1), 57–92.

CAS, R. A. & WRIGHT, J. V. 1987 *Volcanic Successions*. Allen and Unwin.

CASSAR, C., NICOLAS, M. & POULIQUEN, O. 2005 Submarine granular flows down inclined planes. *Phys. Fluids* **17** (10), 103301.

CELLAI, D., CREGAN, V., CURTIS, M., FOWLER, A., HINCH, J., HOCKING, G., MCGUINNESS, M., MURNANE, J., O'BRIEN, S. & SMITH, N. 2012 Particle size segregation in granular flow in silos. Technical Report from MACSI's 2012 Problem-Solving Workshop with Industry MACSI/ESGI/0032. Mathematics Applications Consortium for Science & Industry.

COSTA, J. E. & WILLIAMS, G. 1984 Debris flow dynamics. *Tech. Rep.* 84–606. (videotape) U.S. Geological Survey.

DEBOEUF, S., LAJEUNESSE, E., DAUCHOT, O. & ANDREOTTI, B. 2006 Flow rule, self channelization, and levees in unconfined granular flows. *Phys. Rev. Lett.* **97**, 158303.

DINGLER, J. R. & ANIMA, R. J. 1987 Subaqueous grain flows at the head of carmel submarine canyon, california. *J. Sediment. Petrol.* **59** (2), 280–286.

DOLGUNIN, V. N. & UKOLOV, A. A. 1995 Segregation modelling of particle rapid gravity flow. *Powder Technol.* **83**, 95–103.

DURAN, J. 1999 *Sands, Powders, and Grains: An Introduction to the Physics of Granular Materials*. Springer New York.

DYER, F. C. 1929 The scope for reverse classification by crowded settling in ore-dressing practice. *Eng. Min. J.* **127** (26), 1030–1033.

EDWARDS, A. N. & GRAY, J. M. N. T. 2014 Erosion-deposition waves in shallow granular free-surface flows. *J. Fluid Mech.*, Submitted.

FAN, Y., BOUKERKOUR, Y., BLANC, T., UMBANHOWAR, P. B., OTTINO, J. M. & LUEPTOW, R. M. 2012 Stratification, segregation, and mixing of granular materials in quasi-two-dimensional bounded heaps. *Phys. Rev. E* **86**, 051305.

FAN, Y., SCHLICK, C. P., UMBANHOWAR, P. B., OTTINO, J. M. & LUEPTOW, R. M. 2014 Modelling size segregation of granular materials: the roles of segregation, advection and diffusion. *J. Fluid Mech.* **741**, 252–279.

FAN, Y., UMBANHOWAR, P. B., OTTINO, J. M. & LUEPTOW, R. M. 2013 Kinematics of monodisperse and bidisperse granular flows in quasi-two-dimensional bounded heaps. *Proc. Roy. Soc. A* **469** (2157), 20130235.

FAN, Y. I. & HILL, K. M. 2011 Theory for shear-induced segregation of dense granular mixtures. *New J. Phys.* **13** (9), 095009.

FÉLIX, G. & THOMAS, N. 2004 Relation between dry granular flow regimes and morphology of deposits: formation of levées in pyroclastic deposits. *Earth & Planetary Sci. Lett.* **221**, 197–213.

FISHER, R. V. & MATTINSON, J. M. 1968 Wheeler gorge turbidite-conglomerate series California - inverse grading. *J. Sediment. Petrol.* **38** (4), 1013–1023.

FORTERRE, Y. 2006 Kapiza waves as a test for three-dimensional granular flow rheology. *J. Fluid Mech.* **563**, 123–132.

FORTERRE, Y & POULIQUEN, O 2003 Long-surface-wave instability in dense granular flows. *J. Fluid Mech.* **486**, 21–50.

FORTERRE, Y. & POULIQUEN, O. 2008 Flows of dense granular media. *Ann. Rev. Fluid Mech.* **40** (1), 1–24.

GAJJAR, P. & GRAY, J. M. N. T 2014 Asymmetric flux models for particle-size segregation in granular avalanches. *J. Fluid Mech.* **757**, 297–329.

GAJJAR, P., VAN DER VAART, K., THORNTON, A. R., JOHNSON, C. G., ANCEY, C. & GRAY, J. M. N. T. 2016 Asymmetric breaking size-segregation waves in dense granular free-surface flows. *J. Fluid Mech.* **794**, 460–505.

GDR MIDI 2004 On dense granular flows. *Eur. Phys. J. E* **14**, 341–365.

GOLDHIRSCH, I. 2010 Stress, stress asymmetry and couple stress: from discrete particles to continuous fields. *Granul. Matter* **12** (3), 239–252.

GOLICK, L. A. & DANIELS, K. E. 2009 Mixing and segregation rates in sheared granular materials. *Phys. Rev. E* **80** (4), 042301.

GRAY, J. M. N. T. & ANCEY, C. 2011 Multi-component particle size-segregation in shallow granular avalanches. *J. Fluid Mech.* **678**, 535–588.

GRAY, J. M. N. T. & ANCEY, C. 2015 Particle-size and -density segregation in granular free-surface flows. *J. Fluid Mech.* **779**, 622–668.

GRAY, J. M. N. T. & CHUGUNOV, V. A. 2006 Particle-size segregation and diffusive remixing in shallow granular avalanches. *J. Fluid Mech.* **569**, 365–398.

GRAY, J. M. N. T. & EDWARDS, A. N. 2014 A depth-averaged $\mu(I)$-rheology for shallow granular free-surface flows. *J. Fluid Mech.* **755**, 503–534.

GRAY, J. M. N. T, GAJJAR, P. & KOKELAAR, P. 2015 Particle-size segregation in dense granular avalanches. *C. R. Physique* **16** (1), 73–85.

GRAY, J. M. N. T. & KOKELAAR, B. P. 2010 Large particle segregation, transport and accumulation in granular free-surface flows. *J. Fluid Mech.* **652**, 105–137.

GRAY, J. M. N. T., SHEARER, M. & THORNTON, A. R. 2006 Time-dependent solutions for particle-size segregation in shallow granular avalanches. *Proc. Roy. Soc. A* **462**, 947–972.

GRAY, J. M. N. T., TAI, Y. C. & NOELLE, S. 2003 Shock waves, dead-zones and particle-free regions in rapid granular free-surface flows. *J. Fluid Mech.* **491**, 161–181.

GRAY, J. M. N. T. & THORNTON, A. R. 2005 A theory for particle size segregation in shallow granular free-surface flows. *Proc. Roy. Soc. A* **461**, 1447–1473.

GRAY, J. M. N. T., WIELAND, M. & HUTTER, K. 1999 Free surface flow of cohesionless granular avalanches over complex basal topography. *Proc. Roy. Soc. A* **455**, 1841–1874.

GUILLARD, F., FORTERRE, Y. & POULIQUEN, O. 2014 Lift forces in granular media. *Phys. Fluids* **26** (4), 043301.

HADAMARD, J. 1922 *Lectures on Cauchy's Problem in Linear Partial Differential Equations*. New Haven, CT, USA.: Yale University Press.

HAJRA, S. K. & KHAKHAR, D. V. 2004 Sensitivity of segregation of mixtures in quasi-two-dimensional fluidized layers. *Phys. Rev. E* **69**, 031304.

HAPPEL, J. & BRENNER, H. 1965 *Low Reynolds number hydrodynamics*. Englewood Cliffs, New Jersey, USA: Prentice-Hall, Inc.

HILL, K. M. & TAN, S. D. 2014 Segregation in dense sheared flows: gravity, temperature gradients, and stress partitioning. *J. Fluid Mech.* **756**, 54–88.

HOGG, A. J. & PRITCHARD, D. 2004 The effects of hydraulic resistance on dambreak and other shallow inertial flows. *J. Fluid Mech.* **501**, 179–212.

HUNTER, R. E. 1985 Subaqueous sand-flow cross strata. *J. Sediment. Res.* **55** (6), 886–894.

HUNTER, R. E. & KOCUREK, G. 1986 An experimental study of subaquaeous slipface deposition. *J. Sediment. Res.* **56** (3), 387–394.

HUPPERT, H. E. 1982 The propagation of two-dimensional and axisymmetric viscous gravity currents over a rigid horizontal surface. *J. Fluid Mech.* **121**, 43–58.

HUPPERT, H. E. & SIMPSON, J. E. 1980 The slumping of gravity currents. *J. Fluid Mech.* **99**, 785–799.

IVERSON, R. M. 1997 The physics of debris-flows. *Reviews in Geophysics* **35**, 245–296.

JAEGER, H. M., NAGEL, S. R. & BEHRINGER, R. P. 1996 Granular solids, liquids, and gases. *Rev. Mod. Phys.* **68** (4), 1259–1273.

JENKINS, J. T. 2006 Dense shearing flows of inelastic disks. *Phys. Fluids* **18** (10), 103307.

JENKINS, J. T. & SAVAGE, S. B. 1983 A theory for the rapid flow of identical, smooth, nearly elastic, spherical particles. *J. Fluid Mech.* **130**, 187–202.

JOHANSON, J. R. 1978 Particle segregation ... and what to do about it. *Chem. Eng.* **May**, 183–188.

JOHNSON, C. G., KOKELAAR, B. P., IVERSON, R. M., LOGAN, M., LAHUSEN, R. G. & GRAY, J. M. N. T. 2012 Grain-size segregation and levee formation in geophysical mass flows. *J. Geophys. Res.* **117**, F01032.

JOP, P., FORTERRE, Y. & POULIQUEN, O. 2005 Crucial role of sidewalls in granular surface flows: consequences for the rheology. *J. Fluid Mech.* **541**, 167–192.

JOP, P., FORTERRE, Y. & POULIQUEN, O. 2006 A constitutive relation for dense granular flows. *Nature* **44**, 727–730.

JOSEPH, D. D. & SAUT, J. C. 1990 Short-wave instabilities and ill-posed initial-value problems. *Theor. Comp. Fluid Dyn.* **1**, 191–227.

KAMRIN, K. 2010 Nonlinear elasto-plastic model for dense granular flow. *Intl J. Plast.* **26** (2), 167–188.

KHAKHAR, D. V., MCCARTHY, J. J. & OTTINO, J. M. 1999 Mixing and segregation of granular materials in chute flows. *Chaos* **9** (3), 594–610.

KOKELAAR, B. P., GRAHAM, R. L., GRAY, J. M. N. T. & VALLANCE, J. W. 2014 Fine-grained linings of leveed channels facilitate runout of granular flows. *Earth Planet. Sci. Lett.* **385**, 172–180.

KUMARAN, V. 2006 The constitutive relation for the granular flow of rough particles, and its application to the flow down an inclined plane. *J. Fluid Mech.* **561**, 1–42.

KUMARAN, V. 2008 Dense granular flow down an inclined plane: from kinetic theory to granular dynamics. *J. Fluid Mech.* **599**, 121–168.

LACEY, P. M. C. 1954 Developments in the theory of particle mixing. *Journal of Applied Chemistry* **4** (5), 257–268.

LAGRÉE, P.-Y., STARON, L. & POPINET, S. 2011 The granular column collapse as a continuum: Validity of a two-dimensional Navier-Stokes model with a μ(I)-rheology. *J. Fluid Mech.* **686**, 378–408.

MAITRA, N. K. & COULSON, J. M. 1948 The unit operation of mixing part 2: A study of the rate of mixing of solid particles. *Journal of the Imperial College Chemical Engineering Society* **4** (135), 135–156.

MALLOGGI, F., LANUZA, J., ANDREOTTI, B. & CLÉMENT, E. 2006 Erosion waves: Transverse instabilities and fingering. *Europhys Lett.* **75** (5), 825–831.

MARKS, B. & EINAV, I. 2011 A cellular automaton for segregation during granular avalanches. *Granul. Matter* **13** (3), 211–214.

MARKS, B., ROGNON, P. & EINAV, I. 2012 Grainsize dynamics of polydisperse granular segregation down inclined planes. *J. Fluid Mech.* **690**, 499–511.

MAY, L. B. H., GOLICK, L. A., PHILLIPS, K. C., SHEARER, M. & DANIELS, K. E. 2010*a* Shear-driven size segregation of granular materials: Modeling and experiment. *Phys. Rev. E* **81**, 051301.

MAY, L. B. H., SHEARER, M. & DANIELS, K. E. 2010*b* Scalar conservation laws with nonconstant coefficients with application to particle size segregation in granular flow. *J. Nonlinear Sci.* **20** (6), 689–707.

MCCLENAGHAN, M. B. 2011 Overview of common processing methods for recovery of indicator minerals from sediment and bedrock in mineral exploration. *Geochem.: Explor. Environ., Anal.* **11** (4), 265–278.

MCELWAINE, J. & NISHIMURA, K. 2000 Size segregations in snow avalanches. In *IUTAM Symposium on Segregation in Granular Flows* (ed. A. D. Rosato & D. L.

Blackmore), *Solid Mechanics and Its Applications*, vol. 81, pp. 81–88. Springer Netherlands.

MIDDLETON, G. V. 1970 Experimental studies related to problems of flysch sedimentation. In *Flysch Sedimentology in North America* (ed. J. Lajoie), pp. 253–272. Toronto: Business and Economics Science Ltd.

MIDDLETON, G. V. & HAMPTON, M. A. 1976 Subaqueous sediment transport and deposition by sediment gravity flows. In *Marine sediment transport and environmental management* (ed. D. J. Stanley & D. J. P. Swift), pp. 197–218. Wiley.

MORLAND, L. W. 1992 Flow of viscous fluids through a porous deformable matrix. *Surv. Geophys.* **13** (3), 209–268.

NITYANAND, N., MANLEY, B. & HENEIN, H. 1986 An analysis of radial segregation for different sized spherical solids in rotary cylinders. *Metall. Trans. B* **17** (2), 247–257.

OLSEN, J. L. & RIPPIE, E. G. 1964 Segregation kinetics of particulate solids systems I. Influence of particle size and particle size distribution. *J. Pharm. Sci.* **53** (2), 147–150.

OTTINO, J. M. & KHAKHAR, D. V. 2000 Mixing and segregation of granular materials. *Ann. Rev. Fluid Mech.* **32** (1), 55–91.

PIERSON, T. C. 1986 Flow behavior of channelized debris flows, Mount St. Helens, Washington. In *Hillslope Processes* (ed. A. D. Abrahams), pp. 269–296. Winchester, MA.: Allen and Unwin.

POULIQUEN, O. 1999 Scaling laws in granular flows down rough inclined planes. *Phys. Fluids* **11** (3), 542–548.

POULIQUEN, O., CASSAR, C., JOP, P., FORTERRE, Y. & NICOLAS, M. 2006 Flow of dense granular material: towards simple constitutive laws. *J. Stat. Mech.* **2006** (07), P07020.

POULIQUEN, O., DELOUR, J. & SAVAGE, S. B. 1997 Fingering in granular flows. *Nature* **386**, 816–817.

POULIQUEN, O. & FORTERRE, Y. 2002 Friction law for dense granular flows: application to the motion of a mass down a rough inclined plane. *J. Fluid Mech.* **453**, 133–151.

POULIQUEN, O. & FORTERRE, Y. 2009 A non-local rheology for dense granular flows. *Philos. T. Roy. Soc. A* **367** (1909), 5091–5107.

POULIQUEN, O. & VALLANCE, J. W. 1999 Segregation induced instabilities of granular fronts. *Chaos* **9** (3), 621–630.

RAZIS, D., EDWARDS, A. N., GRAY, J. M. N. T. & VAN DER WEELE, K. 2014 Arrested coarsening of granular roll waves. *Phys. Fluids* **26** (12), 123305.

RIPPIE, E. G., OLSEN, J. L. & FAIMAN, M. D. 1964 Segregation kinetics of particulate solids systems II. Particle densitysize interactions and wall effects. *J. Pharm. Sci.* **53** (11), 1360–1363.

ROGERS, A.R. & CLEMENTS, J. A. 1972 The examination of segregation of granular materials in a tumbling mixer. *Powder Technol.* **5** (3), 167–178.

ROGNON, P. G., ROUX, J. N., NAAIM, M. & CHEVOIR, F. 2007 Dense flows of bidisperse assemblies of disks down an inclined plane. *Phys. Fluids* **19** (5), 058101.

ROSATO, A. D., STRANDBURG, K. J., PRINZ, F. & SWENDSON, R. H. 1987 Why the brazil nuts are on top - size segregation of particulate matter by shaking. *Phys. Rev. Lett.* **58**, 1038–1040.

RUBAN, A. I. & GAJJAR, J. S. B. 2014 *Fluid Dynamics: Part 1: Classical Fluid Dynamics*. Oxford, U.K.: Oxford University Press.

SAVAGE, S. B. & HUTTER, K. 1989 The motion of a finite mass of granular material down a rough incline. *J. Fluid Mech.* **199**, 177–215.

SAVAGE, S. B. & LUN, C. K. K. 1988 Particle size segregation in inclined chute flow of dry cohesionless granular solids. *J. Fluid Mech.* **189**, 311–335.

SCHMINCK, H. U. 1967 Graded lahars in type sections of ellensburg formation south-central washington. *J. Sediment. Petrol.* **37** (2), 438–448.

SCHRÖTER, M., ULRICH, S., KREFT, J., SWIFT, J. B. & SWINNEY, H. L. 2006 Mechanisms in the size segregation of a binary granular mixture. *Phys. Rev. E* **74** (1), 011307.

SCHULZE, D. 2008 *Powders and Bulk Solids*. Springer Berlin Heidelberg.

SCOTT, A. M. & BRIDGWATER, J. 1975 Interparticle percolation: A fundamental solids mixing mechanism. *Ind. Eng. Chem. Fund.* **14** (1), 22–27.

SHINBROT, T. & MUZZIO, F. J. 2000 Nonequilibrium patterns in granular mixing and segregation. *Phys. Today* **53** (3), 25–30.

SILBERT, L. E., ERTAS, D., GREST, G. S., HALSEY, T. C., LEVINE, D. & PLIMPTON, S. J. 2001 Granular flow down an inclined plane: Bagnold scaling and rheology. *Phys. Rev. E* **64** (5, 1), 051302.

SOHN, Y. K. & CHOUGH, S. K. 1993 The Udo Tuff cone, Cheju Island, South Korea: transformation of pyroclastic fall into debris fall and grain flow on a steep volcanic cone slope. *Sedimentology* **40** (4), 769–786.

STANDELMANN, R. 1988 Colossal feats of engineering. *The UNESCO Courier* **16** (9), 12–16, 'Egypt of the Pharaohs'.

STARON, L., LAGRÉE, P.-Y. & POPINET, S. 2012 The granular silo as a continuum plastic flow: The hour-glass vs the clepsydra. *Phys. Fluids* **24** (10), 103301.

STARON, L., LAGRÉE, P.-Y. & POPINET, S. 2014 Continuum simulation of the discharge of the granular silo. *Eur. Phys. J. E* **37** (1), –.

STARON, L., LAGREÉE, P.-Y. & POPINET, S. 2013 Discharge of a granular silo as a visco-plastic flow. *AIP Conf. Proc.* **1542**, 1290–1293.

STARON, L. & PHILLIPS, J. C. 2014 Segregation time-scale in bi-disperse granular flows. *Phys. Fluids* **26** (3), 033302.

STARON, L. & PHILLIPS, J. C. 2015 Stress partition and microstructure in size-segregating granular flows. *Phys. Rev. E* **92**, 022210.

TAKAGI, D. & HUPPERT, H. E. 2010 Flow and instability of thin films on a cylinder and sphere. *J. Fluid Mech.* **647**, 221–238.

TAKAGI, D., MCELWAINE, J. N. & HUPPERT, H. E. 2011 Shallow granular flows. *Phys. Rev. E* **83**, 031306.

THORNTON, A. R. & GRAY, J. M. N. T. 2008 Breaking size-segregation waves and particle recirculation in granular avalanches. *J. Fluid Mech.* **596**, 261–284.

THORNTON, A. R., GRAY, J. M. N. T. & HOGG, A. J. 2006 A three-phase mixture theory for particle size segregation in shallow granular free-surface flows. *J. Fluid Mech.* **550**, 1–25.

THORNTON, A. R., WEINHART, T., LUDING, S. & BOKHOVE, O. 2012 Modeling of particle size segregation: calibration using the discrete particle method. *Int. J. Mod. Phys. C* **23** (8), 1240014.

TRAIN, D. 1960 Mixing of pharmaceutical solids: The general approach. *J. Am. Pharm. Assoc.* **49** (5), 265–271.

TRIPATHI, A. & KHAKHAR, D. V. 2011 Rheology of binary granular mixtures in the dense flow regime. *Phys. Fluids* **23**, 113302.

TUNUGUNTLA, D., BOKHOVE, O. & THORNTON, A. R. 2014 A mixture theory for size and density segregation in shallow granular free-surface flows. *J. Fluid Mech.* **749**, 99–112.

TUNUGUNTLA, D., THORNTON, A. R. & WEINHART, T. 2015 From discrete elements to continuum fields: Extension to bidisperse systems. *Comp. Part. Mech.* , In Press.

VAN DER VAART, K., GAJJAR, P., EPELY-CHAUVIN, G., ANDREINI, N., GRAY, J. M. N. T. & ANCEY, C. 2015 Underlying asymmetry within particle size segregation. *Phys. Rev. Lett.* **114**, 238001.

VALLANCE, J. W. & SAVAGE, S. B. 2000 Particle segregation in granular flows down chutes. In *IUTAM Symposium on segregation in granular materials* (ed. A. D. Rosato & D. L. Blackmore). Kluwer.

WEINHART, T., LUDING, S. & THORNTON, A. R. 2013 From discrete particles to continuum fields in mixtures. *AIP Conf. Proc.* **1542** (1), 1202–1205.

WIEDERSEINER, S., ANDREINI, N., EPELY-CHAUVIN, G., MOSER, G., MONNEREAU, M., GRAY, J. M. N. T. & ANCEY, C. 2011 Experimental investigation into segregating granular flows down chutes. *Phys. Fluids* **23**, 013301.

WILLIAMS, J. C. 1976 The segregation of particulate materials - review. *Powder Technol.* **15** (2), 245–251.

WILLIAMS, S. C. 1968 The mixing of dry powders. *Powder Technol.* **2** (1), 13–20.

WOODHOUSE, M. J., THORNTON, A. R., JOHNSON, C. G., KOKELAAR, B. P. & GRAY, J. M. N. T. 2012 Segregation-induced fingering instabilities in granular free-surface flows. *J. Fluid Mech.* **709**, 543–580.